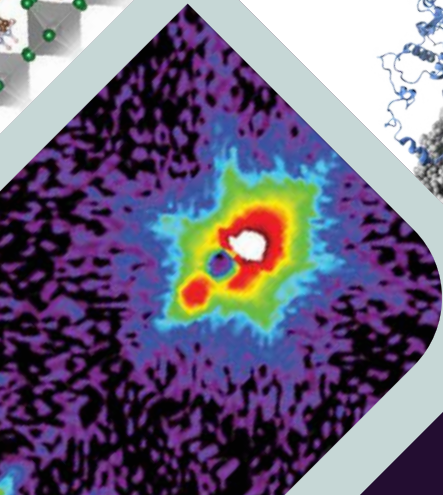
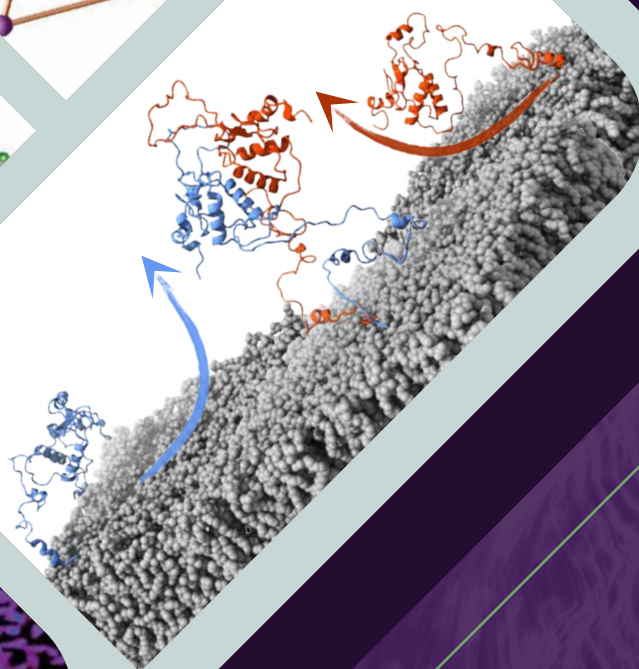
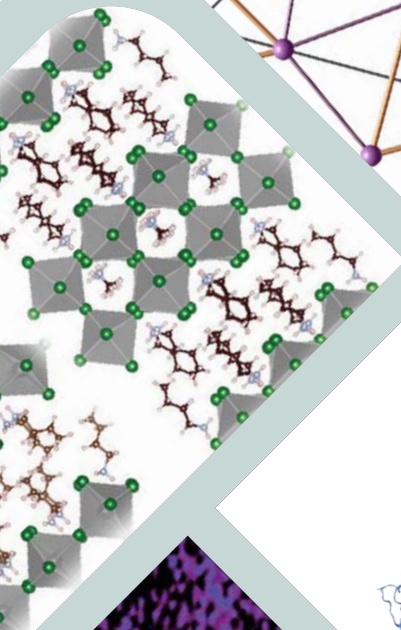
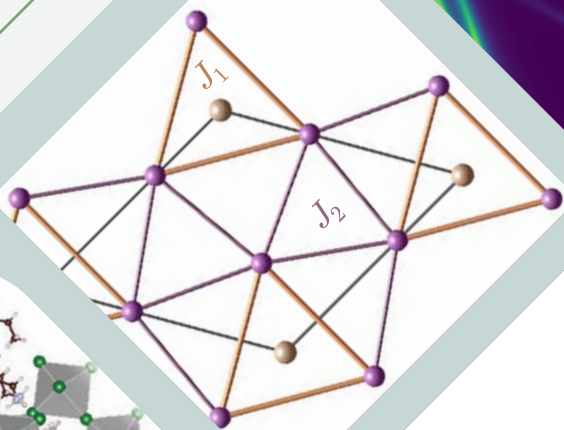
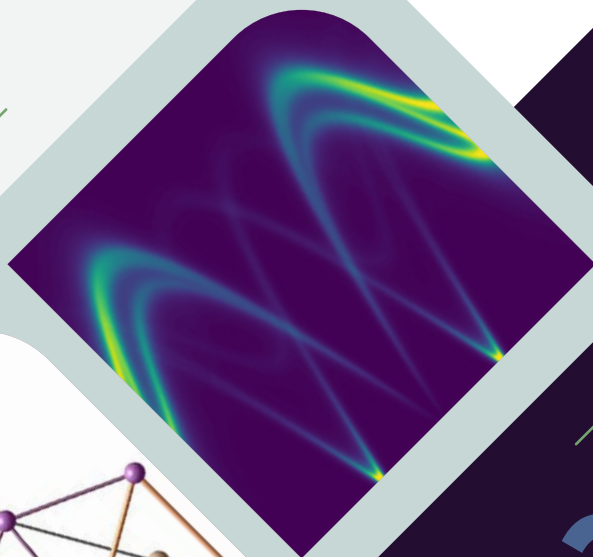


NIST CENTER FOR
NEUTRON RESEARCH

ACCOMPLISHMENTS
AND OPPORTUNITIES

NIST SP 1294



2023

NIST
National Institute of
Standards and Technology
U.S. Department of Commerce



ON THE COVER

The NCNR's neutron source provides a valuable research tool for a wide variety of scientific fields from biological systems, engineering materials, to magnetic structures, and more. The cover features data from only a few of the experiments highlighted in this report.



NIST SPECIAL PUBLICATION 1294

2023 NIST Center for Neutron Research Accomplishments and Opportunities

James M. Adams, Director (Acting)

Steven R. Kline, Editor

This publication is available free of charge from:

<https://doi.org/10.6028/NIST.SP.1294>

DECEMBER 2023



U.S. Department of Commerce
Gina M. Raimondo, Secretary

National Institute of Standards and Technology
Laurie E. Locascio, NIST Director and Under Secretary of Commerce for Standards and Technology

DISCLAIMER

Certain commercial entities, equipment, or materials may be identified in this document to describe an experimental procedure or concept adequately. Such identification is not intended to imply recommendation or endorsement by the National Institute of Standards and Technology, nor is it intended to imply that the entities, materials, or equipment are necessarily the best available for the purpose. Throughout the text, unless otherwise stated, q (or Q) refers to the momentum transfer. Error bars in figures and uncertainties in the text represent one standard deviation unless otherwise stated.

National Institute of Standards and Technology Special Publication 1294,
87 pages (December 2023)

CODEN: NSPUE2

This publication is available free of charge from:
<https://doi.org/10.6028/NIST.SP.1294>

Table of Contents

2	FOREWORD	
3	THE NIST CENTER FOR NEUTRON RESEARCH	
4	NIST CENTER FOR NEUTRON RESEARCH INSTRUMENTS	
	ANALYTICAL CHEMISTRY	
6	Prompt gamma ray activation analysis for determining chemical composition of 3D printing and casting materials used in biomedical applications, R. L. Paul, <i>et al.</i>	
	BIOSCIENCES	
8	α -Synuclein fibril formation in the presence of lipid bilayer discs, M. Dubackic, <i>et al.</i> (CHRNS)	
10	Observing dimer formation with neutron reflectometry: HIV-1 Nef at the lipid membrane, F. Heinrich, <i>et al.</i>	
12	Tales of two tails: nanoscale bending dynamics in chain asymmetric lipid membranes, E. G. Kelley, <i>et al.</i> (CHRNS)	
	CHEMICAL PHYSICS	
14	Non-cryogenic air separation using aluminum formate, $\text{Al}(\text{HCOO})_3$ (ALF), D. Mullangi, <i>et al.</i>	
16	<i>In situ</i> neutron reflectometry of tungsten oxide films to probe the evolution of Li-ion battery anode/electrolyte interfaces, E. D. Rus, <i>et al.</i>	
18	Influence of inorganic layer thickness on methylammonium dynamics in hybrid perovskite derivatives, A. A. Koegel, <i>et al.</i> (CHRNS)	
20	Wall-polymer interactions and morphology around interfaces determine polymer mobility and CO_2 uptake of solid-supported amine CO_2 sorbents, H. J. Moon, <i>et al.</i>	
	CONDENSED MATTER	
22	Three-dimensional structure of hybrid magnetic skyrmions determined by neutron scattering, W. L. N. C. Liyanage, <i>et al.</i> (CHRNS)	
24	Neutron spectroscopy of the spin-orbital excitons in HoBi, J. Gaudet, <i>et al.</i> (CHRNS)	
26	Neutron-scattering sum rules, symmetric exchanges, and helicoidal magnetism in MnSb_2O_6 , E. Chan, <i>et al.</i> (CHRNS)	
28	Formation of a simple cubic antiferromagnet through charge ordering in a double Dirac material, T. Berry, <i>et al.</i>	
30	Boron's dramatic enhancement of the voltage-controlled antiferromagnetic switching in $\text{B:Cr}_2\text{O}_3$ spintronics devices, A. Mahmood, <i>et al.</i>	
	ENGINEERING PHYSICS	
32	Assessment of dose reduction strategies in wavelength-selective neutron tomography, M. C. Daugherty, <i>et al.</i>	
	GEOLOGY	
34	Gas diffusion through variably-water-saturated zeolitic tuff: implications for transport following a subsurface nuclear event, C. W. Neil, <i>et al.</i>	
	INSTRUMENTATION	
36	The Autonomous Formulation Laboratory: self-driving phase mapping using SAXS and SANS, P. A. Beaucage, <i>et al.</i>	
38	Classification and authentication of materials using prompt-gamma-ray-activation analysis, N. A. Mahynski, <i>et al.</i>	
	SOFT MATTER	
40	Rapid ordering of block copolymer films by hiking down the free energy landscape in sequential solvent and thermal annealing, K. Sharma, <i>et al.</i>	
42	Correlating the diffusion of water in model polyamides to their performance as reverse osmosis desalination membranes, K. Ito, <i>et al.</i> (CHRNS)	
44	Relationship between ion transport and phase behavior in polymer blend electrolytes, J. Lee, <i>et al.</i>	
46	Tracking the real-time kinetics and internal structure of light-initiated nanogel-based hydrogels using neutrons, M. J. Majcher, <i>et al.</i> (CHRNS)	
	ADVANCES IN MEASUREMENT	
48	Advanced polarization analysis capability on VSANS, W. C. Chen, <i>et al.</i> (CHRNS)	
49	Watching ionic motion switch magnetism in multi-region patterned devices, S. Sheffels, <i>et al.</i>	
50	A different angle on bending neutron beams, C. Kapahi, <i>et al.</i>	
51	NEUTRON SOURCE OPERATIONS	
53	NEW NIST NEUTRON SOURCE	
56	FACILITY DEVELOPMENT	
58	SERVING THE SCIENCE AND TECHNOLOGY COMMUNITY	
61	THE CENTER FOR HIGH RESOLUTION NEUTRON SCATTERING (CHRNS)	
71	2023 AWARDS	
74	PUBLICATIONS: AUGUST 1, 2022 TO JULY 31, 2023	
85	INSTRUMENTS AND CONTACTS	
86	NIST CENTER FOR NEUTRON RESEARCH CONTACTS	

Foreword



It is my distinct pleasure to present this year's annual report for the NIST Center for Neutron Research, my first since being appointed as the Center's Director earlier this year. 2023 was a year packed with activity, as we endeavor to return the NCNR to a normal operating posture while simultaneously maintaining the vibrancy and productivity of our research programs in neutron science. The NCNR achieved a vitally

important milestone in March 2023 when the reactor was taken critical for the first time since the February 2021 refueling incident that resulted in a damaged fuel element and contamination of the reactor primary system. We subsequently operated the reactor at low power for purposes of reactor testing, operator training and licensing, and evaluating the efficacy of our efforts aimed at removing residual nuclear fuel debris remaining in the primary cooling system.

Operating at low power levels, these operations revealed that while the overwhelming majority of vessel contamination was removed successfully, a small amount of nuclear fuel debris remains. Though small, this limited quantity poses significant operational complexities that prohibit us from re-establishing normalized operations at 20 MW. As such, our staff are planning additional mitigation efforts directed towards further reducing the level of primary system contamination. The NCNR has also made noteworthy progress discharging its obligations under the Nuclear Regulatory Commission-issued Confirmatory Order. Of note, improvements in the NCNR's nuclear safety culture are well underway, which the staff have thoroughly embraced.

As recovery efforts continue, our technical staff continue to support our user community, facilitating analysis of data, applications for beamtime at other facilities, and support for collaborations. As presented in this report, in this year alone these efforts directly led to over 250 publications and countless experiments performed across the globe. Our sample environment team has supported many of these experiments, from technical consultation to shipping sample environments to support for user experiments. In this way, we are striving to build our internal expertise, learn best practices from other facilities, and maintain a vigorous user community as we work toward future scientific operations at the NCNR.

Over the past year, the NCNR made substantial progress towards a number of major facility upgrades. In collaboration with Dr. Norman Wagner of the University of Delaware, we made significant progress towards completing our new Neutron Spin Echo (NSE) spectrometer. This instrument, which is funded by the National Science Foundation, is on schedule for completion in 2024. After commissioning, the NSE spectrometer will be an essential component of the NSF/NIST partnership known as CHRNS: the Center for High Resolution Neutron Scattering. The NSE instrument will truly be world-class, enabling new capabilities for characterizing long-timescale motions in materials, particularly in soft matter. Work towards long-planned upgrades of the cold source moderator and portions of the guide network are also progressing well. The new cold source cryostat is currently undergoing acceptance testing at NCNR, and all new shielding and guides needed for the initial phase of work are on-site. When installed, the new cold source is expected to double the cold neutron flux at the longer neutron wavelengths important to neutron condensed-matter science, thereby significantly increasing the data rate for guide-hall instruments. Moreover, the guide replacements will provide additional gains for instruments on three of our neutron guidelines. Going forward, NCNR staff are carefully planning the timeline and procedures for installation of the new cold source, installation of the new cold neutron guides, performance of essential reactor plant maintenance activities, and continued reactor operator training and qualification. Taken together with the improvements in safety culture, these efforts will support a markedly increased capacity at the NCNR for user experiments and other NIST mission needs.

All told, the NCNR is slowly and steadily recovering from the event of February 2021, moving towards resumption of full operations under normalized conditions. This recovery is a monumentally difficult task and represents a true testament to the professionalism, diligence, drive and determination of our dedicated NCNR staff members. The NCNR's collective activities and operations are all directed toward fulfilling our central mission of enabling U.S.-based neutron science. I invite you to peruse this collection of research and facility highlights to see for yourself the fascinating work performed by the outstanding NCNR staff.

A handwritten signature in black ink, appearing to be the name of the Director, written in a cursive style.

The NIST Center for Neutron Research

Neutrons provide a uniquely effective probe of the structure and dynamics of materials ranging from water moving near the surface of proteins to magnetic domains in memory storage materials. The properties of neutrons (outlined below) can be exploited using a variety of measurement techniques to provide information not otherwise available. The positions of atomic nuclei in crystals, especially of those of light atoms, can be determined precisely. Atomic motion can be directly measured and monitored as a function of temperature or pressure. Neutrons are especially sensitive to hydrogen, so that hydrogen motion can be followed in H-storage materials and water flow in fuel cells can be imaged. Residual stresses such as those deep within oil pipelines or in highway trusses can be mapped. Neutron-based measurements contribute to a broad spectrum of activities including engineering, materials development, polymer dynamics, chemical technology, medicine, and physics.

The NCNR's neutron source provides the intense, conditioned beams of neutrons required for these types of measurements. In addition to the thermal neutron beams from the heavy water moderator, the NCNR has two liquid hydrogen moderators, or cold sources which supply neutrons to three-fourths of the instruments. One is a large area moderator and the other is smaller, but with high brightness. These moderators provide long wavelength guided neutron beams for industrial, government, and academic researchers.

There are currently 30 experiment stations: 12 are used for neutron physics, analytical chemistry, or imaging, and 18 are beam facilities for neutron scattering research. The subsequent pages provide a schematic description of our instruments. More complete descriptions can be found at <https://www.nist.gov/ncnr/neutron-instruments>.

The Center supports important NIST measurement needs but is also operated as a major national user facility with merit-based access made available to the entire U.S. technological community. Each year, approximately 2000 research participants from government, industry, and academia from all areas of the country are served by the facility (see page 58). Beam time for research to be published in the open literature is without cost to the user, but full operating costs are recovered for proprietary research. Access is gained mainly through a web-based, peer-reviewed proposal system with user time allotted by a beamtime allocation committee twice a year. For details see <https://www.nist.gov/ncnr/obtaining-beam-time>. The National Science Foundation and NIST co-fund the Center for High Resolution Neutron Scattering (CHRNS) that currently operates five of the world's most advanced instruments (see page 61). Time on CHRNS instruments is made available through the proposal system. Some access to beam time for collaborative measurements with the NIST science staff can also be arranged on other instruments.

Why Neutrons?

Neutrons reveal properties not readily probed by photons or electrons. They are electrically neutral and therefore easily penetrate ordinary matter. They behave like microscopic magnets, propagate as waves, can set particles into motion, losing or gaining energy and momentum in the process, and they can be absorbed with subsequent emission of radiation to uniquely fingerprint chemical elements.

WAVELENGTHS – in practice range from ≈ 0.01 nm (thermal) to ≈ 1.5 nm (cold) ($1 \text{ nm} = 10 \text{ \AA}$), allowing the formation of observable interference patterns when scattered from structures as small as atoms to as large as biological cells.

ENERGIES – of millielectronvolts, the same magnitude as atomic motions. Exchanges of energy as small as nanoelectronvolts and as large as tenths of electronvolts can be detected between samples and neutrons, allowing motions in folding proteins, melting glasses and diffusing hydrogen to be measured.

SELECTIVITY – in scattering power varies from nucleus to nucleus somewhat randomly. Specific isotopes can stand out from other isotopes of the same kind of atom. Specific light atoms, difficult to observe with X-rays, are revealed by neutrons. Hydrogen, especially, can be distinguished from chemically equivalent deuterium, allowing a variety of powerful contrast techniques.

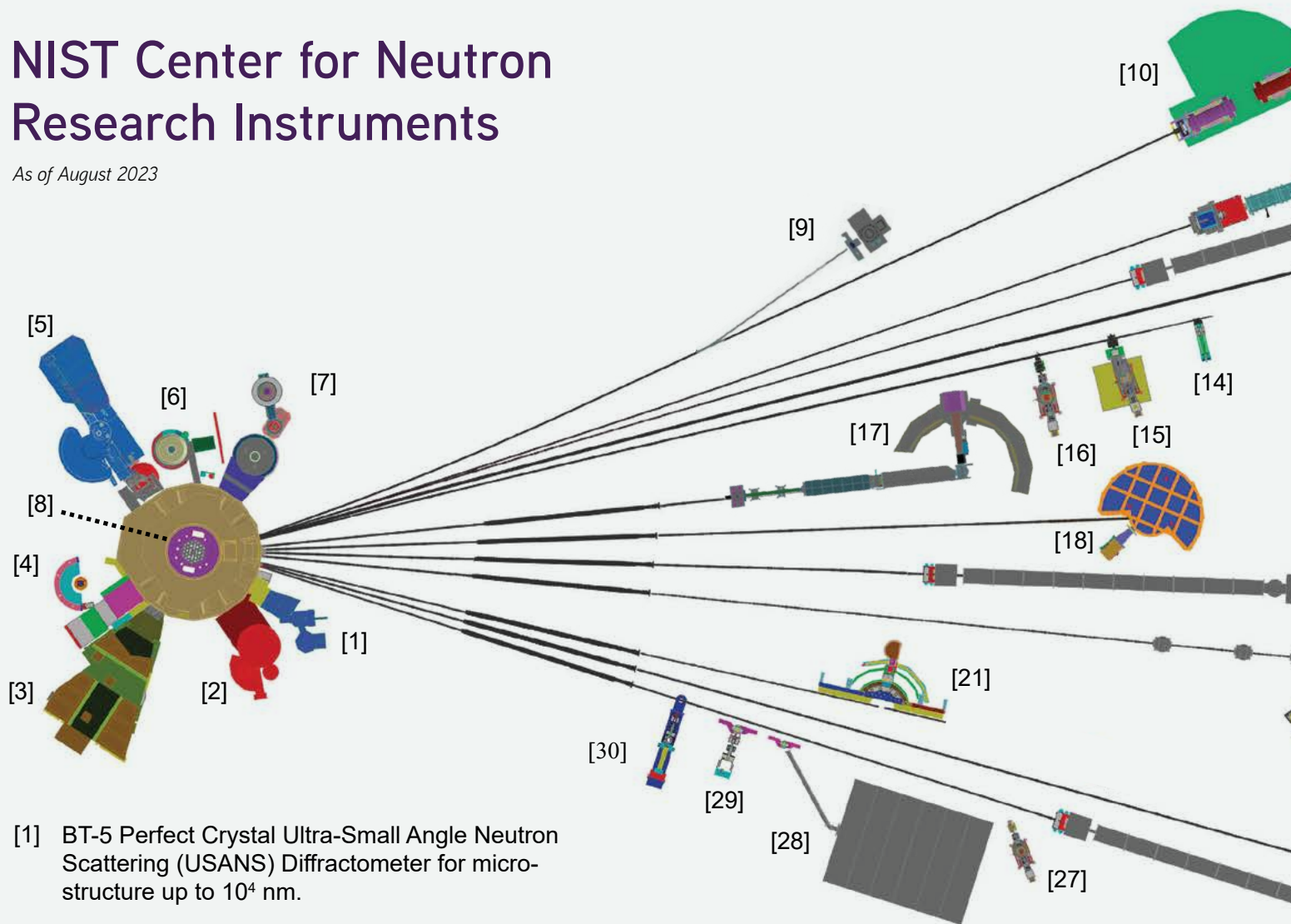
MAGNETISM – makes the neutron sensitive to the magnetic moments of both nuclei and electrons, allowing the structure and behavior of ordinary and exotic magnetic materials to be detailed precisely.

NEUTRALITY – of the uncharged neutrons allows them to penetrate deeply without destroying samples, passing through walls that condition a sample's environment, permitting measurements under extreme conditions of temperature and pressure.

CAPTURE – characteristic radiation emanating from specific nuclei capturing incident neutrons can be used to identify and quantify minute amounts of elements in samples as diverse as ancient pottery shards and lake water pollutants.

NIST Center for Neutron Research Instruments

As of August 2023



[1] BT-5 Perfect Crystal Ultra-Small Angle Neutron Scattering (USANS) Diffractometer for micro-structure up to 10^4 nm.

[2] BT-4 Filter Analyzer Neutron Spectrometer with cooled Be/Graphite filter analyzer for chemical spectroscopy and thermal triple axis spectrometer.

[3] BT-2 Neutron Imaging Facility for imaging hydrogenous matter in large components such as water in fuel cells and lubricants in engines, in partnership with General Motors and DOE.

[4] BT-1 Powder Diffractometer with 32 detectors; incident wavelengths of 0.208 nm, 0.154 nm, and 0.120 nm, with resolution up to $\Delta d/d \approx 8 \times 10^{-4}$.

[5] BT-9 Multi Axis Crystal Spectrometer (MACS II), a cold neutron spectrometer for ultra high sensitivity access to dynamic correlations in condensed matter on length scales from 0.1 nm to 50 nm and energy scales from 2.2 meV to 20 meV.



[6] BT-8 Engineering Diffractometer optimized for depth profiling of residual stresses in large components.

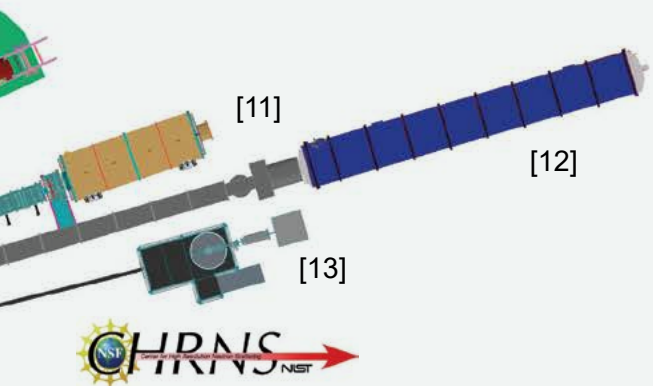
[7] BT-7 Thermal Triple Axis Spectrometer with large double focusing monochromator and interchangeable analyzer/detectors systems.

[8] VT-5 Thermal Neutron Capture Prompt Gamma-ray Activation Analysis Instrument used for quantitative elemental analysis of bulk materials including highly hydrogenous materials ($\approx 1\%$ H) such as foods, oils, and biological materials.

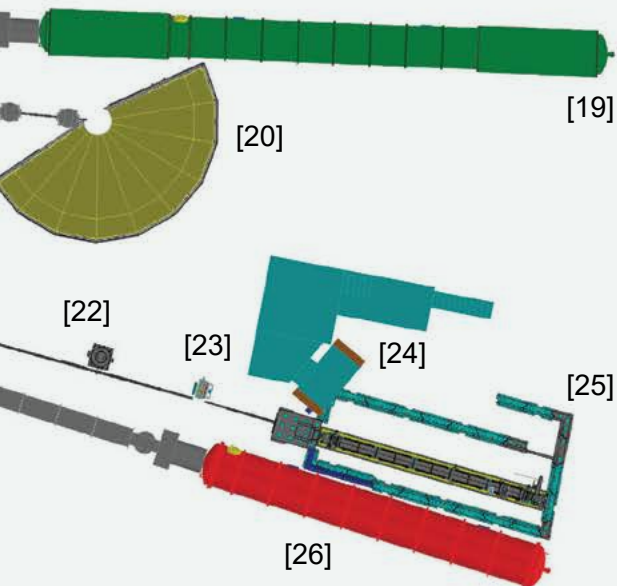
[9] NG-A' Cold Neutron Depth Profiling for profiling of subsurface elemental composition.

[10] NG-A Neutron Spin-Echo Spectrometer (NSE) for measuring dynamics from 5 ps to 100 ns.





The Center for High Resolution Neutron Scattering (CHRNS) is a partnership between NIST and the National Science Foundation that develops and operates neutron scattering instrumentation for use by the scientific community. The following instruments are part of the Center: 5 (MACS II), 10 (NSE), 17 (CANDOR), 18 (HFBS), and 19 (vSANS).



- [11] NG-B 10 m SANS for macromolecular structure measurements. **nSoft**
- [12] NG-B 30 m SANS for microstructure measurements.
- [13] NG-C Neutron lifetime experiment.
- [14] NG-D Cold neutron capture Prompt Gamma Activation Analysis, for quantitative elemental analysis of bulk materials
- [15] NG-D MAGIK off-specular reflectometer for studies of thin-film samples with in-plane structure.

- [16] NG-D Polarized Beam Reflectometer (PBR) for measuring reflectivities as low as 10^{-8} to determine subsurface structure.
- [17] NG-1 CANDOR Chromatic Analysis Diffractometer or Reflectometer, capable of high throughput measurements.
- [18] NG-2 Backscattering Spectrometer (HFBS), high intensity inelastic scattering instrument with energy resolution $< 1 \mu\text{eV}$ for studies of motion in molecular and biological systems.
- [19] NG-3 VSANS for single measurement investigation of lengths from 1 nm to 2 micron.
- [20] NG-4 Disk Chopper Time-of-Flight Spectrometer for diffusive motions and low energy dynamics. Wavelengths from $\approx 0.18 \text{ nm}$ to 2.0 nm and energy resolutions from $\approx 2 \text{ meV}$ to $< 10 \mu\text{eV}$.
- [21] NG-5 Spin-Polarized Triple Axis Spectrometer (SPINS) using cold neutrons with position sensitive detector capability for high-resolution studies.
- [22] NG-6 Precision measurement of the magnetic dipole moment of the neutron.
- [23] NG-6 Precision measurement of neutron flux.
- [24] NG-6 LAND detector development, neutron source calibration, and neutron cross section measurement
- [25] NG-6 Cold Neutron Imaging Facility for imaging hydrogenous matter in large components such as water in fuel cells and lubricants in engines.
- [26] NG-7 30 m SANS for microstructure measurements, in partnership with ExxonMobil and University of Minnesota's IPrime.
- [27] NG-7 PHADES Cold neutron test station.
- [28] NG-7 Neutron Interferometry and Optics Station with perfect crystal silicon interferometer. A vibration isolation system provides exceptional phase stability and fringe visibility.
- [29] NG-7 Neutron Physics Interferometry Test Bed for quantum information science.
- [30] NG-7 Horizontal Sample Reflectometer allows reflectivity measurements of free surfaces, liquid/vapor interfaces, as well as polymer coatings.

Prompt gamma ray activation analysis for determining chemical composition of 3D printing and casting materials used in biomedical applications

R. L. Paul,¹ M. M. Mille,² D. J. Turkoglu,^{1,3} and H. H. Chen-Mayer¹

Three-dimensional (3D) printing holds great promise for the custom fabrication of phantoms for medical imaging and radiation dosimetry applications. However, a major barrier to progress is the limited variety of suitable commercially available materials. Besides the anatomical resemblance which can be achieved by image-driven 3D replication, it is important that the printed phantoms simulate the radiation interaction properties of human tissue and bone specific to biomedical applications, in particular the X-ray macroscopic attenuation properties, which can be calculated theoretically only if the atomic composition is known. Rather than relying on manufacturer's nominal specifications, it is often necessary to measure the material's composition directly. However, tissue equivalent materials tend to be low density and composed of light elements such as H, O, C, and N, which cannot be measured by common X-ray analysis techniques.

In this investigation, prompt gamma-ray activation analysis (PGAA), a nondestructive, multi-element analysis technique suitable for the measurement of light elements, was used to measure the elemental compositions of several 3D printing and casting materials to determine their suitability for simulating human tissue. Elements are identified and quantified by measurement of gamma-rays emitted when the sample is exposed to a neutron beam. Materials analyzed included a plastic material (designated as PLA Plastic, with a nominal formula of $C_3H_4O_2$) and two urethane rubber compounds (designated as Urethane Rubber A and Urethane Rubber B) chosen as simulants for soft tissue, and a silicone rubber material (Silicone Rubber A) and mineral filled urethane casting resin (Urethane Resin A) used to simulate bone. The exact names of the commercial materials used have been screened because the manufacturers may consider the elemental composition of their products to be proprietary information.

For analysis purposes, the materials were 3D printed or cast into disks that were 10 mm in diameter and 2 mm to 2.5 mm thick. Analyses were performed using the cold neutron PGAA instrument in the NCNR. Emitted prompt gamma rays were measured using a high purity germanium detector. Gamma-ray signals were processed using digital electronics, and spectra were collected, displayed, and analyzed using a computer workstation with commercial software. Elements measured included H, C, N (matrix elements in

the soft tissue simulants), as well as Na, Mg, Si, P, Cl, K, Ca and Ti, which were more prevalent in the bone simulants. Since oxygen could not be measured directly, the O content was estimated by subtracting the masses of all elements measured by PGAA from the total mass of the material. Element mass fractions were determined using a standardless, absolute PGAA method, which involves using tabulated partial gamma emission cross sections and measured energy dependent detector efficiencies. As a quality check, hydrogen, carbon, and nitrogen were also determined using mixtures of urea and graphite as standards. Mass fractions determined for these elements using standards were identical to those obtained using the standardless method within experimental uncertainties. As a further quality check, the composition of the PLA plastic measured by PGAA agreed with the nominal formula within experimental uncertainties.

X-ray mass attenuation coefficients ($cm^2 g^{-1}$) and electron stopping powers ($MeV cm^2 g^{-1}$) were determined for casting and 3D printing materials, based on compositions measured by PGAA and densities provided by the manufacturers. The X-ray mass attenuation coefficients were determined using the online NIST XCOM database (available at <https://www.nist.gov/pml/xcom-photon-cross-sections-database>), while electron stopping power for each material was determined using the NIST ESTAR database (available at <http://physics.nist.gov/Star>). For determination of the best matches with actual human tissue and bone, X-ray mass attenuation coefficients and electron stopping powers were determined for the ICRU (International Commission on Radiation Units and Measurements) materials adipose, deflated lung, skeletal muscle, and cortical bone, using elemental compositions provided in the literature [1].

In Figure 1, X-ray mass attenuation coefficients are plotted vs. energy to determine the best synthetic material match for each ICRU material as regarding radiological properties. ICRU tissues (solid and dashed lines) are compared with casting/3D printing materials (data with symbols). The curves are separated into 3 main groups, with PLA giving the best match for muscle and lung, urethane rubber compounds best mimicking the properties of adipose tissue, and silicone rubber and urethane resin yielding the best match for cortical bone. In the electron stopping power plot (Figure 2), there are two groups with the cortical bone and bone simulant materials separated from the rest, and for all practical purposes, materials are

¹ Material Measurement Laboratory, National Institute of Standards and Technology, Gaithersburg, MD 20899

² Division of Cancer Epidemiology and Genetics, National Cancer Institute, National Institutes of Health, Rockville, MD 20850

³ USNC-Tech, Seattle, WA 98199

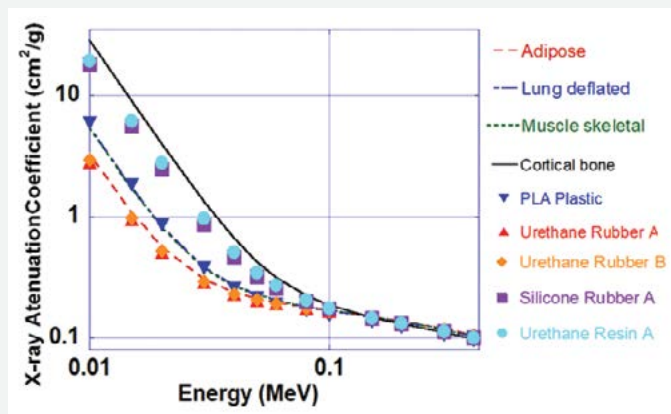


FIGURE 1: X-ray mass attenuation coefficients determined for printing and casting simulants and ICRU materials vs. photon energy.

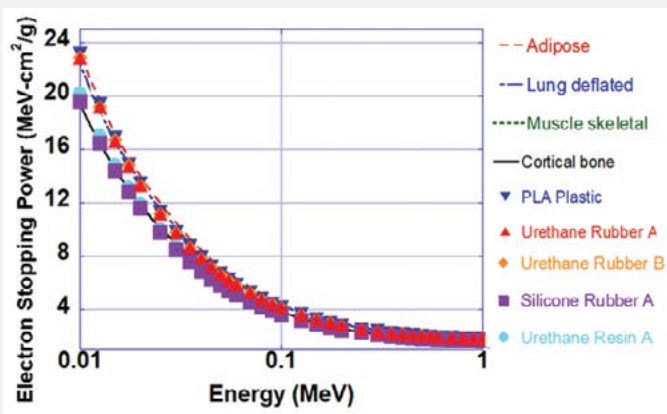


FIGURE 2: Electron stopping power determined for printing and casting simulants and ICRU materials vs. electron energy.

indistinguishable within each group. Figure 3 shows the fractional difference in X-ray mass attenuation (μ_m) between each ICRU material and its closest synthetic material match, calculated as: fractional difference = $(\mu_m(\text{ICRU material}) - \mu_m(\text{simulant})) / \mu_m(\text{simulant})$.

As expected, PLA plastic and the urethane rubber materials yield the best matches for soft tissues, while the urethane resin and silicone rubber provide the best matches for bony material. These results indicate that prompt gamma-ray activation analysis can provide an accurate assessment of elemental compositions of printing and casting materials for their suitability as tissue simulants for medical imaging and radiotherapy applications.

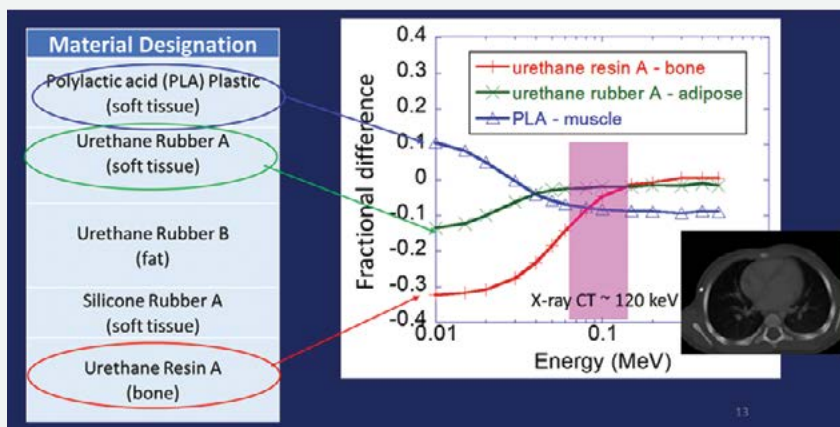


FIGURE 3: Fractional difference in X-ray mass attenuation coefficient between each ICRU material and its closest synthetic material match vs. photon energy.

REFERENCE

- [1] International Commission on Radiation Units and Measurements, "Tissue substitutes in radiation dosimetry and measurement," ICRU Report No. 44 (ICRU, Bethesda MD, 1989).

α -Synuclein fibril formation in the presence of lipid bilayer discs

M. Dubackic,¹ Y. Liu,^{2,3} E. G. Kelley,² C. Hetherington,⁴ M. Haertlein,⁵ J. M. Devos,⁵ S. Linse,⁶ E. Sparr,¹ and U. Olsson¹

Amyloid fibrils are protein self-assemblies that are associated with a number of neurodegenerative diseases, including Alzheimer's and Parkinson's disease (PD). The exact role of the amyloid fibrils in these diseases is not completely understood. However, converging lines of evidence implicate that some specific interactions between certain amyloid proteins and cell membranes, which seem to coexist during the process of fibril formation, lead to the damage of cell membrane, and eventually, cell death [1]. One protein whose amyloid fibrils have been found in patients diagnosed with PD is α -synuclein (α Syn). α Syn is expressed in the brain where it is proposed to interact with lipid membranes through the adsorption of protein monomers. As seen for various other amyloid proteins, interactions between α Syn and lipid membranes during the fibril formation have been shown to affect the membrane structure, both *in vivo* [2] and *in vitro* [3]. Here we investigate the effects of α Syn adsorption and fibril formation on a model lipid membrane, which are monitored by contrast matching small-angle neutron scattering (SANS) using protonated lipids and deuterated protein in D₂O solvent [4]. SANS data were recorded at 37 °C on the Center for High Resolution Neutron Scattering vSANS instrument at the NCNR. The lipid concentration was 2.1 mmol/L and the α Syn concentration was 0.4 mmol/L in 10 mmol/L MES buffer at pH = 5.5.

The model lipid membranes in this study were lipid bilayer discs, composed of a mixture of two phospholipids: 70% zwitterionic phosphatidylcholine (DMPC) and 30% anionic phosphatidylserine (DMPS). A cut through a circular lipid disc is schematically illustrated in the top right inset of Figure 1.

As shown in Figure 1, the addition of α Syn monomers leads to a significant shape-change of the lipid bilayer discs. We attribute the change to the adsorption of α Syn monomers, as it is well known that α Syn adsorbs onto negatively charged membranes. The α Syn-induced lipid disc deformation causes a significant elongation of the originally circular discs to a parallelepiped shape (Figure 1), with an axial ratio of the order of 10. As will be discussed further below, deformation appears to occur under constant lipid aggregation number.

Upon the fibril formation, protein monomers desorb from the lipid discs as they get recruited into the growing fibrils. As the protein desorbs, the lipid discs return to their original, circular shape. This reversal of the disc shape was studied by time-resolved SANS (Figure 2a). Interestingly, the data at different time points are well described by a linear combination of the scattering profile of pure lipid discs, $I_d(q)$, and scattering profile of parallelepiped shaped discs, $I_p(q)$, obtained in the first 15 min after addition of α Syn[4]. Thus, we write $I(q,t) = f(t)I_d(q) + (1-f(t))I_p(q)$, where $f(t)$ is the fraction of discs that had recovered to their original circular shape, at a given time t . The linear combination implies a strongly cooperative adsorption, where deformed lipid discs with adsorbed protein coexist with circular lipid discs without adsorbed protein. This kind of cooperativity has also been observed recently for α Syn adsorption onto lipid vesicle [5]. Moreover, it also implies that the lipid disc deformation is reversible and occurs at a constant lipid aggregation number.

Disc micelles are generally circular because this shape minimizes the line energy associated with the highly curved rim (which we here expect to be enriched in the charged lipid). Elongation increases the circumference. The corresponding increase in line energy can be balanced by the spontaneous adsorption of α Syn molecules if they have a particular preference for the high charge density rim.

In Figure 2b we present how $f(t)$ varies with t . At $t = 0$, $f \approx 0$. Then after a lag time of ca. 1 h, $f(t)$ begins to increase with t , reaching a maximum value of ca. 0.7 after 8 h. Adsorbed α Syn molecules are in reversible equilibrium with molecules dissolved in the bulk, and the decrease in the adsorbed amount is expected to reflect the decrease in the bulk monomer concentration.

The present results point to highly cooperative α Syn adsorption onto mixed zwitterionic/anionic lipid discs which causes the discs to elastically deform into an elongated shape. The observed deformation, where the length of the rims increases, is presumably due to the preferred adsorption at disc rim, which is expected to be enriched in the charged lipid.

¹ Physical Chemistry, Lund University, SE-22100 Lund, Sweden

² NIST Center for Neutron Research, National Institute of Standards and Technology, Gaithersburg, MD 20878

³ Chemical and Biomolecular Engineering Department, University of Delaware, Newark, DE 19716

⁴ National Center for High Resolution Electron Microscopy, Centre for Analysis and Synthesis, Lund University, SE-22100, Lund Sweden

⁵ Life Sciences Group, Institut Laue-Langevin, 38000 Grenoble, France

⁶ Biochemistry and Structural Biology, Lund University, SE-22100 Lund, Sweden

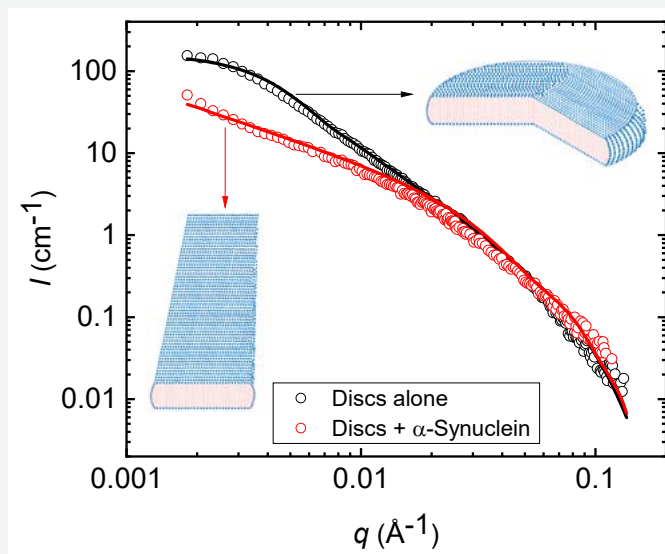


FIGURE 1: SANS patterns of a pure lipid bilayer disc suspension (black open circles) and in the presence of α Syn monomers (red open circles), obtained during first 15 min upon addition of α Syn to the lipid disc suspension. Solid lines represent model fits. The black solid line corresponds to circular disc model and the red solid line to a parallelepiped model. Insets show schematic illustration of circular lipid discs present in the absence of protein (top right) and in the presence of α Syn monomers (bottom left). In these illustrations, the lipid alkyl chain region is colored red, while the blue color represents the headgroup region.

Investigation of interaction between α Syn and lipid bilayer discs allows the comparison of adsorption preferences between curved and the flat membranes, which has not been extensively studied. We show that the adsorption of α Syn monomers onto the membrane surface leads to a deformation from circular discs to elongated structures. Additionally, these deformations are characterized by an increase in the area of curved domains and decrease in the area of the flat ones, which further suggest that α Syn has a preference for the curved surfaces. Furthermore, we show that the desorption of α Syn monomers occurs as the monomers start to self-assemble into amyloid fibrils, and that this desorption is a cooperative process.

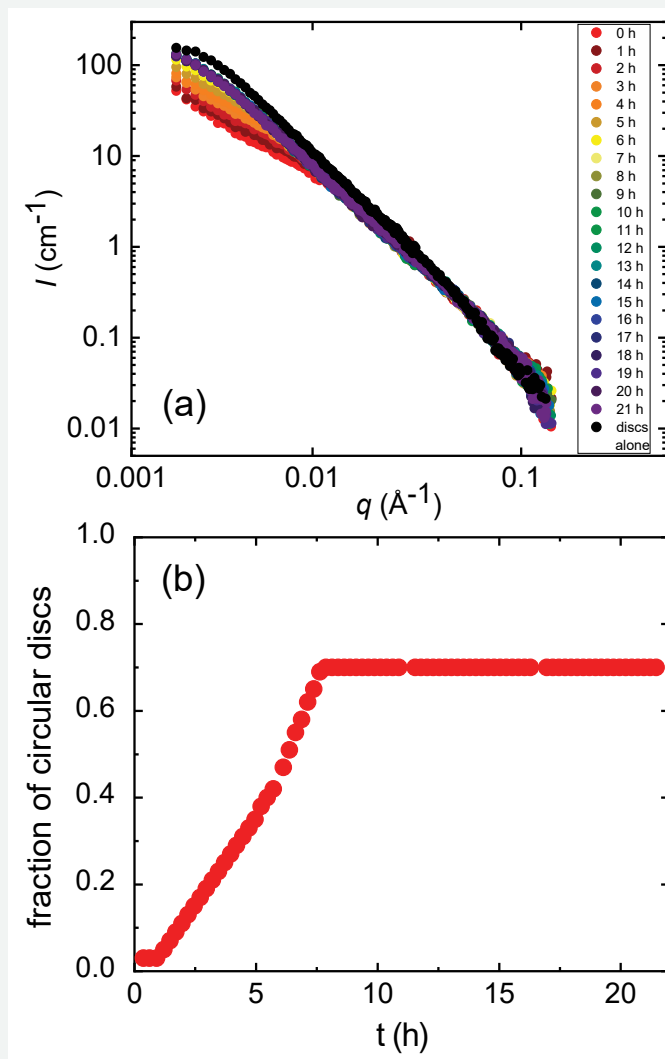


FIGURE 2: (a) Time-resolved SANS profiles plotted for 22 h with 1 h resolution and comparison with pure lipid disc suspension (black circles). (b) Variation with time of the fraction of circular discs, $f(t)$.

REFERENCES

- [1] M. Gonzalez-Garcia, G. Fusco, A. De Simone, *Front Cell Dev Biol*, **9**, 642623 (2021).
- [2] B. Winner *et al.*, *Proc Natl Acad Sci USA*, **108**(10), 4194 (2011).
- [3] K. M. Danzer *et al.*, *J Neurosci*, **27**(34), 9220 (2007).
- [4] M. Dubackic *et al.*, *Langmuir*, **38**(33), 10216 (2022).
- [5] K. Makasewicz *et al.*, *ACS Chem Neurosci*, **12**(12), 2099 (2021).

Observing dimer formation with neutron reflectometry: HIV-1 Nef at the lipid membrane

F. Heinrich,^{1,2} C. E. Thomas,³ J. J. Alvarado,³ and T. E. Smithgall³

Human immunodeficiency virus-1 (HIV-1) is the lentivirus responsible for acquired immunodeficiency syndrome (AIDS). It infects cells of the human immune system, such as T cells, and uses four unique helper proteins to hijack the cell's machinery and make more copies of itself. One of these proteins is Nef, expressed early in the viral life cycle. It enhances viral infectivity, replication, and immune escape of HIV-infected cells. In mice, expression of Nef alone causes an AIDS-like syndrome, demonstrating its essential role in disease progression. Conversely, individuals infected with HIV-1 strains lacking functional Nef expression often fail to progress to AIDS, even without antiviral therapy. Therefore, Nef has emerged as a high-value target in understanding HIV infections and suppressing AIDS [1].

Nef is a flexible protein that attaches to the host cell membrane (Figure 1). It has a core domain that binds to other Nef proteins and cellular partners. The core domain is connected to a flexible anchor domain that is terminated with a lipidated tether (myristate) that inserts into the lipid membrane. Nef promotes virus functions without possessing intrinsic biochemical activity. Instead, it directly interacts with diverse host cell signaling proteins, and it manipulates intracellular trafficking pathways in ways that help the virus to replicate and escape detection by the immune system. Studies have established that two Nef proteins need to form pairs (homodimers) at the cell membrane for most, if not all, of its functions. However, the structure and dynamics of Nef and its complexes with other proteins are hard to determine because of their flexibility and the complexity of the membrane. A team of researchers from the University of Pittsburgh, NIST, and Carnegie Mellon University has used a combination of neutron reflectometry (NR), molecular simulations, and X-ray crystallography to reveal how Nef dimers form and behave on model membranes (Figure 1).

NR is a technique that can measure the structure of flexible membrane-bound proteins in conditions that mimic their natural environment [2]. Researchers at NIST have learned to prepare model membranes that reflect the composition of the host cell membrane and added wild-type myristoylated Nef or a mutant of Nef that cannot dimerize at increasing concentrations (Figure 2). While NR showed that the core domain of Nef explores a range of distances

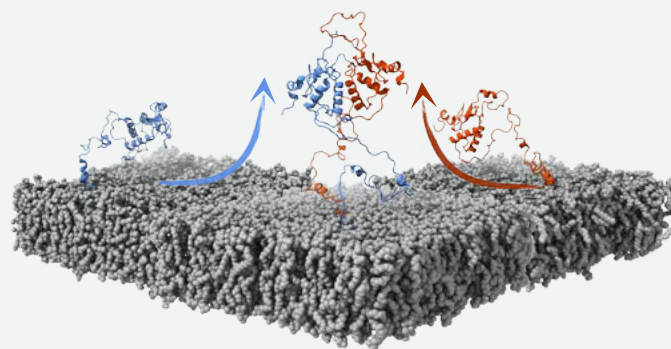


FIGURE 1: Illustration of HIV-1 Nef dimer formation at the membrane bilayer. Monomeric Nef (single blue and orange proteins) first binds the lipid membrane (grey) via its N-terminal lipid anchor. This myristoylated anchor domain connects the lipid anchor and the globular core domain of Nef. The core and anchor domains of monomeric Nef are free to explore the entire conformational space, and the core domain often is in close contact with the lipid membrane. When two monomeric Nef proteins encounter each other (center), dimer formation is mediated by contacts between two core domains. After forming a dimer, the two core domains are, on average, further away from the membrane than the monomer because the two anchor domains impose conformational constraints. This extension prepares the complex for binding to proteins in the host cell and alters signaling and trafficking pathways that enhance the viral life cycle.

from the membrane, specific information about Nef configurations cannot be obtained from the NR data alone. Particularly, NR does not provide direct structural information concerning dimerization as it gives only an average protein structure along planes parallel to the lipid membrane. Specifically, NR provides time and ensemble-averaged one-dimensional structural profiles of the membrane and the protein along the membrane normal.

Integrative modeling strategies are routinely applied to obtain three-dimensional information with greater structural detail than provided by NR alone. Leveraging computational experience from Carnegie Mellon University, a range of molecular simulations were performed on monomers and dimers of Nef. Figure 1 shows snapshots from these simulations. Backbone torsion angle Monte Carlo (MC) simulations were used to stake out the entire conformational space available to monomeric and dimeric Nef, and Molecular Dynamics (MD) simulations probed how specific interactions between protein residues and with the membrane may lead to a preference in assuming only a subset of the allowed configurations. Combining MC and MD simulations thereby probes the entropic (randomness) and enthalpic (energy) contributions to the binding and dimerization of Nef at the membrane while providing additional structural detail. MD simulations, whose trajectories are actively steered by the NR data, were performed to identify discrepancies in unbiased MD simulations with respect to the experimental evidence. In agreement with previous work on similar peripheral membrane proteins [3], the collaboration identified that structural ensembles of wild-type Nef

¹ Department of Physics, Carnegie Mellon University, Pittsburgh, PA 15213

² NIST Center for Neutron Research, National Institute of Standards and Technology, Gaithersburg, MD 20899

³ University of Pittsburgh School of Medicine, Pittsburgh, PA 15219

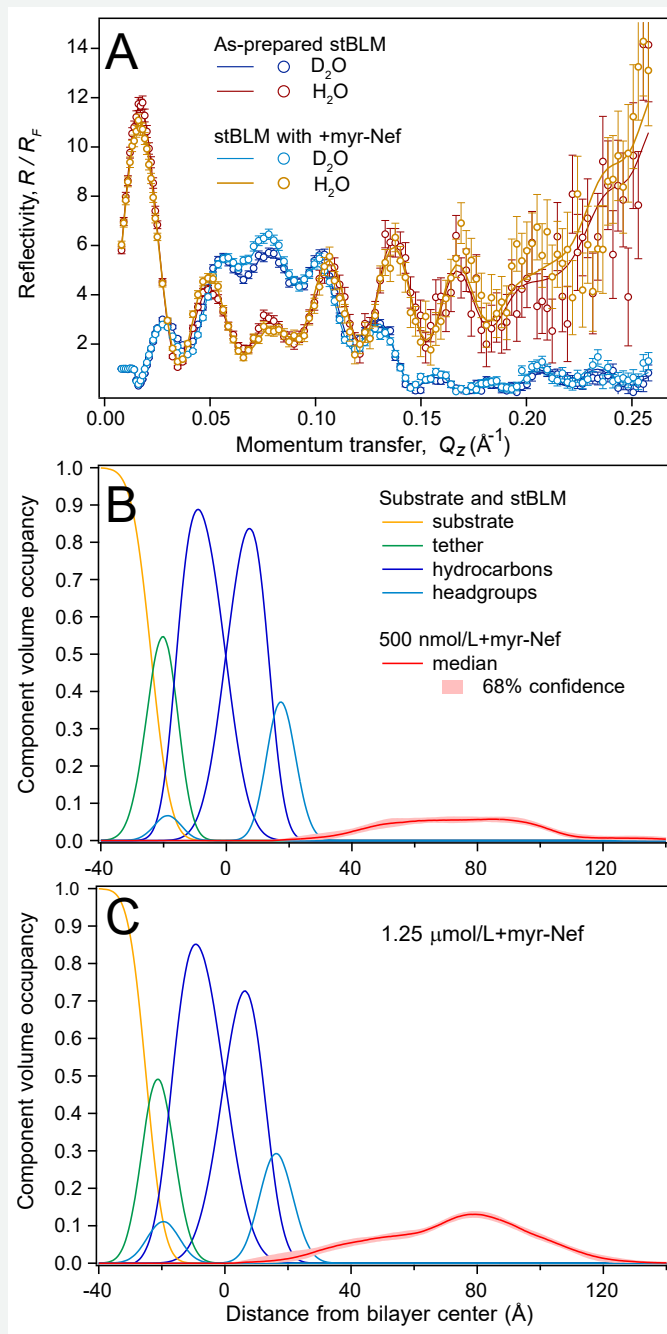


FIGURE 2: NR characterization of membrane-associated, myristoylated wt HIV-1 Nef. (A) Exemplary data sets before and after adding Nef from solution, measured with D₂O and H₂O-based buffer immersing a sparsely-tethered bilayer lipid membrane (stBLM). (B and C) Component volume occupancy profiles along the membrane normal for two protein solution concentrations. Shaded areas show 68% confidence intervals for the protein component. With increased protein concentration, a peak at 80 \AA from the bilayer center develops in agreement with dimer formation (see Figure 3).

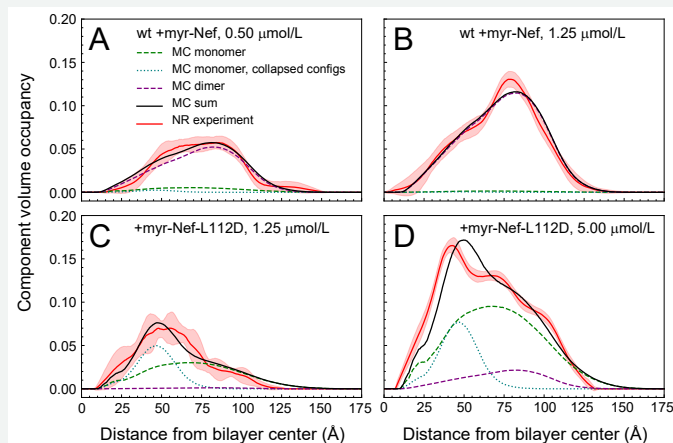


FIGURE 3: Modeling of NR-derived protein profiles with ensemble averages from backbone torsion angle MC simulations. NR data from wt Nef is best described by the MC ensemble of the dimer in its entirety. In contrast, NR data from dimerization-deficient Nef-L112D is a linear combination of ensemble averages of the dimer, the monomer, and a sub-ensemble of membrane-collapse monomer in which the core-domain closely interacts with the lipid bilayer.

dimers and dimer-deficient Nef-L112D mutants are predominantly entropic (Figure 3). Only the core domain of dimerization-deficient Nef-L112D significantly interacts with the lipid membrane. Dimerization of Nef leads to a larger average distance of the core domains from the membrane, which prepares the complex for the binding of host cell proteins. The mechanism behind the uplifting of the dimer is the combined action of the two anchor domains that provide an increased stiffness of the membrane tether and thereby limit the accessible configuration space to larger core domain distances from the membrane.

This study provides direct biophysical evidence that Nef associates with the membrane as a homodimer with its structured core region displaced from the membrane for partner protein engagement. A comparison to the dimerization-defective mutant Nef-L112D demonstrates that the dimerization interface identified in crystal structures stabilizes the membrane-bound dimer. The ensemble of membrane-bound dimeric Nef is dominated by entropy, which provides the protein with the maximum flexibility to engage different host-cell proteins and adds to a growing list of signaling proteins that use entropy-driven mechanisms for their interactions at the membrane. Future studies will extend this work to complexes of Nef dimers with host cell signaling proteins and explore the effect of small molecule Nef inhibitors on dimer formation in the membrane environment. This work has been recently published in the *Journal of Molecular Biology* [4].

REFERENCES

- [1] N. Laguette, C. Bregnard, *et al.*, *Mol. Aspects Med.* **31**, 418 (2010).
- [2] F. Heinrich and M. Lösche, *Biochim. Biophys. Acta* **1838**, 2341 (2014).
- [3] F. Heinrich, Q. N. Van, *et al.*, *Biophys J* **120**, 4055 (2021).
- [4] F. Heinrich, C. E. Thomas, *et al.*, *J Mol Biol* **435**, 168009 (2023).

Tales of two tails: nanoscale bending dynamics in chain asymmetric lipid membranes

E. G. Kelley¹ and M. Nagao^{1,2,3}

Each cell in our body is surrounded by a lipid membrane. Most of the lipids found in these membranes have hydrophobic acyl tails that have similar numbers of carbons. A far less studied class of lipids is those with two hydrophobic tails that have very different lengths. These unusual lipids are referred to as 'mixed chain' or 'chain asymmetric lipids' and are often found in specific membranes within a cell or specific cell types. For example, sphingolipids that are enriched in the outer leaflet of plasma membranes and in the nervous system have asymmetric tails that can vary in length from 2 to 28 carbons. What is even more fascinating is that recent lipidomic studies have shown that some yeasts compensate for a lack of unsaturated fatty acids by synthesizing asymmetric lipids with saturated chains.

There are very few studies on the biophysical properties of chain asymmetric lipids in literature, but the limited data available seem to suggest that the differences in tail length play an important role in regulating membrane dynamics. However, exactly how tail length asymmetry regulates the membrane dynamics is unclear as the results show seemingly contradictory effects. Nuclear magnetic resonance spectroscopy (NMR) measurements indicated that the acyl tail motions at the millisecond time scale were enhanced in mixed chain lipids [1] while fluorescence recovery after photobleaching studies (FRAP) suggested that the diffusion coefficient of a chain asymmetric lipid was almost identical to that of an analogous chain symmetric lipid with the same average number of hydrocarbons in the tail [2]. Meanwhile, simulation studies showed that chain length asymmetry increased the friction between the two bilayer leaflets by as much as a factor of 4, which would significantly slow down any processes that required changes in the membrane shape such as endocytosis or cell division [3]. In other words, there is conflicting experimental evidence showing that chain asymmetric lipids either speed up, slow down, or have no effect on the membrane motions.

To better understand how this unusual class of lipids affects the membrane dynamics at the molecular scale, here we use neutron spin echo spectroscopy (NSE) to study the collective fluctuations of model chain asymmetric lipids [4]. We measured the bending fluctuations of bilayers prepared with 1-myristoyl-2-stearoyl-sn-glycero-3-phosphocholine (14:0-18:0 PC, MSPC) and 1-stearoyl-2-myristoyl-sn-glycero-3-phosphocholine (18:0-14:0 PC, SMPC). These lipids are composed of the same hydrophilic headgroup and same hydrophobic tails that differ in length by 4 carbons but differ

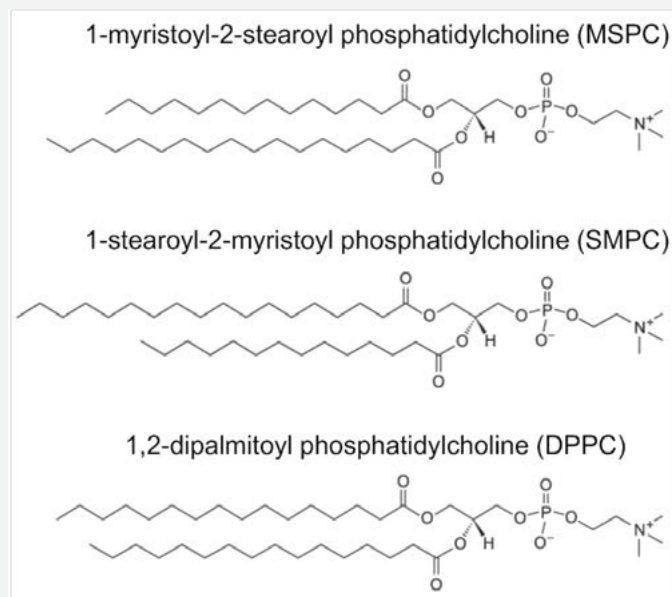


FIGURE 1: Chemical structures of model chain-asymmetric lipids and corresponding chain-asymmetric phospholipids. All lipids have a total of 32 carbons in the acyl tails.

in how the tails are connected to the headgroups as shown in Fig. 1. We compare the dynamics measured for MSPC and SMPC with those measured for a well-studied, chain symmetric lipid with the same average number of carbons in the tails, 1,2-dipalmitoyl-sn-glycero-3-phosphocholine (16:0-16:0 PC, DPPC).

Shown in Fig. 2 are the intermediate scattering functions for MSPC, SMPC, and DPPC measured at approximately the same relative temperature to the respectively lipid melting temperature (T_m). The NSE data were analyzed with a model that accounted for the vesicle diffusion and membrane fluctuations that fit the data well at low q values, $q < 1 \text{ nm}^{-1}$. At higher q values ($q > 1 \text{ nm}^{-1}$) and shorter time scales ($t < 20 \text{ ns}$) the curves measured for MSPC and SMPC did not approach 1, indicating that there was a faster dynamic process occurring in the chain asymmetric membranes that was not captured by the current model and already suggesting a major differences in the dynamics of the chain-asymmetric and -symmetric lipid membranes.

The model fits to the data indicated that the bending dynamics also were faster in the chain asymmetric lipid membranes compared to DPPC. The relaxation times in turn are directly related to the effective bending modulus of the membranes, \bar{K} , a measure of the energy required to bend the membrane at the nanoscale. As shown in Fig. 3, the \bar{K} values measured for MSPC and SMPC were similar but notably less than the value for DPPC, where the $\approx 30\%$ to 40% reduction in \bar{K} suggested that the mixed chain lipid membranes are effectively softer and easier to bend.

¹ NIST Center for Neutron Research, National Institute of Standards and Technology, Gaithersburg, MD 20899

² Department of Materials Science and Engineering, University of Maryland, College Park, MD 20742

³ Department of Physics and Astronomy, University of Delaware, Newark, DE 19716

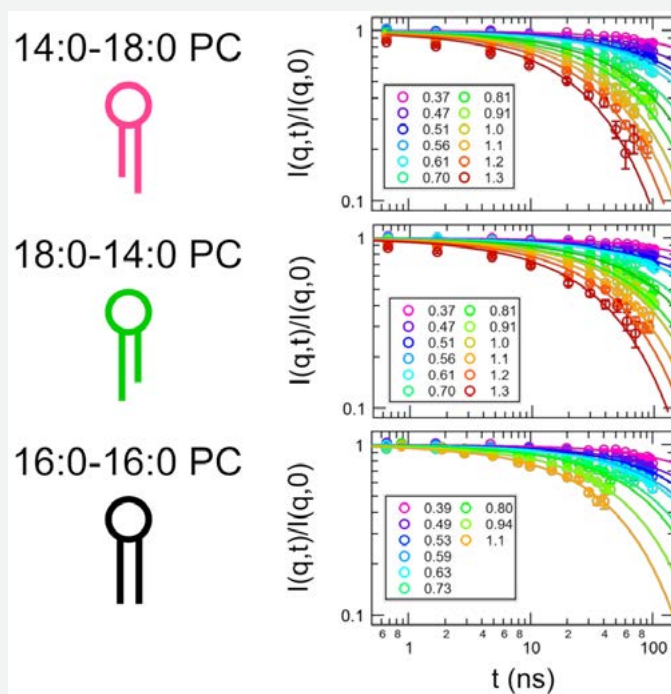


FIGURE 2: Intermediate scattering functions measured on the NGA-NSE instrument at the NCNR for MSPC (top), SMPC (middle) and DPPC (bottom) (points) and fits to a model that accounts for the diffusion of the vesicles and membrane fluctuations (lines). Numbers in the legend are the corresponding $\bar{\kappa}$ values with units of nm^{-1} .

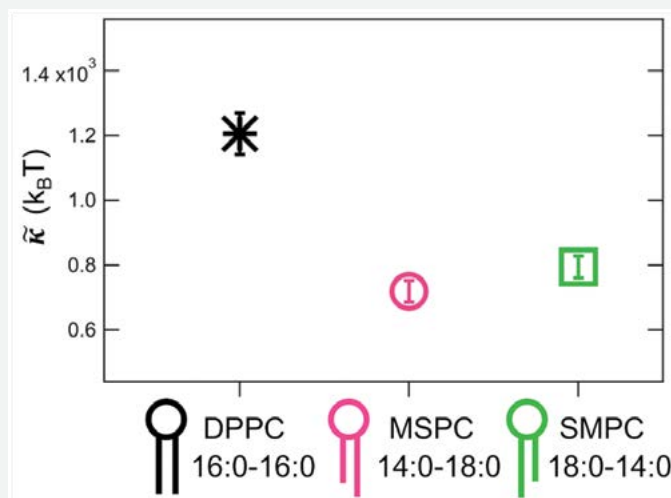


FIGURE 3: Comparison of the effective bending modulus, $\bar{\kappa}$, from NSE measurements of asymmetric and symmetric lipids with the same average number of carbons in the tails at the same relative temperature, $T - T_m \approx 10$ °C.

The faster dynamics at short time scales and enhancement of the bending fluctuations measured with NSE were seemingly counterintuitive to structural studies that showed chain asymmetric lipids for more interdigitated bilayers where the longer of the two acyl tails penetrates into the opposite leaflet [5]. Such an increase in the interactions between the leaflets in the asymmetric lipid membranes might be expected to slow down the local rearrangement of the lipid molecules as the membrane bends, which would be seen as an increase in the $\bar{\kappa}$ values for MSPC and SMPC, not the measured decrease. While the measured decrease in $\bar{\kappa}$ was unexpected, the results do provide some evidence as to why yeast cells would compensate for a lack of unsaturated lipids by synthesizing saturated chain asymmetric lipids. Unsaturated lipids are also an important regulator of membrane fluidity, where incorporating a single double bond into each lipid tail reduces the rigidity by approximately 30% compared to membrane composed of saturated lipids with same number of carbons in the tails. Here we see a similar decrease in $\bar{\kappa}$ by making the tail lengths asymmetric.

The enhanced nanoscale dynamics measured in the chain asymmetric lipid membranes highlight how a subtle change in lipid chemical structure can significantly impact the properties of the corresponding membranes. For the same total number of carbons in the acyl tails, moving 2 carbons from one tail to the other, *i.e.* going from DPPC (16:0-16:0 PC) to MSPC (14:0-18:0 PC) or SMPC (18:0-14:0 PC) reduced the bending modulus by almost 40%. While the mechanism by which tail length asymmetry softens the membranes is still unknown, a series of studies from almost 30 years ago may provide some hints. It is hypothesized that rather than forming a static, interdigitated structure as seen in the diffraction studies, the longer of the acyl tails is instead highly dynamic and rapidly samples both its own leaflet and regions of the opposing leaflet. The NSE data seem to suggest that these previously reported rapid acyl tail motions propagate to the collective bending fluctuations at the nanosecond timescales involving tens to hundreds of lipids. It is also highly likely that tail length asymmetry will have different effects on the membrane dynamics at different length scales and time scales. Future neutron scattering studies of dynamic processes ranging from the motions of the individual lipid molecules to the collective bending and thickness fluctuations will further bridge the molecular and macroscopic scales and provide new insights into why cells use asymmetric lipids to regulate the biophysical properties of their membranes.

REFERENCES

- [1] H. A. Hallady, R. E. Stark, S. Ali, R. Bittman, *Biophys. J.* **58**, 1449 (1990).
- [2] V. Schram, T. E. Thompson, *Biophys. J.* **69**, 2517 (1995).
- [3] W. K. den Otter, S. A. Shkulipa, *Biophys. J.* **93**, 423 (2007).
- [4] E. G. Kelley, M. P. K. Frewein, O. Czakkel, M. Nagao, *Symmetry*, **15**, 191 (2023).
- [5] M. P. Frewein, M. Doktorova, F. A. Heberle, H. L. Scott, E. F. Semeraro, L. Porcar, G. Pabst, *Symmetry*, **18**, 1441 (2021).

Non-cryogenic air separation using aluminum formate, Al(HCOO)₃ (ALF)

D. Mullangi,¹ H. A. Evans,² T. Yildirim,² Y. Wang,³ Z. Deng,¹ Z. Zhang,³ T. T. Mai,⁴ F. Wei,⁵ J. Wang,¹ A. R. Hight Walker,⁴ C. M. Brown,^{2,6} D. Zhao,³ P. Canepa,^{1,3} and A. K. Cheetham^{1,7}

Production of oxygen (O₂) from air is an important commercial process with upwards of 50 billion dollars in global market value annually. The O₂ gas is widely used in numerous applications, ranging from its large-scale use in steel production to medical uses for the treatment of people with breathing problems and other conditions. These different applications require O₂ with various levels of purity, ranging from > 90% (medical grade) to greater than 99.5% (manufacturing). However, purifying O₂ is quite difficult, as O₂ and N₂ are physically/chemically similar, with N₂ making up nearly 80 percent of air with O₂ comprising most of the remainder. On a commercial scale, air separation is usually achieved either through the cryogenic (< 183 K) distillation of liquid air, since oxygen boils at 90 K and nitrogen at 77 K, or by the preferential adsorption of N₂ from dry air using lithium-containing zeolites in a pressure swing adsorption process at ambient temperatures. Ultimately, cryogenic distillation infrastructure is cost intensive, but can produce ultra-high purity O₂, whereas zeolites require less cost input, but cannot achieve the ultra-high O₂ purities seen by cryogenic distillation. However, the advantages of solid sorbents are clear, as they are much easier to handle, generally less energy intensive, and can provide O₂ purification methods with less infrastructure investment. The only issue is that many solid adsorbents lack strong enough preference for O₂ vs N₂, or vice-versa.

During the last decade, there has been a significant effort to develop metal-organic frameworks (MOFs) as selective sorbents for the capture, storage, and release of oxygen. Metal-organic frameworks (MOFs), with their high surface areas, tunable pore sizes, surface functionality, and structural diversity, offer several advantages as the next-generation solid adsorbent materials for O₂ purification. However, MOFs also possess limitations of their own. These materials are usually sensitive to humidity, possess poor mechanical properties, and, for many high-performing MOF materials, are comprised of complex ligand precursors that may be too costly for large-scale applications.

However, in recent work conducted by scientists from the NCNR and international collaborators from the National University of Singapore,

they describe how one of the simplest of all MOFs, aluminum formate, Al(HCOO)₃ (ALF) achieves excellent air separation whilst possessing many industrially attractive attributes [1]. Namely, ALF is a mechanically and chemically robust material that can be made from the inexpensive and widely available starting reagents, aluminum hydroxide and formic acid (final material cost ~2 dollars per kg). Most importantly, the material exhibits excellent O₂ adsorption properties and very high kinetic O₂/N₂ selectivities (> 100's, the aforementioned commercial zeolites have a N₂/O₂ selectivity of roughly 5). ALF has also separately been shown to be highly industrially relevant for CO₂ capture and hydrocarbon purification [2, 3].

The remarkable O₂ adsorption performance of ALF is rooted in its crystal structure, where two types of cavities exist (Figures 1 e, f). The most important of these cavities, denoted as the large cavity (LC), adsorbs O₂ molecules that strongly associate with atoms of the ALF crystal structure framework. The second cavity, denoted as the small cavity (SC), has inward-pointing formate hydrogens that hydrogen bond with adsorbed O₂ molecules, but which prove to be less important interactions compared to the interactions seen between O₂ and the large cavity. This structural insight was made possible by *in situ* O₂ dosed neutron powder diffraction data of ALF taken at the NIST Center for Neutron Research (BT-1) and were instrumental to understanding how the cavities of ALF fill preferentially with O₂ (Figure 1a). This neutron powder diffraction data was further complimented by rapid acquisition X-ray diffraction data taken at Argonne National Laboratory, which provided kinetic tracking of O₂ adsorption into the crystal structure of the material over 240 minutes (Figure 1 b, c, d). This understanding of cavity preferential filling is only available through crystallographic probes like diffraction, as crystallography deals with the exact atomic positions of constituent atoms of a given sample.

Further material characterization on the O₂ adsorption properties on ALF were carried out at the NCNR, where adsorption and desorption O₂ isotherms with ALF were measured in the temperature range of 125 K–298 K. ALF displays effective peak O₂ adsorption at pressures between 0 bar and 1.2 bar at 190 K, with ~ 3.5 mmol/g being adsorbed at 1.2 bar. At ~ 0.21 bar (the partial pressure of O₂ in air),

¹ Department of Materials Science and Engineering, National University of Singapore, 9 Engineering Drive 1, 117575 Singapore

² NIST Center for Neutron Research, National Institute of Standards and Technology, Gaithersburg, MD 20899

³ Department of Chemical and Biomolecular Engineering, National University of Singapore, 4 Engineering Drive 4, 117585 Singapore

⁴ Physical Measurement Laboratory, National Institute of Standards and Technology, Gaithersburg, MD 20899

⁵ Institute of Materials Research and Engineering, Agency for Science Technology and Research, 2 Fusionopolis Way, Innovis, Singapore, 138634

⁶ Department of Chemical and Biomolecular Engineering, University of Delaware, Newark DE 19716

⁷ Materials Research Laboratory, University of California, Santa Barbara, CA 93106

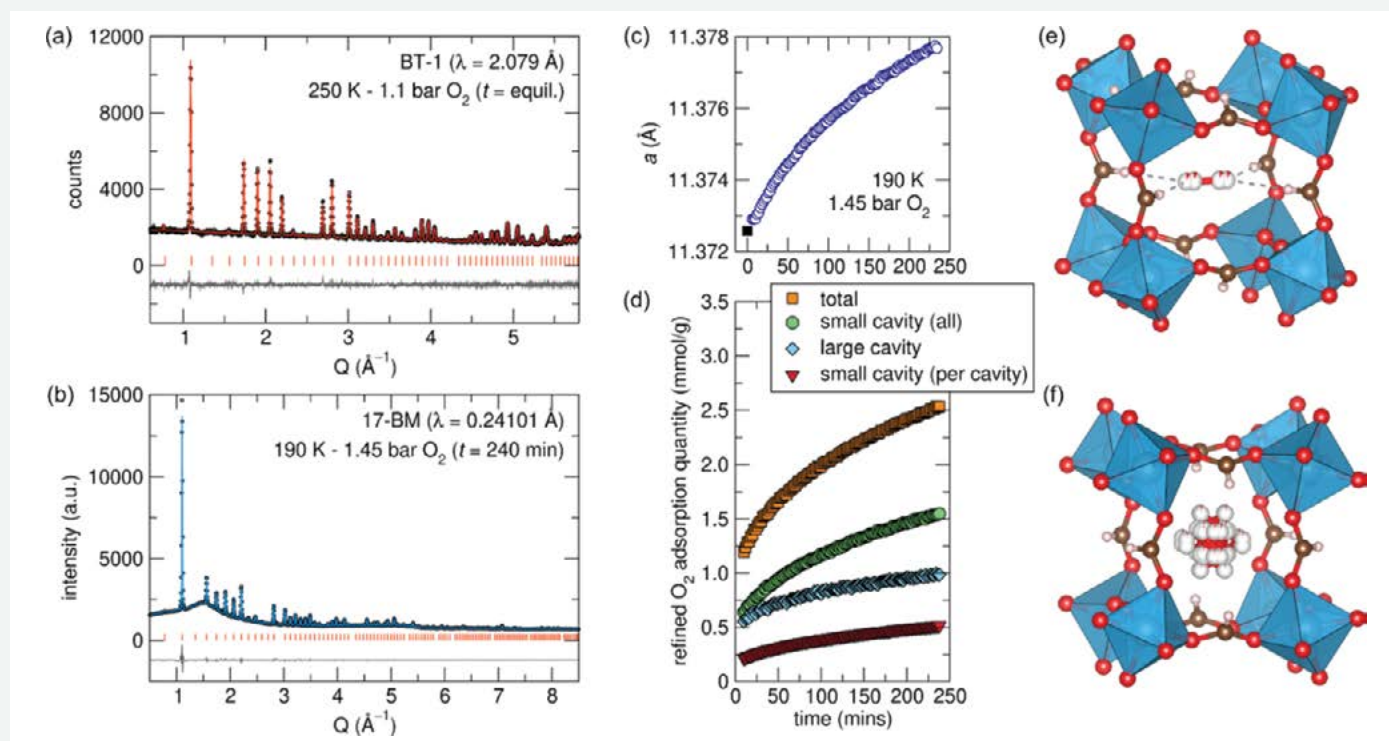


FIGURE 1: Rietveld refinement results of *in-situ* neutron and synchrotron X-ray diffraction experiments of ALF under constant O₂ pressures. (a) Rietveld fit of neutron dataset of ALF under 1.1 bar O₂ at 250 K after 6 hours of equilibration. [NCNR, BT1, $\lambda = 2.079$ Å] SG = $Im\bar{3}$, $a = 11.3808(1)$ Å, $R_{wp} = 2.81\%$, $R_p = 2.24\%$. Black circles = data, red line = fit, red ticks = predicted *hkl*s, grey line = difference. (b) representative fit of synchrotron X-ray diffraction data [APS, 17-BM, $\lambda = 0.24101$ Å] at 190 K under 1.45 bar O₂. Shown data is for the 240-minute dataset. SG = $Im\bar{3}$, $a = 11.3811(1)$ Å, $R_{wp} = 2.24\%$, $R_p = 1.40\%$. Black circles = data, blue line = fit, red ticks = predicted *hkl*s, grey line = difference. (c) and (d) show results from sequential Rietveld refinements of 17-BM data where ALF was exposed to 1.45 bar of O₂ at 190 K and monitored over the course of 240 minutes. Data point sizes are commensurate with error bars (1 σ). (c) Change in the unit cell parameter *a* as a function of time of ALF under 1.45 bar O₂ between 0 and 240 minutes. (d) Refined O₂ occupancy normalized to mmol/g over the course of the experiment. (e) Structural depiction of the small cavity of ALF filled with O₂ from the Rietveld refinement results from the 240-minute dataset. (f) Structural depiction of the large cavity of ALF with a disordered O₂ molecule inside.

effective peak O₂ adsorption with ALF is also seen near 190 K with an adsorption of ≈ 1.5 mmol/g. This notable non-cryogenic temperature O₂ adsorption is even more impressive when coupled with ALFs high O₂/N₂ selectivity at 200 K, which was proved with dynamic breakthrough experiments with a simulated dry air containing 21% O₂ with N₂ as the balance.

It was also demonstrated by the collaborative team that chemical modifications to the aluminum formate crystal structure can be used to tune the speed and selectivity of the adsorption in ALF. In the study, the team targeted an ALF material which replaced some Al with iron (Fe). The material isolated and studied is known as ALF-Fe and had an Al:Fe ratio of 40:60. Interestingly, ALF-Fe showed markedly similar behavior to ALF in terms of absolute adsorption behavior, but with the advantage of having approximately 3-fold faster O₂ adsorption. The structure of ALF-Fe had a distorted structure when compared to ALF, which produced different pathways within the crystal structure for how adsorbed gas could move through the system.

In conclusion, a combination of adsorption, diffraction, and spectroscopic and computational investigations (not described here) have given a detailed insight into the selective adsorption of O₂ from air into aluminum formate, ALF. It was also demonstrated that metal

substitution to the ALF family of compounds is a viable tool for tuning the selectivity and kinetics of the systems. It was emphasized in the work how ALF differs from most prior MOF studies for selective binding of O₂. Namely, it appears that the excellent O₂/N₂ separation performance in ALF is due to molecular sieving that takes advantage of the small difference between the kinetic diameters of O₂ and N₂. The findings show that pore size engineering in MOFs is a powerful tool for designing new materials for air separation. With its great application potential for non-cryogenic air separation demonstrated, ALF also has a significant advantage compared with all other MOFs in terms of its ease of synthesis, low-cost and scalability.

REFERENCES

- [1] D. Mullangi, H. A. Evans, T. Yildirim, Y. Wang, Z. Deng, Z. Zhang, T. T. Mai, F. Wei, J. Wang, A. R. Hight Walker, C. M. Brown, D. Zhao, P. Canepa, A. K. Cheetham. *J. Am. Chem. Soc.* **145**(17), 9850 (2023).
- [2] H. A. Evans, D. Mullangi, Z. Deng, Y. Wang, S. B. Peh, F. Wei, J. Wang, C. M. Brown, D. Zhao, P. Canepa, A. K. Cheetham, *Sci. Adv.*, **8**(44), eade1473. (2022).
- [3] Z. Zhang, Z. Deng, H. A. Evans, D. Mullangi, C. Kang, S. B. Peh, Y. Wang, C. M. Brown, J. Wang, P. Canepa, A. K. Cheetham, *J. Am. Chem. Soc.* **145**(17), 11643 (2023).

In situ neutron reflectometry of tungsten oxide films to probe the evolution of Li-ion battery anode/electrolyte interfaces

E. D. Rus¹ and J. A. Dura²

The structures that form at the electrode/electrolyte interface in Li-ion batteries, *i.e.* the solid electrolyte interface/interphase (SEI), play a significant role in battery safety and performance, yet are poorly understood because they are extremely thin, and must be studied *in situ* since they are delicate, reactive, and change with electrochemical potential [1]. Neutron Reflectometry (NR) is one of the few techniques that can study these interfaces *in situ* with the required sub-nanometer accuracy and precision, in their native environment, and with an applied potential [2]. Tungsten was selected as a model non-lithiating electrode with optimal neutron scattering length density (SLD) for elucidating the SEI structure. Studies of electrodes with only native oxide [3] and with a thicker thermally grown tungsten oxide [4] were carried out to understand how SEI formation was affected by surface oxide. The tungsten oxide also served as a model conversion electrode.

Lithium-ion batteries commonly use electrolyte solutions with mixed carbonate solvents. Solutions comprised of ethylene carbonate (EC), diethyl carbonate (DEC), and lithium hexafluorophosphate were employed in the two studies considered here. To understand how the two solvent components contributed to SEI formation on native oxide electrodes, solutions with both solvents deuterated, with only DEC deuterated, and with both solvents at natural isotopic abundance were compared. Fits of NR data collected at +0.25 V vs Li/Li⁺ showed the SEI consisted of a two-layer structure (Fig. 1). The SLD of the inner SEI (*i.e.* the layer closer to the electrode) was not strongly affected by the deuteration of the solvent, indicating that it did not incorporate a large amount of solvent-derived species. This and the low value of the inner SEI SLD suggest it consisted of lithium rich species such as Li₂O or Li¹H (with the ¹H derived from sources other than the solvents, since in one instance they were both fully deuterated). The SLD of the outer SEI on the other hand did show a strong dependence on the deuteration of the solvent, suggesting it either incorporated a large amount of solvent-derived ¹H containing species or that it had a large amount of solution filled porosity.

When the electrode was polarized to more oxidizing potentials (+2.65 V vs Li/Li⁺), the SLD of the inner layer increased, consistent with the removal of lithium atoms and possibly of ¹H-containing species. Ten potential cycles between +0.25 V and +2.65 V, resulted in lower contrast between the inner and outer surface layers, which may be indicative of intermixing of the layers. The SLD of the inner SEI

depended on the solvent deuteration after cycling, suggesting cycling introduced solution filled porosity or solvent derived species into the inner layer. The higher average SLD of the two SEI layers indicated the possible loss of ¹H initially present in this layer into solution.

While the tungsten electrodes used in the first study were meant to serve as non-lithiating electrodes, a thin native oxide film was always present on the surface. To help understand the role this layer played in SEI formation and to serve as a model conversion type electrode (CTE), tungsten oxide thin films on tungsten were prepared by thermal oxidation in air. Combined analysis of X-ray and neutron reflectometry showed the oxide layer was WO₃, and that the remaining tungsten layer was slightly oxidized (with an O/W atomic ratio of about 0.04–0.12). NR was measured over a cycle of potential holds between +2.5 V and +0.25 V (Fig. 2). As the electrode was polarized to more reducing potentials, an SEI qualitatively similar to that seen at native oxide electrodes formed, the tungsten oxide/CTE layer grew thicker, and its SLD decreased. Its thickness and SLD did not follow the tie line (--- in Fig. 2) calculated for the mixture (1-x) WO₃ + x (W+3Li₂O), where x is the fraction of WO₃ that has reacted. Expansion of the CTE was evident only at the most reducing potential, +0.25 V. Here, the CTE layer was somewhat thinner and its SLD not quite as low as expected for W+3Li₂O, possibly indicating it contained more than 16% unreacted WO₃. (Note this calculation assumes all unreacted material is WO₃, though Li_xWO₃ may also be present.) Upon re-oxidation, the SLD profiles were similar to those for the initial reduction, though with hysteresis. The SLD depth profile progression is not consistent with establishment of a diffusional profile in the surface normal direction and did not show a phase transformation front. However, it might be consistent with rapid through-film diffusion along grain boundaries followed by in-plane propagation. At +0.25 V, the CTE had a uniform SLD, indicating that it reached a uniform composition. Any metallic W produced by the conversion reaction was well interspersed with other species in the W oxide layer and did not add to the underlying W layer.

The inner SEI was roughly three times thicker than that observed at the first hold at +0.25 V for the native tungsten oxide and had a lower SLD (perhaps due to the presence of a larger amount of ¹H from adventitious from sources such as hydroxide groups in the thicker tungsten oxide) while the outer SEI was of similar thickness. The SLD depth profile of the thermal oxide electrode at +0.25 V was not a proportionately thicker version of what was observed

¹ Materials Measurement Laboratory, National Institute of Standards and Technology, Gaithersburg, MD 20899

² NIST Center for Neutron Research, National Institute of Standards and Technology, Gaithersburg, MD 20899

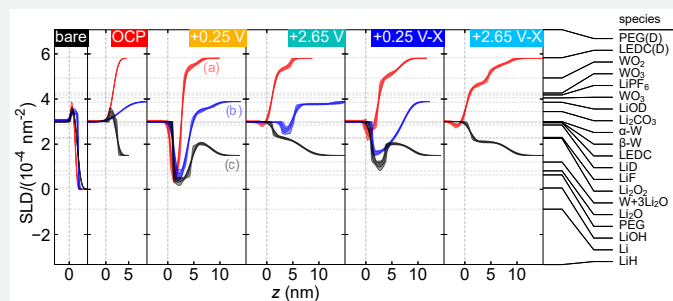


FIGURE 1: Comparison of the fitted SLD profile for each contrast at each applied potential and a list of SEI candidate species with corresponding SLDs [3]. Red curves (a) are for both solvents deuterated, blue (b) for only DEC deuterated, and black (c) for both solvents at natural isotopic abundance. The two values for the WO_3 SLD indicate upper and lower limits of densities (hexagonal WO_3 excluded).

for the native oxide electrode at this potential, showing that the layer structure observed for native oxide electrodes was not simply associated with oxide reduction products. The greater thickness of the inner SEI for the thermal oxide electrode could be associated with the greater amounts of adventitious ^1H , increased surface roughness, a combination of these, or other factors.

In conclusion, precise *in situ* Neutron Reflectometry with isotopic contrast variation as a function of electrochemical potential allowed direct verification of the two layer SEI structure, with a low porosity inner layer consisting of Li_2O , and possibly with LiH derived from ^1H present on the surface of the as made electrodes, and the outer layer which was either porous, derived from the organic solvents, or both. The conversion type electrode did not evolve within a charge/discharge cycle in a manner consistent with a diffusional concentration profile in the surface normal direction and did not show a phase front. Results also indicate that surface contamination of the electrode with hydrogen plays a part in the initial SEI formation but can be removed with cycling. Such results can play an important role in improving battery the SEI, leading to greater battery safety and longevity, and understanding the lithiation profiles that may be used to enable faster charging.

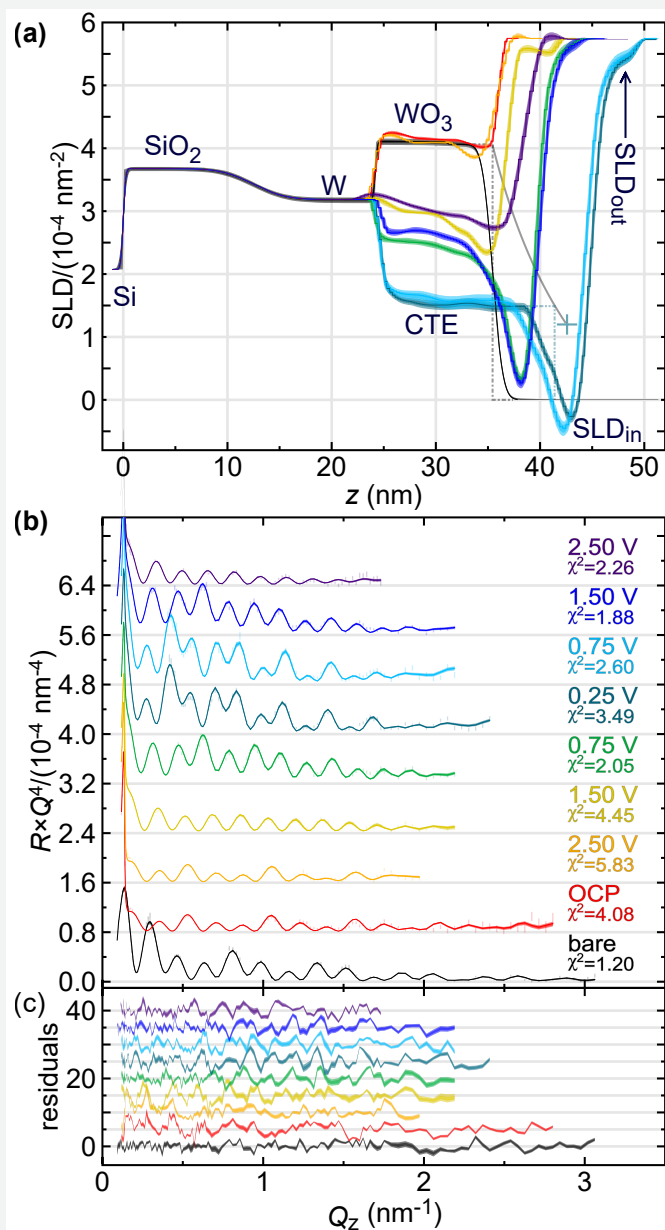


FIGURE 2: Results for the thermally oxidized tungsten film electrode. (a) Neutron SLD depth profiles resulting from fits to (b) *in situ* NR data collected at the indicated potentials (and NR of the bare wafer in helium prior to the *in situ* measurements) with corresponding fits (solid bands) and (c) residuals. Values of χ^2 and potentials are color coded. Confidence bands of 68% and 95% for the fits are shown as darker and lighter shaded bands. The "+" marker near 43 nm, $1.2 \times 10^{-4} \text{ nm}^{-2}$ indicates the expected extent and SLD of the CTE for reduction of WO_3 to $\alpha\text{-W}$ and Li_2O . The dashed curve is the tie line described in the text.

REFERENCES

- [1] J. E. Owejan, J. P. Owejan, S. C. DeCaluwe, J. A. Dura, *Chem. Mater.* **24** (11), 2133 (2012).
- [2] J. A. Dura, E. D. Rus, P. A. Kienzle, B. B. Maranville, *Nanolayer Research*, Imae, T., Ed. Elsevier: Amsterdam, 155 (2017).
- [3] E. D. Rus, J. A. Dura, *ACS Appl Mater Interfaces* **11** (50), 47553 (2019).
- [4] E. D. Rus, J. A. Dura, *ACS Appl Mater Interfaces* **15** (2), 2832 (2023).

Influence of inorganic layer thickness on methylammonium dynamics in hybrid perovskite derivatives

A. A. Koegel,¹ I. W. H. Oswald,¹ C. Rivera,¹ S. L. Miller,¹ M. J. Fallon,¹ T. R. Prisk,² C. M. Brown,² and J. R. Neilson¹

The field of solution-processable semiconductors has undergone rapid development owing to the discovery of hybrid halide semiconductors. The prototypical hybrid halide semiconductor based on the perovskite structure with the formula ABX_3 (A = (in)organic cation, B = metal, X = halide) is composed of three-dimensional (3D) corner-connected $[BX_6]$ octahedra with the A-site cation filling the cuboctahedral void. The $CH_3NH_3PbI_3$ perovskite has excellent charge transport and visible light absorption. This prototypical structure can be further modified with the incorporation of large organic cations, such as n-butylammonium (nBA) or phenylethylammonium (PEA) [1], which disrupt the 3D connectivity and reduce dimensionality as shown in Figure 1. These so-called, “Ruddlesden-Popper” compounds form a homologous series of phases with the chemical formulae, $(R-NH_3)_2(A)_{n-1}B_nX_{3n+1}$, with the series spanning compounds containing layers comprised of a single BX_6 octahedron ($n = 1$) up to 7 octahedra thick ($n = 7$). This change in octahedral layer thickness drastically affects the thermodynamic stability of the materials, as well as the optoelectronic properties, such as reduced band gaps and resistivity, increased carrier lifetimes, and smaller exciton binding energies at higher octahedral layer thicknesses. These relationships highlight the importance of structural control of a material when targeting a specific property.

The incorporation of large organic cations into the perovskite structure provides access to electronic dynamics beyond those of the 3D perovskite. We have previously shown the organic cation dynamics are coupled to the inorganic structure and thus optoelectronic properties in layered perovskite derivatives containing single-octahedron thick layers (e.g., $n = 1$) [2]. As the inorganic framework and organic “spacers” are closely coupled, it is necessary to understand what role the organic cations play in influencing the electronic dynamics in the multi-layered ($n > 1$) perovskites. These neutron spectroscopy studies reveal that organic cation rotational dynamics influence the inorganic structure, the formation of excitons (both free and self-trapped) and subsequent light emission in layered perovskites. We report the cation rotational dynamics of $(d-nBA)_2(MA)_{n-1}PbI_{3n+1}$ ($d-nBA = CD_3(CD_2)_3NH_3^+$, $MA = CH_3NH_3^+$, $n = 2$ and 3) with fixed-widow scans on HFBS, and quasi-elastic neutron scattering (QENS) on DCS spectrometers at the NCNR [3].

The mean-squared displacements (MSD, Figure 2) of the two materials with different octahedral layer thicknesses show similar spatial extent of hydrogen motion in methylammonium ($CH_3NH_3^+$) and $CD_3(CD_2)_3NH_3^+$ ($d-nBA$). The deuteration of the n-butylammonium cations minimizes its contribution to the quasi-elastic scattering, thus allowing us to directly monitor the methylammonium and ammonium headgroup hydrogen dynamics. The discontinuities in the MSD at 183 K in both samples are representative of a significant decrease in organic cation dynamics and correspond to the previously measured transitions upon cooling. The hysteresis in the MSD at 203 K upon heating in $(d-nBA)_2(MA)_2Pb_2I_7$ and 186 K upon heating in $(d-nBA)_2(MA)_2Pb_3I_{10}$ is brought on by phase transitions restricting organic cation motion. Temperature-dependent quasi-elastic neutron scattering spectra illustrate that these phase transitions reduce the cation spatial and temporal dynamics.

The EISFs (Figure 3) for each n -member are well modeled by the rotations of $CH_3NH_3^+$ and $d-nBA$ constrained by symmetry-adapted motions derived from the room temperature crystal structures. $CH_3NH_3^+$ is constrained by the C_3 symmetry along the C-N axis of the molecule and the pseudo- C_4 symmetry of the cuboctahedral void it occupies. Since the $d-nBA$ only contains H on the ammonium head group it is constrained by C_3 symmetry along the C-N axis. Models were developed to include the two contributions over the various temperature ranges and fit to the EISFs.

The relatively static dynamics of $d-nBA$ in these materials provides the $CH_3NH_3^+$ with a set of preferred orientations; however, the interactions between $d-nBA$ and $CH_3NH_3^+$ are decreased upon an increase of inorganic layers leading to shorter $CH_3NH_3^+$ residence times through the screening effects provided by thicker inorganic layers. The phase transitions at $T < 183$ K in these layered materials directly correlate to a restriction of the $CH_3NH_3^+$ dynamics, where the C_4 tumbling is frozen out. The reduced $CH_3NH_3^+$ rotational dynamics also coincide with a decrease in measured changes in the carrier mobility and lifetime.

¹ Colorado State University, Fort Collins, CO 80523

² NIST Center for Neutron Research, National Institute of Standards and Technology, Gaithersburg, MD 20899

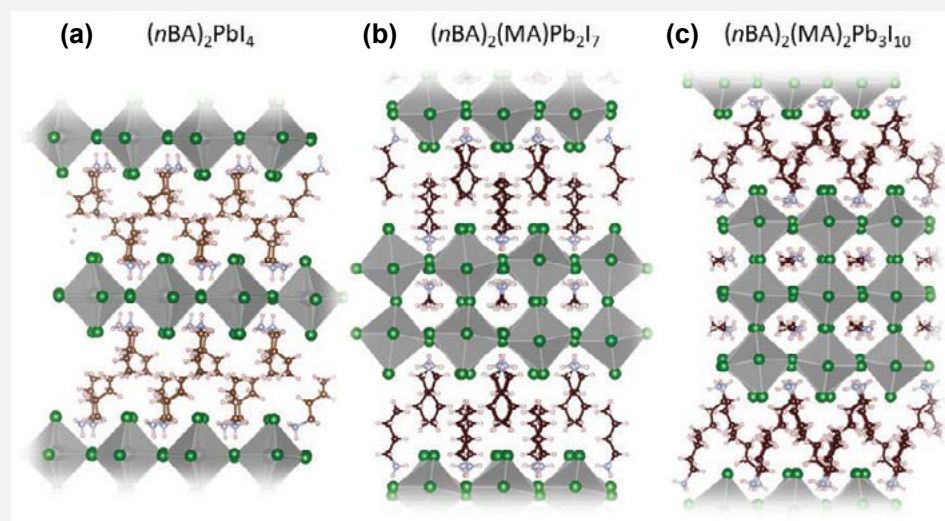


FIGURE 1: Illustrations of the crystal structures of (a) $(n\text{BA})_2\text{PbI}_4$, $n = 1$, (b) $(n\text{BA})_2(\text{MA})\text{Pb}_2\text{I}_7$, $n = 2$, and (c) $(n\text{BA})_2(\text{MA})_2\text{Pb}_3\text{I}_{10}$, $n = 3$. $n\text{BA} = \text{CH}_3(\text{CH}_2)_3\text{NH}_3^+$, $\text{MA} = \text{CH}_3\text{NH}_3^+$; gray = Pb, green = I, brown = C, blue = N, pink = H.

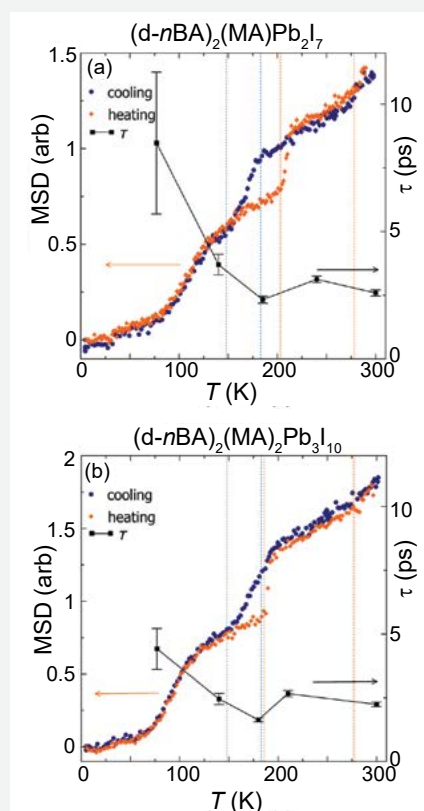


FIGURE 2: Mean-squared displacements (MSD, left axis) and residence times (τ , ps, right axis) of hydrogen motion in (a) $(d\text{-}n\text{BA})_2(\text{MA})\text{Pb}_2\text{I}_7$ and (b) $(d\text{-}n\text{BA})_2(\text{MA})_2\text{Pb}_3\text{I}_{10}$. MSDs upon cooling (blue) and heating (orange) were collected from 5 K to 300 K. Phase transitions determined from differential scanning calorimetry values are highlighted with dashed lines (orange for heating, blue for cooling.) Residence times of hydrogen rotations (black squares, right y-axis) from 77 K to 300 K determined from the half-width-at-half-maximum of quasi-elastic neutron spectra and show shorter residence times for $(d\text{-}n\text{BA})_2(\text{MA})_2\text{Pb}_3\text{I}_{10}$. Error bars represent 1σ .

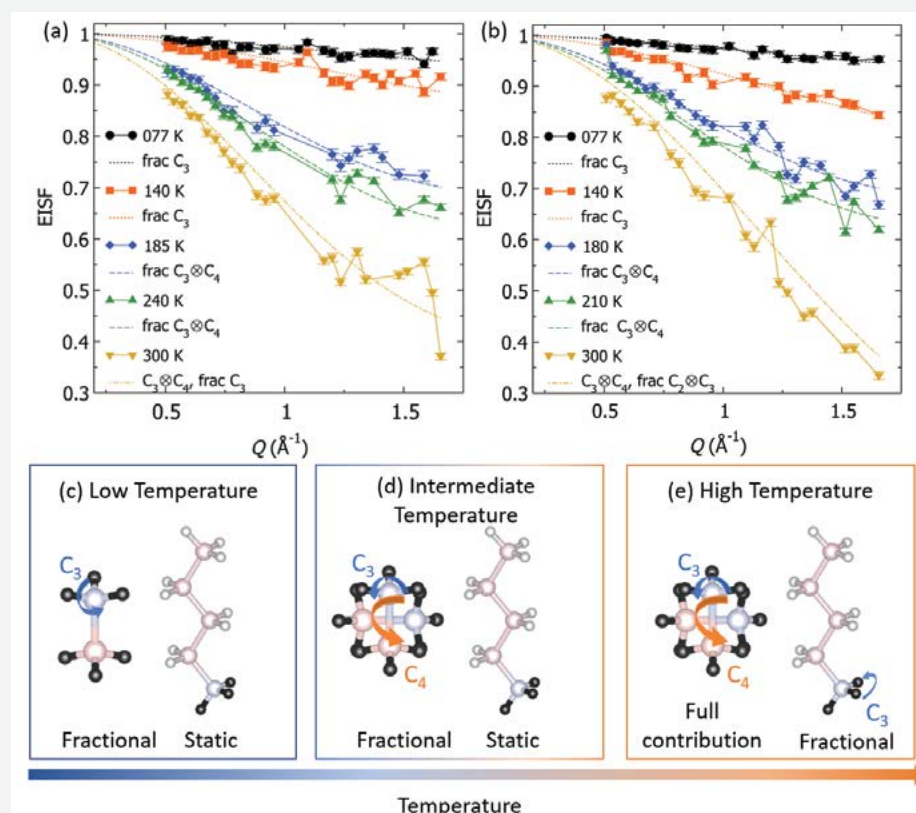


FIGURE 3: Top: Elastic Incoherent Structure Factors (EISF) of (a) $(d\text{-}n\text{BA})_2(\text{MA})\text{Pb}_2\text{I}_7$ and (b) $(d\text{-}n\text{BA})_2(\text{MA})_2\text{Pb}_3\text{I}_{10}$ at 77 K to 300 K extracted from QENS data with jump models describing $\text{C}_3 \otimes \text{C}_4$ motion of CH_3NH_3^+ with fractional C_3 motion of the $d\text{-}n\text{BA}\text{-NH}_3^+$ headgroup (dot-dashed), $\text{C}_3 \otimes \text{C}_4$ of CH_3NH_3^+ only (dashed), and fractional $\text{CH}_3\text{NH}_3^+ \text{C}_3$ rotations (dotted). Bottom: Organic cation rotations modeled in the three different temperature regimes. Error bars represent 1σ .

REFERENCES

- [1] C. C. Stoumpos, D. H. Cao, D. J. Clark, J. Young, J. M. Rondinelli, J. I. Jang, J. T. Hupp, M. G. Kanatzidis, *Chem. Mater.* **28**, 2852 (2016).
- [2] A. A. Koegel, E. M. Mozur, I. W. H. Oswald, N. H. Jalarvo, T. R. Prisk, M. Tyagi, J. R. Neilson, *J. American Chem. Soc.* **144**, 1313 (2022).
- [3] A. A. Koegel, I. W. H. Oswald, C. Rivera, S. L. Miller, M. J. Fallon, T. R. Prisk, C. M. Brown, and J. R. Neilson, *Chem. Mater.* **34**, 8316 (2022).

Wall-polymer interactions and morphology around interfaces determine polymer mobility and CO₂ uptake of solid-supported amine CO₂ sorbents

H. J. Moon,¹ J.-M. Y. Carrillo,² J. Leisen,³ B. G. Sumpter,²
N. C. Osti,⁴ M. Tyagi,^{5,6} and C. W. Jones¹

The rising atmosphere CO₂ level necessitates deployment of carbon capture from ambient air, often called direct air capture (DAC). The ultra-dilute CO₂ concentration of ~775 mg/m³ (400 ppm) in air requires development of efficient separation materials, and solid-supported amines are among the most promising platforms. Such sorbents exhibit high CO₂ uptake provided by amine-CO₂ interactions typically forming carbamate or bicarbonate. They also enable energy-efficient regeneration compared to aqueous amines. To minimize amine leaching or evaporation from the support during thermal cycling, polymeric amines have generally been used. As solid supports, mesoporous oxides that can offer sufficient pore space to encapsulate a large quantity of amino polymers have been widely used. Among diverse solid-supported amines, poly(ethyleneimine) confined in mesoporous SBA-15 (PEI/SBA-15) has been widely studied.

Within PEI/SBA-15, CO₂ first passes through readily accessible free volume (mostly open pore space), finds available amine sites and interacts with them. Once readily accessible amines are occupied, CO₂ molecules must diffuse through the amine polymer phase, where amine mobility determines CO₂ diffusivity and thus CO₂ uptake rates. In prior empirical studies, PEI/SBA-15 systems generally exhibit higher CO₂ uptake with increasing sorption temperatures up to a certain point, with lower uptake at then higher temperatures [1]. Such a trend contradicts thermodynamics, considering that sorption is exothermic and therefore sorption should decrease with increasing temperature. This trend can be rationalized by polymer diffusion limited CO₂ uptake at lower temperatures as heating enhances polymer mobility, which improves CO₂ diffusivity. To this end, amine mobility has been considered one of the key factors determining the performance of the PEI/SBA-15 for CO₂ capture.

However, characterizing the motion of PEI contained in porous supports is a challenge. One can picture PEI in SBA-15 like honey in the honeycomb at ambient conditions, and the structure and dynamics of the polymer in the porous phase has not been effectively probed. Most conventional laboratory techniques available

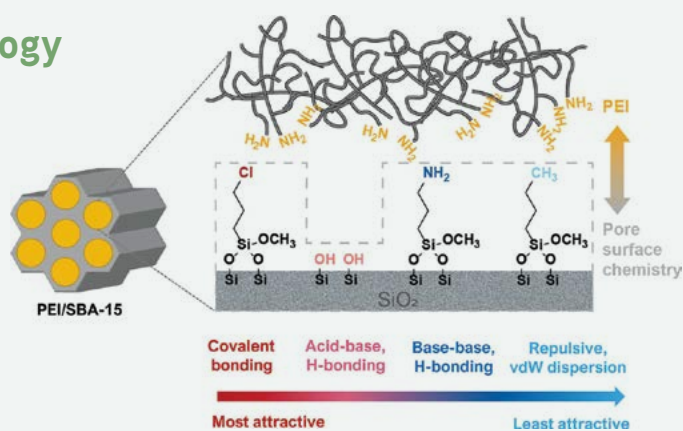


FIGURE 1: Schematic structure of PEI/SBA-15 with four types of wall-PEI interactions.

to adsorption researchers allow for the characterization of solid supports but have limited ability to probe the soft amines confined in the supports. Our group has deployed quasi-elastic neutron scattering (QENS) as an effective tool in characterizing amine motion in the soft/hard composite PEI/SBA-15 material [2]. Given the neutron's penetrable properties, they can reach the soft amine phase and interact with the nuclei of hydrogen-rich PEI (with SBA-15 being relatively hydrogen-deficient), yielding information about the PEI motions. Using QENS, we probed PEI/SBA-15 with varied pore wall properties to understand how wall-PEI interactions impact PEI mobility [3]. Figure 1 shows the types of wall-PEI interactions sought.

We expected that attractive PEI-wall interactions would lower PEI mobility at the interfaces, leading to the slowest mobility of PEI around chloropropylsilane functionalized walls that form covalent bonds with the PEI chains and the fastest mobility for PEI around hydrophobic alkyl chains. However, our hypothesis was refuted by QENS. As shown in Figure 2, larger QENS broadening was observed for the PEI around aminosilanes compared to alkylsilanes (*i.e.*, P40NH₂ vs. P40CH₃), meaning that PEI exhibited higher mobility around aminosilanes. Here, P40Cl was only partly aged so that only limited PEI chains were covalently bonded to the pore walls. Subsequent QENS (done in ORNL) measurements after extending aging and reaction time showed that P40Cl showed lower PEI mobility compared to P40SiOH.

We rationalized the seemingly counterintuitive trend of PEI mobilities (*i.e.*, P40NH₂ vs. P40CH₃) by considering the complexity of the interfaces. At the wall-PEI interfaces with grafted chains, interplay among PEI chains, grafted chains, and solid walls may result in unique structures and mobility of the PEI and grafted chains. Figure 3 shows the plausible structures of the wall-grafted chains and PEI around the PEI-wall interfaces based on solid-state NMR

¹ Georgia Institute of Technology Atlanta, GA 30332

² Center for Nanophase Materials Sciences, Oak Ridge National Laboratory, Oak Ridge, TN 37830

³ Georgia Institute of Technology, Atlanta, GA 30332

⁴ Neutron Scattering Division, Oak Ridge National Laboratory, Oak Ridge, TN 37830

⁵ NIST Center of Neutron Research, National Institute of Standards and Technology, Gaithersburg, MD 20899

⁶ University of Maryland, College Park, MD 20742

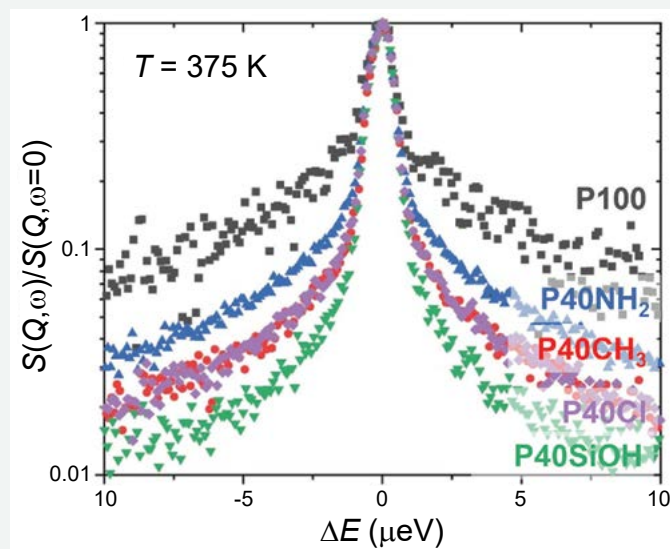


FIGURE 2: QENS spectra showing varied extent of PEI mobility upon different wall-PEI interactions. Nomenclature used—P100: bulk, non-confined PEI, P40X: 40 wt% PEI in PEI/SBA-15 composite, with X representing end group of the grafted chains or silanols.

($^1\text{H } T_1$ - T_2 relaxation correlation) and MD simulation. Amine groups on the grafted chains appeared to coordinate with hydrophilic parts of the walls (such as ungrafted silanols), effectively reducing PEI-wall coordination (Figure 3, P40NH₂). On the other hand, alkyl chains may not effectively block PEI-wall interactions (Figure 3, P40CH₃).

Lastly, we investigated the effect of PEI mobility in terms of CO₂ capture performance. We expected that faster PEI motion can be directly related to faster CO₂ diffusion in PEI domains, resulting in faster CO₂ uptake rates. Figure 4 shows the fractional uptake as a function of time. From P40Cl, we observe notably fast uptake at an early stage, presumably caused by the small amount of PEI distributed on the external surface of the SBA-15 support (as grafted chloropropyl chains are also distributed to the outer surfaces). While sorbents other than P40Cl do not have significant PEI coating the external surface, P40SiOH showed faster uptake compared to P40CH₃ and P40NH₂, though slower PEI motions in P40SiOH. This could be understood by considering the remaining void space in the sorbent, in which CO₂ can freely diffuse. P40NH₂ and P40CH₃ showed lower void volume in the pores due to the volumes occupied by the grafted chains. Lastly, comparing P40CH₃ and P40NH₂, which had similar PEI dispersion (macroscopic) and void volume in the pores, faster CO₂ uptake was observed in P40NH₂, as PEI had better mobility. These results clearly show that morphology controls rapid uptake at early stage while the PEI dynamics dominate the gradual uptake at later stage.

In summary, the way PEI interacts with silica support walls influenced PEI mobility. Due to the complex structures of PEI in SBA-15 with grafted chains, the trend of PEI mobility did not follow the simple predicted trend (*i.e.*, stronger PEI-wall attraction leading to lower PEI mobility). Instead, interplay among pore walls, grafted chains, and PEI resulted in unique chain configurations of the grafted

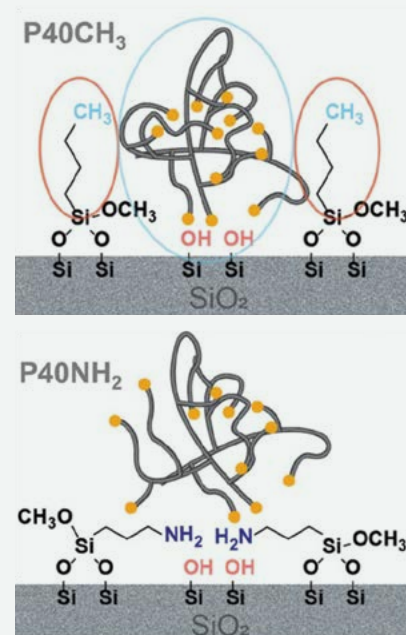


FIGURE 3: Plausible structures of grafted chains and PEI at wall-PEI interface.

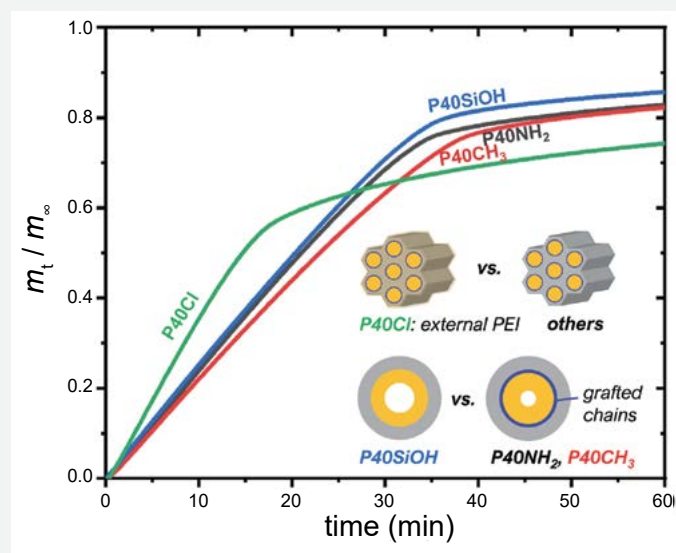


FIGURE 4: CO₂ uptake performance of sorbents and proposed reasons.

chains, PEI morphology and mobility. A combination of QENS and solid-state NMR effectively painted a comprehensive picture of the dynamic properties of PEI, allowing us to elucidate structure-property relationships in terms of the design of the wall-polymer interfaces of PEI/SBA-15 systems, which might then be extended to the general class of solid-supported amine CO₂ sorbents.

REFERENCES

- [1] X. Xu, C. Song, J. M. Andresen, B. G. Miller, A. W. Scaroni, *Energy Fuels*. **16** (6), 1463 (2002).
- [2] A. Holewinski, M. A. Sakwa-Novak, J. Y. Carrillo, M. E. Potter, N. Ellebracht, G. Rother, B. G. Sumpter, C. W. Jones, *J. Phys. Chem. B*. **121** (27), 6721 (2017).
- [3] H. J. Moon, J. Y. Carrillo, J. Leisen, B. G. Sumpter, N. C. Osti, M. Tyagi, C. W. Jones, *J. Am. Chem. Soc.* **144** (26), 11664 (2022).

Three-dimensional structure of hybrid magnetic skyrmions determined by neutron scattering

W. L. N. C. Liyanage,¹ N. Tang,² L. Quigley,² J. A. Borchers,³ A. J. Grutter,³ B. B. Maranville,³ S. K. Sinha,⁴ N. Reyren,⁵ S. A. Montoya,⁴ E. E. Fullerton,⁴ L. DeBeer-Schmitt,⁶ and D. A. Gilbert^{1,2}

Magnetic skyrmions are chiral spin textures. They are of interest in fundamental research and present unique opportunities to develop advanced spintronic technologies. These magnetic structures can be described as a continuous wrapping of spins into closed, coplanar loops in which the spins in the cores and perimeters are oriented in opposite, out-of-plane directions. The coplanar loop can have magnetic moments oriented along the radial direction (orthogonal to the loop axis, aka Néel-type) or the azimuthal direction (along the loop axis, aka Bloch-type). We have discovered a new skyrmion structure, called a hybrid skyrmion, which we propose is constructed of Néel-type wrapping on either end of the skyrmion tube and Bloch-type wrapping in-between [1-3]. This configuration reduces stray magnetic fields in the system, decreasing the overall magnetic energy and increasing the stability. The hybrid skyrmion structure also presents opportunities for new studies of fundamental physics, including magnetic dynamics [4]. As the 3D spin configuration is responsible for the topology and stability of the skyrmion, it is critical to determine the full structure experimentally. However, this is exceedingly challenging to do because the configuration has only magnetic contrast and is embedded within the material.

The penetrating nature and magnetic sensitivity of neutrons makes it possible to measure the 3D structure of skyrmions. Polarized-neutron reflectometry (PNR), employed in the conventional specular configuration, is the standard technique used to determine the magnetic depth profile of a film. A quick consideration of the skyrmion suggests that there should be no magnetic signal in a PNR measurement because the closed-loop structure has moments in all directions, and thus the in-plane magnetization averages to zero. However, skyrmions are large, so the neutron coherence length spans a non-integer number of skyrmions, resulting in a non-zero moment [5]. Small-angle-neutron scattering (SANS) is a complementary technique that illuminates the sample with neutrons along the sample-normal direction, e.g. parallel to the skyrmion tubes. The resulting diffraction pattern captures the projected structure of the skyrmion tubes and lattice. Finally, grazing-incidence SANS (GISANS) combines PNR and SANS, illuminating the sample at grazing incidence and measuring the specular and off-specular

reflections as a function of scattering angle, thereby capturing both the in-plane and out-of-plane structures.

For this study [6], hybrid skyrmions were prepared in thin films with a nominal structure of $[\text{Fe} (3.6 \text{ \AA}) / \text{Gd} (4.0 \text{ \AA})]_{120}$ on Si. Following a previously published field procedure, the film was populated with hybrid skyrmions. The SANS data in Fig. 1a confirm that the skyrmions form an ordered-hexagonal lattice. The hexagonal peaks occur at a radius of $|Q| = 0.00298 \text{ \AA}^{-1}$, corresponding to an inter-skyrmion spacing of 211 nm. PNR measurements were performed in the skyrmion state at room temperature and in an out-of-plane magnetic field of 195 mT. The reflectometry pattern is shown in Fig. 1b. A representative model of the magnetic and nuclear depth profile was developed. Using the Refl1D analysis program, a simulated reflectometry profile was calculated from the model and compared to the experimental results. The model was systematically refined until the simulated and experimental reflectometry profiles closely matched, as shown in Fig. 1c. This model provides the nuclear structure of the film, including layer thicknesses and roughnesses, as well as a small residual magnetization, which is present because the transverse coherence length of the neutron overlaps with a non-integer number of skyrmions [5]. The refined profile also shows that the magnetization is slightly larger at the ends of the skyrmion tube. Since the measured magnetization is the result of the in-plane winding of the skyrmion, this suggests that the in-plane width of the winding is larger at the ends, *i.e.*, in the Néel-type cap regions.

GISANS measurements were performed on the vSANS instrument, with the scattering from a single incident angle shown in Fig. 1d. The diffraction pattern shows three peaks, one located at $Q_x = 0$, corresponding to specular reflection (equivalent to specular reflection from PNR), and two flanking peaks at $Q_x = \pm 0.00338 \text{ \AA}^{-1}$, which reflects the in-plane spacing of the skyrmion. As the sample is tilted through a series of angles relative to the incident neutron beam, the three peaks shift to larger Q_z positions. The peak intensities change because the sample is a thin-film, and they effectively encode the depth-profile as in a PNR measurement. Since the off-specular peak results from the in-plane structure and tilting the sample as described probes the depth profile, the GISANS measurement captures the full 3D structure of the skyrmion.

¹ Department of Physics and Astronomy, University of Tennessee, Knoxville, TN 37996

² Materials Science and Engineering Department, University of Tennessee, Knoxville, TN 37996

³ NIST Center for Neutron Research, National Institute of Standards and Technology, Gaithersburg, MD 20899

⁴ Center for Memory and Recording Research, University of California, San Diego, CA 92093

⁵ Unité Mixte de Physique, CNRS, Thales, Université Paris-Saclay, Palaiseau 91767, France

⁶ Neutron Scattering Division, Oak Ridge National Laboratory, Oak Ridge, TN 37830

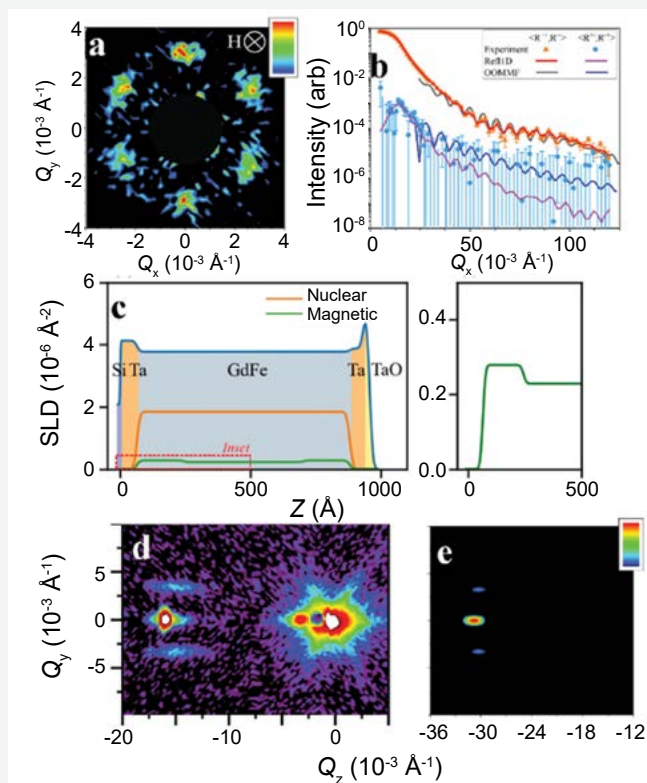


FIGURE 1: Data for a Gd/Fe skyrmion thin film. (a) SANS scattering pattern; (b) PNR profile; (c) converged nuclear and magnetic profile; (d) GISANS pattern; (e) simulated GISANS pattern.

To analyze these results, the nuclear depth profile (Fig. 1c) was used to define a simulated sample. The known magnetic properties (such as the saturation magnetization) were defined within the simulated parameter space, while other parameters (such as the exchange stiffness) were estimated from the published literature. Using NIST's Object Oriented Micromagnetic Framework (OOMMF) simulation platform, the 3D magnetic structure was simulated and allowed to achieve its stable configuration. The scattering profile from the simulated structure was calculated and compared to the experimental results. Following an iterative procedure, the estimated energy parameters were adjusted, the model refined, and the new scattering profile calculated and compared to the experiment.

The simulated GISANS pattern is shown in Fig. 1e, and the simulated reflectometry pattern is shown in Fig. 1b. The refined magnetic profile, shown in Fig. 2a, confirms the hybrid structure, with Néel-type skyrmions on the ends of the tube and Bloch-type winding at the equator. The width of the in-plane winding can be extracted from the simulation and is shown in Fig. 2b. Indeed, the width of the skyrmion boundary is shown to be larger at the ends of the skyrmion tube compared to the middle. The total in-plane magnetization at each depth resulting from this increased width (that is, $1-|M_z|/M_s$, from the OOMMF simulation) can be compared with the measured magnetization (from the PNR results) in Fig. 2c. Since the measured magnetization is the result of a fractional overlap, these values are related by a proportionality constant. This comparison shows

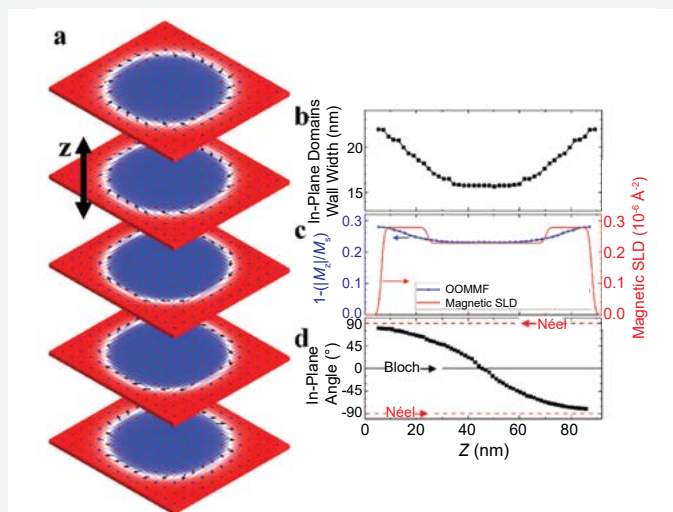


FIGURE 2: (a) Refined simulation profile of a magnetic skyrmion tube. (b) Width of the in-plane winding from OOMMF. (c) Comparison of the total in-plane magnetization from OOMMF with the Ref1D magnetic profile. (d) In-plane wrapping angle of the magnetization versus depth.

excellent agreement, with the OOMMF results showing a more gradual change in the magnetization over ≈ 13 nm while the Ref1D model identified the increased magnetization over ≈ 18 nm. The OOMMF model also allows the direction of the in-plane winding to be extracted; recall that for Néel-type winding the spins in the skyrmion wrapping orient radially inward while in the Bloch region they orient azimuthally. This angle is extracted at each depth along the length of the skyrmion tube and plotted in Fig. 2d. Interestingly, the angle changes continuously with depth and does exhibit the discrete Néel/Bloch/Néel regions predicted initially. Furthermore, there seems to be little correlation between the width of the in-plane winding and the Néel or Bloch character.

In summary, the 3D structure of magnetic hybrid skyrmions was measured using a combination of PNR, SANS, and GISANS, as well as using micromagnetic simulations to analyze the results and verify the structure. The refined magnetic profile is thus grounded in both the well-established physics of magnetism and experimentally determined scattering. Skyrmion tubes have Néel-type ends with a Bloch-type equator. The width of the in-plane winding was confirmed to be larger at the ends versus the equator, but this did not explicitly correspond to the angle of the in-plane winding. These nuanced details collectively quantify the topological structure of the hybrid skyrmion and provide clues to achieving improved stability.

REFERENCES

- [1] R. D. Desautels *et al.*, *Phys. Rev. Matter.* **3**, 104406 (2019).
- [2] S. A. Montoya *et al.*, *Phys. Rev. B* **95**, 224405 (2017).
- [3] S. A. Montoya *et al.*, *Phys. Rev. B* **95**, 024415 (2017).
- [4] N. Tang *et al.*, *Advanced Materials*, **35**, 2300416 (2023).
- [5] D. A. Gilbert *et al.*, *Nature Communications* **6**, 8462 (2015).
- [6] W. L. N. C. Liyanage *et al.*, *Phys. Rev. B* **107**, 184412 (2023).

Neutron spectroscopy of the spin-orbital excitons in HoBi

J. Gaudet,^{1,2,3} H.-Y. Yang,⁴ E. M. Smith,⁵ T. Halloran,¹ J. P. Clancy,⁵ J. A.-Rodriguez-Rivera,^{2,3} G. Xu,² Y. Zhao,^{2,3} G. Sala,⁶ A. A. Aczel,⁶ B. D. Gaulin,⁵ F. Tafti,⁴ and C. L. Broholm^{1,2}

Rare-earth monpnictides RX (R = Ce to Yb and X = N, As, Sb, or Bi) crystallize into a face-centered cubic lattice with only two ions per unit cell (Fig. 1A). Despite this chemical simplicity, these materials exhibit complex, coupled magnetic and electric properties. This is exemplified in HoBi, where plateaus in the magnetoresistance and resistivity are affected by various metamagnetic transitions [1] (see Fig.1 B, C, and D). First-principles and band-structure calculations suggest that magnetism can stabilize topological nontrivial electronic bands that generate protected surface states [2]. Motivated by the interplay between magnetism and transport in HoBi, we performed neutron-scattering experiments to determine the spin structure and associated spin dynamics [3]. Using single-crystal neutron and X-ray scattering methods, we found that a type-II antiferromagnetic (AFM) state develops concomitantly with a tetragonal lattice distortion below the Néel temperature $T_N = 5.7$ K. Neutron diffraction alone cannot determine the spin orientation within this AFM state unambiguously, but a detailed analysis of the spin dynamics demonstrates that the spins align along the tetragonal axis. We also derived a microscopic spin Hamiltonian for HoBi, which is essential to understand the magnetic and electric properties of the rare-earth monpnictides.

We identified the order of the magnetic phase transition in HoBi by measuring the temperature dependence of the heat capacity (C_p) using a long-pulse heat method. The C_p data (Fig. 2A) show a sharp peak near $T_N = 5.7$ K, with a thermal hysteresis of 13(2) mK. On both heating and cooling, a plateau is visible in the time dependence of the sample temperature near T_N (inset of Fig. 2A). The plateaus and thermal hysteresis indicate that the phase transition at T_N is first order.

We further characterized the magnetic phase transition using single-crystal X-ray and neutron scattering methods. The X-ray scattering data show that the (H00), (OKO), and (OOL) structural Bragg peaks split below T_N [3], while the (HHH) structural peaks remain unaffected. These observations indicate that a tetragonal distortion occurs within the magnetic state, where the c -axis is elongated relative to the a and b axes. The neutron scattering data show that new magnetic Bragg peaks, indexed by the ordering wave

vector $k = (1/2, 1/2, 1/2)$, appear below T_N . This is indicative of a type-II AFM state (Fig. 2C), where the spin structure can be described as FM sheets of spins that are stacked in an AFM fashion along [111]. The local orientation of the spins within each FM sheet cannot be constrained by symmetry analysis due to the first-order nature of the phase transition. Furthermore, because the diffraction pattern is averaged over a multi-domain sample, the local orientation of the Ho^{3+} spins could not be accurately determined. As seen in Fig. 1A, an identical diffraction pattern is obtained for all type-II AFM structures that have a local spin orientation matching the ensemble of red spins drawn on the $r = (000)$ Ho^{3+} site. The Ising anisotropy of the in-field magnetization data [3] and the tetragonal distortion suggest, but do not prove, that the spins point along the tetragonal c -axis. A proper analysis of the spin dynamics was needed to demonstrate this.

Using the MACS spectrometer at NIST, we investigated the paramagnetic fluctuations in HoBi by measuring the neutron quasielastic scattering at 12 K over an extensive Q -region within the (HHL) plane. The data are shown in Fig. 3A and reveal “butterfly”-shaped diffuse scattering centered at $Q = (\pm 1/2, \pm 1/2, \pm 1/2)$. This diffuse paramagnetic scattering can be parametrized (Fig. 3B) by assuming a dominant 2nd nearest-neighbor (n.n.) Heisenberg AFM interaction J_2 and a weaker 1st n.n. Heisenberg FM interaction J_1 with $|J_2/J_1| = 2.2(1)$. We also measured the neutron inelastic scattering in the paramagnetic state (Fig. 3C) and observed nondispersive magnetic excitations near 7 meV. These local excitations originate from transitions between different crystal-field levels associated with the Ho^{3+} spin-orbit ground-state manifold. We performed point-charge calculations to estimate the CEF Hamiltonian for HoBi, which predict multiple states between 0 meV and 0.2 meV, a second group of CEF states between 6 meV and 7 meV, and a third group of CEF states between 9 meV and 10 meV. This CEF Hamiltonian reproduces the neutron inelastic scattering at 12 K (Fig. 3D). Only the CEF excitations between the first and second group of states can be observed because the predicted scattering intensity between the first and third group is about 250 times weaker. Our CEF Hamiltonian also reproduces the temperature dependence of the high-temperature heat capacity and magnetic susceptibility, which further validates our calculations.

¹ The Johns Hopkins University, Baltimore, MD 21218

² NIST Center for Neutron Research, National Institute of Standards and Technology, Gaithersburg, MD 20899

³ University of Maryland, College Park, MD 20742

⁴ Boston College, Chestnut Hill, MA 02467

⁵ McMaster University, Hamilton, Ontario, Canada L8S 4M1

⁶ Oak Ridge National Laboratory, Oak Ridge, TN 37831

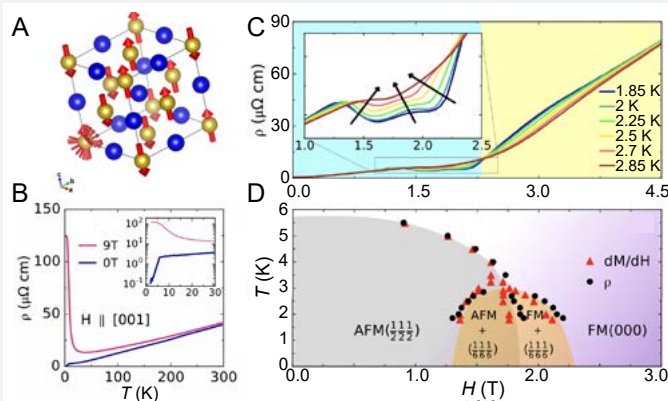


FIGURE 1: Data for HoBi. (A) Crystal and spin structure; the yellow (blue) spheres are the Ho (Bi) ions. The ensemble of red spins drawn on the Ho^{3+} ion at $r = (000)$ depicts the local spin orientations that are consistent with the neutron diffraction data refinement. (B) Temperature dependence of the electrical resistivity. The inset shows the huge drop in resistivity that occurs when magnetic order sets in [1]. (C) Temperature dependence of the magnetoresistance. Kinks develop at low-fields due to metamagnetic transitions [1]. (D) Magnetic phase diagram under a [110] field determined from kinks in the magnetoresistance and steps in the magnetization [1].

Upon cooling through T_N , three well-defined spin excitations develop at 1.7(2) meV, 7.4(2) meV, and 9.0(3) meV (Fig. 3E). These excitations are weakly dispersive, exhibit peak intensity at the magnetic wave vectors $(\pm 1/2, \pm 1/2, \pm 1/2)$, and consistent with spin-orbital excitons, which are crystal-field excitations that can propagate through the lattice due to n.n. exchange interactions. We modeled these excitons using a pseudo-boson theory that incorporates the J_1 and J_2 interactions (constrained by $|J_2/J_1| = 2.2$) and the CEF effect. In this theory, both the energy and neutron scattering intensities of the excitons depend on the spatial orientation of the ordered Ho^{3+} spins. Taking advantage of this fact, we found that the low-energy INS spectrum can only be reproduced with a [001] (tetragonal) local spin anisotropy (see the resulting model in Fig. 3F). This result resolves the ambiguity encountered with neutron diffraction concerning the possible spin structures of HoBi. Our exciton model also allowed us to quantify the exchange interactions, which are comparable to the CEF interactions [3].

In conclusion, HoBi belongs to the family of rare-earth monopnictides, which exhibit strong coupling between electrical transport, magnetism, and electronic band topology. The low-temperature phase transition, which we characterized using single-crystal X-ray and neutron scattering techniques, affects these intertwined properties. We found that HoBi undergoes a tetragonal crystal distortion at $T_N = 5.7$ K. This structural distortion arises concomitantly with type-II AFM order. We determined the local spin orientation of the Ho^{3+} spins within this AFM state by analyzing the effect of the magnetic order on the neutron inelastic scattering spectrum. The spin excitations consist of spin-orbital excitons that respond to an applied magnetic field and are likely responsible for the various observed magnetoresistive features. Similar effects are expected in all magnetic rare-earth monopnictides.

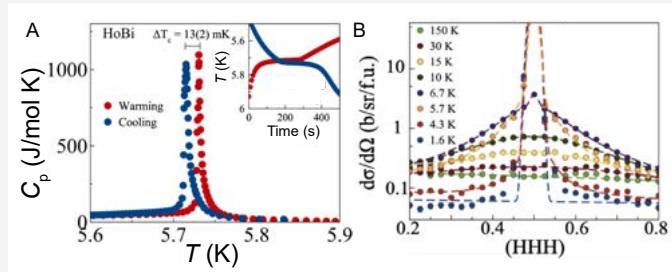


FIGURE 2: (A) Low-temperature heat capacity of HoBi collected using cooling (blue line) and heating protocols (red line). The inset shows the time dependence of the sample temperature, which was collected with a long-pulse method. (B) Single-crystal neutron scattering data at the magnetic $Q = (1/2, 1/2, 1/2)$ Bragg peak collected along the [HHH] direction.

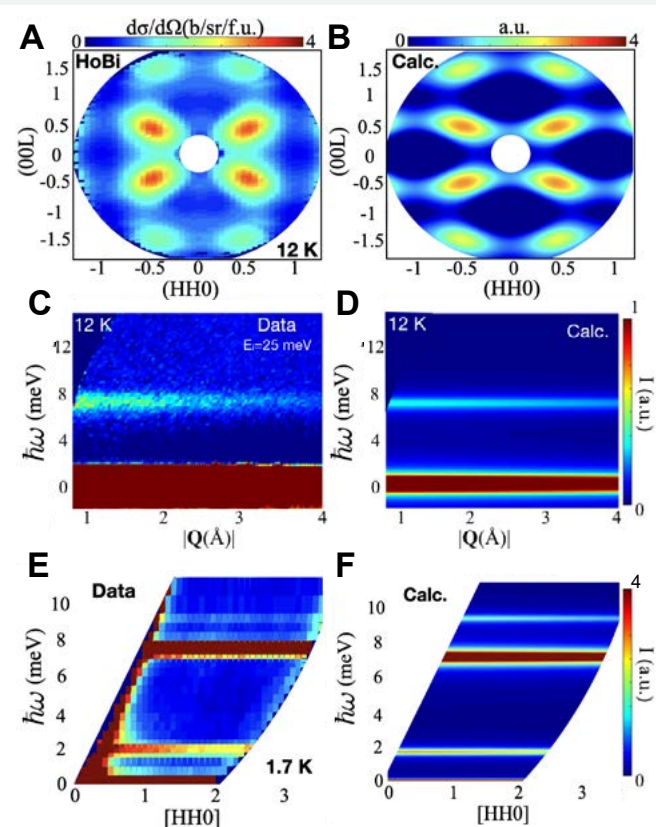


FIGURE 3: (A) Paramagnetic quasielastic scattering measured at 12 K within the (HHL) plane. (B) Calculated paramagnetic scattering. (C) Powder-averaged neutron inelastic scattering collected in the paramagnetic state (12 K). (D) Neutron inelastic scattering from the crystal-field excitations at 12 K, which was obtained using point-charge calculations. (E) Low-temperature (1.7 K) neutron inelastic scattering measured along [HH0]. (F) Neutron inelastic scattering for momentum transfer Q parallel to [HH0]. This spectrum was obtained from a pseudo-boson theory (discussed in the main text) in which the local spin orientation of the Ho^{3+} ions is fixed to point along the [001] tetragonal axis.

REFERENCES

- [1] H.Y. Yang *et al.*, Phys. Rev. B **98**, 045136 (2018).
- [2] Z.M. Wu *et al.*, New J. Phys. **21** 093063 (2019).
- [3] J. Gaudet *et al.*, Phys. Rev. B **107**, 104423 (2023).

Neutron-scattering sum rules, symmetric exchanges, and helicoidal magnetism in MnSb_2O_6

E. Chan,^{1,2} H. Lane,^{2,3,4,5} J. Pásztorová,² M. Songvilay,²
R. D. Johnson,⁶ R. Downie,⁷ J-W. G. Bos,⁷ J. A. Rodriguez-Rivera,^{8,9}
S.-W. Cheong,¹⁰ R. A. Ewings,⁴ N. Qureshi,¹ and C. Stock²

Magnetic materials that lack an inversion center can potentially host coupled magnetic and ferroelectric order parameters while also providing a framework for unusual magnetic excitations like directionally anisotropic (or nonreciprocal) spin-waves. Such materials often consist of magnetic ions in a low-symmetry environment with a complex set of magnetic interactions that couple the structural and magnetic order [1]. We have investigated the magnetic excitations in an array of single crystals of the helicoidal magnet MnSb_2O_6 [2]. Given the complexity of the excitation spectrum, the number of predicted exchange constants, and the ambiguities of the magnetic structure, we take advantage of multiplexed neutron instrumentation to apply the first-moment sum rule of neutron scattering to extract the symmetric exchange constants and compare the results to the excitation spectrum from mean-field linear spin-wave theory.

MnSb_2O_6 crystallizes in the non-centrosymmetric $P321$ (#150) space group and has a chiral crystal structure. The Mn^{2+} ions ($S = 5/2$, $L \approx 0$) are magnetic and order below a Néel temperature $T_N \approx 12$ K with a propagation vector $k = (0, 0, 0.182)$. The magnetic ground state is in dispute and thought to be either a pure cycloidal structure, as shown in Fig. 1(a), or a helicoidal structure where the spin-rotation plane is tilted away from the c -axis, as shown in Fig. 1(b) [3]. In both cases, within each triangle of Mn^{2+} ions in the (ab) -plane, shown as dashed gray lines in Fig. 1(a), the moments are dephased by 120° . Also, the sense of rotation of the spins along the c -axis and within a basal triangle can be described by magnetic parameters η_C and η_T , often called magnetic “chiralities,” which directly couple to the crystal chirality σ through an energy invariant [3]. As Mn^{2+} is not expected to have an orbital degeneracy that would enhance any anisotropy in the magnetic Hamiltonian, like antisymmetric terms, the magnetic interactions should be described by a dominant Heisenberg Hamiltonian $\hat{H} = \sum_{ij} J_{ij} \hat{S}_i \cdot \hat{S}_j$ with the

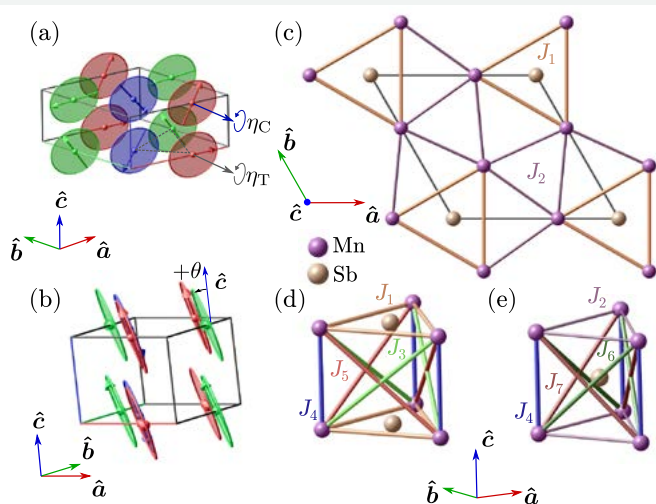


FIGURE 1: (a) Cycloidal magnetic structure with magnetic parameters η_C and η_T describing the sense of rotations of the spins. (b) Tilted magnetic structure where the spin-rotation plane is tilted from the c -axis by an angle θ . (c) Intraplane interactions J_i connecting triangles of Mn ions centered at the lattice origin, and J_2 connecting these triangles. (d) Interplane interactions based on the J_1 triangle: J_4 is the straight interplane interaction, while J_3 and J_5 are diagonal chiral interactions. (e) Interplane interactions based on the J_2 triangle: J_6 and J_7 are diagonal chiral exchange interactions. Oxygen atoms are omitted here for clarity.

symmetric exchange constants J_{ij} corresponding to the seven super-super-exchange (SSE) pathways in MnSb_2O_6 . The nearest-neighbor exchange paths are shown in Fig. 1(c)-(e). Interestingly, the diagonal exchange constants J_3 and J_6 are related to the right-handed helical winding of the Mn-O-O-Mn SSE pathways while J_5 and J_7 are related to left-handed SSE pathways. Thus, these chiral exchange paths are interchanged by inversion symmetry between structurally left- and right-handed crystals [3].

To investigate the magnetic dynamics, neutron spectroscopy was performed on the MACS triple-axis spectrometer on an array of co-aligned single crystals of MnSb_2O_6 [2]. The final neutron energy E_f was fixed to either 2.4 meV or 3.7 meV, providing two datasets. The Hohenberg-Brinkman first-moment sum rule is given by integrating the dynamic spin correlation function over energy [4]:

$$\langle E \rangle(Q) = \int dE E S(Q, E) = -\frac{2}{3} \sum_{ij} n_{ij} J_{ij} \langle \hat{S}_i \cdot \hat{S}_j \rangle [1 - \cos(Q \cdot d_{ij})]$$

Knowing the crystal and magnetic structure of the compound gives the bond vectors d_{ij} and the ground-state equal-time correlation

¹ Institut Laue-Langevin, 71 avenue des Martyrs, CS 20156, 38042 Grenoble Cedex 9, France

² School of Physics and Astronomy, University of Edinburgh, Edinburgh EH9 3JZ, United Kingdom

³ School of Chemistry and Centre for Science at Extreme Conditions, University of Edinburgh, Edinburgh EH9 3FJ, United Kingdom

⁴ ISIS Pulsed Neutron and Muon Source, STFC Rutherford Appleton Laboratory, Harwell Campus, Didcot, Oxon OX11 0QX, United Kingdom

⁵ Georgia Institute of Technology, Atlanta, GA 30332

⁶ Department of Physics and Astronomy, University College London, Gower Street, London WC1E 6BT, United Kingdom

⁷ Institute of Chemical Sciences and Centre for Advanced Energy Storage and Recovery, School of Engineering and Physical Sciences, Heriot-Watt University, Edinburgh EH14 4AS, United Kingdom

⁸ NIST Center for Neutron Research, National Institute of Standards and Technology, Gaithersburg, MD 20899

⁹ University of Maryland, College Park, MD 20742

¹⁰ Rutgers University, Piscataway, NJ 08854

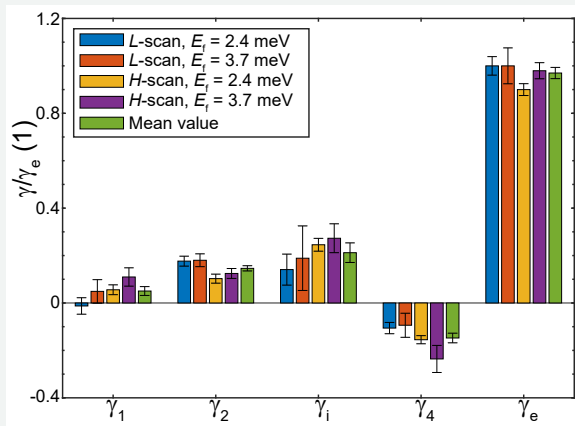


FIGURE 2: Fitted γ parameters for the different analyses and datasets. Mean values (green bars) are calculated by averaging over the four analyses.

function $\langle \hat{S}_i \cdot \hat{S}_j \rangle$ between magnetic sites i and j [3], and this allows one to fit the exchange constants J_{ij} with multiplicity n_{ij} by measuring the first moment in different regions of Q -space. For the pure cycloid or tilted model, respectively shown in Figs. 1(a) and 1(b), the spins corotate in the same plane. Therefore, the scalar product is simply the cosine of the difference in angle between the spins in the same rotation plane, which means this sum-rule analysis is independent of either model. For a fixed scattering vector $Q = (H, H, L)$, the sinusoidal frequency will only depend on the bond distances. We can therefore define the sinusoidal amplitudes γ associated to each of the five distinct bond lengths, which are functions of the exchange constants and the ground-state correlation functions. The data analysis was performed by simplifying the first-moment equation for Q along $[H, 0, 0]$ or $[0, 0, L]$, and these two analyses were performed with both $E_f = 2.4$ meV and $E_f = 3.7$ meV datasets, leading to the four sets of refined parameters γ shown in Fig. 2.

Considering the energy minimization using the experimental propagation vector from diffraction [3], we add a constraint in our system of seven unknown exchange constants, which can be written into six linearly independent equations. As a seventh constraint, we can fix the J_3 exchange parameter, as it mainly affects the upper magnon branch along $(H, H, 0)$. The exchange constants obtained are in good qualitative agreement with experimental observations except at the zone-boundary. On inspection of Fig. 2, the values of γ_4 , which fixes J_4 , may be dominated by the H -scan data measured with $E_f = 3.7$ meV. We therefore considered a case where this value is lowered while also adjusting J_7 , given the relatively large error bar in our analysis, to preserve the same magnetic-ordering wave vector. After refining $J_{4,7}$ to within one or two sigma of the calculated error bar from the first-moment sum rule analysis, we obtained a good description of the data, as shown in Fig. 3(a)-(b) along $[-1, -1, L]$ and Fig. 3(c)-(d) along $[H, H, 0]$. The left-handed

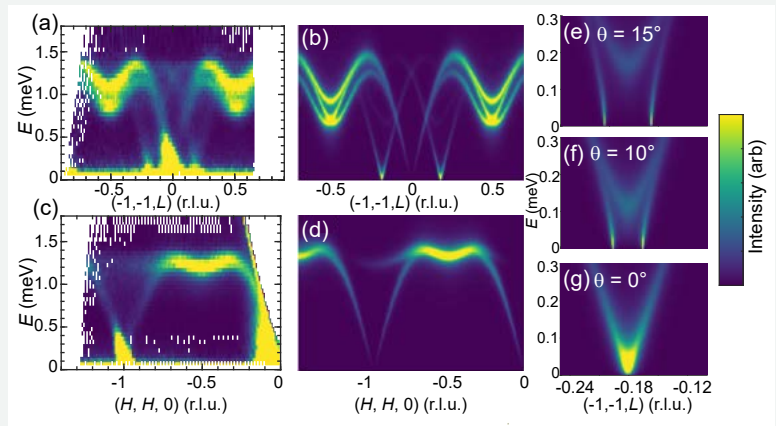


FIGURE 3: (a)-(d) Measured and calculated spin-wave spectra at $T = 1.4$ K. Dispersion along (a)-(b) $(-1, -1, L)$ and (c)-(d) $(H, H, 0)$. The spectra in (b) and (d) are based on theoretical calculations using Green's functions: J_4 was refined to give agreement with the data at the zone boundary, and J_7 was adjusted to preserve the measured ordering wave vector. (e)-(g) Stability of spin-waves as a function of the spin-rotation plane tilt from the c -axis. Long-wavelength excitations were only stable for tilts of $\theta \sim 0^\circ$.

interactions J_3 and J_6 are dominant compared to the right-handed interactions J_5 and J_7 , as expected to impose the structural chirality of MnSb_2O_6 . The spin-wave spectra were calculated using a Green's function approach on a rotating frame [5]. We have also used this approach to compute the magnon dispersion as a function the tilt of the spin rotation plane from the c -axis as shown in Fig.3(e)-(g). Any tilt $\theta \neq 0^\circ$ leads to unstable long-wavelength excitations based on the exchange constants derived from sum rules, thereby favoring the pure cycloidal ground state in the symmetric-only exchange Hamiltonian model.

Using the first-moment sum rule, we have extracted the symmetric exchange constants of the structurally chiral polar magnet MnSb_2O_6 from multiplexed neutron inelastic scattering data. This method only depends on the correlators (angles) between neighboring spins and not on the tilting of the overall spin-rotation plane. Using Green's functions on a rotating frame, we have calculated the spin-wave spectra, which are in good agreement with the data and discussed refined values. We investigated the stability of the magnetic structure in terms of the long-wavelength magnetic excitations present at low energies and find that the pure cycloid model is favored given the exchange constants derived from the first-moment sum rule.

REFERENCES

- [1] S.-W. Cheong, M. Mostovoy, *Nature Mater* **6**, 13 (2007).
- [2] E. Chan, H. Lane, J. Pásztorová, M. Songvilay, R. D. Johnson, R. Downie, J.-W. G. Bos, J. A. Rodriguez-Rivera, S.-W. Cheong, R. A. Ewings, N. Qureshi, C. Stock, *Phys. Rev. B* **107**, 144420 (2023).
- [3] E. Chan, J. Pásztorová, R. D. Johnson, M. Songvilay, R. A. Downie, J.-W. G. Bos, O. Fabelo, C. Ritter, K. Beauvois, Ch. Niedermayer, S.-W. Cheong, N. Qureshi, C. Stock, *Phys. Rev. B* **106**, 064403 (2022).
- [4] P. C. Hohenberg, W. F. Brinkman, *Phys. Rev. B* **10**, 128 (1974).
- [5] H. Lane, M. Songvilay, R. A. Ewings, C. Stock, *Phys. Rev. B* **106**, 054431 (2022).

Formation of a simple cubic antiferromagnet through charge ordering in a double Dirac material

T. Berry,^{1,2} V. C. Morano,² T. Halloran,² X. Zhang,³ T. J. Slade,^{4,5} A. Sapkota,^{4,5} S. L. Bud'ko,^{4,5} W. Xie,⁶ D. H. Ryan,⁷ Z. Xu,⁸ Y. Zhao,^{8,9} J. W. Lynn,⁸ T. Fennell,¹⁰ P. C. Canfield,^{4,5} C. L. Broholm,^{2,11} and T. M. McQueen^{1,2,11}

Topological materials are promising for both technological applications and basic research. Exotic but robust electronic states can be topologically protected (e.g., conducting surface states, the anomalous Nernst effect) and can realize electronic quasiparticles that are direct analogues of particles from the Standard Model. Dirac and Weyl quasiparticles have been observed in Dirac and Weyl semimetals while axion insulators are predicted to support quasiparticles with electrodynamics analogous to the axion, a dark matter candidate [1]. Materials can also host quasiparticles with no counterpart in the Standard Model, as is the case for double Dirac materials. A double Dirac quasiparticle manifests as an eightfold degeneracy in the band structure protected by a nonsymmorphic symmetry, a degeneracy higher than that possible without topological protection [2].

How such topological states interact with magnetic states is largely unexplored. We report on the behavior of EuPd_3S_4 , a magnetic version of the double Dirac material LaPd_3S_4 [3]. EuPd_3S_4 was previously reported to magnetically order in an unknown configuration at $T_N = 2.9$ K. Perplexingly, despite having a cubic crystal structure with one crystallographic Eu site, Mössbauer results are consistent with a $\text{Eu}^{2+}/\text{Eu}^{3+}$ mixed valency in which each valence occurs in an approximately 1:1 ratio. EuPd_3S_4 prompts many unanswered questions: How would eight-fold degeneracies in the band structure be affected by the magnetic order? Could the $\text{Eu}^{2+}/\text{Eu}^{3+}$ ions order below some critical temperature? Given the $J = 7/2$ Eu^{2+} and the $J = 0$ Eu^{3+} , how does the mixed valency affect the magnetic properties? How does charge order itself influence double Dirac electronic states?

Neutron diffraction on the BT7 triple axis spectrometer at NCNR was used to study the magnetic order of antiferromagnetic (AFM) EuPd_3S_4 single crystals with Neel temperature $T_N = 2.85(6)$ K. Despite the challenges posed by the strong absorption of neutrons by Eu, a new set of magnetic Bragg peaks were discovered below T_N (Fig. 1b) revealing $k = (\pi, \pi, \pi)$ AFM order, in which the magnetic unit cell has

lattice parameters $[2a, 2a, 2a]$. With application of a magnetic field, the intensity of the magnetic peaks sharply decreases at a $\mu_0 H = 0.3$ T metamagnetic transition. The peaks continue to lose intensity before disappearing entirely at $\mu_0 H = 2.7$ T, where the material enters a field-polarized paramagnetic state. Curiously, the forbidden (100) reflection appears upon application of field and gains intensity with increasing field up to 3 T (Fig. 1a). The appearance of this reflection at large fields, where the compound is fully magnetized, implies that the corner and center Eu sites, contrary to previous reports, are inequivalent. Specifically, it indicates a field-polarized magnetic structure with simple cubic rather than body centered cubic symmetry and a charge ordered state where Eu^{2+} and Eu^{3+} form interpenetrating simple cubic lattices (Fig. 1e). While $\text{Eu}^{2+}/\text{Eu}^{3+}$ are indistinguishable to neutrons in zero field, only $J = 7/2$ Eu^{2+} is magnetized by the applied field (Fig. 1c,d), which provides contrast between the corner and center sites and breaks the symmetry that otherwise forbids (100). Comprehensive heat capacity measurements are consistent with the field and temperature dependence of the magnetic neutron diffraction, including the Neel transition and the spin flop transition. Together the neutron and heat capacity data were used to construct the temperature-field magnetic phase diagram (Fig. 1f).

The charge ordering hypothesis implies different Coulombic environments about the corner and center Eu sites. This in turn implies breathing of the S atoms, a crystallographic effect lowering the reported space group symmetry. X-ray diffraction work confirms a $\text{Eu}^{2+}/\text{Eu}^{3+}$ charge ordering transition occurs at $T_{\text{CO}} = 340$ K. The refined space group of the high-temperature, high symmetry phase $Pm\bar{3}n$ is lowered to $Pm\bar{3}$ as the charge ordering breaks the n-glide (Fig. 2). With the loss of their nonsymmorphic protecting symmetries, double Dirac states become gapped for $T < T_{\text{CO}}$. Indeed, density functional theory shows the loss of the double Dirac state below 340 K, as it splits into two Dirac states. Depending on the orientation of the magnetic moments, these Dirac cones may persist or become Weyl nodes below $T_N = 2.85(6)$ K.

¹ Department of Chemistry, The Johns Hopkins University, Baltimore, MD 21218

² Institute for Quantum Matter and William H. Miller III Department of Physics and Astronomy, The Johns Hopkins University, Baltimore, MD 21218

³ Department of Chemical and Biomolecular Engineering, The Johns Hopkins University, Baltimore, MD 21218

⁴ Ames Laboratory, U.S. Department of Energy, Iowa State University, Ames, IA 50011

⁵ Department of Physics and Astronomy, Iowa State University, Ames, IA 50011

⁶ Department of Chemistry and Chemical Biology, Rutgers University, Piscataway, NJ 08854

⁷ Physics Department and Centre for the Physics of Materials, McGill University, 3600 University Street, Montreal, Quebec, H3A 2T8, Canada

⁸ NIST Center for Neutron Research, National Institute of Standards and Technology, Gaithersburg, MD 20899

⁹ Department of Materials Science and Engineering, University of Maryland, College Park, MD 20742

¹⁰ Laboratory for Neutron Scattering and Imaging, Paul Scherrer Institut, 5232 Villigen PSI, Switzerland

¹¹ Department of Materials Science and Engineering, The Johns Hopkins University, Baltimore, MD 21218

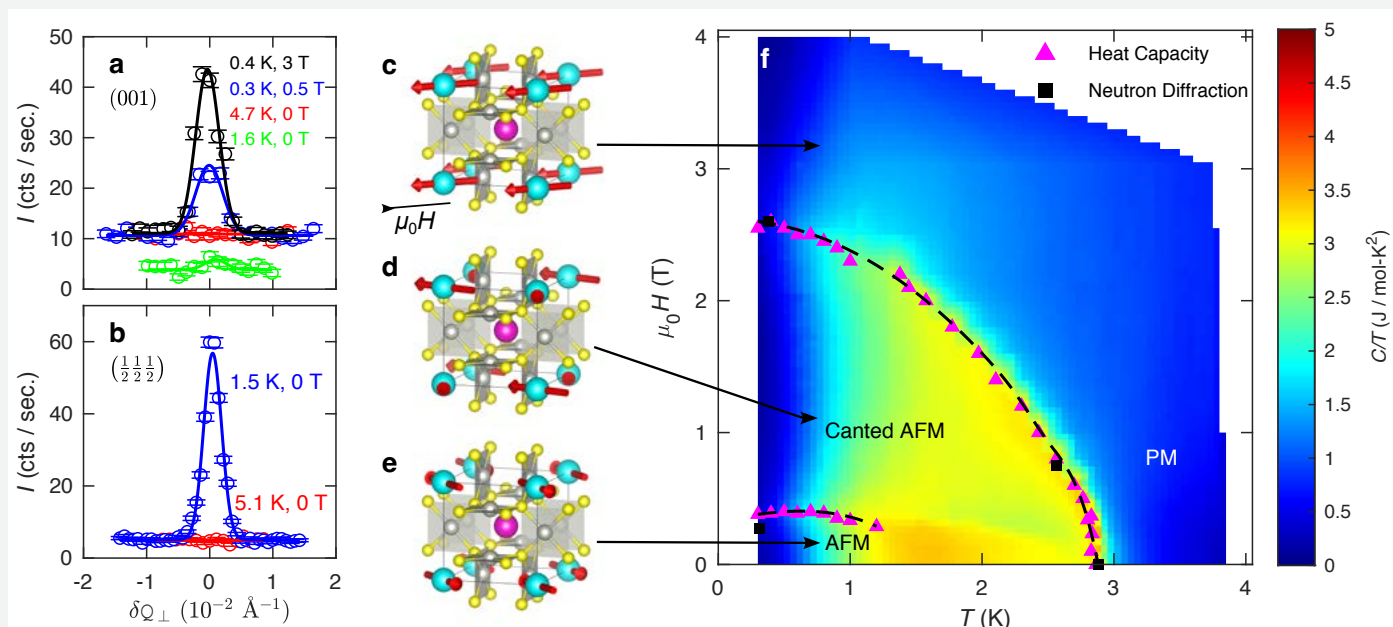


FIGURE 1: Field-dependent magnetic phase diagram. (a) Rocking scans with δQ_{\perp} perpendicular to the (001) direction of wavevector transfer, lying in the (HHL) plane. The (001) reflection has zero nuclear Bragg intensity at $T = 4.7$ K because the nuclei of Eu^{2+} and Eu^{3+} are equivalent. (001) remains absent below T_N in zero magnetic field. As the applied field along (1-10) increases and the Eu^{2+} sublattice becomes magnetized, however, the (001) peak appears. (b) Rocking scans with δQ_{\perp} perpendicular to $(\frac{1}{2}, \frac{1}{2}, \frac{1}{2})$ and within the (HHL) reciprocal lattice plane, showing the development of AFM order below T_N . Gaussian fits are shown in frames (a-b), and error bars represent one standard deviation. (c) The field polarized magnetic state in which all magnetic Eu^{2+} atoms are aligned along the applied (1-10) field direction. (d) The intermediate canted AFM state in which the Eu^{2+} spins cant along the applied field. (e) The multidomain $(\frac{1}{2}, \frac{1}{2}, \frac{1}{2})$ AFM state in the absence of an applied field. Due to domain averaging, the moment directions in the zero-field state cannot be determined by neutron diffraction. Because a small (1-10) field forces the staggered magnetization along (110), we show the moments oriented along (110). (f) Resultant magnetic phase diagram for EuPd_3S_4 . The points indicating phase transitions were determined by inspection of anomalies in the field and temperature dependence of the underlying specific heat and neutron scattering data.

	$T \leq 2.85(6)$ K	$2.85(6)$ K $\leq T \leq 340$ K	$T \geq 340$ K
Inversion symmetry	✓	✓	✓
Time reversal symmetry	✗	✓	✓
Nonsymmorphic symmetry	✗	✗	✓
Space group	$\text{Pm}\bar{3}$	$\text{Pm}\bar{3}$	$\text{Pm}\bar{3}n$
Charge order	✓ (Eu^{2+} and Eu^{3+} , 1:1)	✓ (Eu^{2+} and Eu^{3+} , 1:1)	✗
Magnetism	$(\pi\pi\pi)$ Antiferromagnetic	Paramagnetic	Paramagnetic
Band crossing	R point (2-/4-fold)	R point (4-fold)	R point (8-fold)
Structure Eu^{2+} , Eu^{3+} , Pd and S			

FIGURE 2: Overview of phase transitions in EuPd_3S_4 . Above $T = 340$ K, the $\text{Eu}^{2+}/\text{Eu}^{3+}$ valence fluctuates, and EuPd_3S_4 adopts a $\text{Pm}\bar{3}n$ structure with inversion, time reversal, and a nonsymmorphic n-glide that produce double Dirac fermions at the R point. The emergence of charge order below $T = 340$ K removes the n-glide and results in gapping out of the double Dirac point to yield a pair of 4-fold degenerate states. This charge order produces a simple cubic magnetic lattice upon which G-type AFM order forms below $T = 2.85(6)$ K. Depending on the spin direction in the ground state, the 4-fold degeneracies are preserved or split into pairs of 2-fold degenerate states.

This work reports perhaps the first example of a rare earth based simple cubic Heisenberg antiferromagnet and allows exploring its properties as a function of temperature and field. Furthermore, it demonstrates how both charge and spin order can alter topologically nontrivial electronic states in double Dirac materials. From the perspective of neutron science, it shows how a diffraction investigation of magnetic order on a triple axis spectrometer can reveal charge order even in the presence of large absorption.

REFERENCES

- [1] N. Armitage, E. Mele, A. Vishwanath, *Reviews of Modern Physics* **90**, 015001 (2018).
- [2] B. Bradlyn *et al.*, *Science* **353**, 558 (2016).
- [3] T. Berry *et al.*, <https://doi.org/10.48550/arXiv.2303.02218> (2023).

Boron's dramatic enhancement of the voltage-controlled antiferromagnetic switching in B:Cr₂O₃ spintronics devices

A. Mahmood,¹ J. Weaver,² S. Q. A. Shah,¹ W. Echtenkamp,^{1,3} J. W. Lynn,⁴ P. A. Dowben,¹ and C. Binek¹

Spintronics, where the magnetic spin rather than charge degree of freedom is employed, is an emerging field that enables the next-generation electronic devices [1]. Antiferromagnetic spintronics can provide voltage controlled Néel vector rotation of the nanomagnetism, enabling ultralow power, ultrafast, and nonvolatile memory and logic devices. Cr₂O₃ is a magnetoelectric antiferromagnet that may be employed in spintronic devices if the material's properties can be tuned to facilitate operation in ambient conditions and in CMOS environments. In particular, the magnetic ordering Néel temperature, T_N , must be adjustable to values significantly above room temperature. This has recently been achieved with the incorporation of boron into Cr₂O₃ thin films, B:Cr₂O₃, which increases the ordering temperature and enables direct voltage control of the vector rotation of the magnetism [2].

Questions that need to be addressed so that we might understand how boron aids in this tuning are: (1) how much boron is needed, and (2) where the boron is in the thin film device structure. Answering these questions provide the required information to optimize device performance and their future manufacturing processes. Cold Neutron Depth Profiling (cNDP) is a technique ideally suited to determine the amount and distribution of the boron in the chromia thin film. cNDP is a non-destructive analytical neutron capture technique that is highly sensitive to ¹⁰B [3]. cNDP measurements were carried out on films boron-free films, films initially prepared with boron incorporated, and then on the same films after annealing. Fig. 1 shows the boron depth profiles on an initially prepared film and on two different films after annealing at 500 K. The interesting answer is that the boron diffuses to form a surface layer, roughly 50 nm thick. Subsequent X-ray photoemission spectroscopy depth profile measurements on separate annealed samples (since it is a destructive technique) confirmed that the B diffuses to the surface to form a surface distribution [4].

The boron in the surface region enhances the Néel temperature in this region. This ordering temperature can be determined by magnetotransport measurements together with a scaling analysis and utilizing the solution to the mean-field equation which approximates the T dependence of spontaneous (sublattice) magnetization below a critical temperature. The advantage of using the mean-field approximation is that it is independent of

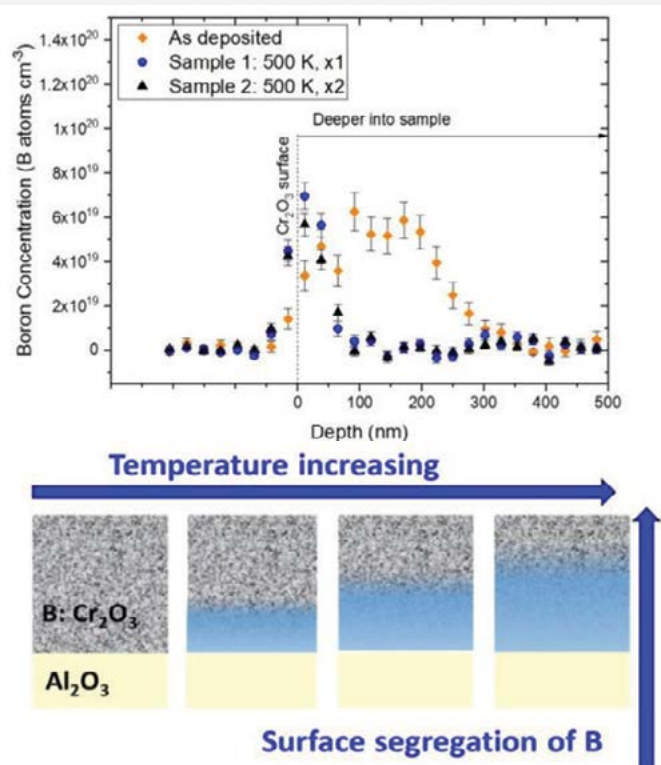


FIGURE 1: (top) cNDP profiles of unannealed and two different samples annealed at 500 K. (bottom) Suggested mechanism of B segregation in the chromia due to annealing over time at elevated temperatures.

dimensionality and symmetry of a spin-Hamiltonian; it does not distinguish between universality classes, but has the advantage of being a meaningful approximation outside the critical region very close to T_N . The results of the analysis are shown in Fig. 2. The solid curve shows the numerical mean field solution, where the position of each data set on the universal curve uniquely determines the critical temperature T_N associated with the data set.

A second, important aspect of the introduction of boron in the surface region is that it enables an applied voltage to control the vector magnetization. The switching voltage required depends on the temperature-dependent magnetic anisotropy and the boron thickness and concentration. Fig. 3 shows deterministic switching at $T = 370$ K, as it follows the voltage pulse application. Sharper data but requiring

¹ Department of Physics & Astronomy and the Nebraska Center for Materials and Nanoscience, University of Nebraska-Lincoln, Lincoln, NE 68588

² Material Measurement Laboratory, National Institute of Standards and Technology, Gaithersburg, MD 20899

³ Department of Electrical & Computer Engineering, University of Minnesota, Minneapolis, MN 55455

⁴ NIST Center for Neutron Research, National Institute of Standards and Technology, Gaithersburg, MD 20899

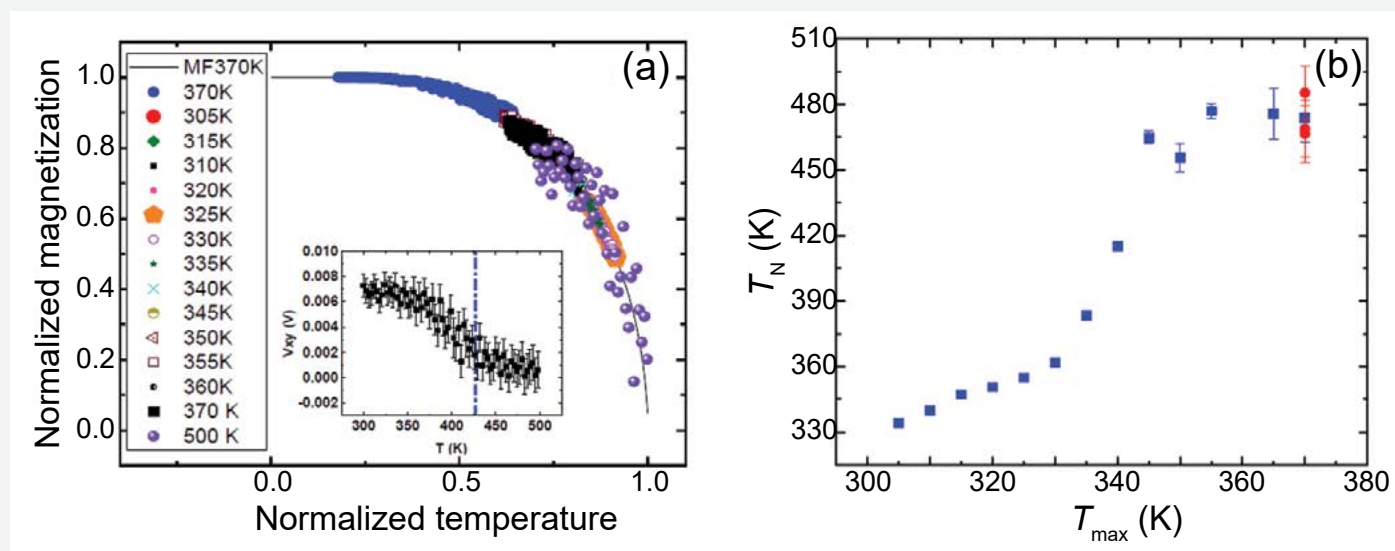


FIGURE 2: (a) Scaling analysis of T-dependent magnetotransport data. The legend displays symbols associated with V_{xy} vs. T and their T_{Nmax} . Solid curve shows the numerical mean-field solution, which serves as master curve for a data collapse of magnetization vs. temperature data. The inset shows a complete V_{xy} vs. T data set which includes data for $T > T_N$, and uncertainty of these data sets are displayed in the inset. Vertical line marks T_N as determined from scaling analysis. (b) Plot of T_N

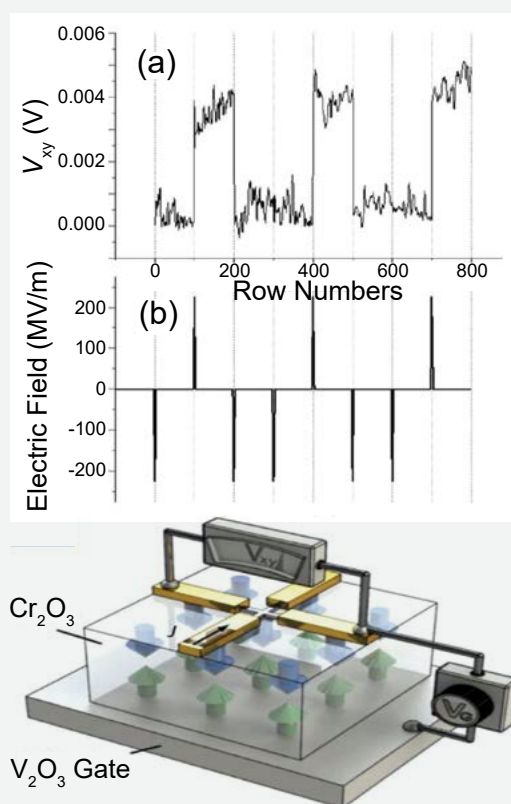


FIGURE 3: (top) Isothermal voltage-controlled switching between high and zero Hall voltage signals at 370 K, corresponding to the application of gate pulse voltage. (bottom). Sketch of the Hall bar device showing V_2O_3 back gate, B-doped Cr_2O_3 film with AFM spin structure, Pt Hall cross with Au electrodes, current density j flowing in direction of black arrow causing signal V_{xy} controlled by gate voltage V_g .

a larger switching voltage were obtained at 295 K and compared. The high voltage state of the transverse Hall signal of $V_{xy} \approx 4$ mV is measured after application of a gate pulse of $V_g = +45$ V (+225 MV/m). The zero state is set after application of $V_g = -45$ V (-225 MV/m). Note that a lower switching voltage of ± 45 V achieves switching at 370 K compared to $V_g \pm 55$ V required for switching at 295 K. A small switching voltage is highly desirable in spintronic applications. Estimates for B: Cr_2O_3 devices suggests voltage-controlled switching gate voltages as low as 4.5 V are feasible, and possibly even lower due to the superior dielectric properties of B-doped chromia, potentially allowing the growth of leakage free samples below 20 nm thickness. The data also allow an estimate of switching speeds on the order of 100 ps.

In summary, we have found that B-doping of the magnetoelectric antiferromagnet Cr_2O_3 increases its magnetic ordering temperature and enables pure voltage control of the Néel vector. In this work we have shown that the B concentration profile in B: Cr_2O_3 films evolves with annealing into a 50 nm surface layer where the Néel temperature is increased from 334 K to a saturation value of $T_{Nsat} \approx 477$ K. Magnetotransport measurements reveal that the boron also enables voltage-controlled rotation of the Néel vector. These beneficial device properties include high operation temperature with potential application for non-volatile memory and logic in CMOS environments as well as reduced switching voltage and are stable over time. This makes B: Cr_2O_3 a promising multifunctional single-phase material for energy efficient, nonvolatile CMOS compatible spintronics applications.

REFERENCES

- [1] A. Hirohata, K. Yamada, Y. Nakatani, I.-L. Prejbeanu, B. Dieny, P. Pirro, B. Hillebrands, *JMMM* **509**, 166711 (2020).
- [2] A. Mahmood, W. Echtenkamp, M. Street, J.-L. Wang, S. Cao, T. Komesu, P. A. Dowben, P. Buragohain, H. Lu, A. Gruverman, A. Parthasarathy, S. Rakheja, C. Binek, *Nature Commun.* **12**, 1674 (2021).
- [3] R. Downing, J. Maki, R. Fleming, *J. of Radioanalytical and Nuclear Chem.* **112**, 33 (1987).
- [4] A. Mahmood, J. Weaver, W. Echtenkamp, S. Q. Abbas Shah, J. W. Lynn, C. Binek, *Advanced Physics Research* DOI: [10.1002/apxr.202300061](https://doi.org/10.1002/apxr.202300061).

Assessment of dose reduction strategies in wavelength-selective neutron tomography

M. C. Daugherty,^{1,2} V. H. Distefano,¹ J. M. LaManna,¹ D. L. Jacobson,¹ P. A. Kienzle,¹ Y. Kim,^{1,3} D. S. Hussey,¹ and P. Bajcsy¹

The unique interactions of neutrons with matter enable a diverse set of image contrasts that range from sub-pixel porosity characterization via dark field imaging to crystal phase mapping with Bragg edge imaging. Defining the wavelength of the neutron beam gives access to these mechanisms which can be used, not only to form two-dimensional images, but also tomograms where the sample is characterized from a set of angular projections to give a full three-dimensional map of the sample. However, neutron sources are both scarce in number and weak in brightness making experiments of this type logistically difficult and prohibitively time consuming. Dose reduction (composing a tomogram of fewer angular projections) is an approach that can alleviate this temporal bottleneck but comes at the expense of image quality. This work looks at computational workflows that are designed to restore image quality of neutron tomograms that have been corrupted by this phenomenon [1].

Aside from the differences in physical interactions, neutron imaging and tomography share many commonalities with X-ray imaging and tomography, which can be a helpful framework for understanding this work and its motivation. Experimentally they are very similar except that for the former, the beam direction is fixed, and the object is rotated through the projection angles. Likewise, the underlying mathematical methods for reconstructing an X-ray tomogram: radon transform, iterative algebraic methods, regularized methods, etc., have high portability to the neutron modality. A key aspect of the temporal bottleneck that needs to be overcome in neutron imaging is the image exposure time. Neutron imaging follows Poisson counting statistics where the signal-to-noise ratio (SNR) grows with the square root of measurement time (doubling SNR requires 4x increase in time). The implication of this behavior combined with the low brightness of neutron sources (by comparison to e.g., synchrotron X-ray sources) necessitates non-trivial image exposure times for high SNR images. Thus, to accelerate experiments we balance SNR in the projection images with artifacts that arise from sparse angular sampling in the tomographic reconstruction.

We collected a high-resolution tomogram (2400 projections) with the polychromatic beam that was used in seeding iterative reconstruction algorithms and training convolutional neural networks (CNNs). The polychromatic reconstruction aids iterative methods by

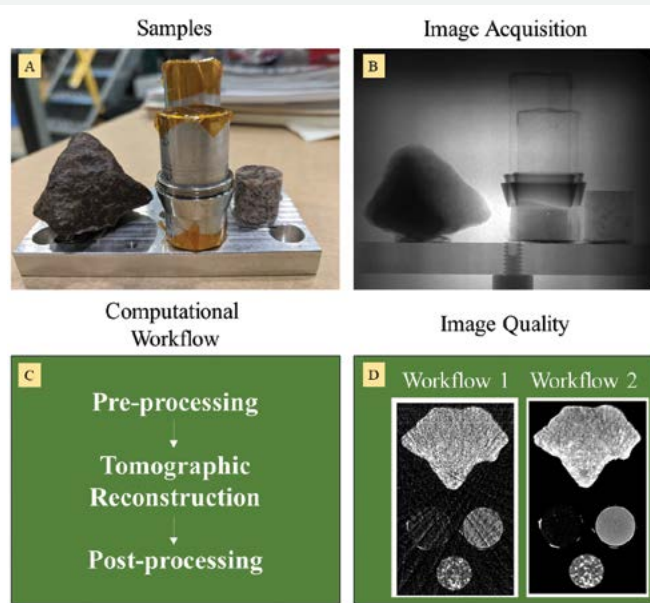


FIGURE 1: An overview of processes for assessing the dose reduction strategies.

supplying *a priori* morphological information and can be synthetically down sampled to simulate sparse monochromatic tomograms for the CNNs. Having this densely sampled tomogram also allows us to quantify the effectiveness of each method with respect to a high-quality reference. We used Bragg-edge imaging to identify the crystal phases in a scene comprised of two standard reference materials (iron powder and potassium feldspar) and two samples with unknown composition (meteorite and granite core) shown in Figure 1. We compared several different reconstruction and de-noising techniques including simultaneous iterative reconstruction technique (SIRT), a regularized iterative reconstruction method that imposes smoothness constraints (total variation minimization with SIRT: TV-SIRT [3]), the stochastic primal dual hybrid gradient method (SPDHG) [4] and three machine learning algorithms: a mixed scale dense convolutional neural network (MS-D Net) [5], the filtered back projection convolutional neural network (FBPConvNet) [6] and the hybrid-domain network (HDNet) [7].

The methods were first applied to the artificially down-sampled (60, 80, 360, 600 and 800 projections) polychromatic datasets to characterize the impact of angular sampling on different image

¹ National Institute of Standards and Technology, Gaithersburg, MD 20899

² Department of Chemical and Biomolecular Engineering, University of Maryland, MD 20742

³ Department of Chemistry and Biochemistry, University of Maryland, MD 20742

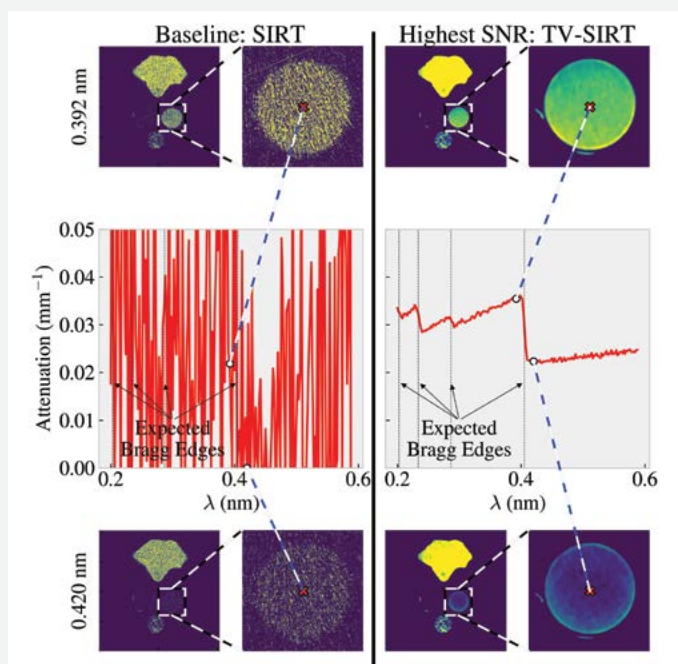


FIGURE 2: Single-voxel resolution of baseline (SIRT; left) and maximum SNR method (TV-SIRT; right).

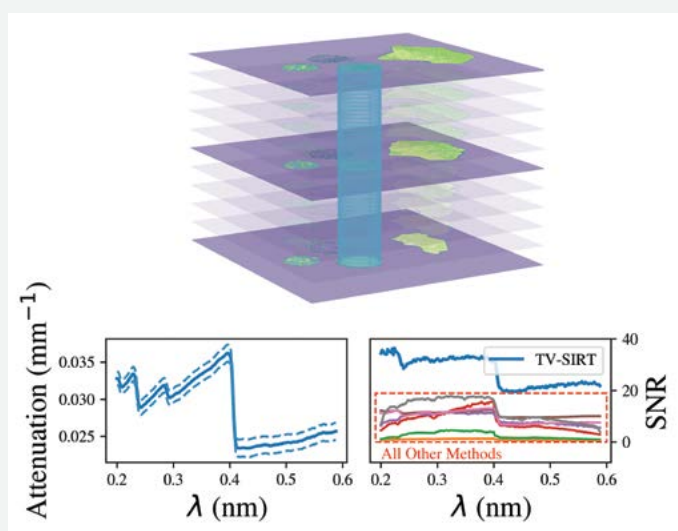


FIGURE 3: Bulk signal-to-noise ratio in standard reference material (iron powder).

quality metrics (e.g., root-mean-squared error) where the ground truth was known (fully sampled polychromatic data). Subsequently, the methods were applied to a dose-reduced monochromatic dataset, where the samples of known composition were used to characterize the voxel resolution and bulk SNR.

Figures 2 and 3 highlight that the TV-SIRT method produced superior single voxel resolution (Figure 2) and the highest SNR of all methods (Figure 3). The left side of Figure 2 shows the baseline (SIRT) where the top and bottom rows show a reconstruction at 0.392 nm and 0.420 nm respectively. The spectrum of the highlighted voxel in the inset (center row) is very noisy across wavelengths for the baseline

with no discernible definition of the expected edges. The right side of this figure shows the reconstruction for TV-SIRT where the image has much smoother contrast as the spectrum.

The highlighted voxel readily resolves the GSAS [2] predicted edge positions for the iron powder (vertical black dashed lines). Likewise, the volumetric rendering in Figure 3 illustrates the cylindrical slice of voxels comprising the iron powder reference material where we sampled over 4 million voxels to quantify bulk statistics in the SRM. The mean attenuation in this slice of voxels is shown in the lower left plot with the \pm standard deviation shown in the dashed lines. The lower right plot shows the SNR (mean / standard deviation) for all the methods for this region, where TV-SIRT exhibited the highest values of all the methods across all the measured wavelengths.

This work examined seven separate methods of improving energy-resolved 3D tomographic reconstructions at neutron imaging beam lines which included common reconstruction algorithms, CNNs, and regularized methods. The novelty of this work is in establishing model-based and ranking relationships between 3D reconstruction accuracy and acquisition time represented by intensity variance, SNR, RMSE, blur, number of 2D projections, number of iterations and seeding of 3D tomographic reconstruction (SIRT), and supervised and de-noising models (HDNet, MS-D Net and FBPCConvNet). An important consideration of our work was the differing SNR over the monochromatic scans. This source of noise differs from the structured noise from sparse angular sampling and proved to be very challenging for the convolutional neural networks to remove. The explicit morphological *a priori* information that is supplied by seeding the iterative methods proved to generate superior images by comparison to the implied noise reduction filters learned by the CNNs.

REFERENCES

- [1] M. C. Daugherty, V. H. Distefano, J. M. LaManna, D. L. Jacobson, P. A. Kienzle, Y. Kim, D. S. Hussey, P. Bajcsy, *Nature Computer Science*, (manuscript accepted).
- [2] A. C. Larson, R. B. V. Dreele, Los Alamos National Laboratory Report LAUR 86-748 (2004).
- [3] E. Y. Sidky, X. Pan, *Physics in Medicine and Biology* **53**, 4777 (2008).
- [4] A. Chambolle, M. J. Ehrhardt, P. Richtarik, C. B. Schonlieb, *SIAM Journal on Optimization* **28**, 2783 (2018).
- [5] D. Pelt, K. Batenburg, J. Sethian, *Journal of Imaging* **4**, 128 (2018).
- [6] K. H. Jin, M. T. McCann, E. Froustey, M. Unser, *IEEE Transactions on Image Processing* **26**, 4509 (2017).
- [7] D. Hu, J. Liu, T. Lv, Q. Zhao, Y. Zhang, G. Quan, J. Feng, Y. Chen, L. Luo, *IEEE Transactions on Radiation and Plasma Medical Sciences* **5**, 88 (2021).

Gas diffusion through variably-water-saturated zeolitic tuff: implications for transport following a subsurface nuclear event

C. W. Neil,¹ H. Boukhalfa,¹ H. Xu,¹ S. D. Ware,¹ J. Ortiz,^{1,2} S. Avendaño,¹ D. Harp,¹ S. Broome,³ R. P. Hjelm,⁴ Y. Mao,^{5,6} R. Roback,¹ W. P. Brug,¹ and P. H. Stauffer¹

Noble gas transport through geologic media has important applications in the characterization of underground nuclear explosions (UNEs). Noble gases produced by UNEs are hard to contain and tend to migrate to the surface where they can be detected via atmospheric monitoring, making them key components for compliance monitoring for the comprehensive nuclear-test-ban treaty (CTBT) [1]. Following a UNE, gaseous radioisotopes, including xenon (Xe) and krypton (Kr), are initially produced in known ratios according to the independent yields of nuclear fission. However, with time and transport distances, their isotopic ratios can become altered by both decay and ingrowth from pre-cursor radionuclides. Therefore, without accurate transport models, it is nearly impossible to distinguish between xenon signatures originating from UNEs and those produced by civilian nuclear facilities [2]. Currently, we lack understanding of key processes that control subsurface noble gas transport, including the sorption of noble gases to geological materials and impacts of variable water saturation.

Previous laboratory studies have shown non-trivial Xe sorption on various geologic media including shale, dolomite, limestone, and sand [3]. One geologic media of particular interest is zeolites. A recent study found that natural zeolites in zeolitic tuff can sorb noble gases, and this sorption is particularly significant for Xe [4]. Many historical US tests were conducted in zeolite-rich subsurface strata, common within Pahute Mesa at the Nevada National Security Site (NNSS) [5], meaning this interaction can be important for understanding and modeling historic gas transport data. However, no previous study related gas transport through zeolitic tuff to the level of rock saturation. In this study, we utilized bench-scale laboratory experiments to characterize the diffusion of krypton, xenon, and sulfur hexafluoride (SF_6) through intact zeolitic tuff at 0%, 17%, 40% 85% and 100% saturation conditions [6]. In addition to diffusion tests, small angle neutron scattering (SANS) was conducted to assess the size distribution of the pores being filled by water as saturation was increased.

The rock core sample was taken from the NNSS and analyzed using quantitative X-ray diffraction (QXRD). Results indicated that the zeolites present in the rock were primarily mordenite and heulandite, which combined made up nearly 70% of the rock. Other minerals detected include cristobalite, quartz, plagioclase, alkali feldspar, and montmorillonite. The core sample was cut into 5 cm sections and trimmed to ensure a uniform flat surface was in contact with either side of the diffusion cell. The non-face radial edges of the core were coated with a UV-curable polymer to prevent gas migration along the radial edge of the cylindrical samples. After fully curing,

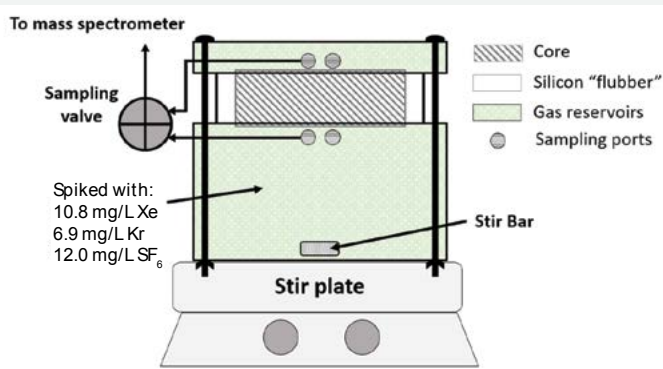


FIGURE 1: Diffusion Cell Schematic

the sides were coated with a silicone primer while the circular top and bottom faces of the core were covered with tape to prevent contact with silicone. The core was placed in a square mold and Room Temperature Vulcanization (RTV) silicone was added to form a molding around the core. The molded silicone acted as a gasket to seal off the two halves of the diffusion cell, which consists of two cylindrical reservoirs machined out of plexiglass (Figure 1).

To begin a diffusion experiment, we spiked the large reservoir, which contained ambient air, with 1 mL each of Xe, Kr and SF_6 tracers while measuring their ion current on a mass spectrometer. This injected volume corresponds to a concentration of 10.8 mg/L for Xe, 6.9 mg/L for Kr, and 12.0 mg/L SF_6 (2000 ppmV each). Once the ion current (*i.e.*, concentration) reached a constant value (within several minutes), we recorded the concentration as the initial concentration, C_0 (*i.e.*, $C_0(t=0)$). Next, we automated the process of moving a selector valve to switch between measuring the spiked and smaller reservoir, such that the small reservoir is measured for 1 minute every 10 minutes to monitor breakthrough and the spiked reservoir is measured for 2 minutes every hour to monitor changes in the C_0 concentration (*i.e.*, $C_0(t)$). This process was repeated for the different rock saturation volumes. Breakthrough curves and concentration drops in the spiked chamber are presented in Figure 2.

¹ Los Alamos National Laboratory, Los Alamos, NM 87545

² The Johns Hopkins University, Baltimore, MD 21218

³ Sandia National Laboratories, Albuquerque, NM 87185

⁴ National Security Education Center, Los Alamos National Laboratory and the New Mexico Consortium, Los Alamos, NM 87545

⁵ University of Maryland, College Park, MD 20742

⁶ NIST Center for Neutron Research, National Institute of Standards and Technology, Gaithersburg, MD 20899

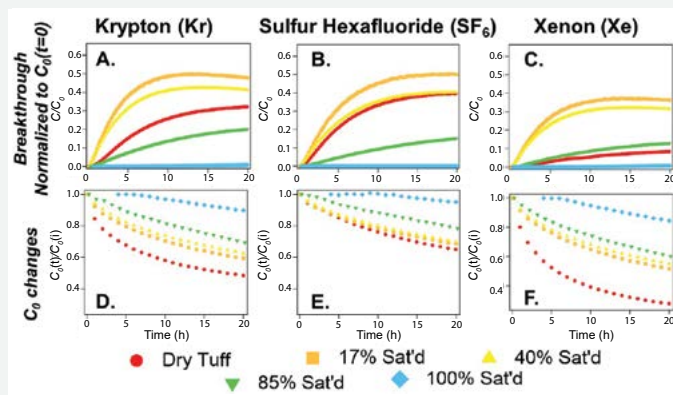


FIGURE 2: Diffusion breakthrough curves for (A) Kr, (B) SF_6 , and (C) Xe, normalized to the initial measured C_0 ($C_0(t=0)$); Changes in the spiked concentration (C_0) with time for (D) Kr, (E) SF_6 , and (F) Xe.

We observed that under dry conditions, SF_6 had the fastest breakthrough, while Kr was slightly slower and Xe is the slowest. Increasing saturation from dry to 17% unexpectedly resulted in faster breakthrough for all three gases. However, when saturation was increased further to 40%, breakthrough for the three gases dropped relative to the 17% saturation system but remained faster than in the dry system. Once saturation was increased again to 85%, breakthrough for Kr and SF_6 was slower than that in the dry system, but for Xe, breakthrough at 85% saturation remained faster than in the dry system. Finally, for the fully saturated system, breakthrough is slowest for all three gases, with slightly faster breakthrough of Xe and Kr relative to SF_6 .

Changes in the spiked concentration in the large diffusion chamber clearly demonstrated interactions between the zeolitic tuff core and gases, which can account for breakthrough differences. For the dry xenon system, the C_0 concentration dropped to nearly 30% of the initial spiked value after 20 hours. This drop is larger than that of Kr (47% remaining) and SF_6 (64% remaining), indicating preferential sorption of Xe. Upon partial saturation to 17%, there was a dramatic decrease in Xe uptake by the core, although there was still a larger C_0 decrease for Xe (52% remaining) relative to Kr (59% remaining) and SF_6 (69% remaining). This trend continued, with increasing saturation leading to a smaller drop in C_0 for all three gases. Thus, trends such as the faster breakthrough for gases in the 17% saturated system are likely related to the stronger concentration gradient in that due to decreased sorption.

Partial saturation up to 17% greatly decreased interactions between zeolitic tuff and gases, as observed in C_0 changes. SANS was utilized to give insight into this observed phenomenon. Fitted pore size distributions (Figure 3A) showed that when water with a scattering length density matching that of the tuff matrix was introduced to a zeolitic tuff powder sample, a significant portion of the smallest pores were filled first, as indicated by the decrease in their abundance relative to larger pores. Figure 3B presents the fraction of pores that are filled. While logically it may seem easier to fill larger sized pores, results show that at both saturations, greater than 10%

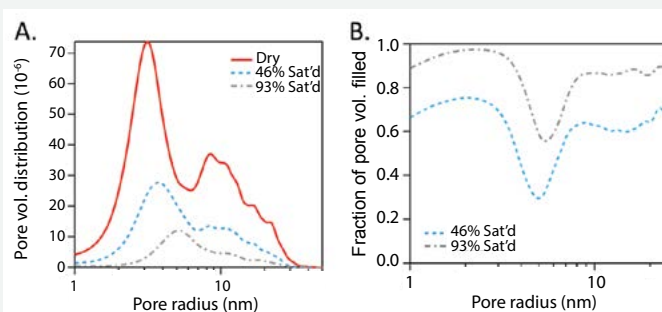


FIGURE 3: (A) Fitted pore size distribution for zeolitic tuff with increasing water content, showing that smaller pores will preferentially fill first. Size distributions were derived from SANS measurements. (B) Fraction of filled pores across the fitted size range.

more of the smaller pores were filled. These pores have a radius of approximately 3 nm, consistent with the previously reported peak pore size of naturally-occurring zeolites, between 2 nm to 4 nm in radius [7]. This finding suggests that small pores, possibly belonging to natural zeolites, preferentially fill upon partial saturation with water, supporting the dramatic change in gas transport behavior upon partial saturation to 17%.

This observation provides critical new insight into how the presence of zeolites and water can impact the transport of nuclear signature gases in the field. Increased retardation of Xe during subsurface transport due to sorption by zeolites at low water saturations will lead to signature fractionation of the gases, altering the elemental ratios expected from a subsurface test. Understanding this process and properly incorporating it into subsurface transport models is crucial to accurately constraining the expected elemental ratios utilized to discern a nuclear test from other radioisotope sources. In addition, these results show the importance of experimentally investigating specific interactions between the rock matrix and gases of interest, such as Xe. By using gases such as SF_6 to determine geologic properties in the field, it can be difficult to capture these gas-specific matrix interactions.

REFERENCES

- [1] C. R. Carrigan, Y. Sun, *Pure Appl. Geophys.* **171**(3-5), 717 (2014).
- [2] J. D. Lowrey, S. R. Biegalski, A. G. Osborne, M. R. Deinert, *Geophys. Res. Lett.* **40**(1), 111 (2013).
- [3] M. J. Paul, S. R. Biegalski, D. A. Haas, H. Jiang, H. Daigle, J. D. Lowrey, J.D., *J. Environ. Radioact.* **187**, 65 (2018).
- [4] J. Feldman, M. Paul, G. Xu, D. X. Rademacher, J. Wilson, T. M. Nenoff, *J. Environ. Radioact.* **220**, 106279 (2020).
- [5] G. K. Moncure, R. C. Surdam, H. L. McKague, *Clays Clay Miner.*, **29**, 385 (1981).
- [6] C. W. Neil, H. Boukhalfa, H. Xu, S. D. Ware, J. Ortiz, S. Avendano, D. Harp, S. Broome, R. P. Hjelm, Y. Mao, R. Roback, W. P. Brug, P. H. Stauffer, *J. of Environ. Radioactivity* **250**, 106905 (2022).
- [7] S. Milićević, V. Milošević, D. Povrenović, J. Stojanović, S. Martinović, B. Babić, *Clays Clay Miner.* **61**(6), 508 (2013).

The Autonomous Formulation Laboratory: self-driving phase mapping using SAXS and SANS

P. A. Beaucage¹ and T. B. Martin²

Fundamental advances in material properties and performance drive societal advances from carbon fiber composites in aircraft to advanced vaccines and other biotherapeutics. Despite this importance, the materials development and innovation lifecycle is extremely slow. For instance, carbon fiber composites and messenger RNA were both originally discovered/developed in the 1950s; carbon fiber was first applied at scale in passenger aircraft in the 2010s and mRNA-based therapeutics were first rolled out in 2020. Autonomous experimentation approaches, which fuse informatics and advanced modeling with human expertise, have shown great promise for accelerating this lifecycle through targeted material development. Extending these advances to formulations and mesoscale structures has proven challenging, however, due to the diffuse and non-unique nature of the characterization tools available and the complexity of such materials, which routinely have tens to hundreds of components. We report the development of the Autonomous Formulation Laboratory (AFL), a fusion of hardware, software, models, and instrumentation that can automatically assess a corpus of data, identify phase boundaries, target measurements to maximize information gain, and finally prepare and measure scattering from an arbitrary liquid mixture to repeat this cycle. The platform has delivered a 25-fold reduction in the amount of time needed to map an example phase diagram and has been tested and used in close collaboration with *n*Soft member companies at sources around the world including the Cornell High Energy Synchrotron Source, the Advanced Photon Source, the Swiss Spallation Neutron Source at the Paul Scherrer Institute, and the ISIS Neutron and Muon Source, and is ready for collaborative development at the NCNR.

The AFL's autonomous measurement loop (Figure 1) is broken into several distinct, replaceable portions: labeling of small-angle scattering data into phases, extrapolation of this discrete phase data into a continuous field with associated uncertainty, selection of the next measurement point using a combination of user direction and that phase uncertainty, and finally robotic preparation and measurement of the next sample. Each component of the AFL loop was developed in-house and has been validated/tuned on scattering data, with extensive ability to refine the performance of the component for the dataset: for instance, the onset of crystalline order or structure factor peaks often needs different classification parameters than a system with form factor differences, which are

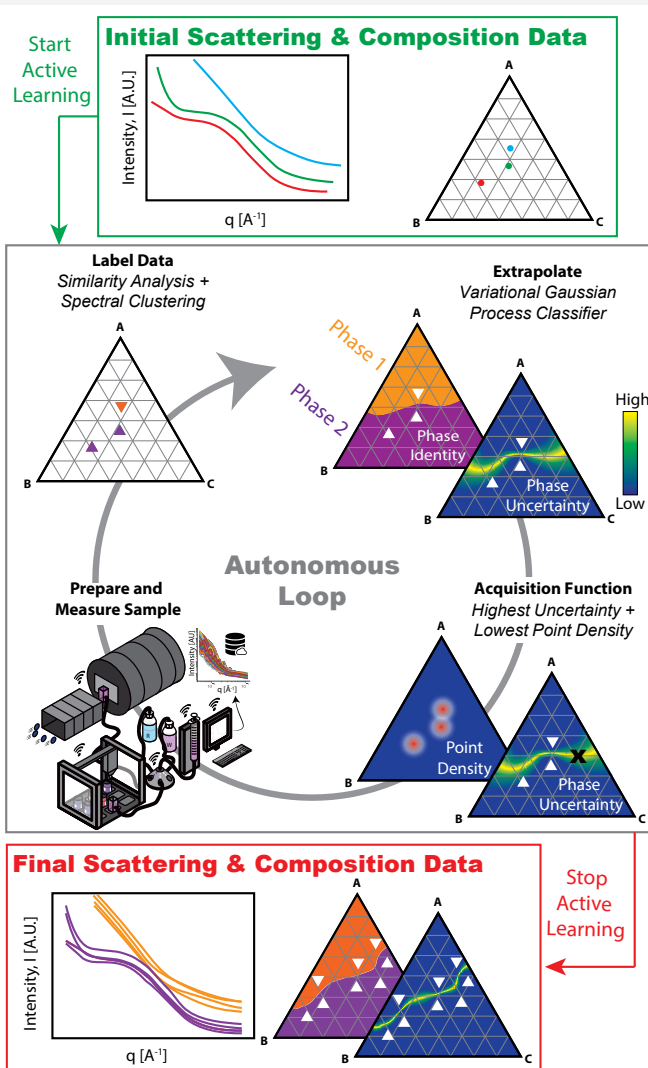


FIGURE 1: Autonomous Experiment Loop. A pool of data is loaded into the system from random points, prior hand measurements, or simulations. From this pool of data, the system automatically measures the differences between the data and clusters them into similar regions or “phases”. This map of phase as a function of composition is then fit with a Gaussian Process regressor to provide a probability of finding each phase across composition space, or more directly, the “most likely” phase at each point. The associated uncertainty of fit is used together with human-input rules (maximum uncertainty for a particular phase, etc.) to choose a next point to measure. The AFL hardware platform then solves a “recipe” for this sample, prepares the sample with a pipettor, transfers it to a neutron or X-ray beam, measures it, and adds the data to the pool of data and begins again. Alternately, on user input or a success metric, the system can stop the loop and return a complete phase map and pool of scattering data for further analysis.

¹ NIST Center for Neutron Research, National Institute of Standards and Technology, Gaithersburg, MD 20899

² Materials Measurement Laboratory, National Institute of Standards and Technology, Gaithersburg, MD, 20899

typically much more subtle. Another frequently-optimized step is the next-measurement selection: we frequently encounter the need to balance high-resolution measurements of the location of phase boundaries with overall exploration and discovery of new phases. We strike this balance by incorporating several processing steps on the uncertainty map before choosing the next point, such as thresholding and choosing randomly from among all points within a certain bound of the maximum uncertainty.

The hardware platform of the AFL, first developed and reported here in 2020 and subsequently published for open replication [1], has also been completely redesigned to reduce the typical sample transfer and cell cleaning overhead from ≈ 10 min to ≈ 90 s. This has been accomplished by changing to a pneumatic transfer system using inert gas instead of a syringe pump and was directly motivated by an *nSoft* company interested in measuring latex-titanium dispersions (paints) in the platform. During this re-engineering, the control and data systems of the robot have been re-engineered to fit within a durable shipping case with approximate dimensions $1 \text{ m} \times 1 \text{ m} \times 1 \text{ m}$; the robot can run without significant unpacking by simply removing the case lid and making connections to 120V or 240V power, network, and nitrogen. This platform (Figure 2) can be shipped to any other facility via air freight and has been used for experiments at the Swiss Spallation Neutron Source (SINQ) at the Paul Scherrer Institute, the Advanced Photon Source at Argonne National Laboratory, and the Cornell High Energy Synchrotron Source. We now have four individual AFL platforms, including one permanently stationed on a NIST SAXS laboratory source, one at the NCNR, one traveling, and one permanently installed in a fume hood for preparation/handling of volatile and other hazardous materials. Other scattering facilities, *nSoft* companies, and at least two academic groups are actively contributing to the open hardware design of the AFL platform by building replicas at their own facilities with enhancements targeted to their needs, but shared by all AFL platforms, with a common software framework and open hardware designs. When the NCNR reopens for user operations, we look forward to expanding the AFL's access to more *nSoft* members and other users.

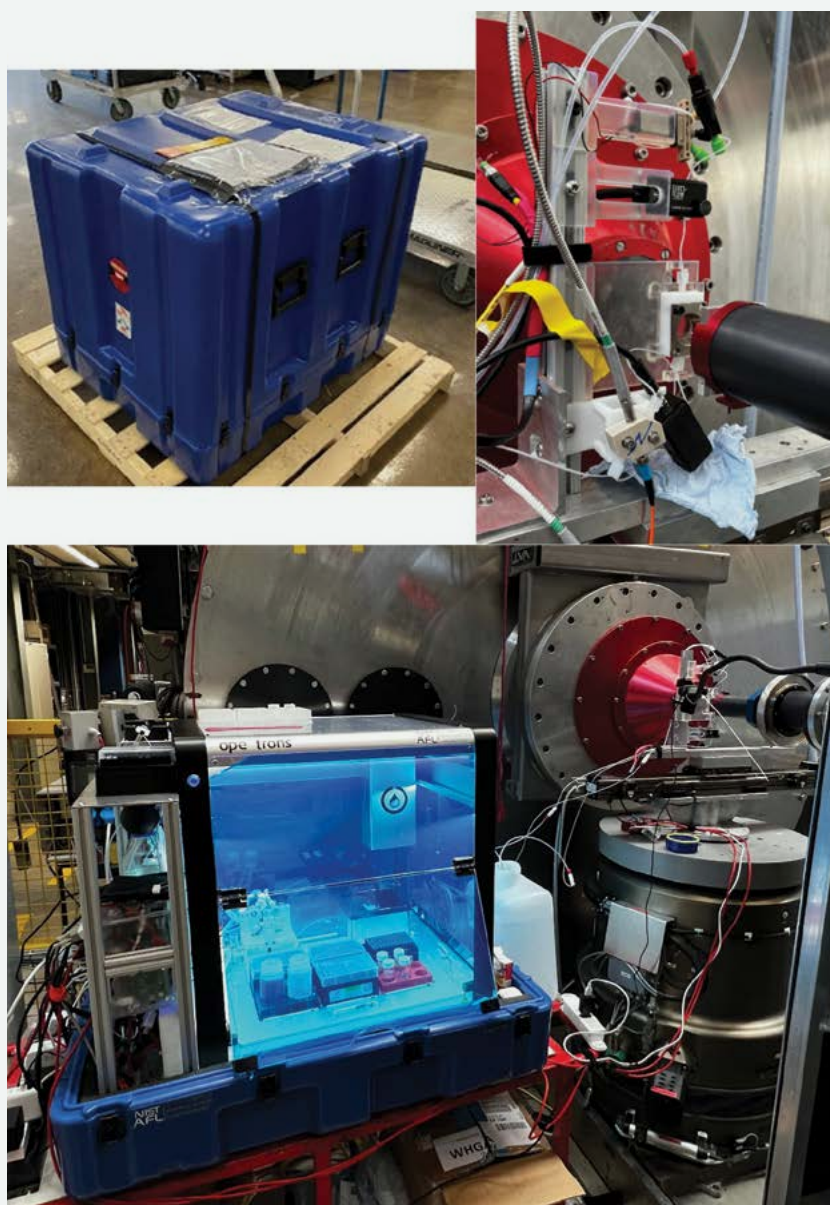


FIGURE 2: Photographs of the mobile AFL platform. Top left: AFL in shipping case, ready for transport. Bottom: AFL running an experiment at the Paul Scherrer Institute in Villigen, Switzerland. Top right: a close-up of the measurement cell during this experiment.

In summary, we have developed software and hardware capable of autonomously mapping soft matter/mesoscale phase diagrams using SAXS and SANS. The platform delivers an approximately 25x speedup compared to dense grid sampling and has been demonstrated in acceleration of block copolymer-based formulations [2]. The platform fuses advanced classification approaches with Gaussian Process regression and a custom-developed sample preparation and transfer system. Ongoing experiments in collaboration with NCNR staff apply the platform to industrial problems in coatings, biotherapeutics, personal care products, materials for carbon capture and sequestration, and other areas.

REFERENCES

- [1] P. Beaucage, T. Martin, *Chem. Mater.* **35** (3), 846 (2023).
- [2] T. Martin, P. Beaucage, *submitted* (2023).

Classification and authentication of materials using prompt-gamma-ray-activation analysis

N. A. Mahynski, J. I. Monroe, D. A. Sheen, R. L. Paul, H. H. Chen-Mayer, and V. K. Shen

In prompt-gamma-ray-activation analysis (PGAA), as neutrons are captured by the atomic nuclei in an irradiated sample, prompt-gamma rays are emitted and recorded by a high-purity germanium (HPGe) detector, producing high-resolution gamma-ray spectra. The spectra generally cover a high-dimensional (multi-channel) energy space occupied by the gamma peaks characteristic of the nuclei in the sample. Conventional spectral analysis of the energy and intensity of a peak can be used to quantify the amount of an isotope in a material. To obtain multi-elemental information, an expert must perform a peak-by-peak analysis, comparing the spectra against tabulated gamma-ray emission energies and probabilities, which is a time-consuming and potentially error-prone task. As a non-destructive technique, PGAA has been widely used as an online monitoring tool in industrial and field settings, for example, in cement production [1] It can also be used to detect explosive materials [2, 3] There are many situations when such rapid, approximate, compositional analysis of a material is necessary without any prior knowledge about the material.

In this work, we used the PGAA spectrum as a holistic signature and explore how well it can be used to distinguish between a range of different materials without the need to perform traditional peak-by-peak analysis. Since prompt-gamma emissions do not depend on the chemical (electronic) state of a material, a PGAA spectrum can provide a simplified picture solely based on the atomic composition. Unlike other non-targeted, spectroscopic-analysis methods, PGAA spectra contain contributions from each isotope present in a sample that undergoes the nuclear activation process. Therefore, it may contain enough information to discriminate between many different classes of materials and complex mixtures. We explored whether accurate predictive models can be developed for this purpose. To do so, we made retrospective use of PGAA data acquired at NGD on various standard reference materials (SRMs) and other common materials to train these models. Facilities have amassed hundreds of PGAA spectra over the years, and these can serve as training datasets (Fig. 2).

We evaluated machine-learning models and other multivariate methods at discriminative and authentication tasks. We only attempted to model materials for which PGAA spectra have been collected on at least 10 different samples. The remaining materials were then used to test each model's detection capabilities after training.

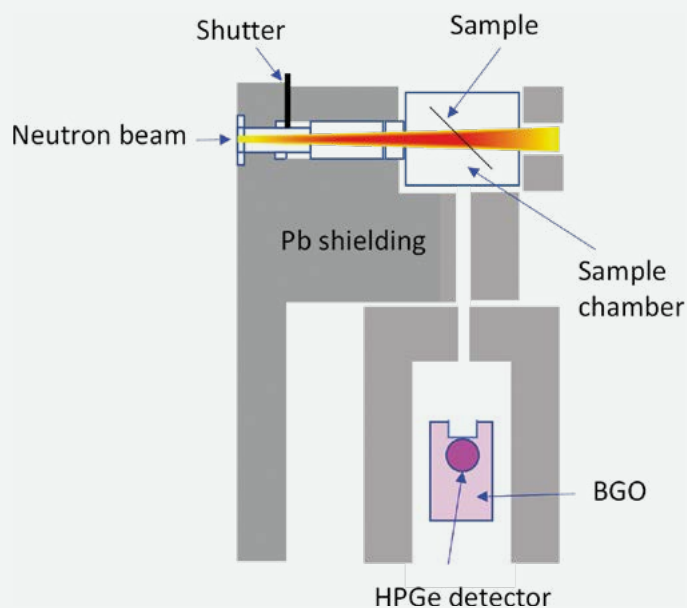


FIGURE 1: Schematic drawing of the NCNR PGAA instrument at NGD.

A spectrum often contains counts in 16,000 evenly spaced energy channels that cover a range of up to approximately 12 MeV. The energy channels of the PGAA training spectra were recalibrated so that all data are on a common energy scale. The channels were then binned (four channels per bin) and a common low- and high-energy cut-off was imposed. All spectra were normalized to their respective total gamma event counts. Some spurious artifacts due to detector electronics were removed. Additionally, variance thresholding was used to identify and remove energy bins containing mostly background noise. Because the pre-processed spectra have roughly 4,000 bins, we had to perform dimensionality reduction. Here, we used principal-components analysis (PCA). The number of principal components and the variance threshold are tunable hyperparameters.

All predictive models were built using pipelines in scikit-learn [4] and compatible python packages. A pipeline used for training models includes these steps: variance threshold, balance classes, center/scale, and dimensionality reduction. The final step in a pipeline is the model, which yields a prediction. Different pipelines may contain different pre-processing steps with various hyperparameters, which are optimized using cross-validation.

Pipelines that use class models to distinguish the classes were evaluated. Class models termed “data-driven soft independent modeling by class analogy” (DD-SIMCA) [5] were developed. These models can be trained in a rigorous or a compliant form that makes use of alternative classes for additional information. The compliant model and the rigorous model yielded nearly identical results.

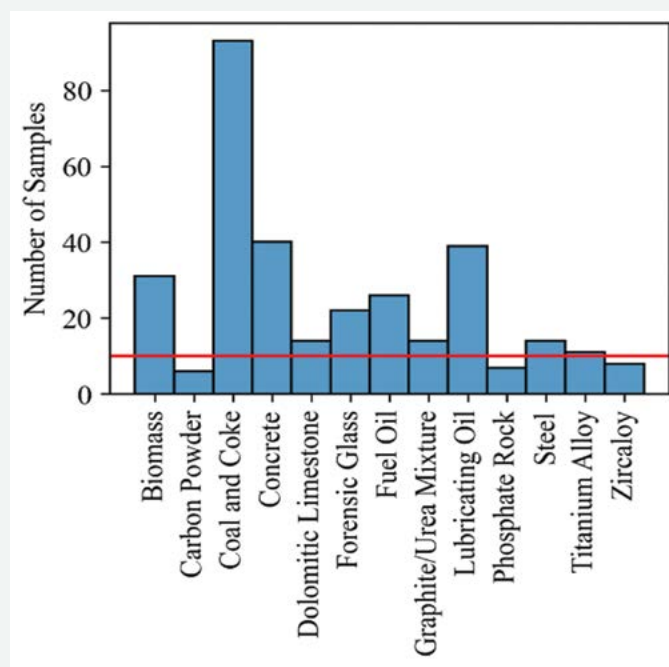


FIGURE 2: Category of materials for which PGAA spectra are available for use in the training. The horizontal red line indicates the minimum number of observations (10) needed to be considered for modeling.

The acceptance plot for the optimal compliant DD-SIMCA models is shown in Fig. 3a. Out of the training data only 1 of the 74 Coal and Coke samples ended up being erroneously rejected, and only 2 out of 25 Biomass samples were incorrectly accepted by the final compliant model. On the test set (Fig. 3b) the model's sensitivity and specificity [6] are both equal to 1. This suggests that accurate class models can be developed for PGAA spectra, which perform as well as soft PLS-DA or discriminative models.

In addition to the class model reported here, we developed a variety of other models to differentiate between materials using PGAA spectra. A complete version of this work appears in [7]. We caution that all conclusions reached here are based on models trained using laboratory prepared samples, many of which are standard reference materials. In practice, intra-class variance is expected to be higher in many real-world materials; this is likely to make it harder for models to achieve good performance. Regardless, this study illustrates that PGAA spectra can be used to develop high-performance models for many classes of materials.

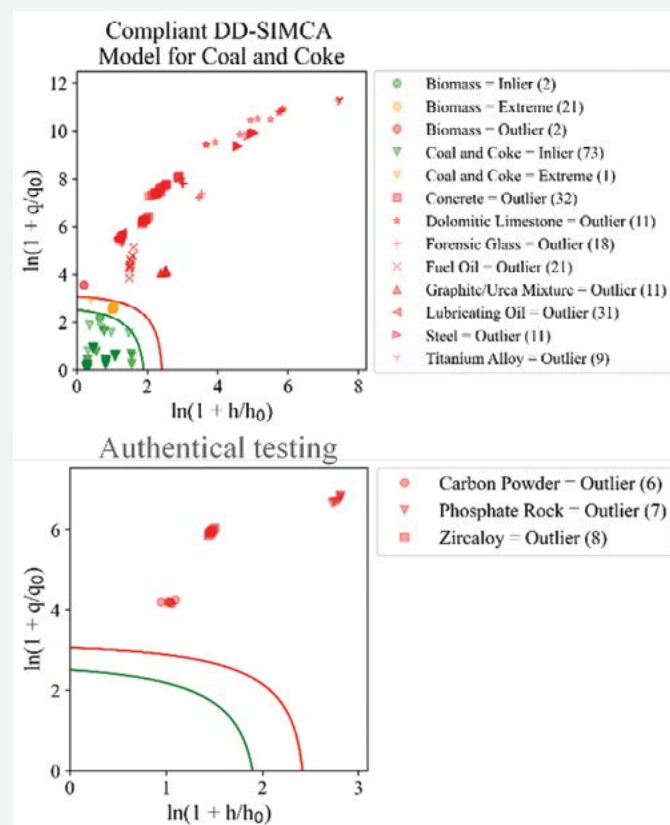


FIGURE 3: (a) Acceptance plots for DD-SIMCA models of Coal and Coke when trained to be compliant. Predictions made on the training set are shown. Green symbols are accepted as a member of the class by the model, yellow and red are rejected, and different symbols are used to denote different classes. The green curve is the acceptance boundary for class membership, while the red line is an outlier threshold corresponding to the same significance level based on Ref. [5]. (b) Predictions made for the classes that were not used to train any models.

REFERENCES

- [1] E. Eftekhari-Zadeh *et al.*, *Journal of Physics* **88**, 24 (2017).
- [2] W. V. Nunes *et al.*, *Applied Radiation and Isotopes* **56**, 937 (2002).
- [3] K. Hossny *et al.*, *Sci Rep* **10**, 13467 (2020).
- [4] F. Pedregosa *et al.*, *Journal of Machine Learning Research* **12**, 2858 (2011).
- [5] L. Breiman, *Mach Learn* **45**, 5 (2001).
- [6] P. Oliveri, *Anal Chim Acta* **982**, 9 (2017).
- [7] N. A. Mahynski *et al.*, *J. Radioanalytical and Nuclear Chemistry*, <https://doi.org/10.1007/s10967-023-09024-x>

Rapid ordering of block copolymer films by hiking down the free energy landscape in sequential solvent and thermal annealing

K. Sharma,¹ A. Agrawal,¹ A. Masud,¹ S. K. Satija,² J. F. Ankner,³ J. F. Douglas,⁴ and A. Karim¹

Block copolymer (BCP) films have potentially advanced applications in functional materials and devices by virtue of their ability to macroscopically self-assemble into processable ordered structures, yet with feature size at the nanoscale. Future applications of BCPs range from organic transistors to nanofiltration membranes to synthetic color. By virtue of simple or complex covalent joining of two or more chemically distinct polymers, BCPs can exhibit a variety of geometrical structures such as lamellar, gyroid, cylinders and spheres. Nonetheless, the ordering kinetics and ultimate morphology and defects in block copolymer (BCP) films are heavily influenced by the chosen processing pathway. This is due to the distinct enthalpic and entropic forces that drive the ordering process, which can vary significantly depending on the processing history. It is widely recognized that conventional thermal annealing (TA) at elevated temperature of BCPs results in achieving the lowest BCP free-energy state and structure, however with extensive TA, making the process inefficient and environmentally unfriendly. Here, we demonstrate that the same desired low-energy structures can be obtained more rapidly by an initial direct solvent immersion (DIA) or solvent vapor annealing (SVA), followed by followed by a short TA, for significantly reduced overall ordering time.

Integrating DIA (or SVA) followed by TA in a sequential manner, with individually controlled process times $t_{DIA} + t_{TA}$, accelerated the overall BCP self-assembly process, with repeat layer spacing periodicity, L_o , comparable to TA alone. The process replaces a single large energetic barrier of BCP melt process-ordering, with two consecutive steps having individually smaller ordering barriers.

A series of PS-*b*-PMMA BCPs with molecular masses ranging from $M_n = 36.5$ kg/mol to 89 kg/mol was investigated to understand the transition from a DIA annealed microstructure (domain size, $L_{o,DIA} \approx 0.5L_{o,TA}$) to a TA microstructure with the equilibrium domain size ($L_{o,TA}$). Analysis using Atomic Force Microscopy (AFM) revealed smaller island/hole heights for the DIA-treated film, which was also observed as reduced domain sizes on fitting neutron reflectivity (NR) data. These DIA-annealed films were then subjected to TA at 180 °C (for $M_n = 36.5$ kg/mol to 66 kg/mol) and 200 °C (for $M_n = 89$ kg/mol) in a vacuum for 24 h. AFM measurements showed a transition to the standard thermally annealed L_o

microstructure with similar transition kinetics. To study the transition kinetics, DIA-equilibrated films were thermally annealed at the same temperatures for shorter durations to achieve partially re-ordered metastable states that may represent different transition states towards the subsequent TA microstructure. AFM scans of the surface topography of these films showed that in as little as 15 minutes of TA at 180 °C, changes in surface morphology occurred, with increased island/hole height and thereby an undulating film surface. Subsequent thermal annealing gradually refined the microstructure, resulting in fully developed island/hole topography (domain size = $L_{o,TA}$) with sharp domain boundaries over the following hours. Lower molecular mass BCP films exhibited a rapid transition to a refined microstructure at 180 °C with larger TA domains, while higher molecular mass polymers required longer sequential thermal annealing times to achieve well-developed larger TA domains. The island/hole heights measured by AFM showed exponential growth in the required transition times from the DIA ($\approx 0.5L_{o,TA}$) domain size to the TA ($L_{o,TA}$) domain size, with increasing BCP molecular mass.

The sequential DIA+TA processing times and Solvent Vapor Annealing (SVA)+TA processing times were always much lower than TA-only times, especially for the highest molecular mass BCP studied. To study the transition mechanism in detail, DIA-annealed films were thermally treated at lower temperatures (160 °C for $M_n = 36.5$ kg/mol and 51 kg/mol, and 180 °C for $M_n = 66$ kg/mol and 89 kg/mol) for short durations in a vacuum. AFM scans revealed an undulating-surface transition morphology with large-height features. Low M_n BCPs with a pre-existing DIA morphology showed accelerated development of the subsequent thermal morphology even at low temperatures. On the other hand, high molecular mass DIA-treated BCPs required longer sequential TA at 180 °C to transition to a multilayered and then single layered island/hole with $L_{o,TA}$ microstructure. Figure 1(a) plots the average island/hole sizes from $L_{o,DIA}$ to $L_{o,TA}$ with sequential annealing time for $M_n = 36.5$ kg/mol to 89 kg/mol. Figure 1(b) plots the average transition times to achieve $L_{o,TA}$ using TA-only, DIA+TA, and SVA+TA processes.

To investigate the effect of the degrees of “metastable” DIA order on subsequent thermal ordering transitions, PS-*b*-PMMA block copolymer films with a molecular mass of $M_n = 66$ kg/mol were subjected to a relatively short DIA treatment followed by thermal

¹ University of Houston, Houston, TX 77204

² NIST Center for Neutron Research, National Institute of Standards and Technology, Gaithersburg, MD 20899

³ Oak Ridge National Laboratory, Oak Ridge, TN 37830

⁴ Materials Science and Engineering Division, National Institute of Standards and Technology, Gaithersburg, MD 20899

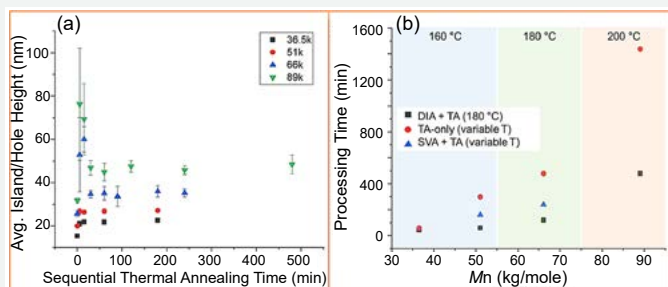


FIGURE 1: (a) Average island/hole size vs. sequential TA times; (b) average processing times to achieve $L_{o,TA}$ using TA-only, DIA+TA, and SVA+TA processes vs. M_n [1].

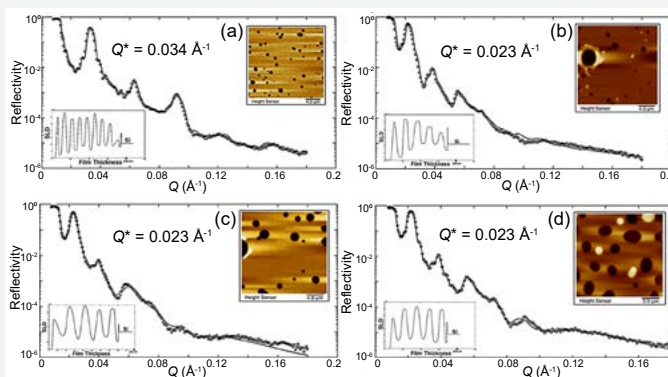


FIGURE 2: Neutron reflectivity data (o) and fits (-) along with scattering length density profiles (bottom left) for dPS-b-PMMA ($M_n = 62$ kg/mol) films and corresponding AFM images for PS-b-PMMA ($M_n = 66$ kg/mol). (a) Films annealed via DIA for 1.5 h; (b) Films annealed via DIA for 1.5 h followed by thermal annealing at 180 °C for 1 h; (c) Films DIA annealed for 1.5 h followed by thermal annealing at 180 °C for 5 h; (d) Films DIA annealed for 1.5 h followed by thermal annealing at 180 °C for 24 h. The values for Q^* in the inset are the positions of Bragg peaks [1].

annealing at a high temperature (180 °C) for only 2 hours. The AFM analysis of this experimental set revealed that even a mere 5-minute DIA treatment, known to initiate DIA assembly according to previous research by Longanecker *et al.*, was sufficient to enhance the transition to a larger domain size during subsequent thermal annealing [2].

Figure 2 presents Neutron Reflectivity (NR) analysis performed on both DIA equilibrated films and those subjected to successive thermal annealing for lamellar dPS-b-PMMA with a molecular mass of 62 kg/mol. The NR data fit and corresponding Scattering Length Density (SLD) profiles are displayed, along with the accompanying AFM height images for $M_n = 66$ kg/mol films treated under identical conditions. These measurements verified domain restructuring observations made by studying the island/hole morphology using the AFM and confirmed the transition in microstructure throughout the film thickness. The films treated with Direct Immersion Annealing (DIA) exhibited a distinct oscillation in the Scattering Length Density (SLD) throughout the film depth, with an average domain size of 25 nm. After only 1 hour of thermal treatment, the reflectivity profile showed a shift of the Bragg peak to a lower Q (scattering vector)

value, indicating the formation of larger domains (inverse relation between size and Q), and the SLD profile obtained from the fitted NR data displayed well-defined oscillations, confirming the presence of a periodic lamellar structure with an increased average domain size of 35 nm. Subsequent thermal annealing further refined the microstructure, as evidenced by improvements in the SLD profiles for films annealed for 5 h and 24 h. Intermediate thermal annealing times were also investigated using NR scans, and the fitted data shows an evolution of the SLD profile with sequential TA, providing a comprehensive understanding of the transient internal microstructure transition. Neutron reflectivity analysis thus confirmed the complete transition of the microstructure to the final TA-ordered state through faster kinetics compared to traditional thermal annealing alone.

A significantly shorter processing time can yield well-ordered block copolymer films with the desired equilibrium domain structure ($L_{o,TA}$) typically achieved through long-time traditional melt annealing. This is achieved through a sequential process that involves immersing the film in a solvent mixture (DIA) or exposure to solvent vapor (SVA), which results in the formation of a partially ordered metastable state very rapidly but with a smaller domain size. Subsequent thermal annealing (TA) then drives the structure towards its global minimum, resulting in the desired well-ordered state. The optimized DIA+TA process involves a DIA step that rapidly generates a partially ordered state, creating a minimally stratified ordered structure with smaller domain spacing and large chain junction spacing. This partially ordered BCP structure then evolves into the equilibrium domain structure through relatively short sequential TA times. Consequently, the overall processing time is significantly reduced compared to the traditional method of annealing disordered BCP films. The results of this study indicate that in the thermal ordering of as-cast disordered BCP films, a substantial energy barrier must be overcome to construct a weakly ordered lamellar structure due to the slow diffusion of BCP molecules, combined with wetting-driven parallel lamellar orientation only from the substrate and air interfaces. By leveraging the high molecular mobility enabled by DIA, this slow diffusive ordering barrier during TA is circumvented, setting up the lamellar scaffold for rapid TA reordering.

In summary, NR and AFM confirm the internal film and top surface morphology to establish that a short DIA (or SVA), to set-up a nascent lamellar profile, that can be well ordered by TA, is more energy efficient than TA alone. This has important ramifications for applications of BCP films due to its roll-to-roll production compatibility for rapid industrial processing.

REFERENCES

- [1] K. Sharma *et al.*, *ACS Appl Mater Interfaces* **15**, 21562 (2023).
- [2] M. Longanecker *et al.*, *Macromolecules* **49**, 8563 (2016).

Correlating the diffusion of water in model polyamides to their performance as reverse osmosis desalination membranes

K. Ito,¹ V. J. Witherspoon,¹ C. R. Snyder,¹ M. Tyagi,² T. B. Martin,² P. A. Beaucauge,² R. C. Nieuwendaal,¹ R. S. Vallery,³ D. W. Gidley,⁴ J. D. Wilbur,⁵ D. Welsh,⁵ C. M. Stafford,¹ and C. L. Soles¹

The increasing scarcity of clean drinking water is one of the most pressing challenges facing the world today. While there are myriad strategies to desalinate seawater, most technologies tend to be energy intensive which creates other societal issues. Reverse osmosis (RO) membranes that allow fresh water to permeate through the membrane while rejecting salt ions are currently the most viable, energy affordable solution to desalinate seawater. A key component of RO membranes is a thin (≈ 100 nm) crosslinked polyamide (PA) layer that enables the selective transport of water relative to salt ions and is synthesized via interfacial polymerization of a trifunctional acid chloride monomer (TMC) and a difunctional amine monomer (MPD). The permeance of fresh water through the membrane, a key metric of performance, depends not only on the material properties of the PA, but also its thickness. This convolution of the thickness and materials properties makes it difficult to develop an understanding of how changes in chemistry or processing affects membrane performance and has led to debate in the literature as to the underlying mechanism of water transport through the PA membrane (solution diffusion vs pore flow). Measurements that are sensitive to the molecular mechanism of transport are critically needed to develop a deeper understanding of how structure and dynamics of the PA membrane relate to macroscopic performance.

In close collaboration with DuPont Water Solutions, we prepared a series of PA membranes with controlled variations in chemistry. Specifically, we systematically reduced the crosslink density of the PA network by replacing a fraction of the tri-functional acid chloride monomer (TMC) with a di-functional acid chloride (IPC) monomer, which acts as a chain extender. These membranes were arbitrarily labeled membranes #6 through #10. Surprisingly, the addition of 0.15 molar fraction of IPC (to reduce the crosslink density of the network) led to a $\approx 30\%$ increase in salt passage, consistent with a loosening of the network structure, but also a $\approx 30\%$ decrease in water permeance, counter to the conventional permeability-selectivity tradeoffs observed in many membrane applications. In a separate study, we leveraged solid state NMR and FTIR measurements to accurately quantify the degree of crosslinking and the corresponding concentration of functional groups in these membranes [1]. The measurements revealed that the incorporation

of 0.15 molar fraction of IPC resulted in approximately a 2x reduction in the crosslink density (the TMC crosslinker moieties) and led to approximately an 80% increase in the molar fraction of unreacted (terminal) free amine moieties coming from terminal MPD units. We argued that the combination of reduced crosslink density and increased concentration of free amines led to greater swelling of the PA layer in water. However, the question remained why membrane #10, which swells more and holds more water, exhibited a reduced water permeance in comparison to membrane #6 (more water should lead to higher permeance).

To address this question, our most recent study [2] leveraged QENS to characterize the motion of the water molecules moving inside this PA membrane series and related those motions to both the microstructure of the membranes (as captured by PALS and SANS/WAXS) and ultimately the performance of the membranes, schematically shown in Figure 1. Here we focused on membranes #6 and #10, the two extremes in terms of membrane performance. As QENS is primarily sensitive to the incoherent dynamics of the hydrogen containing species, QENS spectra in D_2O saturated membranes were used to quantify the dynamics of the polymer components in the hydrated membrane, while QENS spectra of H_2O saturated membranes reflect the dynamics of the hydrated membrane plus the water inside the membrane. We subtracted the H_2O hydrated spectra from the D_2O hydrated spectra to obtain spectra that were representative of just the water inside the membrane, and we were able to fit the both the Q dependence of the Lorentzian FWHMs and the Q dependence of the EISF with the confined diffusion model of Volino [3]. At low Q the water appears confined, but at high Q it moves in accordance with a classic jump-diffusion model.

The translational diffusion coefficients from this analysis for membranes #6 and #10 are shown in Figure 2. These results clearly show that at the molecular scale, water diffuses more slowly in membrane #10 than #6, even though membrane #10 is more hydrated and contains more water. We believe that the higher water content in membrane #10 is driven by (a) the higher concentration of polar free amines and (b) the reduced crosslink density. This opening of the network is consistent with the greater salt passage through membrane #10. However, the increased interactions between water and the free amines slows down the diffusive processes,

¹ Materials Science and Engineering Division, National Institute of Standards and Technology, Gaithersburg, MD 20899

² NIST Center for Neutron Research, National Institute of Standards and Technology, Gaithersburg, MD 20899

³ Department of Physics, Grand Valley State University, Allendale, MI 49401

⁴ Physics Department, University of Michigan, 450 Church Street, Ann Arbor, MI 48109

⁵ DuPont Water Solutions, Edina, MN 55439

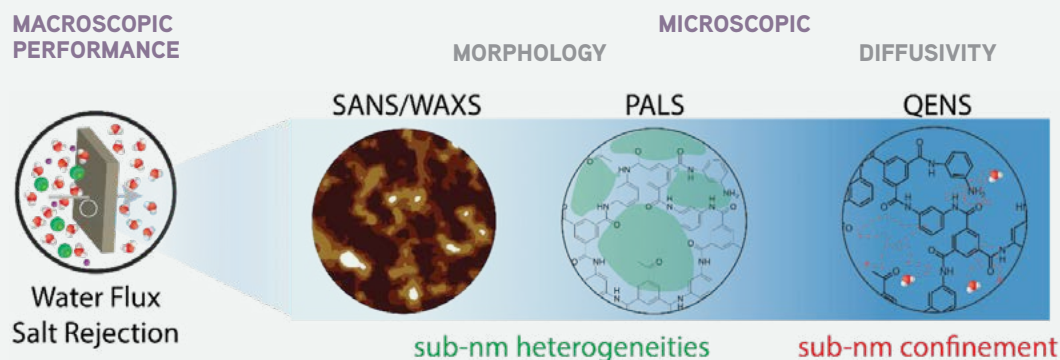


FIGURE 1: In this study, we correlate macroscopic performance (water flux and salt rejection) of PA-based membranes to the microscopy morphology and diffusivity as measured by SANS/PALS and QENS, respectively.

which is consistent with decreased permeance in membrane #10. Additional insight was gained from both PALS and SANS on the same membranes [2]. The PALS data suggested that membrane #6 (highest crosslinked density) displayed more steric hindrance and thus larger “pores” when compared to membrane #10, likely a consequence of the monomer rigidity and rapid reaction rate that freezes in the microstructure and inhibits local packing. SANS data revealed that the water appears to enter the membrane uniformly across all length scales (*i.e.* affine deformation) and there was no evidence of local pockets of water opening up inside the membrane.

Included in Fig 2 are analogous translational diffusion coefficients of water as measured by QENS in a range of materials and environments. The comparison of the translational diffusion coefficients of water across the broad spectrum of materials and environments presented in Fig 2 is very insightful. First, we note that the diffusion coefficient of water in the rigid and non-interacting nanoscale pores of the MCM-41 substrates is comparable to bulk or free water. This is in strong contrast to the transport of water through the AEM membrane, where the diffusion coefficient of water is about an order of magnitude slower. In this case, the strong interactions of water with the ions adds significant impedance at the molecular scale. Like the AEM, Nafion (a proton exchange membrane) also adds impedance to water transport. At low water content ($\lambda = 1$), the impedance to diffusion is high, but as the water content increase ($\lambda = 16$), this impedance is diminished as there is more free water in the material. When we introduce membranes #6 and #10 to this comparison, we see that the polar free amines have a similar effect as the ionic groups in the AEM and Nafion—a greater free amine concentration in the membrane leads to increased impedance. It is notable that the previous Dow PA material, which exhibited generally less swelling, also has a much higher translational diffusion coefficient and is nominally consistent with hypothesis about the reduced free amine content.

The potential insights here into designing PA materials for RO membranes is profound. It is safe to assert that the rigid, porous MCM-41 functions by a pore flow mechanism. It is also reasonable to assert that water solvates the ions in AEMs and functions by solution

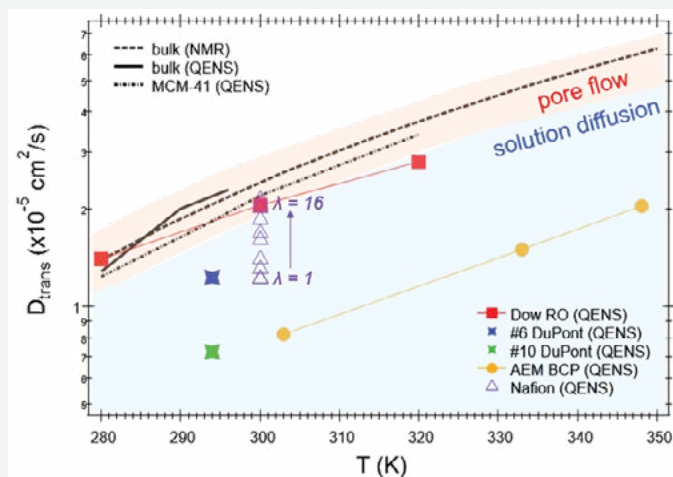


FIGURE 2: Plot of translational diffusion coefficients of water as measured by QENS in various environments, including DuPont membranes #6 and #10 studied here, a different PA membrane material from Dow, and AEM membrane, and Nafion as a function of hydration from $\lambda = 1$ to 16. For comparison, we include the diffusion coefficients of water in bulk and porous MCM-41 substrates, as well as bulk water by NMR. The data presented here suggest that high performance RO membranes function more by a pore flow mechanism than solution diffusion.

diffusion. In this respect, the increase in the diffusivity when going from membrane #10 to #6, combined with increase in the membrane permeance and salt rejection, suggests that high performance RO membranes might function by pore flow. This is supported by the observation that the Dow PA (which we unfortunately do not have performance data on) can achieve diffusivities equal to the MCM-41. This study illustrates that the diffusive motions of water on the picosecond time scale and the sub-nm length scale provides important insights into the molecular mechanisms that govern transport in PA-based membranes.

REFERENCES

- [1] R. C. Nieuwendaal *et al.*, *J. Membr. Sci.*, **648**, 120346 (2022).
- [2] V. J. Witherspoon *et al.*, *J. Membr. Sci.* **678**, 121670 (2023).
- [3] F. Volino and A. Dianoux. *Mol. Phys.*, **41**, 271 (1980).

Relationship between ion transport and phase behavior in polymer blend electrolytes

J. Lee,^{1,2,3} K. W. Gao,^{1,2,3} N. J. Shah,^{1,2} C. Kang,^{3,4} R. L. Snyder,^{3,4} B. A. Abel,⁵ L. He,⁶ S. C. M. Teixeira,^{7,8} G. W. Coates,^{3,4} and N. P. Balsara^{1,2,3}

Polymer electrolytes can replace the flammable organic solvents used in current rechargeable lithium batteries. The performance of electrolytes in lithium batteries depends on the mobility of lithium cations and the efficacy of electrolytes is related to the product $\kappa\rho_+$, where κ is ionic conductivity and ρ_+ is the current fraction carried by the cation [1, 2]. The challenge of designing electrolytes with $\kappa\rho_+$ values higher than that of poly(ethylene oxide) (PEO) mixed with lithium bis(trifluoromethanesulfonyl) imide (LiTFSI) is significant. In most polymers, efforts to increase ρ_+ led to a disproportionate decrease in κ [3, 4].

Through a collaboration spanning laboratories across the United States, the possibility of obtaining polymer electrolytes with high $\kappa\rho_+$ values by blending two polymers was investigated. Namely by blending PEO with a more polar polymer, poly(1,3-dioxolane) P(EO-MO). In a previous publication lead by the Balsara group, polymer blend electrolytes comprising PEO, poly(1,3,6-trioxocane) P(2EO-MO), and LiTFSI were studied [5]. In the present study [6], both PEO/P(EO-MO)/LiTFSI and P(EO-MO)/P(2EO-MO)/LiTFSI blends were examined. Small angle neutron scattering (SANS) was used to study the phase behavior of these blends at different salt concentrations, quantified by the molar ratio r of Li ions in the salt to O atoms in the polymer.

The measured absolute SANS intensity $I(q)$ as a function of the magnitude of scattering vector q for the polymer blends electrolytes is shown in Figure 1. The macrophase-separated dPEO/P(EO-MO)/LiTFSI blends show a sharp upturn of $I(q)$ below $q = 0.4 \text{ nm}^{-1}$, when the salt concentration r is 0.02 ~ 0.06, as shown in Figure 1(a). The macrophase-separated dP(EO-MO)/P(2EO-MO)/LiTFSI blends show a similar signature but the sharp upturn of $I(q)$ is seen at q values ranging from 0.4 nm^{-1} to 1.0 nm^{-1} , when the salt concentration r is ≥ 0.01 , as shown in Figure 1(b). The lack of a sharp upturn of $I(q)$ in the q range noted above it is taken as a signature of a one-phase blend. In the absence of salt, both dPEO/P(EO-MO) and dP(EO-MO)/P(2EO-MO) blends are one-phase. Adding LiTFSI in dilute concentrations results in macrophase separation in both cases. At higher salt concentrations above $r = 0.08$,

the dPEO/P(EO-MO)/LiTFSI blends become one-phase again. In contrast, the dP(EO-MO)/P(2EO-MO)/LiTFSI blends remain macrophase-separated in all salt concentrations studied.

Figure 2 illustrates the relationship between the electrochemical properties of the polymer blend electrolyte and the blend phase behavior $\kappa\rho_+$ is plotted as a function of r for three systems: PEO/LiTFSI, P(EO-MO)/LiTFSI, and PEO/P(EO-MO)/LiTFSI blends.

The dependence of $\kappa\rho_+$ of PEO/LiTFSI and P(EO-MO)/LiTFSI on r is similar, within experimental error, yet the dependence of $\kappa\rho_+$ of PEO/P(EO-MO)/LiTFSI blends on r is not similar to that of the homopolymer electrolytes. Figure 2(a) shows that at $r = 0.05$, $\kappa\rho_+$ of polymer blend electrolytes is 0.08 mS/cm while that of the homopolymer electrolytes is 0.16 mS/cm. In contrast, at $r = 0.14$, $\kappa\rho_+$ of polymer blend electrolytes is 0.26 mS/cm while that of the homopolymer electrolytes is 0.10 mS/cm. The main difference between the two chosen r values is their phase behavior: the polymer blend electrolyte at $r = 0.14$ is one-phase, while the polymer blend electrolyte at $r = 0.05$ is macrophase-separated. It is evident that one-phase polymer blend electrolytes can exhibit efficacies that are higher than homopolymer electrolytes. Figure 2(b) further shows a plot of $\kappa\rho_+$ as a function of r for three systems: P(EO-MO)/LiTFSI, P(2EO-MO)/LiTFSI, and P(EO-MO)/P(2EO-MO)/LiTFSI blends. The dependence of $\kappa\rho_+$ on r is similar for all three systems. All of the polymer blend electrolytes in Figure 2(b) are macrophase-separated.

In conclusion, we have examined the possibility of optimizing ion transport in polymer electrolytes by blending two different polymer blends. In most of the polymer blend electrolytes, the measured $\kappa\rho_+$ was either lower than or comparable to that of the homopolymer electrolytes. An exception to this was however found for the one-phase PEO/P(EO-MO)/LiTFSI blends electrolytes at high salt concentrations. The molecular underpinnings of both thermodynamic and ion transport properties remain to be established and SANS will continue to provide critical measurement capabilities for this type of study.

¹ Department of Chemical and Biomolecular Engineering, University of California, Berkeley, CA 94720

² Materials Sciences Division, Lawrence Berkeley National Laboratory, Berkeley, CA 94720

³ Joint Center for Energy Storage Research (JCESR), Argonne National Laboratory, Lemont, IL 60439

⁴ Department of Chemistry and Chemical Biology, Cornell University, Ithaca, NY 14850

⁵ Department of Chemistry, University of California, Berkeley, CA 94720

⁶ Neutron Scattering Division, Oak Ridge National Laboratory, Knoxville, TN 37830

⁷ NIST Center for Neutron Research, National Institute of Standards and Technology, Gaithersburg, MD 20899

⁸ Center for Neutron Science, Department of Chemical and Biomolecular Engineering, University of Delaware, Newark, DE 19716

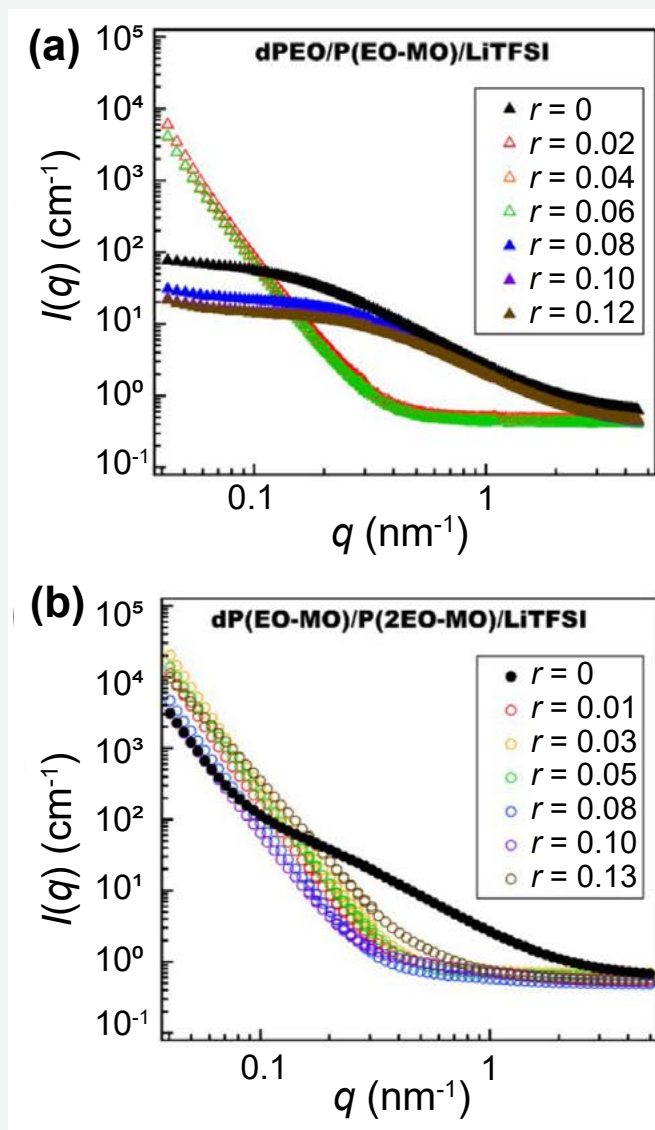


FIGURE 1: Measured absolute SANS intensity versus the magnitude of scattering vector (q) at 90 °C for (a) dPEO/P(EO-MO)/LiTFSI and (b) dP(EO-MO)/P(2EO-MO)/LiTFSI polymer blend electrolytes at different salt concentrations (r). Filled symbols correspond to one-phase electrolytes. Open symbols correspond to macrophase-separated electrolytes. Error bars represent one standard deviation based on Poisson counting statistics.

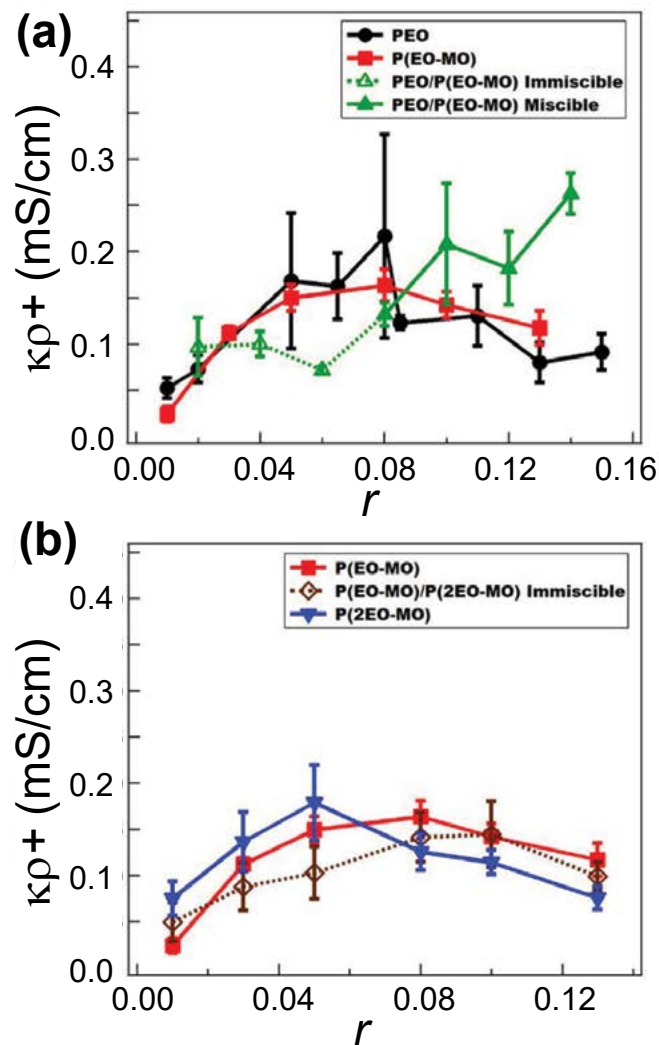


FIGURE 2: Efficacy, $\kappa\rho^+$, of PEO/P(EO-MO)/LiTFSI and P(EO-MO)/P(2EO-MO)/LiTFSI polymer blend electrolytes as a function of r compared to each homopolymer/LiTFSI (PEO, P(EO-MO), P(2EO-MO)) at 90 °C. Solid lines imply one-phase systems and dashed lines imply macrophase-separated systems. Error bars represent the standard deviation of at least three measurements.

REFERENCES

- [1] J. Evans, C. A. Vincent, P. G. Bruce, *Polymer*, **28**, 2324 (1987).
- [2] M. Watanabe, S. Nagano, K. Sanui, N. Ogata, *Solid State Ion.*, **28–30**, 911 (1988).
- [3] W. Zhang, J. Nie, F. Li, Z. L. Wang, C. A. Sun, *Nano Energy*, **45**, 413 (2018).
- [4] Q. Zheng, D. M. Pesko, B. M. Savoie, K. Timachova, A. L. Hasan, M. C. Smith, T. F. Miller, G. W. Coates, N. P. Balsara, *Macromolecules*, **51**, 2847 (2018).
- [5] K. W. Gao, W. S. Loo, R. L. Snyder, B. A. Abel, Y. Choo, A. Lee, S. C. M. Teixeira, B. A. Garetz, G. W. Coates, N. P. Balsara, *Macromolecules*, **53**, 5728 (2020).
- [6] J. Lee, K. W. Gao, N. J. Shah, C. Kang, R. L. Snyder, B. A. Abel, L. He, S. C. M. Teixeira, G. W. Coates, N. P. Balsara, *Macromolecules*, **55**, 11023 (2022).

Tracking the real-time kinetics and internal structure of light-initiated nanogel-based hydrogels using neutrons

M. J. Majcher,¹ S. Himbert,¹ F. Vito,¹ M. A. Campea,¹ R. Dave,¹ G. Vestergaard Jensen,² M. C. Rheinstadter,¹ N. M. B. Smeets,¹ and T. Hoare¹

Hydrogels, networks of polymers with a high affinity to water, have attracted interest in a variety of biomedical applications due to their controllable porosity and mechanics that mimic soft tissues. The micro- and/or nanostructure of the hydrogel determines the efficacy of the hydrogel in each targeted application, with the structure of the gel directly related to both the diffusivity of drugs, cells, or nutrients through the gel (drug delivery/tissue engineering) and the contact angle/degree of hydration of the gel (anti-fouling materials). In this context, understanding how to control the morphology of hydrogels is critical to rationally engineer gels for biomedical applications.

Most conventional hydrogels are fabricated by crosslinking water-soluble linear polymers. However, hydrogel can also be formed by crosslinking pre-formed nanogels or microgels (hydrogel particles with a diameter < 1 micron) to form a *nano/microgel network hydrogel* [1]. The key mechanical, diffusional, and sorption properties of such hydrogels can be controlled by both the size and crosslink density within the nano/microgel building blocks (*intra-*) as well as the density and type of crosslinks between those building blocks (*inter-*), providing multiple levers for controlling hydrogel properties. However, elucidating the structure of nanogel-based hydrogels is challenging. Micro/nanogels have pre-existing elasticity that competes with the surrounding (inter-particle) crosslinking reaction; as such, the structure of the micro/nanogel may change to different degrees during bulk crosslinking, with potentially significant implications in terms of the local porosity, water content, and thus functionality of the resulting hydrogel.

In this work, we used commercial corn starch-based nanoparticles (SNPs) formed via an extrusion process as building blocks for fabricating nanogel-based hydrogels. SNPs are extremely small (20 nm to 50 nm average diameter), are based on a natural, cell-compatible and hydrolytically degradable material (starch), and are available inexpensively at commercial scales, making SNP-based hydrogels relevant to both high value biomedical applications as well as commodity (e.g. agriculture or bioremediation) applications. Hydrogels were formed via the methacrylation of the SNPs followed by light-initiated free radical photopolymerization, either by self-crosslinking SNPs (as reported in our previous paper [2]) or crosslinking with methacrylated soluble starch (SS).

Small-angle neutron scattering (SANS) is particularly useful for studying the morphology of SNP-based hydrogels given that the mesh size of the SNPs, the mesh size between the SNPs in the hydrogel, and the absolute size of the SNPs all lie within the accessible SANS length scale (1 nm to 200 nm). While we and others have previously used SANS to report the *final* morphologies of various hydrogels, tracking the development of the morphology *during* the polymerization process is much less common. While photopolymerization is the most common method to fabricate coatings and biomedical hydrogels, the rapid speed of photopolymerization (seconds to minutes) and the need for external irradiation to drive gelation make its kinetics hard to study using SANS; indeed, to our knowledge, such kinetic data had not previously been reported.

In this work, we collaborated with the scientists at NIST to apply the very small angle neutron scattering angle (vSANS) beamline at CHRNS to track photopolymerization kinetics. The vSANS beamline enables simultaneous detection of scattered neutrons over a wide q -range without moving the detector, enabling data acquisition over the relevant length scales of hydrogels at the speed of photopolymerization. The UV irradiation accessory coupled with the capacity to quickly move samples in and out of the beam allowed us to (semi)-continuously irradiate the sample while tracking morphology changes in near-real time. In-line photopolymerizations were performed with different SNP or SS concentrations, different building block morphologies (e.g. soluble starch only, SNPs only, and combinations of SNPs and soluble starch) as well as charged SNPs that electrostatically repel prior to gelation. The corresponding SANS curves switch from a primarily linear fit in the mid- q range to a concave fit in the mid- q range as gelation occurs, with the concave feature developing systematically as a function of the irradiation time for photocrosslinking to different magnitudes for different precursors (Figure 1).

To quantify the network development during photocrosslinking, scattering profiles were fit using Shibayama's approach of combining an Ornstein-Zernicke scattering term with a Lorentzian term to account for the presence of domains (here, the denser SNPs relative to the less dense inter-SNP region) as well as the dynamics of the gel network (Equation 1) [3]. While morphological insight could be gained from analyzing the time-dependent development of each

¹ McMaster University, 1280 Main St W., Hamilton, ON, Canada L8S 4L7

² NIST Center for Neutron Research, National Institute of Standards and Technology, Gaithersburg, MD 20899

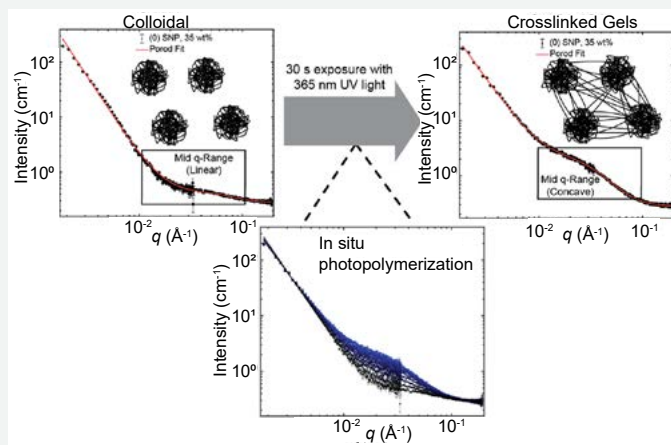


FIGURE 1: Schematic showing the evolution of network formation from concentrated SNP colloids to crosslinked SNP gels over a 30 s total exposure time to 365 nm light.

fitting parameter, the fluid scale s_{oz} was particularly reflective of the kinetics of gelation; by fitting the trend in the fluid scale parameter as a function of time using a characteristic time constant $1/\tau_s$ and a stretch parameter β_s describing chain relaxation ($\beta_s < 1$ corresponds to anisotropic relaxation in the gel network) [4] (Equation 2), the nanoscale network evolution can be tracked in real time.

$$I(Q) = \frac{S_{porod}}{Q^n} + \frac{S_{oz}}{1+(Q\xi)^m} + b \quad (1)$$

$$s_{oz}(t) = e - \left(\frac{1}{\tau_s} t\right)^{\beta_s} \quad (2)$$

A representative example of the data acquired is shown in Figure 2. While all the SNPs remain as distinct nanoparticles following photopolymerization into bulk hydrogels (as reflected by the consistent best fit Porod exponents), photocrosslinking of uncharged SNPs results in an increase in the correlation length (*i.e.* mesh size) and a decrease in the fluid exponent. Both these results suggest that the polymer chains within the SNPs are “pulled” by the bulk gelation process to induce swelling at the SNP-bulk gel interface. When SS is instead used as the crosslinker, much smaller changes in SNP hydration are observed, consistent with the increased flexibility of the SS chains instead primarily deforming in response to the stresses introduced during the bulk gelation process. When charge is introduced to the system, local *deswelling* of the charged SNPs was observed at very short timescales as SNPs rearrange into colloidal crystal-like structures, consistent with the high viscosity of the initial pre-gel solutions; as such, while less *covalent* crosslinking occurs during the photocrosslinking of such samples, the *electrostatic* repulsion between the close-packed SNPs still results in the formation of stiffer gels. Of note, these microscale interpretations could be correlated directly with small-amplitude oscillatory shear rheology measurements in which photocrosslinking is conducted directly on a rheometer, linking bulk gelation directly to the microstructure evolution.

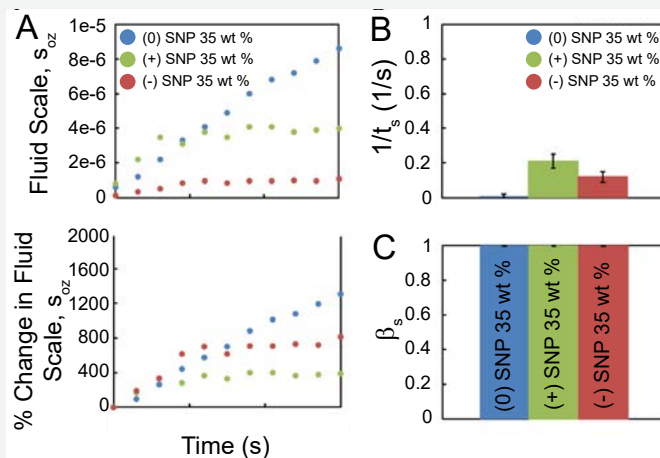


FIGURE 2: Representative changes in the fluid scale over 30 s of UV exposure (A—top = absolute values, bottom = percent changes over the irradiation time) and best-fit time constant ($1/\tau_s$, B) and stretch parameter (β_s , C) for 25 wt% homogenous SNP hydrogels formed in the beamline [5]. (0) SNP = neutral SNPs, (+) SNP = cationic SNPs, (-) SNP = anionic SNPs as the building block (all methacrylated to the same degree). Error bars represent \pm standard deviation).

Overall, these results yield unique insight into what is happening to micro/nanogel building blocks as they are crosslinked into bulk hydrogels. Nanogels may swell (neutral SNPs) or deswell (repulsive charged SNPs) during photopolymerization depending on the initial interactions between the SNPs and whether a flexible crosslinker (SS) is added; such results were previously inaccessible due to the experimental limitations of tracking fast photopolymerization with conventional SANS. The technique is generally applicable to track the role of the charge, morphology, and/or size of other types of soft building blocks for forming photocrosslinked hydrogels. Such results are essential to understand how small and large molecules diffuse through the resulting micro/nanogel-based gel networks (key to the rational design of drug delivery vehicles) as well as how water is partitioned within such hydrogels (key to the rational design of anti-fouling hydrogel coatings). The results are also relevant to designing shape memory hydrogel “muscles” in which the building blocks are engineered to introduce pre-stresses into the network that can subsequently be relaxed as the network degrades and/or is externally stimulated.

REFERENCES

- [1] M.A. Campea, M.J. Majcher, A. Lofts, T. Hoare, *Adv. Funct. Mater.* **31**, 2102355 (2021).
- [2] M.J. Majcher, C.L. McInnis, S. Himbert, R.J. Alsop, D. Kinio, M. Bleuel, M.C. Rheinstadter, N.M.B. Smeets, T. Hoare, *Carbohydrate Polym.* **236**, 115998 (2020).
- [3] T. Norisuye, N. Masui, Y. Kida, D. Ikuta, E. Kokufuta, S. Ito, S. Panyukov, M. Shibayama, *Polymer* **43**, 5289 (2002).
- [4] K. Gorska, A. Horzela, K.A. Penson, G. Dattoli, G.H.E. Duchamp, *Fract. Calc. Appl. Anal.* **20**, 260 (2017).
- [5] M.J. Majcher, S. Himbert, F. Vito, M.A. Campea, R. Dave, G. Vettergaard Jensen, M.C. Rheinstadter, N.M.B. Smeets, T. Hoare, *Macromolecules* **55**, 7303 (2022).

Advanced polarization analysis capability on VSANS

W. C. Chen,¹ K. L. Krycka,¹ S. M. Watson,¹ J. G. Barker,¹
J. Gaudet,^{1,2} H. Burrall,¹ and J. A. Borchers¹

In this highlight, we describe the development of a uniaxial-polarization-analysis capability on the recently commissioned Very-Small-Angle-Neutron-Scattering (VSANS) instrument [1]. Improvements in neutron-polarizing devices, such as supermirror polarizers, adiabatic radio-frequency (RF) spin flippers [2], and ³He spin analyzers [3], as well as the ability to obtain data at all *Q* values in one measurement on VSANS, are greatly facilitating routine polarized beam experiments and have substantially enhanced polarized neutronic performance by providing, for example, an initial flipping ratio of over 100, which allows for detection of weak magnetic features with a higher sensitivity [4].

We have implemented two polarized-beam configurations for uniaxial-polarization analysis on VSANS (Fig. 1), one with the neutron polarization at the sample position oriented perpendicular to the beam at high and low magnetic fields, and the other with the neutron polarization parallel to the beam at low magnetic fields. A double V-shaped, *m* = 3.5 supermirror polarizer in a transmission geometry is used to polarize the incident neutron beam vertically (along *y*) and provides a polarization of 99% for wavelengths between 5.5 Å and 8.0 Å. A home-designed adiabatic RF spin flipper is used to flip the neutron polarization of the incident beam with an efficiency of over 0.999 [2]. A uniform, vertical field of 2.9 mT maintains the incident neutron polarization after the supermirror polarizer and upon beam exit. At the end of the neutron guide, a vacuum tube equipped with a vertical magnetic field (panel A in Fig. 1) extends the beam aperture of the incident beam as close to the sample as possible. For the high-field configuration, an iron-yoked electromagnet provides a magnetic field along *x* at the sample of up to 1.6 T. For the low-field configuration, a pair of coils provides a field of ≈ 66 mT at the sample at a current of 20 A and a separation of 48 mm between the coils. In each configuration, various magnetic-field devices, either short-sectioned permanent magnets or longitudinal solenoids, have been implemented to ensure adiabatic spin transport just before and after the sample. As a check, flipping ratios of up to 290 were obtained on the transmitted beam using a special ³He cell with the neutron polarization near unity [1]. Typical flipping ratios for polarized-beam experiments are ≈ 100 for optimized intensity.

The key component of the polarized-beam setup is the ³He spin analyzer, which doesn't affect the neutron beam path and provides a spatially uniform polarizing efficiency. We have developed a magnetically shielded solenoid (MSS) that significantly reduces the

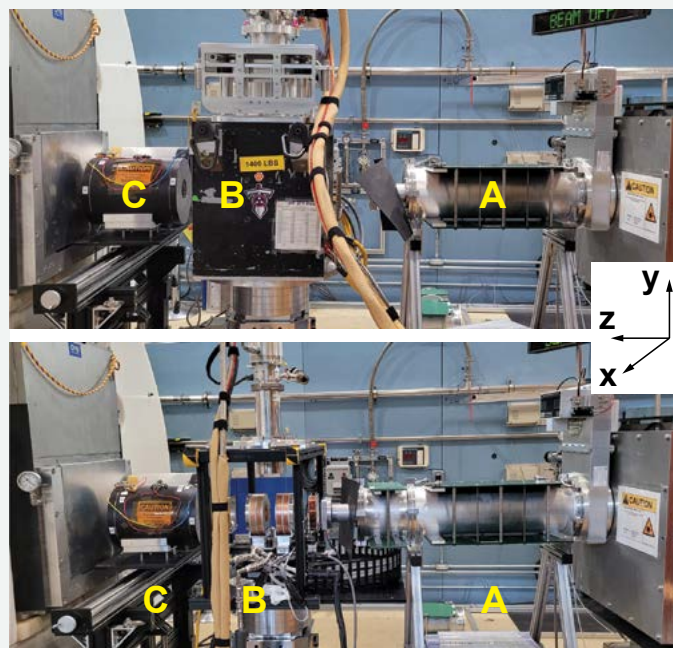


FIGURE 1: Polarized VSANS setup near the sample area for the high-field (top photo) and low-field (bottom photo) configurations. Neutrons travel from right to left (along *z*). The configuration with the neutron polarization perpendicular to the beam at low fields is accomplished by rotating the low field coils by 90 degrees (not shown). Three major components are visible: (A) a vacuum tube with a vertical guide field; (B) an electromagnet (top photo) or a pair of coils (bottom photo) that provides the field at the sample position; and (C) a magnetically shielded solenoid. The CCR assembly and the platform for the multi-sample exchanger are located on top of the electromagnet/coils.

volume-averaged transverse field gradient over the ³He cell. This increases the relaxation time of the ³He cells by placing non-identical compensation coils centered on non-identical holes in the mu-metal end caps [3]. The compact MSS is 25 cm in diameter, 33 cm long, and has 9-cm and 16-cm holes on the upstream and downstream endcaps, respectively. The sizes of the endcap holes were chosen to match the divergence of the scattered beam, minimize the field gradient over the ³He cell volume, and maximize the *Q* coverage. The maximum *Q* is 0.13 Å⁻¹ for the high-field configuration and up to 0.18 Å⁻¹ for the low-field configuration, both at a wavelength of 5.5 Å without off-setting the detector. The relaxation times of the ³He cells lie between 250 h and 300 h, which allows for operation of a polarized-beam experiment for 3 days without swapping the ³He cell.

These advances in the polarized-neutron configuration, coupled with the simultaneous coverage of the full *Q* range in a single measurement on VSANS, will make routine uniaxial-polarization analysis on VSANS available to meet the growing interest in a wide range of scientific applications.

REFERENCES

- [1] J.G. Barker *et al.*, J. Appl. Crystallogr. **55**, 271-283 (2022).
- [2] W.C. Chen *et al.*, Rev. Sci. Instrum. **92**, 063906 (2021).
- [3] W.C. Chen *et al.*, Rev. Sci. Instrum. **91**, 105102 (2020).
- [4] W.C. Chen *et al.*, J. Phys.: Conf. Ser. **2481**, 012006 (2023).

¹ NIST Center for Neutron Research, National Institute of Standards and Technology, Gaithersburg, MD 20899

² University of Maryland, College Park, MD 20742

Watching ionic motion switch magnetism in multi-region patterned devices

S. Sheffels,¹ P. P. Balakrishnan,² M. Huang,¹ S. Muramoto,³
J. A. Borchers,² J. A. Dura,² A. J. Grutter,² and G. S. D. Beach¹

In the past few years, it has become possible to control the magnetic, electronic, and optical properties of ultrathin films through voltage-induced ion motion. The magnetic branch of this research, known as magneto-ionics, is particularly promising for information storage and processing applications. It has recently been demonstrated that hydrogen (H) can be pushed into and pulled out of a magnetic system, such as a cobalt (Co) / gadolinium oxide (GdO_x) multilayer, and thereby modulate the size and direction of the magnetic moments within the film for potential applications as a magnetic sensor. This type of device is illustrated schematically in Fig. 1(a). However, the underlying physics and chemistry that enable this behavior are poorly understood, and hydrogen motion is particularly challenging to characterize, as the low atomic number render H nearly invisible to X-ray and electron probes. We have combined polarized neutron reflectometry (PNR) and time-of-flight secondary ion mass spectrometry (ToF SIMS) to obtain a detailed picture of the physics and chemistry within these promising devices [1].

PNR is a powerful tool for measuring the depth-dependent chemistry and magnetism in thin film heterostructures, especially as it related to H, which has an unusually large negative scattering factor for neutrons. ToF SIMS, on the other hand, uses a mass spectrometer to identify atoms and molecules sputtered from the film to create a detailed chemical depth profile. While ToF SIMS has less depth resolution than PNR, it can uniquely identify chemical species, giving complementary information.

To accomplish this, we patterned a large array of 1 mm² × 1 mm² devices onto a Si wafer as shown in Fig. 1(b). By switching all of the individual devices, we can measure 30 mm² of operational devices simultaneously, but the reflectivity from the inactive regions of the sample must also be accounted for. We used image analysis software to precisely characterize the area of each different device region [2]. We developed a highly coupled model in which each of the 7 different types of regions on the sample surface contributed to the total reflectivity signal proportional to their area [3]. Furthermore, we used the evolution of chemical profiles from ToF SIMS to significantly constrain the model.

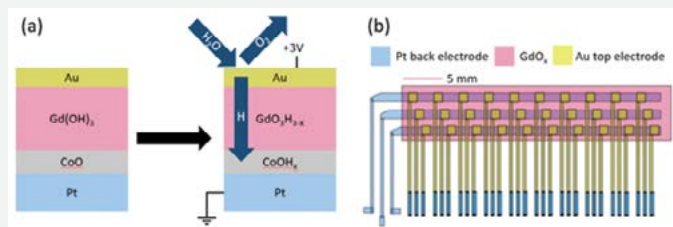


FIGURE 1: (a) Schematic of magneto-ionic device operation. (b) Schematic of magneto-ionic device array. Thirty 1 mm² devices of GdO_x/Co are switched by applying voltage between the top and bottom electrodes. The neutron beam covers the entire area including 7 different regions of various combinations of bare Si/SiO₂ substrate, electrodes, and magnetically active stack.

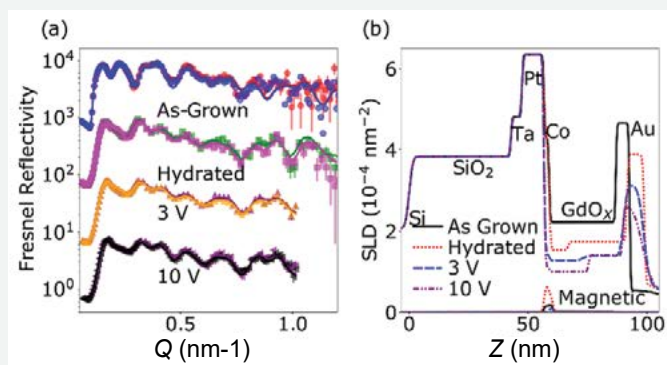


FIGURE 2: (a) PNR data and fits (b) Fitted SLD profiles of the active stack.

This method is highly successful, allowing us to understand subtle features in the data (Fig. 2(a)). The extracted chemical and magnetic depth profiles (Fig. 2(b)) reveal massive incorporation of H into the GdO_x, as manifested in a sharply reduced nuclear scattering length density (nSLD), and some oxidation of Co seen as a higher-than-expected nSLD. As voltage is applied, the Co nSLD decreases and the magnetic scattering length density (mSLD) is reduced, as hydrogen enters the Co layer and suppresses the magnetization. ToF SIMS reveals that the hydrogen reversibly converts some GdO_x and Co to a metal-hydroxide compound, such as Gd(OH)₃ or Co(OH)₂, which thereby modulates the magnetism.

Thus, by using these two powerful techniques together, we can study complex devices of small area in their operational configuration, unveiling the important role of hydrogen-oxygen interfacial reaction in enabling these magneto-ionic devices to function.

REFERENCES

- [1] S. Sheffels, *et al.*, Appl. Phys. Lett. **122**, 022407 (2023).
- [2] W. Rasband, ImageJ, <https://imagej.nih.gov/ij> U. S. National Institutes of Health, Bethesda, MD, USA (1997–2018).
- [3] P.A. Kienzle, J. Krycka, N. Patel, I. Sahin, Refl1D [Computer Software]. College Park, MD: University of Maryland. <https://github.com/reflectometry/refl1d>

¹ Department of Materials Science and Engineering, Massachusetts Institute of Technology, Cambridge, MA 02139
² NIST Center for Neutron Research, National Institute of Standards and Technology, Gaithersburg, MD 20899
³ Material Measurement Laboratory, National Institute of Standards and Technology, Gaithersburg, MD 20899

A different angle on bending neutron beams

C. Kapahi,^{1,2} D. Sarenac,^{1,3} M. Bleuel,^{4,5} D. G. Cory,^{1,6} B. Heacock,⁴ M. Henderson,^{1,2} I. Taminiau,⁷ D. A. Pushin,^{1,2} and M. G. Huber⁴

In neutron optics, all materials have an index of refraction that is barely different than vacuum ($|1-n| \approx 10^{-5}$). As a result, modern neutron optical devices require a series of individual prisms or lenses to even weakly deflect or focus a neutron beam [1]. This significant amount of material not only increases device cost and complexity but also reduces the number of transmitted neutrons through inelastic scattering and absorption. A typical MgF_2 compound neutron lens could absorb up to 33% of an incident neutron beam. Neutron flux is already a limited experimental commodity, so exploring entirely new design limits could lead to new optical component solutions.

Nanofabrication techniques have already seen application in neutron optics in generating high-aspect ratio phase gratings which enable large-area neutron interferometers [2] and orbital angular momentum generating fork-grating arrays [3]. These structures are limited to micrometers in scale and are suitable for diffraction-based devices; however, diamond turning machines enable the construction of structures that are millimeters in scale containing micrometer-sized features, with nanometer surface flatness. Exploiting this capability, an aluminum triangular array refractive prism (TARP), shown in Figure 1, containing an array of prisms machined to 2° angles is feasible to construct. The design, fabrication, and realization of the TARP was enabled by the Quantum Colaboratory facilities, with machining provided by Neutron Optics in Waterloo, Canada. The production and assembly of the TARP components enable manufacturing at scale for real-world applications (spectroscopy, focussing, SANS, interferometry, etc.). The function of the TARP was validated at the BT-5 Ultra Small Angle Neutron Scattering (USANS) instrument [4].

Experimental results are compared with a Monte Carlo simulation, shown in Figure 2a), including machining imperfections modeled as flat prism apices. Figure 2b) shows why the TARP is superior: the dramatic increase in quality factor calculated using beam deflection

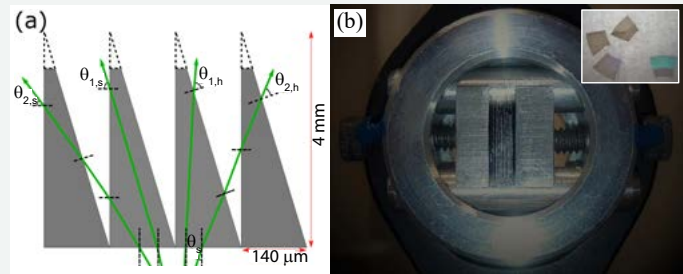


FIGURE 1: (a) Schematic of the TARP with neutron paths indicated as green lines. Imperfect prism apices are modeled as flat tops. (b) Custom aluminum assembly containing a TARP, fitted to a 1 inch optics mount. Inset shows individual, unmounted prisms.

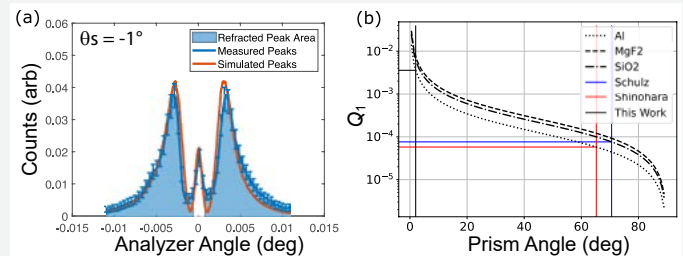


FIGURE 2: (a) Comparison of the TARP USANS measurements (blue) with Monte Carlo simulation (red) taken at $\theta_s = -1^\circ$, showing agreement between experiment and simulation. (b) Quality-factor, Q_1 , for a neutron prism as a function of prism angle. Different materials are considered as black lines of different styles. Prism angles utilized in other neutron prism experiments are shown as solid vertical lines, with the corresponding quality factors marked by horizontal lines [5, 6].

and neutron transmission, $Q_1 = \Delta\theta \cdot T$, as the prism angle decreases. While MgF_2 is typically used in neutron lenses and prisms due to its higher refractive index and lower absorption, the design of the TARP outweighs the material limitations of aluminum.

With the support and fabrication facilities of Transformative Quantum Technologies a new frontier has been opened for prism-based neutron interferometers and neutron Fresnel prisms. A TARP-like device with prism angles between 1° and 2.61° could act as a neutron lens with focal length $f = 2.77$ m and spot size of 1 mm, achieving an intensity gain of > 100 . Alternatively, a TARP fabricated from magnetic materials could act as a polarizing neutron beamsplitter. These next-generation devices, as well as more efficient, space-saving, and cost-effective neutron optical devices, are enabled by the new design direction trail-blazed by the TARP described here.

¹ Institute for Quantum Computing, University of Waterloo, Waterloo, ON, Canada, N2L3G1
² Department of Physics, University of Waterloo, Waterloo, ON, Canada, N2L3G1
³ Department of Physics, University at Buffalo, State University of New York, Buffalo, NY 14260
⁴ National Institute of Standards and Technology, Gaithersburg, MD 20899
⁵ Department of Materials Science and Engineering, University of Maryland, College Park, MD 20742
⁶ Department of Chemistry, University of Waterloo, Waterloo, ON, Canada, N2L3G1
⁷ Neutron Optics LP, Waterloo, ON N2L0A7, Canada

REFERENCES

[1] M. R. Eskildsen, *et al.*, *Nature*, **391**, 6667 (1998).
 [2] D. Sarenac *et al.*, *Phys Rev Lett*, **120**, 11 (2018).
 [3] D. Sarenac *et al.*, *Sci Adv*, **8**, 46 (2022).
 [4] C. Kapahi *et al.*, *Quant Beam Sci*, **7**, 10 (2023).
 [5] J. Schulz, *et al.*, *Nucl Instrum Methods Phys Res A*, **729**, 334 (2013).

Neutron Source Operations

PATH TO REACTOR RESTART

Following the fuel failure event of February 3, 2021, significant resources went into recovery, cleanup, and regulatory interactions. Cleanup of the reactor and primary system proceeded to a point where all identified material had been removed, from both the reactor vessel and primary system, but the possibility remained of trace amounts of unclad fissionable material still existing in the system. To address this, extensive analysis was done and a license amendment request to allow reactor operations with small amounts of fissionable debris present near the core was submitted to the Nuclear Regulatory Commission (NRC) on October 19, 2022. After several rounds of informal discussions and official responses to requests for additional information, this license amendment was approved on February 1, 2023.

In 2022, after considerable evaluations and inspections, the decision was made to not reuse any fuel elements that were present in the core during the fuel failure event. As a result, alternative fuel loading analyses were made to optimize core configurations using a combination of fresh fuel and 7-cycle elements that remained on site and available for use. As these analyses were different than those used for the original fuel management schemes (OFMS), another license amendment request was submitted to NRC to clarify required analyses for alternative fuel management schemes that would be needed for the initial core and subsequent cycles to get back to the equilibrium OFMS. This amendment request was submitted to NRC on February 1, 2023, with a request for exigent NRC processing. This amendment was approved on March 2, 2023.

In the 2 ½ years since the fuel failure event, NCNR personnel have submitted nine official reports to NRC, submitted four responses to requests for additional information, negotiated a lengthy confirmatory order, and submitted three successful license amendment requests. These efforts culminated in an NRC public meeting to discuss reactor restart, held at NIST on March 2, 2023. On March 10, NRC issued permission to restart the reactor. This was the first time that NRC had ever issued restart permission to a reactor that had exceeded a safety limit.

The reactor reached initial criticality on March 16, 2023. Low power testing proceeded throughout the spring and summer. Because of the remaining debris near the reactor core, increased levels of fission products were seen during operation. Although these levels were well below regulatory limits, short-term mitigation actions have been implemented to reduce the potential for personnel contamination and limit potential effluent releases. Several teams of engineers, operators, and health physicists have been formed to investigate longer-term actions to both limit the potential for fission product releases and attempt to further identify and remove remaining fissionable material near the core with the goal of achieving high power operation in 2024.



FIGURE 1: Senior Reactor Operators Jacob Seiter and Joshua Campbell preparing to insert a fuel element in preparation for restart, assisted by Ashton Dyson, Dominic Carratini, and David Griffin.

AUTOMATIC SHUTOFF OF CO₂ FLOW INTO CONFINEMENT UPON A MAJOR SCRAM

The NIST Center for Neutron Research (NCNR) is equipped with a Carbon Dioxide (CO₂) gas system used to minimize the amount of air exposed to the neutron flux around the reactor. The minimization of exposure is necessary due to the small amount of Argon in air, which would become radioactive. Ar-40 captures neutrons and transmutes into Ar-41, which is a radioactive isotope with a half-life of 1.83 hours and emits strong beta and gamma particles. The reduction of radioactive argon production is accomplished by purging the voids around the reactor structures with CO₂ gas. Any leakage of CO₂ gas from these voids is exhausted by normal confinement ventilation throughout the stack.

The incident on February 3, 2021, caused a major scram of the reactor automatically initiating actions to seal confinement and switch to a reduced emergency confinement ventilation alignment.

It did not, however, shutoff CO₂ gas flow into confinement. Since the building is sealed during major scram, additional gas flow leads to the buildup of CO₂ gas, creating an asphyxiation hazard. This was unexpectedly discovered by reactor operations staff attempting to perform reactor recovery tasks a few days after the incident.

After the conclusion of the NRC's investigation into the February 3, 2021, incident, the NRC's director of the Office of Enforcement released a confirmatory order based on an agreement made between the NCNR and NRC. As part of the response, the NCNR chose to implement an engineered solution that involved the installation of a new CO₂ shutoff valve in the A-wing basement, shown in Figure 2, that automatically secures CO₂ gas to the confinement building upon a major scram. The installation of this automatic shutoff valve ensures the flow of CO₂ gas into confinement is shut off upon a major scram reducing the possibility of an asphyxiation hazard. This project satisfied the confirmatory order's task well in advance of the deadline set by the NRC and is another important step on the path to reactor restart.



FIGURE 2: The newly installed CO₂ shutoff valve.

New NIST Neutron Source

The mission of the NCNR is to “Assure the availability of neutron measurement capabilities to meet the needs of U.S. researchers from industry, academia, and other government agencies.” The NBSR reactor at NIST first went critical in 1967. In the 55+ years since the facility has undergone multiple source, facility, and instrument upgrades to remain at the forefront of neutron research. In 1985 the NBSR was relicensed to double power (from 10 MW to 20 MW). NIST broke ground on a major cold neutron research facility in 1987 which led to a rapidly increasing demand from the research community as state-of-the-art cold neutron instruments came online throughout the 1990s. The performance also improved significantly from upgrades to the cold neutron source (CNS) in 1995 and 2002. In 2011, the cold neutron experimental area was nearly doubled, allowing the installation of five new beamlines serving seven additional instruments, and a small liquid hydrogen (LH₂) CNS was dedicated to the MACS instrument. Each improvement led systematically to an increased demand beyond available capacity from the scientific community. Since 1985, the number of participants in neutron research at the NCNR soared from a few hundred to nearly three thousand, leading to nearly 350 publications each year. This trend is expected to continue as NIST is currently preparing for the installation of a liquid deuterium (LD₂) CNS which will provide significant gains in the cold neutron spectrum below 5 meV and more than compensate for eventual conversion to low enrichment uranium (LEU). Concurrently, the three oldest cold neutron beamlines at the facility will be renewed and upgraded.

This impressive growth has occurred because neutron measurements play a key role in the discovery and development of new materials, advancing technologies that promise to improve the quality of life for all Americans. These areas include biopharmaceuticals, drug delivery systems, personal care products, advanced polymers, energy conversion and storage technologies, chemical production, and separation, advanced data storage systems, quantum information technologies, dissipation-free electronics, and advanced engineering materials such as those produced through additive manufacturing. In the era of big data, AI, and combinatorial materials synthesis, neutron scattering is a leading tool for guiding the design, discovery, and characterization of new materials. It is therefore not surprising that despite continual performance upgrades, the requested-to-available neutron beam time has increased to nearly 3. Overarchingly, the aging reactor requires longer outages and larger reactor maintenance expenditures to maintain safe and reliable operations. Some reactor components are not easily replaceable or serviceable, or they depend on obsolete technology.

Therefore, the central question of how NIST can best provide a source of neutrons into the future must be addressed. A 2018 assessment of the NCNR by the National Academies of Sciences, Engineering, and Medicine [1] recognized that *“Loss of this facility would have a strongly negative impact on neutron science within the United States and the scientific disciplines that the NCNR serves.”* Furthermore, *“NCNR should commission a detailed assessment of*

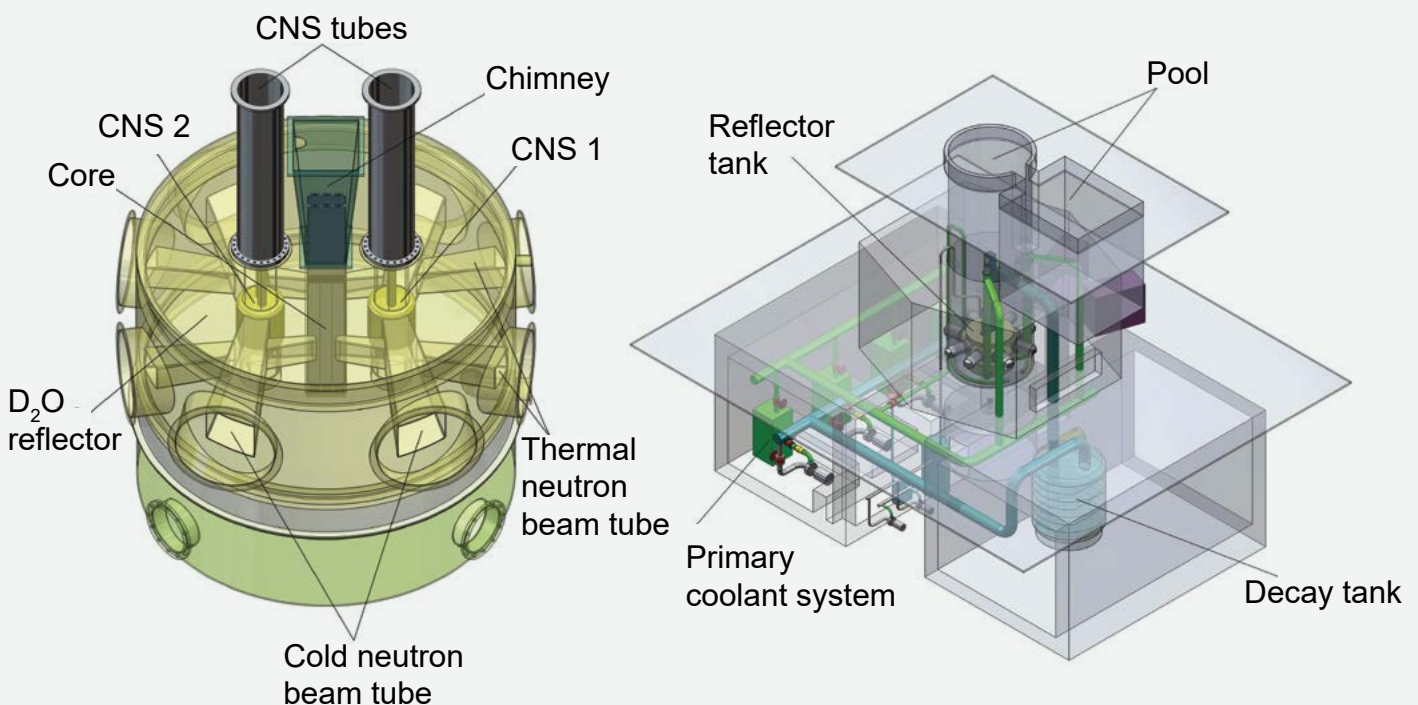


FIGURE 1: Isometric views of the present concepts of the NNS core (with two LD₂ CNSs) and the reactor building.

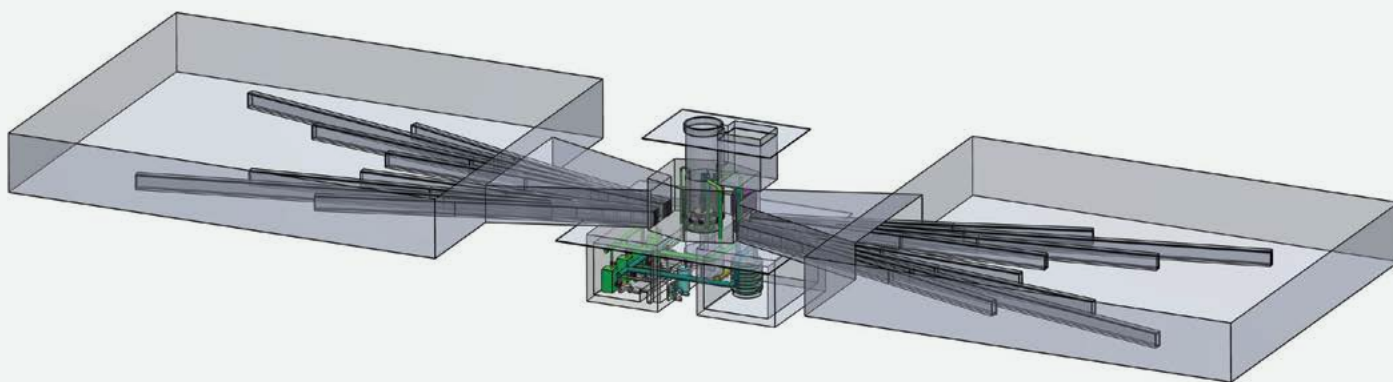


FIGURE 2: Conceptual facility layout with opposing cold neutron guide halls shown with 16 cold neutron guides viewing two CNSs. The reactor block is at the center. Thermal beams (not shown) emerge approximately perpendicular to the cold neutron beams.

the current facility and begin the conceptual design of a new reactor.”

The American Physical Society in their 2018 report [2] on neutron sources recommended: *“The United States should initiate an effort to competitively design and build a new generation of LEU-fueled [low-enriched uranium fueled] high-performance research reactors that would satisfy all needs presently met by current HEU-fueled [high-enriched uranium fueled] U.S. high-performance research reactors and provide new capabilities.”* Other recent reports that highlight the important contributions of neutron scattering and imaging techniques to a broad range of scientific disciplines and technology have been published by the U.S. Department of Energy (2020) [3] and the Swiss Academies (2021) [4].

Prior to these recommendations, a NIST study on future options for neutrons at NIST was already underway. The report of this study concluded that keeping the existing reactor operational is undesirable not only because of the long-term uncertainty in the condition of the reactor vessel and thermal shield but more importantly because it could not allow any further expansion of the neutron beams. A rehabilitated reactor would address the issue of aging management and may expand user facilities. However, the many unknowns involved with removing and replacing the reactor vessel and thermal shield, and the long downtime required make this option less desirable. The overall conclusion was that a replacement reactor is the best option to ensure a reliable neutron source at NIST over the long term. A new reactor located at NIST can be constructed while the current one continues to operate and would take advantage of the infrastructure and personnel in place at the NCNR with a proven track record of running a world-class and cost-effective neutron science facility. In anticipation of the need to plan for its replacement, NIST assembled a NIST/NCNR—Brookhaven National Laboratory (BNL) collaborative group to define top-level functions and requirements and to develop a pre-conceptual design of a replacement reactor and neutron scattering facilities.

Foremost, the reactor operation must be safe, reliable, and efficient with a high availability factor and built on a time scale that minimizes disruption to US neutron research. The current global nuclear policy also mandates the use of “low-enriched” uranium as the reactor

fuel. The design should promote straightforward maintenance, accessibility to serviceable components, and upgradability. A ground-up reconfiguration incorporating lessons learned from the design and facility layout of the NCNR and other installations around the world allow significant performance upgrades over the present facility. Importantly, these gains can be realized with a reactor design including established safety analysis models and construction solutions which are key to an efficient regulatory review, licensing, and construction process. An appealing option that satisfies these combined conditions is a forced-cooled reactor core in a pool with a heavy water reflector surrounding a compact core for optimum neutron delivery. The emphasis is on increasing both facility capacity and performance through optimized beam extraction, neutron optics, state-of-the-art instrumentation, and signal-to-noise enhancements which have the potential to produce order-of-magnitude gains, rather than increasing the reactor power, which typically generates gains that can only scale linearly, is less cost-effective, complicates the licensing process, and increases the scale and challenges associated with core heat extraction. As such, the present concept (dubbed the NIST Neutron Source, or NNS) (Fig. 1) would operate at 20 MW with a compact, light water-cooled 3×3 LEU fuel array surrounded by a heavy water-reflector tank containing two (vertically-introduced) LD₂ CNSs and beam tube penetrations. Tangential beam arrangements mitigate fast neutron and gamma contamination and twin CNSs in vertical thimbles greatly facilitate serviceability and upgradability over the present horizontal thimble arrangement of the NBSR.

An initial facility layout concept extracting cold neutron beams in opposing directions from each CNS, with thermal beams in an approximately perpendicular direction is illustrated in Fig. 2. From initial studies up to perhaps 50 cold and thermal neutron instruments could be accommodated with high-performance, low-background cold neutron guides, with additional end-positions provided by benders on side locations at multiple levels from tall guides, together with monochromatic beam positions.

The under-moderated compact core eliminates the compromises of the sparse NBSR fuel assembly array allowing the NNS CNS to be placed in, and thermal beams extracted from, regions much

closer to the thermal flux peak in the D₂O reflector (peak unperturbed thermal flux = $5.3 \times 10^{14} \text{ cm}^{-2}\text{s}^{-1}$) that are unincumbered by fuel assemblies. Unperturbed flux is assessed with the bare core and D₂O reflector without the beam penetrations and cold neutron sources. Conversely perturbed flux is assessed with these features introduced. This is illustrated in Fig. 3. Despite comparable simulated perturbed thermal flux peaks of about $3.55 \times 10^{14} \text{ cm}^{-2}\text{s}^{-1}$ (NBSR) and $3.63 \times 10^{14} \text{ cm}^{-2}\text{s}^{-1}$ (NNS), simulations based on an LD₂ CNS design predict a cold neutron ($< 5 \text{ meV}$) brightness 3.5 times greater for the NNS than currently available at the NCNR. Factoring in solid angle and illumination improvements of the cold neutron guide array yields an order of magnitude increase in transmittable cold neutron current is achievable at the same reactor power. Additional brightness gains are possible from moderate increases in the CNS vessel diameter and further intensity and signal-to-noise gains are achievable at the instruments with instrument-optimized neutron optics unlocking areas of research previously restricted by time and data quality constraints. Radiation heat load simulations confirm that the CNSs can be placed as close to the fuel as shown.

At initial startup (commissioning), the NNS would deliver measurement capabilities comparable to those of the existing NBSR neutron source by operating, at a minimum, one cold source delivering cold neutrons to one of the guide halls. Once both guide halls are fully operational, the facility would provide new measurement opportunities and substantially increase the neutron measurement capacity of the nation.

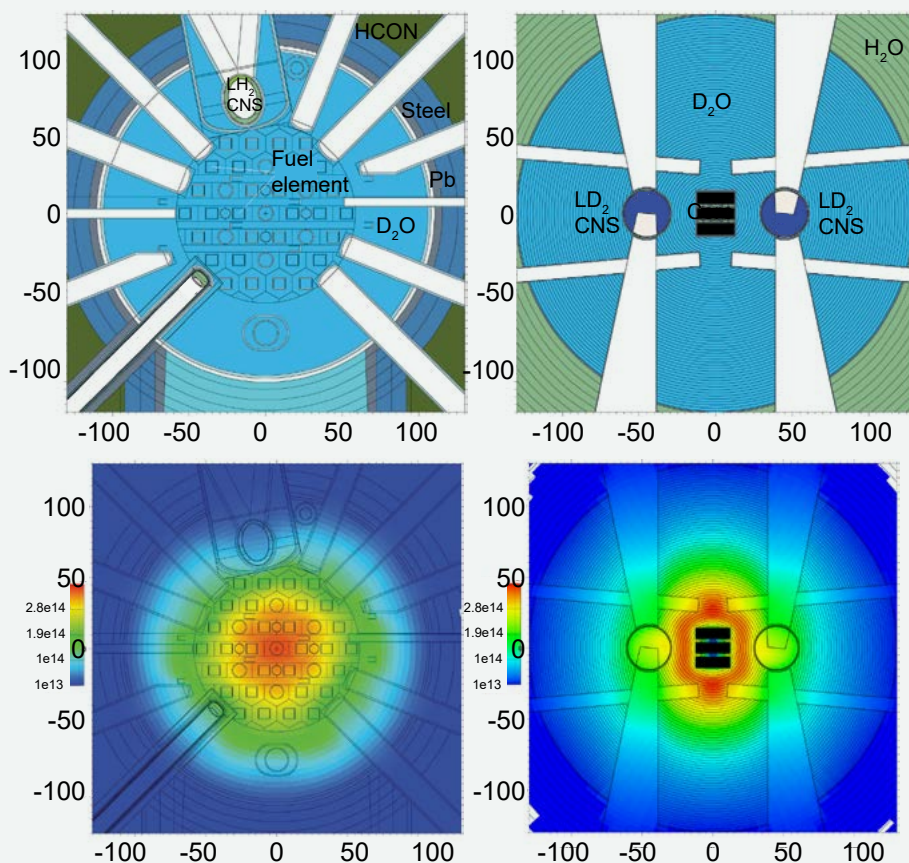


FIGURE 3: Top row: MCNP models for the NBSR (left) and NNS (right) shown on the same spatial scales. Center row: Thermal neutron flux ($< 300 \text{ meV}$) shown on the same spatial scales and normalized to the same intensity scale for ease of comparison. The horizontal and vertical scales are in cm.

REFERENCES

- [1] N. A. Sciences, "An Assessment of the Center for Neutron Research at the National Institute of Standards and Technology: Fiscal Year 2018," The National Academies Press, Washington, DC, 2018.
- [2] J. D. Wells, *Neutrons for the Nation: Discovery and Applications while Minimizing the Risk of Nuclear Proliferation*. American Physical Society Panel on Public Affairs, 2019.
- [3] Scientific Justification for a U.S. Domestic High-Performance Reactor-Based Research Facility, Report of the Basic Energy Sciences Advisory Committee, U.S. Department of Energy, Office of Science., 2020. [Online]. Available: <https://doi.org/10.2172/1647598>
- [4] Neutron Science Roadmap for Research Infrastructures 2025–2028 by the Swiss Neutron Science Community, Swiss Academies Reports, Vol. 16, No. 7, 2021. [Online]. Available: https://boris.unibe.ch/156933/1/327_Neutron_Science_Roadmap_2021.pdf

Facility Development

PROGRESS ON D₂ COLD SOURCE & GUIDE UPGRADES

NCNR is preparing for major upgrades to the cold source moderator and guide network that supply neutrons to guide hall instruments. Once complete, these upgrades will improve data rates on affected instruments by up to a factor of ten. Although this project is now delayed indefinitely to facilitate reactor operation following the unplanned reactor outage, work continues ahead of eventual execution. The first of two D₂ cryostats (one to install, one spare) is now onsite at NCNR, and is undergoing acceptance testing. All new shielding required for reactor confinement following the cold source replacement is now on-site, and shielding for post-replacement is now in fabrication. Further, all guides needed for confinement are on-site and pre-aligned. Post-confinement design work is proceeding, most notably for the new alpha-gamma 2.0 and upgrades for the neutron interferometry stations on NG-6, and for the imaging station and test beamlines on NG-7.

v-NSE

Installation work is progressing on v-NSE, a new neutron spin echo spectrometer. A collaboration among NIST, the University of Delaware's Center for Neutron Science, & the Julich Center for Neutron Science, and funded by the National Science Foundation, v-NSE will deliver significant gains in data rate, dynamic range, and maximum Fourier time as compared to the previous NIST NSE. All instrument components are now on-site, the airpad dancefloor has been poured, the new superconducting coils are tested and in-place, and integration of NICE instrument control software is largely finished. A plan for warm commissioning is in-place and will proceed as soon as neutrons are available.

INSTRUMENT ELECTRONICS

The CHRNS vSANS (very Small Angle Neutron Scattering) instrument features multiple detectors used to simultaneously characterize sample features corresponding to a broad range of lengthscales. Probing structures up to the mum level requires a high-resolution detector used for measurements at the smallest possible angles—the “v” in vSANS. The original vSANS high-resolution was not strictly a detector, instead it was a neutron camera that was plagued by readout calibration issues and other artifacts. This camera has now been replaced with a more conventional 20 cm x 20 cm ³He area detector that was originally used on the MAGik instrument at NCNR. That detector was refurbished for use at vSANS, installed, and successfully tested during low-power reactor testing operations.

POLARIZED BEAM

The NCNR supports an active program to develop and provide ³He neutron spin filters used for polarized neutron measurements. The vSANS polarization analysis apparatus has recently been adapted

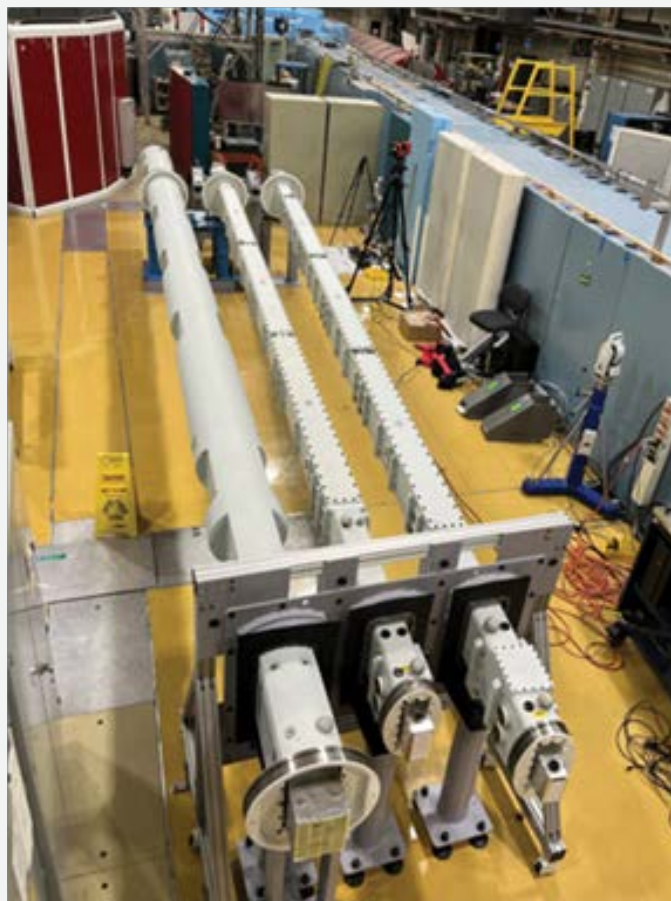


FIGURE 1: Top: Dan Adler and Raphael Erfe performing laser scan acceptance testing on the new D₂ cryostat. Bottom: Fully loaded and pre-aligned neutron guide 5, 6, & 7 penetration casings that will span the confinement building and guide hall walls.

to facilitate polarized beam measurements at low sample fields (< 58 mT). Two configurations are available, corresponding to the neutron polarization at the sample position aligned either parallel



FIGURE 2: v-NSE in Fall 2023, with superconducting coils and epoxy airpad dancefloor in place.

or perpendicular to the beam direction, and can be selected using the instrument control software NICE. Figure 4 shows the setup. Neutron spin transport was optimized with appropriate adiabatic spin rotator(s) and the relaxation time of the ^3He spin analyzer was optimized for user experiments. Other recent highlights include an upgrade of the sample field and neutron manipulation apparatus on the BT-7 Triple Axis Spectrometer, and integration of polarized beam capability into the NICE instrument control software on BT-7 and the CHRNS MACS Spectrometer.

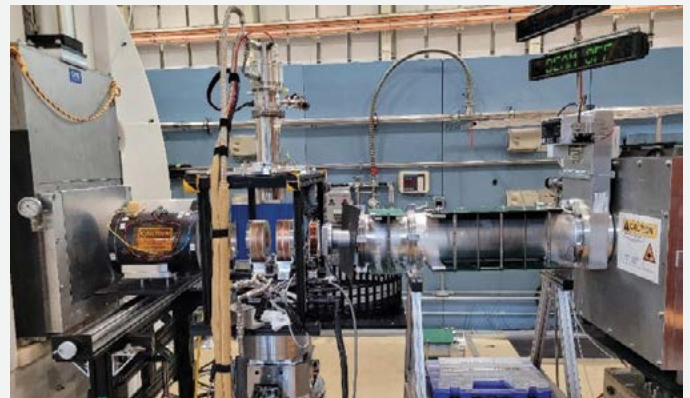


FIGURE 4: Low-field setup for full-polarization measurements at vSANS. Photo at top corresponds to sample field parallel to the beam direction, at bottom is for field perpendicular.

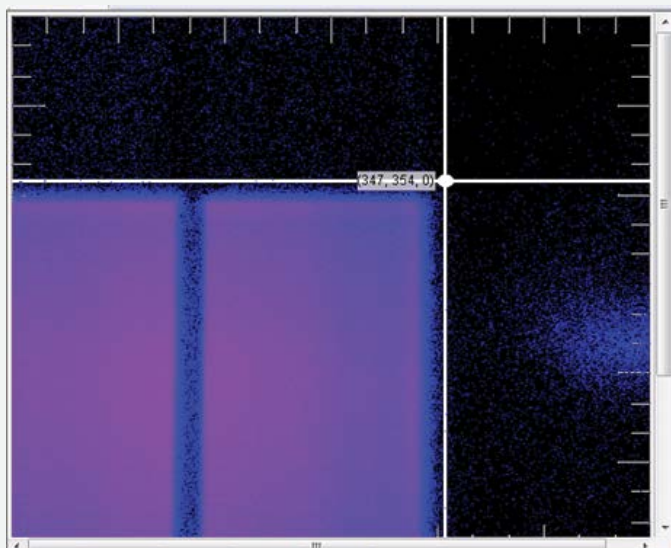


FIGURE 3: Test scan of the new high-resolution position sensitive detector at vSANS.

Serving the Science and Technology Community

The mission of the NIST Center for Neutron Research is to assure the availability of neutron measurement capabilities to meet the needs of U.S. researchers from industry, academia and other U.S. government agencies. To carry out this mission, the NCNR uses several different mechanisms to work with participants from outside NIST, including a competitive proposal process, instrument partnerships, and collaborative research with NIST.

PROPOSAL SYSTEM

Most of the beam time on NCNR instruments is made available through a competitive, peer-review CHRNS proposal process. The NCNR typically issues calls for proposals approximately twice a year. Proposals are reviewed at several different levels. First, expert external referees evaluate each proposal on merit and provide us with written comments and ratings. This is a very thorough process where several different referees review each proposal. Second, the proposals are evaluated on technical feasibility and safety by NCNR staff. Third, we convene our Beam Time Allocation Committee (BTAC) to assess the reviews and to allocate the available instrument time. Using the results of the external peer review and their own judgment, the BTAC makes recommendations to the NCNR Director on the amount of beam time to allocate to each approved experiment. Approved experiments are scheduled by NCNR staff members in consultation with the experimenters.

The BTAC members for the Call for Proposals issued in November 2020 are:

- Pinar Akcora (Stevens Institute of Technology)
- Andrew Allen (NIST Materials Measurement Laboratory)
- Jeffrey Allen (Michigan Technological University)
- Collin Broholm (The Johns Hopkins University)
- Leslie Butler (Louisiana State University)
- Sara Callori (California State University San Bernardino)
- Mark Dadmun (University of Tennessee)
- Kendra Elk (Purdue University)
- Kushol Gupta (University of Pennsylvania)
- John Heron (University of Michigan)
- Michael Hore (Case Western Reserve University)
- Hubert King (ExxonMobil—Retired)
- Valery Kiryukhin (Rutgers University)
- Kai Liu (Georgetown University)
- Martin Mourigal (Georgia Institute of Technology)
- James Neilson (Colorado State University)
- Olivier Soubias (National Institute of Health)
- Stephen Wilson (University of California Santa Barbara)

PARTNERSHIPS

The NCNR may form partnerships with other institutions to fund the development and operation of selected instruments. Partnerships are negotiated for a fixed period and may be renewed if there is mutual interest and a continued need. These partnerships have proven to be an important and effective way to expand the research community's access to NCNR capabilities.

COLLABORATION WITH NIST

Some time on all instruments is available to NIST staff in support of our mission. This time is used to work on NIST research needs, instrument development, and promoting the widespread use of neutron measurements in important research areas, particularly by new users. As a result of these objectives, a significant fraction of the time available to NIST staff is used collaboratively by external users, who often take the lead in the research. Access through such collaborations is managed through written beam time requests. In contrast to proposals, beam time requests are reviewed and approved internally by NCNR staff. We encourage users interested in exploring collaborative research opportunities to contact an appropriate NCNR staff member.

RESEARCH PARTICIPATION AND PRODUCTIVITY

The NCNR continued its strong record of serving the U.S. research community this year. Over the 2023 reporting year, the NCNR served 1407 researchers. (Research participants include users who come to the NCNR to use the facility as well as active collaborators, including co-proposers of approved experiments, and co-authors of publications resulting from work performed at the NCNR.)

NCNR PROPOSAL PROGRAM

INSTRUMENT CLASS	PROPOSALS	DAYS REQUESTED	DAYS ALLOCATED
SANS	274	999	487
Reflectometers	100	648	288
Spectrometers	297	1938	757
Diffraction	32	104	57
Imaging	20	92	38
Total	723	3781	1627

In response to the last two calls for proposals (calls 40 and 41) for instrument time, we received more than 723 proposals, of which 396 were approved and received beam time. The following table shows the statistics for several instrument classes. The oversubscription, *i.e.*, the ratio of days requested on all proposals to the days available, was 2.3 on average. Proposal demand has grown substantially since

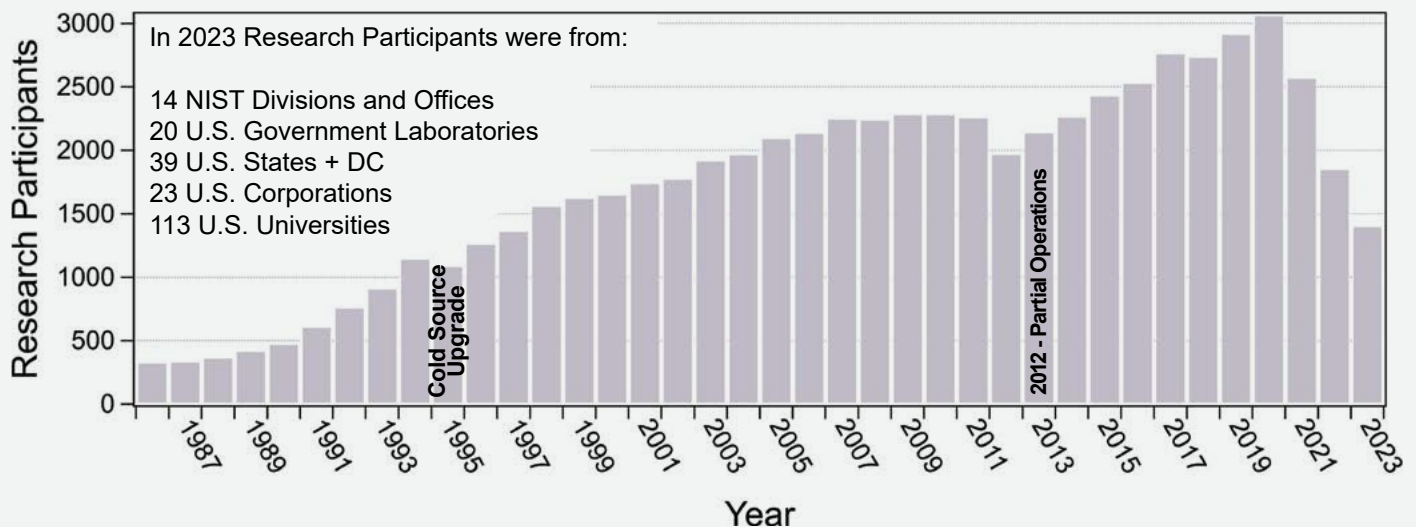


FIGURE 1: Research participants at the NCNR from 1986 to 2023. Fewer operational days in 2020, 2021, 2022, and 2023 due to COVID-19 closures and an unplanned shutdown resulted in reduced numbers of research participants.

the NCNR first began accepting proposals in 1991. Note that the experiments for call 41 will be run following the current outage. (Note that Imaging results from call 41 are not included in the totals.)

USERS GROUP

The NCNR Users Group (NUG) provides an independent forum for all facility users to raise issues to NCNR management, working through its executive officers to carry out this function. All members of the Executive Committee (EC) are elected by NCNR users. The current members of the NUG Executive Committee are Michael Hore (Chair, Case Western University), Jeffrey Richards (Vice Chair, Northwestern University), John Riley (The Dow Chemical Company), Dustin Gilbert (CHRNS Liaison, University of Tennessee), Kimber Stamm Masias (Toyota), Lily Motabar (Student/Postdoc Member, University of Delaware), and Efrain Rodriguez (University of Maryland).

The EC regularly solicits user feedback via a variety of means. The User Group held a well-attended meeting at the virtual American Conference on Neutron Scattering (ACNS) at the University of Colorado Boulder in June 2022 and plans to have another meeting at the ACNS in 2024. The EC also administers a brief email survey that is sent to users approximately one week after the completion of their experiment. Issues identified by the EC are regularly discussed with the NCNR and CHRNS management teams with a focus on resolving those requiring immediate action. The EC also conducted a comprehensive user survey in the winter of 2020. There were more than 160 responses, the majority of whom are CHRNS users. The results from the 2020 survey are posted on the NUG website (<https://nug.umd.edu/index.html>). Working closely with NUG, the NCNR and CHRNS management teams prepared an overview of the response/action plan to the 2020 survey designed to make the user experience more productive and enjoyable (Refer to https://nug.umd.edu/NCNRResponse_to_2020survey_Preamble%20final.pdf).

PANEL OF ASSESSMENT

The major organizational components of NIST are evaluated annually for quality and effectiveness by the National Research Council (NRC), the principal operating agency of both the National Academy of Sciences and the National Academy of Engineering. A panel appointed by the NRC convened on June 20–23, 2023. The panel members included Peter F. Green (National Renewable Energy Laboratory, chair), Ken Anderson (Oak Ridge National Laboratory), Pengcheng Dai (Rice University), Aaron P. Eberle (ExxonMobil), Rosario A. Gerhardt (Georgia Institute of Technology), Christopher R. Gould (North Carolina State University, emeritus), Andrew Harrison (Extreme Light Infrastructure ERIC), Andrew Jackson (European Spallation Source), Megumi Kawasaki (Oregon State University), Thomas K. Kroc (Fermilab), and Andrew T. Smolinski (Armed Forces Radiobiology Research Institute). The report from the previous 2021 Panel of Assessment entitled “An Assessment of the National Institute of Standards and Technology Center for Neutron Research: Fiscal Year 2021” is available at https://www.nist.gov/system/files/documents/2022/02/25/NIST_NCNR_2021_2_24%20final%20report.v2.pdf.

THE CENTER FOR HIGH RESOLUTION NEUTRON SCATTERING (CHRNS)

CHRNS is a national user facility that is jointly funded by the National Science Foundation and the NCNR. Its primary goal is to maximize access to state-of-the-art neutron scattering instrumentation for the research community. It operates five neutron scattering instruments at the NCNR, enabling users from around the nation to observe dynamical phenomena involving energies from ≈ 30 neV to ~ 10 meV, and to obtain structural information on length scales from ≈ 0.1 nm to ~ 3 μ m. A more detailed account of CHRNS activities may be found on page 61 of this report.

PARTNERSHIPS FOR SPECIFIC INSTRUMENTS

NG-7 SANS CONSORTIUM

A consortium that includes NIST, the ExxonMobil Research and Engineering Company, and the Industrial Partnership for Research in Interfacial and Materials Engineering (IPRIME) led by the University of Minnesota, operates, maintains, and conducts research at the 30m SANS instrument located on NG7. Twenty-five percent of the beam time on this instrument is allocated to the general scientific community through the NCNR's proposal system. Consortium members conduct independent research programs primarily in the area of large-scale structure in soft matter. For example, ExxonMobil has used this instrument to deepen their understanding of the underlying nature of ExxonMobil's products and processes, especially in the fields of polymers, complex fluids, and petroleum mixtures.

THE *n*Soft CONSORTIUM

Formed in August 2012, the *n*Soft Consortium allows member companies to participate with NIST in the development of advanced measurements of materials and manufacturing processes and develop their own expertise in state-of-the-art measurement technologies to include in their analytical research programs. *n*Soft develops new neutron-based measurement science for manufacturers of soft materials including plastics, composites, protein solutions, surfactants, and colloidal fluids. Members receive access to leading expertise and training support in neutron technology and soft materials science at NIST. Contact: Jonathan Seppala, *n*Soft Director, jonathan.seppala@nist.gov, 301-975-2836.

NIST/GENERAL MOTORS—NEUTRON IMAGING

An ongoing partnership and collaboration between General Motors and NIST, which also includes Honda Motors through GM's partnership with Honda, continues to yield exciting results using neutron imaging. Neutron imaging has been employed to visualize the operation of fuel cells for automotive vehicle applications. Neutron imaging is an ideal method for visualizing hydrogen, the fuel of electric vehicle engines. These unique, fundamental measurements provide valuable material characterizations that will help improve the performance, increase the reliability, and reduce the time to market introduction of the next generation electric car engines. 25% of the time on the BT-2 Neutron Imaging Facility is made available to the general scientific community through peer-reviewed proposals.

INTERAGENCY COLLABORATIONS

The Smithsonian Institution's Nuclear Laboratory for Archaeological Research is part of the Anthropology Department at the National Museum of Natural History. It has had a longstanding and productive partnership with the NCNR, during which time it has chemically analyzed over 43,100 archaeological artifacts by Instrumental Neutron Activation Analysis (INAA), drawing extensively on the collections of the Smithsonian, as well as on those of many other institutions in this country and abroad. Such chemical analyses provide a means of linking these diverse collections together in order to study continuity and change involved in the production of ceramic and other artifacts.

The Center for Food Safety and Applied Nutrition, U.S. Food and Drug Administration (FDA), maintains laboratory facilities at the NCNR providing agency-wide analytical support for food safety and food defense programs. Neutron activation and low-level gamma-ray detection techniques yield multi-element and radiological information about foods and related materials and provide a metrological foundation for FDA's field investigations and for radiological emergency response planning.

The Center for High Resolution Neutron Scattering (CHRNS)



The Center for High Resolution Neutron Scattering (<https://www.nist.gov/ncnr/chrns>) is a national user facility jointly funded by the National Science Foundation through its Division of Materials Research (grant number DMR-2010792) and by NIST. The CHRNS agreement was renewed for five years beginning on September 1, 2020. The mission of CHRNS is fourfold: (i) to develop and operate neutron scattering instrumentation, with broad application in materials research, for use by the general scientific community; (ii) to promote the effective use of the CHRNS instruments by having an identifiable staff whose primary function is to assist users; (iii) to conduct research that advances the capabilities and utilization of CHRNS facilities; and (iv) to contribute to the development of human resources through educational and outreach efforts. Simply put, CHRNS primary aim is “Maximizing access for the scientific community to transformative neutron scattering instrumentation.” A 2½ minute video, *Getting Great Data with CHRNS* (https://www.ncnr.nist.gov/staff/dimeo/CHRNS_Animation_Final.mp4), highlights and summarizes CHRNS’ focus on advancing neutron scattering measurement capabilities and its prominent role in expanding, educating, and diversifying the community of researchers who use neutron methods.

The scientific community provides essential input through a variety of mechanisms including user surveys, the most recent of which was administered by the NCNR User Group Executive Committee (EC) in 2020 (<https://nug.umd.edu/index.html>). The EC also led a well-attended discussion for neutron users at the recent American Conference on Neutron Scattering (ACNS) held on June 5–9, 2022 at the University of Colorado Boulder. Another meeting of the User Group is anticipated to be held during the next ACNS meeting in 2024. Users are also encouraged to provide input by directly contacting the CHRNS Director, Associate Director, NCNR Director, and/or members of the EC.

SCATTERING INSTRUMENTS

CHRNS provides robust user operations on the following premier neutron scattering instruments: a backscattering spectrometer (HFBS), the Multi-Axis Crystal Spectrometer (MACS), a neutron spin echo (NSE) spectrometer, a very small angle neutron scattering instrument (vSANS), and an innovative white-beam neutron reflectometer (CANDOR) with a unique multiplexing detector bank. Combined, CHRNS instruments can provide structural information on a length scale of 0.1 nm to ~3 microns, and dynamical information on energy scales from ~30 neV to ~10 meV.

The unique strengths of these premier instruments are complementary by design. Specifically, HFBS can resolve motions

with characteristic times of order a few nanoseconds. Since it offers the highest count rate with sub- μeV resolution in the US, it is an ideal choice for high resolution, quasi-elastic neutron scattering (QENS) studies of low-energy dynamics in polymers and biomolecules.

MACS boasts the world’s highest monochromatic cold-neutron flux and routinely is featured in transformative investigations of quantum magnetism. With its 20-detector analyzer array, MACS is well suited for surveys of large regions of reciprocal space, leveraging its exceptional polarized beam capabilities that incorporate a unique toroidal ^3He spin filter.

The NSE instrument provides the highest energy resolution of any neutron spectrometer in North America. It relies upon the Larmor precession of neutrons’ magnetic moments as an internal “clock” attached to each neutron allowing measurements of the final polarization of the neutrons to be directly correlated with the speed of the neutron. This modality results in data being obtained in the time domain rather than in the frequency domain. Fourier times as long as 300 ns (roughly corresponding to an energy resolution of 0.01 μeV) have been achieved for investigations of slow diffusive processes in a range of soft materials notably including polymer nanocomposites, biomembranes, and biopharmaceuticals. A complete upgrade of the NSE is underway with funding received by the University of Delaware, in collaboration with NIST, from the NSF Mid-Scale Research Infrastructure program (DMR-1935956). The new primary coils and detector will increase the maximum Fourier time achievable at a given wavelength by $> 2.5\text{x}$ and reduce count times by a factor of 10 for a given Fourier time.

For soft matter and magnetic structure characterization, the innovative vSANS instrument is meeting the emerging needs of the CHRNS user community. vSANS has a variety of front-end optics choices including three choices of wavelength resolution in addition to the traditional velocity selector and slit collimation as well as the standard pinhole geometry. Three separate, adjustable detectors yield an extended Q range from 0.002 to 7 nm^{-1} in a single instrument setting. The flexible sample area opens possibilities for sophisticated sample environments ranging from capillary rheometers to Peltier temperature blocks to high-field magnets. The 45m instrument can also be readily configured for GISANS (Grazing Incidence Small Angle Neutron Scattering) experiments. All these features can be used with full polarization analysis. These elements together provide unprecedented possibilities not only for structural characterization of materials, but also for time-dependent studies of complex hierarchical structures.

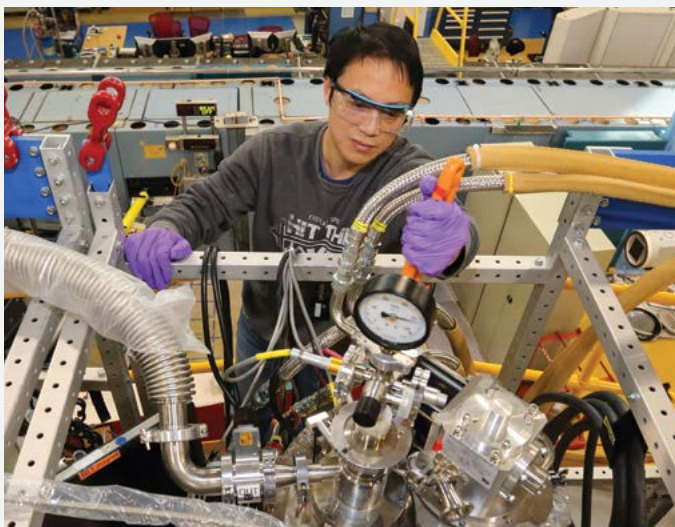


FIGURE 1: Alan Ye (CHRNS Sample Environment Staff) services a cryostat on the mezzanine of the DCS instrument.

A significant addition to the CHRNS instrument suite is CANDOR, which was included for the first time in the Call for Proposals in November of 2020. The novelty of CANDOR lies in its use of a state-of-the-art “energy-dispersive” detector system, which permits a polychromatic beam to impinge on the sample for measurements of either specular and non-specular reflectivity with or without polarized beams. A gain of ≈ 20 compared to the previous generation of neutron reflectometers in service at the NCNR has been realized, and reflectivities as low as 10^{-8} have been measured. This exceptional performance will enable unprecedented structural and kinetic characterization of complex materials from the nanoscale to the mesoscale.

RESEARCH

The wide range of instrument capabilities available in CHRNS support a very diverse scientific program, allowing researchers in materials science, chemistry, chemical engineering, biosciences, geosciences, and condensed matter physics to investigate materials such as polymers, metals, ceramics, magnetic materials, colloids, complex fluids and gels, rocks, and biomaterials. The research community can obtain access to the state-of-the-art CHRNS instrumentation using the CHRNS proposal system. Proposals to use the CHRNS instruments are reviewed on the basis of scientific merit and/or technological importance and broader impacts. In the most recent Call for Proposals in November of 2020, 311 instrument-days were awarded of the 887 days requested on the CHRNS instruments. These experiments will be run immediately following the current unplanned outage. Approximately $\frac{1}{3}$ of NCNR publications (see the “Publications” section on page 74), are based at least in part on research performed using these instruments. This report highlights several CHRNS publications. See the labeled highlights in the table of contents.

SCIENTIFIC SUPPORT SERVICES

CHRNS provides scientific support in the critical areas of sample environment and chemical laboratories. Specifically, CHRNS offers eight well-equipped and well-supplied user laboratories, including a Guide Hall Laboratory which provides a safe environment for CHRNS users to handle activated samples. The laboratory staff continues to make certain that the required equipment and/or supplies are available for users for their experiments.

The sample environment staff ensures that users have the equipment and training needed to make neutron measurements under external conditions of temperature, pressure, magnetic field, humidity, and fluid flow. From mK dilution refrigeration systems to a 1600 °C furnace, the equipment spans a large temperature range. CHRNS also provides access to a variety of flow systems, rheometers, gas-loading systems, superconducting magnets with fields of up to 11 Tesla, and other complex equipment to control parameters such as pressure, humidity, and electric fields. During the unplanned outage CHRNS staff has focused on revising and updating documentation as well as testing and improving the equipment. Ensuring that the available equipment is working and that our staff can support the users in different research areas is critical to guaranteeing continuity of support when the NCNR returns to service.

The procurement, development, and commissioning of sample environment is an essential part of the duties of CHRNS staff. A new power supply unit and polarity switch, purchased for vSANS, will improve the ability to control and stabilize the magnetic fields generated by the vSANS electromagnets. The new power supply provides much higher current precision and stability than previously available on vSANS. Remote control of the supply and switch will allow for a smooth transition from positive to negative field (and vice versa), an operation that could only be done manually at the beamline. These new functionalities will considerably improve the data collected over an extended field range for hysteretic magnetic materials.

As a sub-project of the CHRNS Initiative for the Non-Equilibrium Structure of Materials, a new sample rotation device has been commissioned for MACS to optimally double its count rate by constantly rotating the sample rather than stopping and starting motors. This system utilizes specialized control of the motors and time stamping of the data to provide 360-degrees bi-directional rotation with adjustable limits. It has a positional accuracy of the sample position that exceeds specification ($< 0.0016^\circ$) with a maximum rotation speed of ~ 4 deg/s tested with a 100g load. Overall, this project will enable continuous data collection during sample rotation, resulting in a more efficient neutron count duty cycle.

A new Julabo bath for the new Neutron Spin Echo was purchased and commissioned. This bath will allow users to reach both higher and lower temperatures than were available with the previous

system. CHRNS is also replacing obsolete compressors for our closed-cycle refrigerators to ensure that the systems are in optimal condition for CHRNS users.

INITIATIVE FOR NON-EQUILIBRIUM STRUCTURE OF MATERIALS

The development of new materials requires a deep understanding of how their properties change over time when they are subjected to external perturbations. To help achieve this goal, the Center for High Resolution Neutron Scattering (CHRNS) is developing new tools to study materials out of equilibrium (<https://www.nist.gov/programs-projects/chrns-non-equilibrium-structure-materials-initiative>). The program aims to enhance the nation's capabilities for using neutrons to study the evolution of materials in real time, under processing conditions, *etc.* This advance will enable scientists to study a wide range of phenomena, such as the charge and discharge cycles of batteries, the non-equilibrium structures of complex fluids under shear, the kinetics of reactions, and the formation of biomolecular complexes. With the advent of new neutron scattering instruments that provide enhanced data rates (vSANS, CANDOR, and MACS), the development of a flexible data acquisition system (NICE), and the potential to leverage machine learning, statistical analysis, AI, and automation, CHRNS is well-positioned to supply the advanced capabilities required to characterize materials out of equilibrium using neutron methods.

Specifically, CHRNS is in the process of implementing a systematic methodology for the absolute time-stamping of instrument and sample environment data. The aim is to couple the event-mode scattering data, which is collected with the NICE data acquisition software, with new sample environment capabilities (such as stopped-flow mixing) that are integrated with the same master clock. Since this initiative will also produce complex data sets that can be explored during and after the experiments, CHRNS is developing the data structures, hardware, and software required for facile manipulation and analysis of the data.

During the unplanned reactor outage, CHRNS staff have made substantial headway on advancing this endeavor toward its goals. This year we received the remaining hardware procurements to allow the neutron detection systems to conform to the absolute timing requirements. Implementation involved installing the commercial absolute-time stamping capabilities on MACS and the in-house developed Multipurpose Absolute Time Synchronizer Scaler Enabler (MATISSE) that interfaces with CANDOR and vSANS to assign detector pixel signals with absolute times. The communication standard of the absolute-timed data transmission system is based-upon the Accelerating Data Acquisition, Reduction, and Analysis (ADARA) specification of the Spallation Neutron Source and has been extended to incorporate real-time neutron detections, instrument parameters (motors, monitors), and sample environment

events into instrument networks where the events are ordered in time and stored.

CHRNS is implementing capabilities for time-structured databases and options for the high data-rates expected in which the events are ordered in time and include self-describing data schemas using Apache Kafka API-compatible software and scalable data stores ([Redpanda](#)). LabView-based absolute-time broadcasting has been deployed for slowly responding sample environments (magnets and temperature devices). CHRNS is working towards equipping these devices with plug-and-play capabilities through an implementation of the Sample Environment Communication Protocol (SECoP) in both LabVIEW and Python environments, and we are developing a single driver for NICE for all SECoP compatible hardware. Our current list of SECoP-aware systems includes the *in-house* [CHRNS stopped-flow apparatus](#), [CHRNS potentiostat](#), [CHRNS syringe pump](#), [gas-delivery systems](#), [CHRNS LIPPS](#), [CHRNS cryogenic goniometer](#), most high-field magnets, all He-3/dilution fridges, most closed-cycle and liquid helium cryostats using Lakeshore temperature controllers, and some aspects of rheometers (more work planned). This work is informing us how to reduce the barriers for users to bring their own equipment into the facility and quickly incorporate it into the neutron experimental workflow.

To advance CHRNS capabilities for NR and SANS data analysis, a composition-space modeling tool that builds biological and soft-matter interfacial structural profiles from real-space distributions of sub-molecular components has been developed using portable Jupyter notebooks. The molecular modeling approach directly uses molecular constraints such as volumes, scattering length densities, chemical connectivity, and stoichiometry. Different components, such as lipid bilayers and proteins, can be modeled to overlap each other as expected in real materials. Each subcomponent can also be selectively deuterated, allowing for an atomic-scale model for most biological interfaces using our Python library of lipid bilayers in combination with Protein Data Bank (PDB) structures or arbitrary functional forms. The library has been validated against published SANS data on lipid vesicles, as well as neutron and X-ray diffraction data for stacked lipid membranes.

Recognizing that scripting languages can be a barrier to using software, we made functionalities in the library of Jupyter notebooks available via Streamlit web applications. Starting with vSANS, CHRNS staff designed an app for data viewing, fitting, simulation, experimental optimization, and AI-enabled classification and regression (Figure 2). While the Python backend provides all capabilities behind the scenes, the app features only a minimal user interface, thereby significantly lowering the barrier to using the software. This application goes beyond the previously described biological materials and applies to any system that can be described using the models available in SASCalc, a submodule of [SASView](#).

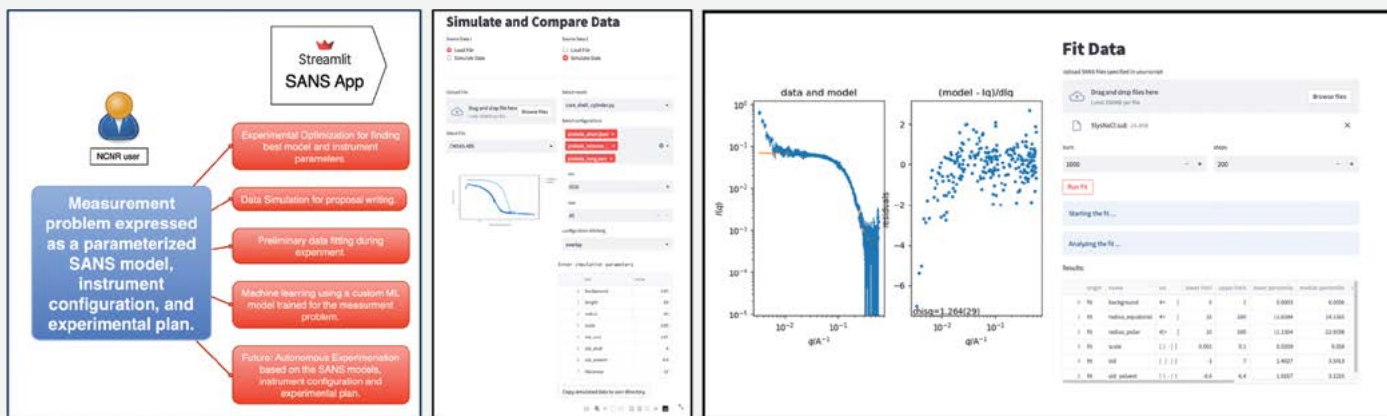


FIGURE 2: The SANS App running on the CHRNS computer clusters. Users can optimize an experiment and simulate or fit SANS data. A machine learning module can be trained for specific models and experimental configurations the user selects. The ML model can then be used on measured data to obtain an initial analysis or starting parameters for a model fit.

ADDITIONAL CHRNS EFFORTS DURING THE UNEXPECTED REACTOR OUTAGE

Proof-of-principle Monte Carlo simulations have shown that the data rate on CANDOR (and other instruments) could be doubled by applying Bayesian statistical analysis and information theoretical concepts. CHRNS has developed an active learning algorithm that chooses optimal next-measurement points along a trajectory to maximize the information content of the data (Figure 3). This algorithm is particularly well suited for deployment at neutron instruments, as it allows for parallel measurement and data processing such that the instrument is never idle. The software implementation is underway, and a publication is nearly submission-ready.

Further increases in the efficiency of data collection at CHRNS instruments are possible through automation of sample preparation and measurement. For CANDOR, CHRNS is developing a comprehensive [liquid handling sample changer](#) that can prepare several soft matter samples in parallel. The system is designed

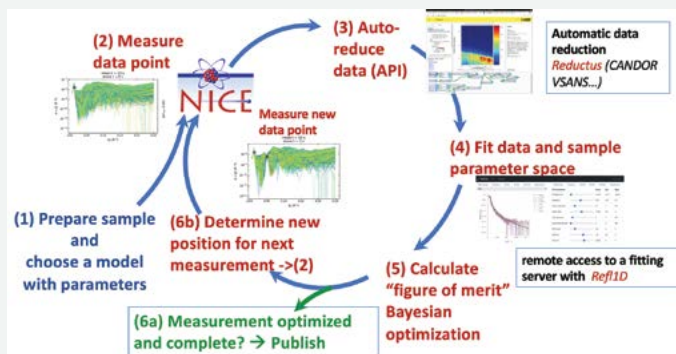


FIGURE 3: Flow diagram for active learning-driven data collection on CANDOR given common experimental systems that can be sufficiently well described by a model (1). A first data point is collected (2) and the data automatically reduced (3). The data is fit, and the model parameters are sampled (4) with the Bayesian optimization of where best to next measure determined (5, 6b). The cycle continues from step (2) until the measurement is deemed complete (6a), and the data and model best describing the data can be published.

with a central liquid handling robot and an auxiliary liquid handling system for each sample. CHRNS has implemented an external server to mediate between the liquid handling robot and external control software. Integration with the NCNR's instrument control software, NICE, is complete; however, the server can also be used in conjunction with active learning driven autonomous measurement engines that are under development. To further support efficiency improvements through automation, CHRNS staff are devising automatic data pipelines that include data collection, reduction, and analysis. In combination, these developments will allow for a fully automatic execution of a subset of experiments at CANDOR. By eliminating wait times due to sample preparation and repetitive user activities such as data reduction and analysis, users will be freed to make better informed real-time scientific decisions. In lieu of neutrons, the system is being prototyped in the lab using a quartz crystal microbalance (QCM) as the measurement device.

CHRNS staff has developed a new scripting interface for NICE to facilitate the deployment of larger modular experiment-control systems in which NICE can act as a subcomponent, whereas previously it was set up to act only as the master control system. Now external controllers can initiate a data-taking session in NICE, and then execute granular adjustments to the experiment environment through the NICE API, prior to each neutron-counting step of a measurement. Data files are written to existing archiving and metadata-extraction pipeline. This capability is critical to the functioning of our AI-guided experimentation and hybrid experiments in which the neutron measurement is carried out simultaneously with other techniques (X-ray, QCM, rheology, etc.) The new interface is currently in the early testing phase.

EDUCATION AND OUTREACH

CHRNS sponsors a variety of educational programs and activities tailored to specific student groups and professions. One of the premier outreach activities is the annual neutron school. During the past few years, the school has continued to attract graduate



FIGURE 4: Attendees and CHRNS Instructors at the 28th CHRNS Neutron School in October 2022.

students, post-docs, and junior professors with a wide range of expertise in areas such as chemistry, engineering, physics, materials science, and biosciences. Following the relaxation of NIST visitor regulations as COVID transmission levels subsided, the 28th Center for High Resolution Neutron Scattering (CHRNS) “School on Methods and Applications of Small Angle Neutron Scattering and Neutron Reflectometry” (October 17–21, 2022) was held in-person at the NCNR for the first time since 2019. The school attracted 41 students from 35 different universities and colleges with a diverse set of educational backgrounds. As with previous neutron schools, the school content was tailored to those with little or no previous experience with neutron scattering methods. It included introductory lectures along with hands-on analysis of data collected using neutron reflectivity and SANS. The school culminated with a mini symposium in which the students gave presentations highlighting their understanding of the data collection and analysis process for one of the featured experiments. The student feedback was very positive and emphasized the accessibility and knowledge of the course instructors.

In a return to the traditional summer timeframe, the next school, the 29th Center for High Resolution Neutron Scattering (CHRNS) “School on Methods and Applications of Neutron Spectroscopy” was held in-person from July 17–21, 2023. The school hosted five experiments, each associated with a different spectroscopic technique, that were designed and run by NCNR instrument scientists. A total of 35 students attended the school from 17 states with research interest ranging from polymer science (26%), hard condensed matter (11%), material science (20%), and magnetic materials (17%) among

others. Each student took part in the three experiments that most closely matched their area of study. The school concluded with the traditional presentation session similar to the SANS/Reflectivity school in October 2022. As with the previous school, the feedback was very positive with the average student rating of 4.6 out of 5 for the spectroscopy school and 4.8 out of 5 for the SANS/Reflectivity school.

Throughout the year staff scientists participated in teaching courses on topics including scattering theory and techniques at nearby universities and at international and national schools. The sixth Fundamentals of Quantum Materials School and Workshop was held at the University of Maryland on January 16–19, 2023. The workshop, which was co-sponsored by CHRNS, brings together senior and junior scientists to address topics at the forefront of current research into quantum materials while also providing practical training for junior scientists. The specific topic of the sixth school was Moire heterostructures. Nick Butch (NCNR Instrument Scientist) co-organized the event which included 35 graduate student/post-doc participants and featured a tour of the NCNR.

Yun Liu (CHRNS vSANS Instrument Scientist), Antonio Faraone (CHRNS Spin Echo Instrument Scientist), Michihiro Nagao (CHRNS Spin Echo Instrument Scientist), Minh Phan (Spin Echo Upgrade Instrument Scientist), and Susana Marujo Teixeira (SANS Instrument Scientist) taught a credited course on SANS for graduate students at the University of Delaware in the spring of 2023. The semester-long neutron scattering course covered both SANS and QENS techniques for soft matter researchers and consisted of two lectures and a recitation each week with periodic homework and quizzes. Students also traveled to the NCNR on April 25, 2023 for a tour



FIGURE 5: Nick Butch (DCS Instrument Scientist) helps students from the Fundamentals of Quantum Materials School and Workshop explore the optics of the new elliptical guide for the future PoLAR instrument.

of the confinement building and the guide hall. NCNR scientists Frank Heinrich (MAGIK Reflectometer Instrument Scientist), Hui Wu (Powder Diffractometer Instrument Scientist) and Jacob LaManna (Imaging Instrument Scientist) then gave three lectures about the applications of different instruments.

On May 1, 2023 Rebecca Dally (Thermal Triple Axis Instrument Scientist) with the assistance of William Ratcliff, Yang Zhao, and Jeffrey Lynn (NCNR Condensed Matter Physics Team Leader) led a one day workshop at the NCNR for Swarthmore College undergraduate students enrolled in the college's PHYS 135 condensed matter physics course. The workshop consisted of a series of lectures on neutron scattering and a tour. Additional staff also participated in a lunch time career panel for the students. The online webinar+workshop on "Scattering Techniques for Soft Matter Characterization" was sponsored by the Soft & Active Matter Materials Lab at Koc University on May 12–13, 2022. The speakers featured in this event included Yun Liu (CHRNS vSANS Instrument Scientist), Frank Heinrich (MAGIK Reflectometer Instrument Scientist), Yimin Mao (SANS Instrument Scientist), Susana Marujo Teixeira (SANS Instrument Scientist), and Antonio Faraone (CHRNS NSE Instrument Scientist).

Daniel Hussey (Cold Neutron Imaging Instrument Scientist) co-organized the 3rd ISRD-RCN (*In-situ* Studies of Rock Deformation-NSF Research Coordination Network) Workshop entitled "Exploring Dynamic Properties of Earth and Planetary Materials Using Neutron Scattering and Imaging" from July 25 to 27, 2023 at the University of Maryland for 38 participants. Multiple NCNR staff members delivered talks during the workshop including Brian Kirby (Research Facility Operations Group Leader), Yun Liu (CHRNS vSANS Instrument Scientist), Juscelino Leao (CHRNS User Services Team Member) and Jacob LaManna (Imaging Instrument Scientist). Participants also took part in a tour of the NCNR during the first day of the workshop.

In 2023, several NCNR staff members also delivered instructional lectures on neutron scattering at universities. Brian Kirby (Research Facilities Operations Group Leader) delivered a talk entitled "Intense Neutron Beams at NIST for Materials Science" on February 8, 2023 as part of the Rochester Institute of Technology's College of Science Distinguished Speakers Series. On April 24, 2023 Craig Brown (NCNR Structure and Dynamics of Materials Team Leader) gave a lecture to 25 attendees at Iowa State University that provided a general introduction to neutron scattering for graduate students. Jeff Lynn (NCNR Condensed Matter Physics Team Leader) gave a lecture entitled "Science and Technology with Neutrons" to 60 attendees of the Sigma Pi Sigma meeting at Towson University on May 5, 2023. Between July 17–19, 2023 Jeff Lynn also led neutron scattering tutorials for approximately 20 participants in the condensed matter physics group at Witwatersrand University in Johannesburg, South Africa. Finally, two NCNR staff members gave lectures on neutron scattering at the 25th National School on Neutron and X-ray scattering held at ORNL from August 6–18, 2023. William Ratcliff (Triple Axis Instrument Scientist) delivered a talk on single crystal diffraction and Chuck Majkrzak (NCNR Surfaces and Interfaces Team Leader) provided an introduction to neutron reflectometry.

As part of its education and outreach effort, CHRNS allows university-based research groups with BTAC-approved experimental proposals to request travel support for an additional graduate student to participate in the experiment. This support is intended to enable new graduate students, for example, to acquire first-hand experience with a technique that they may later use in their own research. Announcements of this program are sent to all university groups whose experimental proposals receive beam time from the BTAC. Recipients of the announcement are encouraged to consider graduate students from under-represented groups for this opportunity. The program is also advertised on the NCNR's website at <https://www.nist.gov/ncnr/chrns/travel-support>. This program is also available for a limited number of travel awards to enable graduate students or post-docs to attend NCNR workshops or related CHRNS-sponsored events.

CHRNS supports universities seeking an NSF INTERN supplemental grant which allows them to station graduate students at NIST for an extended period. This opportunity helps educate the student on neutron scattering to become successful facility users. There have been three recipients who recently sent students to work at the NCNR. Donghui Zhang from Louisiana State University obtained the supplemental grant for her research on structures in amphiphilic coil-comb block copolymers, and her student (Meng Zhang) was at NIST in 2020 and will return upon reactor restart. It is notable that Prof. Zhang recently received a second grant, and she will soon send another student. In addition, Carol Korzeniewski at Texas Tech and Shelly Minter from the University of Utah obtained support for a student to apply neutron reflectometry to polymer electrolytes. Their student (Miharu Koh) from the University of Utah, began her internship in August 2022 and will visit NIST periodically for



FIGURE 6: 2023 CHRNS SURF and CORE summer undergraduate interns.

experiments throughout the remainder of 2023. Marcus Foston from Washington University in St Louis won an award to work on catalyzing lignin depolymerization. He sent two students (Jialiang Zhang, and Jingwen Luo) to the NCCR during the summer of 2023.

For 11 weeks in the summer of 2023, CHRNS participated in NIST's Summer Undergraduate Research Fellowship (SURF) program by hosting ten SURF students (eight in-person, one remote and one hybrid). The students performed research on topics ranging from surfactant-preservation aggregation in biopharmaceutical formulations, to spin texture and domain walls in Weyl semi-metals. SURF student Navid Misaghian from the University of Maryland wrote about his project and experience as a SURF student on the [NIST Taking Measurement Blog](#). The students gave oral presentations describing their work at the NIST SURF colloquium in early August 2023 moderated by Dr. Guebre Tessema, a program director for CHRNS from the National Science Foundation. The colloquium featured a plenary talk by Ethan Gasper from George Mason University entitled "Effects of Solvents on the Assembly of Nanoparticles from Poly(styrene-bethylene glycol)." It is also notable that former SURF students Lizbeth Quigley, Paul Neves, Mark Zic, Kate Meuse, Jessica Opsahl-Ong, Emily Blick, and Carrie Stemple were all co-authors on [seven publications published during this reporting period](#).

CHRNS is pleased to announce the launch in late June 2022 of the new CHRNS Outreach and Research Experience (CORE) program. CORE is a paid internship program that provides undergraduate students with hands-on research and engineering experience under the mentorship of one or more NCCR staff members. CORE has an emphasis on retaining underrepresented groups in STEM and



FIGURE 7: Christopher Stallard, CHRNS CORE student, calibrates the new stopped flow set up at vSANS

is more versatile than a standard summer internship with flexible start and end dates throughout the academic year. The first two CORE interns, both of whom started on October 1, 2022, have now completed their hybrid internships. In addition, CHRNS successfully leveraged the flexibility of the newly launched program to host an additional ten undergraduate students for internships during the summer of 2023. Overall, seven of the twenty SURF and CORE projects this year were hosted by the reactor operations group, which has expanded CHRNS reach to include students with interests more aligned with engineering.



FIGURE 8: 2023 CHRNS SHIP students

CHRNS initiated a Research Experiences for Teachers (RET) program in 2010. Unfortunately, CHRNS was unable to host RET participants on-site during the summer of 2022 due to access restrictions. In 2023 an engineering teacher, Zachary Vaz, from Walt Whitman high school in Bethesda, MD participated in a RET project entitled “High Pressure (HP) Small Angle Scattering Studies on Biomolecular Solutions” under the tutelage of Susana Marujo Teixeira (SANS Instrument Scientist) and Cedric Gagnon (CHRNS SANS Instrument Associate).

The Summer High School Intern Program (SHIP) is a successful, competitive NIST-wide program for students who are interested in performing scientific research. In the summer of 2023 CHRNS hosted six in-person interns from local high schools, two of whom

returned from last summer. The students’ projects included writing a remote interface for developing user models for small angle scattering data, using machine learning for anomaly detection in sample refrigeration systems, and determining sample crystal structure with reinforcement and machine learning. The results of the students’ summer investigations were highlighted in a NIST-wide poster session, as well as in a well-attended symposium at the NCNR in mid-August. Notably, two of the SHIP students will extend their project over the next school year as part of a yearlong high school research class.

The annual Summer Institute for Middle School Science Teachers, sponsored by NIST, is designed to provide middle school science teachers from across the United States with a better understanding of the scientific process. Though the Institute was recently run in a virtual format in response to COVID, middle school teachers returned to the NIST campus this summer for a two-week hybrid experience. This year the Summer Institute included sixteen in-person and ten virtual participants from fourteen states. As part of the institute, CHRNS hosted the teachers on July 14, 2023 for a one-day introduction to neutron scattering with a presentation on how neutrons are produced and their use in understanding the atomic structure of materials. The teachers learned about the types of experiments performed using neutrons after having toured the neutron guide hall. They later engaged in an experiment to grow crystals of “alum” (hydrated aluminum potassium sulfate), a project suitable for middle school students. They also participated in an experiment and lecture designed to be taken back to their classrooms that described diffraction equations and then used laser pointers to generate light bands through a diffraction grating. Throughout the



FIGURE 9: Middle school teachers participate in a chain reaction demonstration during the Middle School Institute in July 2023.



FIGURE 10: Liquid nitrogen demonstration by NCNR staff, Juscelino Leao and Rodrigo Vilaseca, to South Lake Elementary School students as part of Career Day.

day, the teachers had the opportunity to interact with NCNR staff members and student interns. The feedback from the teachers is consistently positive.

Since access restrictions due to COVID-19 were eased during the past year, CHRNS was able to provide specialized tours and activities to various educational groups. Several of the tours were associated with local workshops, as described above, and examples of other tours are provided below. On September 1, 2022 Steven Dewey (Chief Health Physicist), Dan Neumann (CHRNS Director), Joseph Dura (MAGIK Reflectometer Instrument Scientist), and Bryan Remley (Health Physicist) led a tour for 25 attendees of a Health Physics Conference sponsored by NASA. The tour highlighted both scientific and health physics technical achievements of the facility. On January 11, 2023, Shannon Hoogerheide (BL2 Instrument Scientist) gave a tour to the two local middle school winners of the Broadcom Masters science competition. On April 20, 2023, Jeffrey Lynn (NCNR Condensed Matter Physics Team Leader) gave a tour to ten undergraduate students enrolled in Towson University's condensed matter class. On July 31, 2023 Paul Butler (NCNR Macromolecular and Microstructures Team Leader) organized and led a NIST-wide tour for 25 NSF-REU students working within the

MRSEC-funded Center for Hybrid Active and Responsive Materials (CHARM) and Center for Plastic Innovation Lab (CPI) at the University of Delaware. After touring the Atom Scale Device Group Lab in the NIST Biofoundry, the students' visit at the NCNR began with Jeff Lynn giving a lecture entitled "Science and Technology with Neutrons." Afterwards, the students broke into three tour groups led by John Barker (SANS Instrument Scientist), Megan Mitchell (NRC Postdoctoral Fellow), Caitlyn Wolf (NRC Postdoctoral Fellow), and Jeff Krzywon (NCNR SANS Instrument Associate). The tour consisted of five stops at cold neutron imaging (Jacob LaManna, Imaging Instrument Scientist), neutron depth profiling (Jamie Weaver, Depth Profiling Instrument Scientist), 10m SANS (Tyler Martin, *n*Soft Instrument Scientist) and the SPINS triple axis spectrometer (Rebecca Dally, Triple Axis Instrument Scientist).

CHRNS staff members typically give science-based talks or lead hands-on activities and demonstrations, either in-person or virtual, for local K-12 schools. Chuck Majkrzak (NCNR Surfaces and Interfaces Team Leader) and Przemek Klosowski (NCNR IT Specialist) mentored the FIRST Robotics Club at St. Johns College High School, during the 2022-23 academic year for approximately 25 to 35 students at all grade levels from freshman to senior.

In addition, Yimin Mao (SANS Instrument Scientist) staffed a biopolymer-themed booth sponsored by the Department of Materials Science and Engineering at the University of Maryland College Park during their annual Maryland Day celebration on April 30, 2022. The event was open to the entire community and “dedicated to learning, discovery, and new ideas.” Dan Neumann (CHRNS Director), Donald Pierce (Engineering Team Leader), and John Barker (SANS Instrument Scientist) co-organized bi-weekly mentoring for an engineering class at Richard Montgomery High School from January 1–May 5, 2023. In this class, 42 students worked on developing an engineering project. Zoom meetings were held between these students and 16 NCNR staff in which they listened and gave advice to the students on their projects. On May 16, 2023, Brian Kirby (Research Facility Operations Group Leader) participated in a virtual interview with science students at St. Mary’s Colgan High School. Lastly, on May 17, 2023, Juscelino Leao (CHRNS User Services Team Member) and Rodrigo Vilaseca (Engineering Group Member) gave a career day presentation to 68 students at South Lake Elementary School with a < 90% minority student body, the presentation included several liquid nitrogen experiments to show students what happens when objects get very cold.

BROADENING PARTICIPATION IN STEM

Since direct outreach has proven to be an effective means to attract users, CHRNS pursues many avenues for engaging institutions that serve diverse groups. Specific activities include PREM and CREST partnerships. Specifically, a partnership with the Interdisciplinary Materials Research and Education Laboratory (IMREL) at Fayetteville State University (FSU) was established in August 2018 through the NSF PREM (Partnerships for Research and Education in Materials) program (Agreement No. DMR-1827731). The [PREM](#) supports cutting-edge materials research as the context for producing motivated and skilled members of those groups most underrepresented in materials research as future professional leaders. This partnership is organized around a common theme of structure-processing-property correlations of nanomaterials to support student training in research using neutron scattering.

On October 28, 2022, Hui Wu (NCNR Powder Diffraction Instrument Scientist) gave a virtual seminar entitled “Neutron Diffraction and its Applications for Structural Investigation of Energy Materials” for FSU PREM participants. Dr. Wu’s talk was followed by informal discussions of recent results in her collaborative project with FSU researchers. In the October of 2022, post-doc Navadeep Shrivastava participated in the CHRNS neutron school. Finally, in 2023, a PREM graduate student, Menuka Adhikari, has been accepted into the 29th CHRNS Neutron School which will be held in July and a PREM undergraduate, Thomas Murray, is currently participating in a summer internship as part of the recently launched CORE program for undergraduates.

Overall, CHRNS has been proactive in efforts to encourage researchers from these and other MSI’s to pursue research opportunities with CHRNS scientists at neutron facilities around the world through collaborative development of competitive beamtime proposals. CHRNS is engaged in a partnership with California State University, San Bernardino within the NSF CREST (Centers of Research Excellence in Science and Technology) program as part of their new Phase II Center for Advanced Functional Materials (HRD-1914777). Recently, Morgan State University submitted a successful CREST proposal that highlighted partnership opportunities with CHRNS, and a meeting was held on June 7th 2023 between MSU CREST and NCNR staff to discuss the potential for future collaborations. Lastly, the NCNR instrument scientist William Ratcliff, is an advisory board member for the new CREST Center for Research and Education in Quantum Leap Science and Technology that was established at Norfolk State University in 2021.

2023 Awards



Dan Neumann has received the **2022 NIST Distinguished Mentoring Award**. Dan was recognized for his exemplary service to NIST through selfless dedication to the mentoring of staff and users at the Center for Neutron Research.



Ryan Murphy and Kathleen Weigandt of the NCNR along with Paul Salipante (MML) and Steven Hudson (MML) were awarded a **2022 Department of Commerce Bronze Medal**.



The group is recognized for the simultaneous measurement of molecular structure and rheology in complex fluids at the extreme shear rates routinely applied in modern manufacturing.



Paul Butler received a **2022 Department of Commerce Silver Medal**. Paul was recognized for his global leadership in developing the world's leading software for analyzing small-angle-scattering data, which is now used by thousands of researchers worldwide.



Julie Borchers of the NCNR received the **2022 NIST Distinguished Mentoring Award**. Julie is recognized for her tireless mentorship of early-career scientists at NIST.



The team of **Nicholas Maliszewskyj, Kevin Pritchard, Jeffrey Ziegler, Charles Majkrzak, Jean Philippe Chabot, and Ed Binkley** of the NCNR was awarded a **2022 Department of Commerce Silver Medal**. The team is recognized for developing a neutron detector less than 2 mm thick that is over 90% efficient yet exhibits an exceptionally high signal to noise ratio.



Congratulations to the NCNR's **Alex Grutter** who has been recognized by NIST's chapter of Sigma Xi as the **2023 Katharine B. Gebbie Young Scientist Awardee**. The award highlights Alex's work in the use of neutron and X-ray scattering to "greatly advanced our understanding of topological, ionic, multiferroic, and related magnetic nanomaterials."



Nick Butch of the NCNR has been named a **2023 APS Fellow** by the American Physical Society. Nick was cited "For extraordinary and wide-ranging contributions to the synthesis and experimental study of exotic superconducting, magnetic, and topologically nontrivial quantum materials."



The NCNR's **Alan Ye** was recognized by the NIST chapter of Sigma Xi with the **2022 Outstanding Service in Support of NIST Scientists** "For technical excellence and superb dedication going above and beyond in support of the NCNR and neutron users."



Professor **Rachel Seagelman** of the Department of Chemical Engineering at the UC Santa Barbara has won the **Andreas Acrivos Award for Professional Progress in Chemical Engineering**. Rachel is being recognized for pioneering studies of functional soft materials, including semiconducting block polymers, polymeric ionic liquids, and hybrid thermoelectric materials. Her research has made use of the NCNR facilities.



Michael Huber of NIST's Neutron Physics Group has been recognized with the **Arthur S. Flemming Award**, administered by The George Washington University's Trachtenberg School of Public Policy and Public Administration. Michael is being recognized for a host of important scientific applications of neutrons to fundamental problems in basic science, including novel contributions to quantum information science, the application of high-precision neutron scattering-length measurements to benchmark nuclear models, and for the first direct measurement of the neutron charge radius using neutron interference.



Alannah Hallas, Assistant Professor in the Department of Physics and Astronomy at the University of British Columbia has won the **2023 IUPAP Early Career Scientist Prize** in the field of Magnetism. Alannah is being recognized "for outstanding contributions to the discovery of magnetic quantum materials through advanced synthesis methods." Alannah is a frequent user of the NCNR.



Frank Bates, Regents Professor in the Department of Chemical Engineering and Material Science at the University of Minnesota won the **ACS Award in Applied Polymer Science**, sponsored by Eastman Chemical. The national awards encourage the advancement of chemistry in all its branches, support research endeavors, and promote the careers of chemists. Frank is a long-time user of the NCNR facilities.



Michelle Calabrese, Assistant Professor in the Department of Chemical Engineering and Materials Science at the University of Minnesota has been recognized with the **AICHE 35 Under 35 Award**. She has also been recognized as **2023 PMSE Early Stage Investigator** by the American Chemical Society (ACS) Division of Polymeric Materials: Science and Engineering (PMSE). Finally, she has also been selected for the **2023 UKPPG/DPOLY Polymer Lecture Exchange** through the American Physical Society (APS). As a graduate student, Michelle was stationed at the NCNR and her subsequent research has made frequent use of the NCNR.



Professor **Richard Weiss** of the Department of Chemistry at Georgetown University was awarded the **2022 Hillebrand Prize** by the Chemical Society of Washington. Richard is recognized for his contributions to an understanding of the relationship between structure, function and the chemical and photophysical properties of polymers and gels. Richard is a long-time user of the NCNR.



Julie Hipp, Jeff Richards, and Norm Wagner were recognized with the **2023 Best Paper Award** from the Journal of Rheology for their paper “Direct measurements of the microstructural origin of shear-thinning in carbon black suspensions.” Julie was stationed at the NCNR as a graduate student, Jeff was a post-doctoral researcher at the NCNR, both working with Norm at the University of Delaware.



Ellie Clements won the **Best Poster Award** at the 2023 ORNL Neutron Scattering User Meeting held at ORNL in June 2023. Her poster was titled “Intriguing magnetism in the chiral lattice antiferromagnet CoNb_3S_6 .” Ellie is a former NCNR post-doctoral fellow.



Julia Greenfield who received an **Outstanding Poster Award** in the area of Biosciences, Chemistry, and Mathematics at the 30th Annual Sigma Xi Early-Career poster presentation. Her poster was entitled “Characterization of freeze-induced transient high-molecular-weight (HMW) species in BiTE solutions.” Julia was a postdoctoral researcher at the NCNR.



Congratulations to **Corey Frank** who won the **Most Outstanding Poster Award** in the area of Physics, Engineering, and Computer Science at the 30th Annual Sigma Xi Early-Career poster presentation. Her poster was entitled “Understanding unconventional superconductivity in very high magnetic fields.” Corey is a post-doctoral fellow working with the NCNR’s Nick Butch.



Sarah Robinson, a post-doc from PML working on the far-field interferometry IMS project, received an **Outstanding Poster Award** at the 30th Annual Sigma Xi Early-Career poster presentation. She won the award in the area of Physics, Engineering, and Computer Science for her poster entitled “Development of a 5,000+ channel microfluidic dynamic source grating device for neutron interferometry.”

Publications: August 1, 2022 to July 31, 2023

- Abitaev, K., Atanasova, P., Bill, J., Preisig, N., Kuzmenko, I., Ilavsky, J., Liu, Y., Sottmann, T., "In Situ Ultra-Small- and Small-Angle X-ray Scattering Study of ZnO Nanoparticle Formation and Growth through Chemical Bath Deposition in the Presence of Polyvinylpyrrolidone," *Nanomaterials-Basel* **13**(15), 2180 (2023). DOI: [10.3390/nano13152180](https://doi.org/10.3390/nano13152180) [CHNRNS]
- Acharya, G.R., Tyagi, M., Mamontov, E., Hoffmann, P.M., "Diffusion Dynamics of Water and Ethanol in Graphene Oxide," *J. Phys. Chem. B*, in press. DOI: [10.1021/acs.jpcc.2c08960](https://doi.org/10.1021/acs.jpcc.2c08960) [CHNRNS]
- Adawi, H., Bhattarai, S., Lussier, J.-G., Krycka, K., Schroeder, A., "Revealing Magnetic Correlations in Ferromagnetic Alloys with Polarized SANS," *J. Phys. Conf. Ser.* **2481**, 012001 (2023). DOI: [10.1088/1742-6596/2481/1/012001](https://doi.org/10.1088/1742-6596/2481/1/012001) [CHNRNS]
- Aishwarya, A., May-Mann, J., Raghavan, A., Nie, L., Romanelli, M., Ran, S., Saha, S.R., Paglione, J., Butch, N.P., Fradkin, E., Madhavan, V., "Magnetic-Field-Sensitive Charge Density Waves in the Superconductor UTe_2 ," *Nature* **618**(7967), 928 (2023). DOI: [10.1038/s41586-023-06005-8](https://doi.org/10.1038/s41586-023-06005-8)
- Amayuelas, E., Tortora, M., Bartolomé, L., Littlefair, J.D., Paulo, G., Le Donne, A., Trump, B., Yakovenko, A.A., Chorazewski, M., Giacomello, A., Zajdel, P., Meloni, S., Grosu, Y., "Mechanism of Water Intrusion into Flexible ZIF-8: Liquid is not Vapor," *Nano Lett.* **23**(12), 5430 (2023). DOI: [10.1021/acs.nanolett.3c00235](https://doi.org/10.1021/acs.nanolett.3c00235)
- Andrade, P.L., Silva, V.A.J., Krycka, K.L., Leão, J.B., Liu, I.-L., Silva, M.P.C., Albino Aguiar, J., "The Effect of Organic Coatings in the Magnetization of $CoFe_2O_4$ Nanoparticles," *AIP Adv.* **12**(8), 085102 (2022). DOI: [10.1063/5.0078167](https://doi.org/10.1063/5.0078167)
- Andriamirado, M., Balantekin, A.B., Bass, C.D., Bergeron, D.E., Bernard, E.P., Bowden, N.S., Bryan, C.D., Carr, R., Classen, T., Conant, A.J., Delgado, A., Diwan, M.V., Dolinski, M.J., Erickson, A., Foust, B.T., Gaison, J.K., Galindo-Uribarri, A., Gilbert, C.E., Gokhale, S., Grant, C., Hans, S., Hansell, A.B., Heeger, K.M., Heffron, B., Jaffe, D.E., Jayakumar, S., Ji, X., Jones, D.C., Koblanski, J., Kunkle, P., Lane, C.E., Langford, T.J., LaRosa, J., Littlejohn, B.R., Lu, X., Maricic, J., Mendenhall, M.P., Meyer, A.M., Milincic, R., Mueller, P.E., Mumm, H.P., Napolitano, J., Neilson, R., Nikkel, J.A., Nour, S., Palomino, J.L., Pushin, D.A., Qian, X., Roca, C., Rosero, R., Searles, M., Surukuchi, P.T., Sutanto, F., Tyra, M.A., Venegas-Vargas, D., Weatherly, P.B., Wilhelm, J., Woolverton, A., Yeh, M., Zhang, C., Zhang, X., "Calibration Strategy of the PROSPECT-II Detector with External and Intrinsic Sources," *J. Instrum.* **18**(6), P06010 (2023). DOI: [10.1088/1748-0221/18/06/P06010](https://doi.org/10.1088/1748-0221/18/06/P06010)
- Andriamirado, M., Balantekin, A.B., Bass, C.D., Bergeron, D.E., Bernard, E.P., Bowden, N.S., Bryan, C.D., Carr, R., Classen, T., Conant, A.J., Deichert, G., Delgado, A., Diwan, M.V., Dolinski, M.J., Erickson, A., Foust, B.T., Gaison, J.K., Galindo-Uribarri, A., Gilbert, C.E., Gokhale, S., Grant, C., Hans, S., Hansell, A.B., Heeger, K.M., Heffron, B., Jaffe, D.E., Jayakumar, S., Ji, X., Jones, D.C., Koblanski, J., Kunkle, P., Kyzlyova, O., LaBelle, D., Lane, C.E., Langford, T.J., LaRosa, J., Littlejohn, B.R., Lu, X., Maricic, J., Mendenhall, M.P., Meyer, A.M., Milincic, R., Mueller, P.E., Mumm, H.P., Napolitano, J., Neilson, R., Nikkel, J.A., Nour, S., Palomino Gallo, J.L., Pushin, D.A., Qian, X., Roca, C., Rosero, R., Searles, M., Surukuchi, P.T., Sutanto, F., Tyra, M.A., Venegas-Vargas, D., Weatherly, P.B., Wilhelm, J., Woolverton, A., Yeh, M., Zhang, C., Zhang, X., "Final Measurement of the ^{235}U Antineutrino Energy Spectrum with the PROSPECT-I Detector at HFIR," *Phys. Rev. Lett.* **131**(2), 021802 (2023). DOI: [10.1103/PhysRevLett.131.021802](https://doi.org/10.1103/PhysRevLett.131.021802)
- Anitas, E.M., "α-SAS: An Integrative Approach for Structural Modeling of Biological Macromolecules in Solution," *Acta Crystallogr. D* **78**(Part 8), 1046 (2022). DOI: [10.1107/S2059798322006349](https://doi.org/10.1107/S2059798322006349) [CHNRNS]
- Assumin-Gyimah, K.T.A., Dutta, D., Hussey, D.S., Snow, W.M., Langlois, C., Lee, V., "Neutron Phase Contrast Imaging of $PbWO_4$ Crystals for G Experiment Test Masses using a Talbot-Lau Neutron Interferometer," *Classical Quant. Grav.* **39**(24), 245014 (2022). DOI: [10.1088/1361-6382/aca1a4](https://doi.org/10.1088/1361-6382/aca1a4)
- Babu, S.K., Yilmaz, A., Uddin, M.A., LaManna, J., Baltic, E., Jacobson, D.L., Pasaogullari, U., Spendelow, J.S., "A Goldilocks Approach to Water Management: Hydrochannel Porous Transport Layers for Unitized Reversible Fuel Cells," *Adv. Energy Mater.* **13**(16), 2203952 (2023). DOI: [10.1002/aenm.202203952](https://doi.org/10.1002/aenm.202203952)
- Bag, R., Dissanayake, S.E., Yan, H., Shi, Z., Graf, D., Choi, E.S., Marjerrison, C., Lang, F., Lancaster, T., Qiu, Y., Chen, W., Blundell, S.J., Nevidomskyy, A.H., Haravifard, S., "Beyond Single Tetrahedron Physics of the Breathing Pyrochlore Compound $Ba_3Yb_2Zn_5O_{17}$," *Phys. Rev. B* **107**(14), L140408 (2023). DOI: [10.1103/PhysRevB.107.L140408](https://doi.org/10.1103/PhysRevB.107.L140408) [CHNRNS]
- Bakar, R., Darvishi, S., Aydemir, U., Yahsi, U., Tav, C., Menciloglu, Y.Z., Senses, E., "Decoding Polymer Architecture Effect on Ion Clustering, Chain Dynamics, and Ionic Conductivity in Polymer Electrolytes," *ACS Appl. Energy Mater.* **6**(7), 4053 (2023). DOI: [10.1021/acsaem.3c00310](https://doi.org/10.1021/acsaem.3c00310) [CHNRNS]
- Balsara, N., DeBeer-Schmitt, L., Gehring, P., Hallas, A., Haravifard, S., King, H., Lee, Y., Meilleur, F., Rodriguez, E., Saunders, C.N., Xi, Y., "The 11th American Conference on Neutron Scattering," *Neutron News* **34**(1), 2 (2023). DOI: [10.1080/10448632.2023.2166759](https://doi.org/10.1080/10448632.2023.2166759)
- Baroukh, I.R., Gurgen, A., Shen, J.S., Weiss, A.G., "A Preliminary Thermal-Hydraulics Analysis for the NIST Neutron Source," *T. Am. Nucl. Soc.* **127**(1), 1354 (2022). <https://www.ans.org/pubs/transactions/article-52609>
- Baroukh, I.R., Gurgen, A., Shen, J.S., Weiss, A.G., "Preliminary CFD Investigations for the NIST Neutron Source," *T. Am. Nucl. Soc.* **127**(1), 1268 (2022). <https://www.ans.org/pubs/transactions/article-52587>
- Beaucage, P.A., Martin, T.B., "The Autonomous Formulation Laboratory: An Open Liquid Handling Platform for Formulation Discovery using X-ray and Neutron Scattering," *Chem. Mater.* **35**(3), 846 (2023). DOI: [10.1021/acs.chemmater.2c03118](https://doi.org/10.1021/acs.chemmater.2c03118)
- Beausoleil, G., Zillinger, J., Hawkins, L., Yao, T., Weiss, A.G., Pu, X., Jerred, N., Kaoumi, D., "Designing Nuclear Fuels with a Multi-Principal Element Alloying Approach," *Nucl. Technol.*, in press. DOI: [10.1080/00295450.2023.2236796](https://doi.org/10.1080/00295450.2023.2236796)
- Bellur, K., Médici, E.F., Hermanson, J.C., Choi, C.K., Allen, J.S., "Modeling Liquid-Vapor Phase Change Experiments: Cryogenic Hydrogen and Methane," *Colloid Surface. A*, in press. DOI: [10.1016/j.colsurfa.2023.131932](https://doi.org/10.1016/j.colsurfa.2023.131932)
- Bellur, K., Médici, E.F., Hussey, D.S., Jacobson, D.L., LaManna, J., Leão, J.B., Scherschligt, J., Hermanson, J.C., Choi, C.K., Allen, J.S., "Results from Neutron Imaging Phase Change Experiments with LH_2 and LCH_4 ," *Cryogenics* **125**, 103517 (2022). DOI: [10.1016/j.cryogenics.2022.103517](https://doi.org/10.1016/j.cryogenics.2022.103517)
- Bellur, K., Medici, E.F., Hussey, D.S., Jacobson, D.L., LaManna, J., Leao, J.B., Scherschligt, J., Hermanson, J.C., Choi, C.K., Allen, J.S., "Data from Cryo-Neutron Phase Change Experiments with LH_2 and LCH_4 ," *Data Brief* **43**, 108474 (2022). DOI: [10.1016/j.dib.2022.108474](https://doi.org/10.1016/j.dib.2022.108474)
- Berger, J.E., Teixeira, S.C.M., Reed, K., Razinkov, V.I., Sloey, C.J., Qi, W., Roberts, C.J., "High-Pressure, Low-Temperature Induced Unfolding and Aggregation of Monoclonal Antibodies: Role of the Fc and Fab Fragments," *J. Phys. Chem. B* **126**(24), 4431 (2022). DOI: [10.1021/acs.jpcc.1c10528](https://doi.org/10.1021/acs.jpcc.1c10528) [CHNRNS]

- Berger, J.E., Teixeira, S.C.M., Sloey, C.J., Qi, W., Roberts, C.J., "High Pressure Light Scattering of Therapeutic Proteins to Probe Aggregation and Protein-Protein Interactions," *J. Phys. Chem. B* **127**(26), 5742 (2023). DOI: [10.1021/acs.jpcc.2c09118](https://doi.org/10.1021/acs.jpcc.2c09118)
- Bhattarai, S., Adawi, H., Lussier, J.-G., Gebretsadik, A., Dzero, M., Krycka, K.L., Schroeder, A., "Evolution of Short-Range Magnetic Correlations in Ferromagnetic Ni-V Alloys," *Phys. Rev. B* **107**(5), 054409 (2023). DOI: [10.1103/PhysRevB.107.054409](https://doi.org/10.1103/PhysRevB.107.054409) [CHRS]
- Bishop, R.L., "Neutron Activation Analysis," in "Encyclopedia of Geoarchaeology. Encyclopedia of Earth Science Series," edited by Gilbert, A.S., Goldberg, P., Mandel, R.D., Aldeias, V., (Springer, Cham, Switzerland), in press. DOI: [10.1007/978-3-030-44600-0_20-1](https://doi.org/10.1007/978-3-030-44600-0_20-1)
- Biswas, S., Melton, L.D., Nelson, A.R.J., Le Brun, A.P., Heinrich, F., McGillivray, D.J., Xu, A.Y., "The Assembly Mechanism and Mesoscale Architecture of Protein-Polysaccharide Complexes Formed at the Solid-Liquid Interface," *Langmuir* **38**(41), 12551 (2022). DOI: [10.1021/acs.langmuir.2c02003](https://doi.org/10.1021/acs.langmuir.2c02003)
- Bojanowski, C., Wang, G., Weiss, A., Kmak, R., Hebden, A., Legatt, M., Howard, T., Marcum, W., Mohamed, W., Sahin, D., Jaluvka, D., Wilson, E., "National Bureau of Standards Reactor LEU Fuel Element Flow Test Conceptual Design," *ANL/RTR/TM-22/12*, 1 (2022). DOI: [10.2172/1889717](https://doi.org/10.2172/1889717)
- Byrne, J., Worcester, D.L., "The Neutron Lifetime Anomaly: Analysis of Charge Exchange and Molecular Reactions in a Proton Trap," *Eur. J. Phys. A* **58**(8), 151 (2022). DOI: [10.1140/epja/s10050-022-00786-8](https://doi.org/10.1140/epja/s10050-022-00786-8)
- Cai, Y., Gao, J., Li, J.-H., Liu, P., Zheng, Y., Zhou, W., Wu, H., Li, L., Lin, R.-B., Chen, B., "Pore Modulation of Hydrogen-Bonded Organic Frameworks for Efficient Separation of Propylene," *Angew. Chem. Int. Edit.*, in press. DOI: [10.1002/anie.202308579](https://doi.org/10.1002/anie.202308579)
- Cao, Y., Matsukawa, T., Gibbs, A., Avdeev, M., Wang, C.-W., Wu, H., Huang, Q.-Z., Ohoyama, K., Ishigaki, T., Zhou, H., Li, Q., Miao, J., Lin, K., Xing, X., "Quantified Zero Thermal Expansion in Magnetic R₂Fe₁₇-Based Intermetallic Compounds (R = Rare Earth)," *Chem. Mater.* **35**(11), 4549 (2023). DOI: [10.1021/acs.chemmater.3c00915](https://doi.org/10.1021/acs.chemmater.3c00915)
- Castillo, S.R., Nguyen, M.H.L., DiPasquale, M., Kelley, E.G., Marquardt, D., "Mitocans Induce Lipid Flip-Flop and Permeabilize the Membrane to Signal Apoptosis," *Biophys. J.* **122**(11), 2353 (2023). DOI: [10.1016/j.bpj.2023.03.039](https://doi.org/10.1016/j.bpj.2023.03.039) [CHRS]
- Çelikten, O.Ş., Şahin, D., Weiss, A.G., "Highlights of Neutronics Analyses for the Pre-Conceptual NIST Neutron Source Design," *T. Am. Nucl. Soc.* **127**(1), 1153 (2022). <https://www.ans.org/pubs/transactions/article-52560>
- Celikten, O.Ş., Weiss, A.G., Şahin, D., "Comparison of U₃Si₂ and U-10Mo LEU-Fueled Reactor Cores for the Preconceptual NIST Neutron Source Design," in "Proceedings of the 2023 30th International Conference on Nuclear Engineering ICONE30," edited by JSME, (2023 30th International Conference on Nuclear Engineering ICONE30, May 2023, Kyoto, Japan), **ICONE30-1319** (2023).
- Černý, R., Brighi, M., Wu, H., Zhou, W., Dimitrievska, M., Murgia, F., Gulino, V., de Jongh, P.E., Trump, B.A., Udovic, T.J., "Thermal Polymorphism in CsCB₁₁H₁₂," *Molecules* **28**(5), 2296 (2023). DOI: [10.3390/molecules28052296](https://doi.org/10.3390/molecules28052296) [CHRS]
- Chan, E., Lane, H., Pasztorová, J., Songvilay, M., Johnson, R.D., Downie, R., Bos, J.-W.G., Rodriguez-Rivera, J.A., Cheong, S.-W., Ewings, R.A., Qureshi, N., Stock, C., "Neutron Scattering Sum Rules, Symmetric Exchanges, and Helicoidal Magnetism in MnSb₂O₆," *Phys. Rev. B* **107**(14), 144420 (2023). DOI: [10.1103/PhysRevB.107.144420](https://doi.org/10.1103/PhysRevB.107.144420) [CHRS]
- Chaturvedi, V., Ghosh, S., Gautreau, D., Postiglione, W.M., Dewey, J.E., Quarterman, P., Balakrishnan, P.P., Kirby, B.J., Zhou, H., Cheng, H., Huon, A., Charlton, T., Fitzsimmons, M.R., Korostynski, C., Jacobson, A., Figari, L., Garcia Barriocanal, J., Birol, T., Mkhoyan, K.A., Leighton, C., "Room-Temperature Valence Transition in a Strain-Tuned Perovskite Oxide," *Nat. Commun.* **13**(1), 7774 (2022). DOI: [10.1038/s41467-022-35024-8](https://doi.org/10.1038/s41467-022-35024-8)
- Chen, P., Yao, Q., Xu, J., Sun, Q., Grutter, A.J., Quarterman, P., Balakrishnan, P.P., Kinane, C.J., Caruana, A.J., Langridge, S., Li, A., Achinuq, B., Heppell, E., Ji, Y., Liu, S., Cui, B., Liu, J., Huang, P., Liu, Z., Yu, G., Xiu, F., Hesjedal, T., Zou, J., Han, X., Zhang, H., Yang, Y., Kou, X., "Tailoring the Magnetic Exchange Interaction in MnBi₂Te₄ Superlattices via the Intercalation of Ferromagnetic Layers," *Nat. Electron.* **6**(1), 18 (2023). DOI: [10.1038/s41928-022-00880-1](https://doi.org/10.1038/s41928-022-00880-1)
- Chen, W.C., Krycka, K.L., Watson, S.M., Barker, J.G., Gaudet, J., Burrall, H., Borchers, J.A., "Advanced Polarization Analysis Capability on the Very Small-Angle Neutron Scattering Instrument at the NIST Center for Neutron Research," *J. Phys. Conf. Ser.* **2481**(1), 012006 (2023). DOI: [10.1088/1742-6596/2481/1/012006](https://doi.org/10.1088/1742-6596/2481/1/012006) [CHRS]
- Chen, W., Borchers, J., Briber, R., Faraone, A., Gaudet, J., Grutter, A., Press, L., Ratcliff, W., Watson, S., "14th International Polarized Neutrons for Condensed-Matter Investigations (PNCMI) Conference," *Neutron News* **34**(1), 13 (2023). DOI: [10.1080/10448632.2023.2166757](https://doi.org/10.1080/10448632.2023.2166757)
- Chen, X.C., Soulen, C., Burdette-Trofimov, M.K., Tang, X., Liu, C., Heroux, L., Doucet, M., Tyagi, M., Veith, G.M., "Origin of Rate Limitations in Solid-State Polymer Batteries from Constrained Segmental Dynamics within the Cathode," *Cell Rep. Phys. Sci.*, in press. DOI: [10.1016/j.xcrp.2023.101538](https://doi.org/10.1016/j.xcrp.2023.101538) [CHRS]
- Chen-Mayer, H.H., Berke, N.S., Livingston, R.A., "PGAA Measurement of Chloride Diffusion Profiles in Concrete Cylinders," *J. Radioanal. Nucl. Ch.*, in press. DOI: [10.1007/s10967-023-09023-y](https://doi.org/10.1007/s10967-023-09023-y)
- Cheng, L.-Y., Varuttamaseni, A., Kohut, P., Gorgen, A., Sahin, D., Weiss, A.G., "Simulating the Power Noise Response due to Voiding in the NBSR during the February 3rd Incident," in "Proceedings of the 20th International Topical Meeting on Nuclear Thermal Hydraulics," edited by ANS, in press.
- Cook, J.C., King, H.E., Majkrzak, C.F., Sahin, D., Shen, J.S., Celikten, O.S., Diamond, D., Williams, R.E., Newton, T.H., "Proposed NIST Neutron Source User Facility," in *T. Am. Nucl. Soc.* **127**(1), 608 (2022). <https://www.ans.org/pubs/transactions/article-52434>
- Cook, J.C., King, H.E., Majkrzak, C.F., Sahin, D., Diamond, D., Shen, J.S., Celikten, O.S., Williams, R.E., Newton, T.H., "Neutron Delivery Systems Design of the Proposed NIST Neutron Source," *T. Am. Nucl. Soc.* **127**(1), 1020 (2022). <https://www.ans.org/pubs/transactions/article-52528>
- Corona, P.T., Dai, K., Helgeson, M.E., Leal, L.G., "Testing Orientational Closure Approximations in Dilute and Non-Dilute Suspensions with Rheo-SANS," *J. Non-Newton Fluid* **315**, 105014 (2023). DOI: [10.1016/j.jnnfm.2023.105014](https://doi.org/10.1016/j.jnnfm.2023.105014) [CHRS]
- Cui, J., Prisk, T.R., Olmsted, D.L., Su, V., Asta, M., Hayes, S.E., "Resolving the Chemical Formula of Nesquehonite via NMR Crystallography, DFT Computation, and Complementary Neutron Diffraction," *Chem.-Eur. J.* **29**(5), e202203052 (2023). DOI: [10.1002/chem.202203052](https://doi.org/10.1002/chem.202203052)
- DC, M., Shao, D.-F., Hou, V.D.-H., Vailionis, A., Quarterman, P., Habiboglu, A., Venuti, M.B., Xue, F., Huang, Y.-L., Lee, C.-M., Miura, M., Kirby, B., Bi, C., Li, X., Deng, Y., Lin, S.-J., Tsai, W., Eley, S., Wang, W.-G., Borchers, J.A., Tsymal, E.Y., Wang, S.X., "Observation of Anti-Damping Spin-Orbit Torques Generated by In-Plane and Out-of-Plane Spin Polarizations in MnPd₃," *Nat. Mater.* **22**(5), 591 (2023). DOI: [10.1038/s41563-023-01522-3](https://doi.org/10.1038/s41563-023-01522-3)
- Dalton, L.E., LaManna, J.M., Jones, S., Pour-Ghaz, M., "Does ITZ Influence Moisture Transport in Concrete?" *Transport Porous Med.* **144**(3), 623 (2022). DOI: [10.1007/s11242-022-01826-z](https://doi.org/10.1007/s11242-022-01826-z)
- Dalton, L., LaManna, J., Jones, S., Pour-Ghaz, M., "Does the Interfacial Transition Zone Influence Moisture Transport in Concrete?" in "Album of Porous Media," edited by Médiçi, E.F., Otero, A.D., (Springer Nature, Switzerland AG) Chap. **86**, 107 (2023). DOI: [10.1007/978-3-031-23800-0_87](https://doi.org/10.1007/978-3-031-23800-0_87)

- Dang, U., O'Hara, J., Evans, H.A., Olds, D., Chamorro, J., Hickox-Young, D., Laurita, G., Macaluso, R.T., "Vacancy-Driven Disorder and Elevated Dielectric Response in the Pyrochlore $\text{Pb}_{15}\text{Nb}_2\text{O}_{65}$," *Inorg. Chem.* **61**(46), 18601 (2022). DOI: [10.1021/acs.inorgchem.2c03031](https://doi.org/10.1021/acs.inorgchem.2c03031)
- Daugherty, M.C., DiStefano, V.H., LaManna, J.M., Jacobson, D.L., Kienzle, P.A., Kim, Y., Hussey, D.S., Bajcsy, P., "Assessment of Dose-Reduction Strategies in Wavelength-Selective Neutron Tomography," *SN Comput. Sci.* **4**(5), 586 (2023). DOI: [10.1007/s42979-023-02059-7](https://doi.org/10.1007/s42979-023-02059-7)
- Daugherty, M.C., LaManna, J.M., Kim, Y., Baltic, E., Hussey, D.S., Jacobson, D.L., "Neural Networks for Dose Reduced Reconstruction Image Denoising in Neutron Tomography," *Microsc. Microanal.* **28**(Suppl 1), 2040 (2022). DOI: [10.1017/S1431927622007917](https://doi.org/10.1017/S1431927622007917)
- Dhital, C., Dally, R.L., Ruvalcaba, R., Gonzalez-Hernandez, R., Guerrero-Sanchez, J., Cao, H.B., Zhang, Q., Tian, W., Wu, Y., Frontzek, M.D., Karna, S.K., Meads, A., Wilson, B., Chapai, R., Graf, D., Bacsa, J., Jin, R., DiTusa, J.F., "Multi-*k* Magnetic Structure and Large Anomalous Hall Effect in Candidate Magnetic Weyl Semimetal NdAlGe," *Phys. Rev. B* **107**(22), 224414 (2023). DOI: [10.1103/PhysRevB.107.224414](https://doi.org/10.1103/PhysRevB.107.224414)
- DiPasquale, M., Nguyen, M.H.L., Castillo, S.R., Dib, I.J., Kelley, E.G., Marquardt, D., "Vitamin E does not Disturb Polyunsaturated Fatty Acid Lipid Domains," *Biochemistry-US* **61**(21), 2366 (2022). DOI: [10.1021/acs.biochem.2c00405](https://doi.org/10.1021/acs.biochem.2c00405) [CHRNS]
- Ding, L., Colin, C.V., Simonet, V., Stock, C., Brubach, J.-B., Verseils, M., Roy, P., Garcia Sakai, V., Koza, M.M., Piovano, A., Ivanov, A., Rodriguez-Rivera, J.A., de Brion, S., Songvilay, M., "Lattice Dynamics and Spin Excitations in the Metal-Organic Framework $[\text{CH}_3\text{NH}_3][\text{Co}(\text{HCOO})_3]$," *Phys. Rev. Mater.*, in press. DOI: [10.1103/PhysRevMaterials.7.084405](https://doi.org/10.1103/PhysRevMaterials.7.084405) [CHRNS]
- Dissanayake, S., Shi, Z., Rau, J.G., Bag, R., Steinhardt, W., Butch, N.P., Frontzek, M., Podlesnyak, A., Graf, D., Marjerrison, C., Liu, J., Gingras, M.J.P., Haravifard, S., "Towards Understanding the Magnetic Properties of the Breathing Pyrochlore Compound $\text{Ba}_3\text{Yb}_2\text{Zn}_5\text{O}_{11}$ through Single-Crystal Studies," *NPJ Quantum Mater.* **7**(1), 77 (2022). DOI: [10.1038/s41535-022-00488-w](https://doi.org/10.1038/s41535-022-00488-w)
- Doktorova, M., Khelashvili, G., Ashkar, R., Brown, M.F., "Molecular Simulations and NMR Reveal How Lipid Fluctuations Affect Membrane Mechanics," *Biophys. J.* **122**(6), 984 (2023). DOI: [10.1016/j.bpj.2022.12.007](https://doi.org/10.1016/j.bpj.2022.12.007) [CHRNS]
- Dong, Q., Zhang, X., Qian, J., He, S., Mao, Y., Brozena, A.H., Zhang, Y., Pollard, T.P., Borodin, O.A., Wang, Y., Sai Chava, B., Das, S., Zavalij, P., Segre, C.U., Zhu, D., Xu, L., Liang, Y., Yao, Y., Briber, R.M., Li, T., Hu, L., "A Cellulose-Derived Supramolecule for Fast Ion Transport," *Sci. Adv.* **8**(49), eadd2031 (2022). DOI: [10.1126/sciadv.add2031](https://doi.org/10.1126/sciadv.add2031)
- Dubackic, M., Liu, Y., Kelley, E.G., Hetherington, C., Haertlein, M., Devos, J.M., Linse, S., Sparr, E., Olsson, U., " α -Synuclein Interaction with Lipid Bilayer Discs," *Langmuir* **38**(33), 10216 (2022). DOI: [10.1021/acs.langmuir.2c01368](https://doi.org/10.1021/acs.langmuir.2c01368) [CHRNS]
- Dura, J., Weigandt, K., Ogg, R., "Virtual School on Neutron Spectroscopy and Diffraction held by NIST," *Neutron News* **33**(3), 5 (2022). DOI: [10.1080/10448632.2022.2091385](https://doi.org/10.1080/10448632.2022.2091385) [CHRNS]
- Dziura, M., Castillo, S.R., DiPasquale, M., Gbadamosi, O., Zolnierczuk, P., Nagao, M., Kelley, E.G., Marquardt, D., "Investigating the Effect of Medium Chain Triglycerides on the Elasticity of Pulmonary Surfactant," *Chem. Res. Toxicol.* **36**(4), 643 (2023). DOI: [10.1021/acs.chemrestox.2c00349](https://doi.org/10.1021/acs.chemrestox.2c00349) [CHRNS] Elliott, J.P., Osti, N.C., Tyagi, M., Mamontov, E., Liu, L., Serrano, J.M., Cao, K., Liu, G., "Exceptionally Fast Ion Diffusion in Block Copolymer-Based Porous Carbon Fibers," *ACS Appl. Mater. Interfaces* **14**(32), 36980 (2022). DOI: [10.1021/acsami.2c12755](https://doi.org/10.1021/acsami.2c12755) [CHRNS]
- Eo, Y.S., Liu, S., Saha, S.R., Kim, H., Ran, S., Horn, J.A., Hodovanets, H., Collini, J., Metz, T., Fuhrman, W.T., Nevidomskyy, A.H., Denlinger, J.D., Butch, N.P., Fuhrer, M.S., Wray, L.A., Paglione, J., "c-axis Transport in UTe_2 : Evidence of Three-Dimensional Conductivity Component," *Phys. Rev. B* **106**(6), L060505 (2022). DOI: [10.1103/PhysRevB.106.L060505](https://doi.org/10.1103/PhysRevB.106.L060505)
- Evans, H.A., Mullangi, D., Deng, Z., Wang, Y., Peh, S.B., Wei, F., Wang, J., Brown, C.M., Zhao, D., Canepa, P., Cheetham, A.K., "Aluminum Formate, $\text{Al}(\text{HCOO})_3$: An Earth-Abundant, Scalable, and Highly Selective Material for CO_2 Capture," *Sci. Adv.* **8**(44), eade1473 (2022). DOI: [10.1126/sciadv.ade1473](https://doi.org/10.1126/sciadv.ade1473)
- Fajalia, A.I., Alexandridis, P., Tsianou, M., "Structure of Cellulose Ether Affected by Ionic Surfactant and Solvent: A Small-Angle Neutron Scattering Investigation," *Langmuir*, in press. DOI: [10.1021/acs.langmuir.3c00712](https://doi.org/10.1021/acs.langmuir.3c00712)
- Falus, P., Faraone, A., Förster, S., Hong, K., Ohl, M., "Dynamics of the Extended and Intermediate Range Order in Model Polymer Electrolyte Poly(Ethylene Oxide) and Lithium Bis(Trifluoromethanesulfonyl)imide," *Front. Soft Matter.* **3**, 1161141 (2023). DOI: [10.3389/frsfm.2023.1161141](https://doi.org/10.3389/frsfm.2023.1161141) [CHRNS]
- Fang, N., Zhang, S., Xu, Z., Chen, S., Zhang, X., Wu, H., Zhou, W., Zhao, Y., "Layered Porous Molecular Crystals via Interdigitation-Directed Assembly," *Cell Rep. Phys. Sci.*, in press. DOI: [10.1016/j.xcrp.2023.101508](https://doi.org/10.1016/j.xcrp.2023.101508)
- Felix, A., Şahin, D., "A Novel Nuclear Reactor Console Simulator using HoloLens 2," *T. Am. Nucl. Soc.* **127**(1), 99 (2022). <https://www.ans.org/pubs/transactions/article-52305>
- Fenton, S.M., Padmanabhan, P., Ryu, B.K., Nguyen, T.T.D., Zia, R.N., Helgeson, M.E., "Minimal Conditions for Solidification and Thermal Processing of Colloidal Gels," *P. Natl. A. Sci. USA* **120**(25), e2215922120 (2023). DOI: [10.1073/pnas.2215922120](https://doi.org/10.1073/pnas.2215922120) [CHRNS]
- Ford, R.R., Gilbert, P.H., Gillilan, R., Huang, Q., Donnelly, R., Qian, K.K., Allen, D.P., Wagner, N.J., Liu, Y., "Micelle Formation and Phase Separation of Poloxamer 188 and Preservative Molecules in Aqueous Solutions Studied by Small Angle X-ray Scattering," *J. Pharm. Sci.* **112**(3), 731 (2023). DOI: [10.1016/j.xphs.2022.09.019](https://doi.org/10.1016/j.xphs.2022.09.019)
- Frie, B., Griffin, D., Whipple, J., "Procedure Overhaul at the NIST Center for Neutron Research," [Paper presentation]. TRTR & IGORR Research Reactor Conference (June 2023, College Park, MD) (2023). <https://www.trtr.org/2023-conference-archive>
- Gao, B., Chen, T., Huang, C.-L., Qiu, Y., Xu, G., Liebman, J., Chen, L., Stone, M.B., Feng, E., Cao, H., Wang, X., Xu, X., Cheong, S.-W., Winter, S.M., Dai, P., "Disorder-Induced Excitation Continuum in a Spin- $\frac{1}{2}$ Cobaltate on a Triangular Lattice," *Phys. Rev. B* **108**(2), 024431 (2023). DOI: [10.1103/PhysRevB.108.024431](https://doi.org/10.1103/PhysRevB.108.024431) [CHRNS]
- Gao, B., Chen, T., Wu, X.-C., Flynn, M., Duan, C., Chen, L., Huang, C.-L., Liebman, J., Li, S., Ye, F., Stone, M.B., Podlesnyak, A., Abernathy, D.L., Adroja, D.T., Le, M.D., Huang, Q., Nevidomskyy, A.H., Morosan, E., Balents, L., Dai, P., "Diffusive Excitonic Bands from Frustrated Triangular Sublattice in a Singlet-Ground-State System," *Nat. Commun.* **14**(1), 2051 (2023). DOI: [10.1038/s41467-023-37669-5](https://doi.org/10.1038/s41467-023-37669-5)
- Gao, B., Chen, T., Yan, H., Duan, C., Huang, C.-L., Yao, X.P., Ye, F., Balz, C., Stewart, J.R., Nakajima, K., Ohira-Kawamura, S., Xu, G., Xu, X., Cheong, S.-W., Morosan, E., Nevidomskyy, A.H., Chen, G., Dai, P., "Magnetic Field Effects in an Octupolar Quantum Spin Liquid Candidate," *Phys. Rev. B* **106**(9), 094425 (2022). DOI: [10.1103/PhysRevB.106.094425](https://doi.org/10.1103/PhysRevB.106.094425)
- García Sakai, V., Neumann, D., "John R. D. Copley (1944–2022)," *Neutron News* **33**(3), 30 (2022). DOI: [10.1080/10448632.2022.2093087](https://doi.org/10.1080/10448632.2022.2093087)

- Gaudet, J., Yang, H.-Y., Smith, E.M., Halloran, T., Clancy, J.P., Rodriguez-Rivera, J.A., Xu, G., Zhao, Y., Chen, W.C., Sala, G., Aczel, A.A., Gaulin, B.D., Tafti, F., Broholm, C., "Spin-Orbital Order and Excitons in Magnetoresistive HoBi," *Phys. Rev. B* **107**(10), 104423 (2023). DOI: [10.1103/PhysRevB.107.104423](https://doi.org/10.1103/PhysRevB.107.104423) [CHRNS]
- Gilbert, T., Campea, M.A., Preciado Rivera, N., Majcher, M., Alsop, R., Babi, M., Kalab, T., Moran-Mirabal, J., Rheinstadter, M., Hoare, T., "Injectable Poly (N-Isopropylacrylamide)/Poly(Vinylpyrrolidone) Interpenetrating Network Hydrogels Formed via Hydrazone/Disulfide Cross-Linking," *Macromolecules*, in press. DOI: [10.1021/acs.macromol.3c00045](https://doi.org/10.1021/acs.macromol.3c00045)
- Gitgeatpong, G., Zhao, Y., Fernandez-Baca, J.A., Hong, T., Sato, T.J., Piyawongwathana, P., Nawa, K., Saeun, P., Matan, K., "Magnetic Structure and Spin Dynamics of the Quasi-Two-Dimensional Antiferromagnet Zn-Doped Copper Pyrovanadate," *Phys. Rev. B* **106**(21), 214438 (2022). DOI: [10.1103/PhysRevB.106.214438](https://doi.org/10.1103/PhysRevB.106.214438)
- Gu, Q., Carroll, J.P., Wang, S., Ran, S., Broyles, C., Siddiquee, H., Butch, N.P., Saha, S.R., Paglione, J., Davis, J.C.S., Liu, X., "Detection of a Pair Density Wave State in UTe_2 ," *Nature* **618**(7967), 921 (2023). DOI: [10.1038/s41586-023-05919-7](https://doi.org/10.1038/s41586-023-05919-7)
- Gurgen, A., Celikten, O.S., Sahin, D., "Development of Linear Nuclear Channel Noise Detection System," *T. Am. Nucl. Soc.*, **126**(1), 226 (2022). <https://www.ans.org/pubs/transactions/article-51415>
- Gurgen, A., Sahin, D., Whipple, J., "Quantifying Reactor Power Noise—A Case Study on NIST Research Reactor," in "Proceedings of the 2023 30th International Conference on Nuclear Engineering," edited by JSME, (30th International Conference on Nuclear Engineering, May 2023, Kyoto, Japan), **ICONE30-1339** (2023).
- Gvaramia, M., Gutfreund, P., Falus, P., Faraone, A., Nagao, M., Wolff, M., "Neutron Spin Echo Spectroscopy with a Moving Sample," *Sci. Rep.*, in press. DOI: [10.1038/s41598-023-39854-4](https://doi.org/10.1038/s41598-023-39854-4) [CHRNS]
- Halder, A., Klein, R.A., Lively, R., McGuirk, C.M., "Multivariate Zeolitic Imidazolate Frameworks with an Inverting Trend in Flexibility," *Chem. Commun.* **58**(81), 11394 (2022). DOI: [10.1039/d2cc04362a](https://doi.org/10.1039/d2cc04362a)
- Halder, A., Klein, R.A., Shulda, S., McCarver, G.A., Parilla, P.A., Furukawa, H., Brown, C.M., McGuirk, C.M., "Multivariate Flexible Framework with High Usable Hydrogen Capacity in a Reduced Pressure Swing Process," *J. Am. Chem. Soc.* **145**(14), 8033 (2023). DOI: [10.1021/jacs.3c00344](https://doi.org/10.1021/jacs.3c00344)
- Haley, S.C., Maniv, E., Wu, S., Cookmeyer, T., Torres-Londono, S., Aravinth, M., Maksimovic, N., Moore, J., Birgeneau, R.J., Analytis, J.G., "Long-Range, Non-Local Switching of Spin Textures in a Frustrated Antiferromagnet," *Nat. Commun.*, in press. DOI: [10.1038/s41467-023-39883-7](https://doi.org/10.1038/s41467-023-39883-7)
- Halloran, T., Desrochers, F., Zhang, E.Z., Chen, T., Chern, L.E., Xu, Z., Winn, B., Graves-Brook, M., Stone, M.B., Kolesnikov, A.I., Qiu, Y., Zhong, R., Cava, R., Kim, Y.B., Broholm, C., "Geometrical Frustration versus Kitaev Interactions in $BaCo_2(AsO_4)_2$," *P. Natl. A. Sci. USA* **120**(2), e2215509119 (2023). DOI: [10.1073/pnas.2215509119](https://doi.org/10.1073/pnas.2215509119) [CHRNS]
- Halloran, T., Wang, Y., Li, M., Rousochatzakis, I., Chauhan, P., Stone, M.B., Takayama, T., Takagi, H., Armitage, N.P., Perkins, N.B., Broholm, C., "Magnetic Excitations and Interactions in the Kitaev Hyperhoneycomb Iridate β - Li_2IrO_3 ," *Phys. Rev. B* **106**(6), 064423 (2022). DOI: [10.1103/PhysRevB.106.064423](https://doi.org/10.1103/PhysRevB.106.064423)
- Hashemi-Tilehnoee, M., Tsrin, N., Stoudenets, V., Bushuev, Y.G., Chorazewski, M., Li, M., Li, D., Leão, J.B., Bleuel, M., Zajdel, P., Palomo Del Barrio, E., Grosu, Y., "Liquid Piston Based on Molecular Springs for Energy Storage Applications," *J. Energy Storage*, in press. DOI: [10.1016/j.est.2023.107697](https://doi.org/10.1016/j.est.2023.107697) [CHRNS]
- He, L., Deng, S., Shen, F., Chen, J., Lu, H., Tan, Z., Zheng, H., Hao, J., Zhao, D., Ma, Q., "The Performance of General Purpose Powder Diffractometer at CSNS," *Nucl. Instrum. Meth. A*, in press. DOI: [10.1016/j.nima.2023.168414](https://doi.org/10.1016/j.nima.2023.168414)
- Heil, C.M., Patil, A., Vanthournout, B., Singla, S., Bleuel, M., Song, J.-J., Hu, Z., Gianneschi, N.C., Shawkey, M.D., Sinha, S.K., Jayaraman, A., Dhinojwala, A., "Mechanism of Structural Colors in Binary Mixtures of Nanoparticle-Based Supraballs," *Sci. Adv.* **9**(21), eadf2859 (2023). DOI: [10.1126/sciadv.adf2859](https://doi.org/10.1126/sciadv.adf2859) [CHRNS]
- Heinrich, F., Thomas, C.E., Alvarado, J.J., Eells, R., Thomas, A., Doucet, M., Whitlatch, K.N., Aryal, M., Lösche, M., Smithgall, T.E., "Neutron Reflectometry and Molecular Simulations Demonstrate HIV-1 Nef Homodimer Formation on Model Lipid Bilayers," *J. Mol. Biol.* **435**(8), 168009 (2023). DOI: [10.1016/j.jmb.2023.168009](https://doi.org/10.1016/j.jmb.2023.168009)
- Henderson, M.E., Bleuel, M., Beare, J., Cory, D.G., Heacock, B., Huber, M.G., Luke, G.M., Pula, M., Sarenac, D., Sharma, S., Smith, E.M., Zhernenkov, K., Pushin, D.A., "Skyrmion Alignment and Pinning Effects in the Disordered Multiphase Skyrmion Material $Co_5Zn_3Mn_4$," *Phys. Rev. B* **106**(9), 094435 (2022). DOI: [10.1103/PhysRevB.106.094435](https://doi.org/10.1103/PhysRevB.106.094435) [CHRNS]
- Henderson, M.E., Heacock, B., Bleuel, M., Cory, D.G., Heikes, C., Huber, M.G., Krzywon, J., Nahman-Levesqué, O., Luke, G.M., Pula, M., Sarenac, D., Zhernenkov, K., Pushin, D.A., "Three-Dimensional Neutron Far-Field Tomography of a Bulk Skyrmion Lattice," *Nat. Phys.*, in press. DOI: [10.1038/s41567-023-02175-4](https://doi.org/10.1038/s41567-023-02175-4) [CHRNS]
- Hidrovo, I., Dey, J., Meyer, H., Hussey, D.S., Klimov, N.N., Butler, L.G., Ham, K., Newhauser, W., "Neutron Interferometry using a Single Modulated Phase Grating," *Rev. Sci. Instrum.* **94**(4), 045110 (2023). DOI: [10.1063/5.0106706](https://doi.org/10.1063/5.0106706)
- Hiebert, M.E., Weaver, J., Lam, T., Little, N., Hyde, E., Vicenzi, E.P., Phaneuf, R.J., "ALD Deposited Amorphous Alumina Coatings can Slow Glass Alteration," *Phys. Chem. Glasses-B* **63**(4), 97 (2022). DOI: [10.13036/17533562.63.4.07](https://doi.org/10.13036/17533562.63.4.07)
- Himbert, S., D'Alessandro, A., Qadri, S.M., Majcher, M.J., Hoare, T., Sheffield, W.P., Nagao, M., Nagle, J.F., Rheinstädter, M.C., "The Bending Rigidity of the Red Blood Cell Cytoplasmic Membrane," *Plos One* **17**(8), e0269619 (2022). DOI: [10.1371/journal.pone.0269619](https://doi.org/10.1371/journal.pone.0269619) [CHRNS]
- Hoogerheide, D.P., Gurnev, P.A., Rostovtseva, T.K., Bezrukov, S.M., "Voltage-Activated Complexation of α -Synuclein with Three Diverse β -Barrel Channels: VDAC, MspA, and α -Hemolysin," *Proteomics* **22**(5-6), 2100060 (2022). DOI: [10.1002/pmic.202100060](https://doi.org/10.1002/pmic.202100060)
- Horkay, F., Basser, P.J., Geissler, E., "Ion-Induced Changes in DNA Gels," *Soft Matter* **19**(28), 5405 (2023). DOI: [10.1039/D3SM00666B](https://doi.org/10.1039/D3SM00666B) [CHRNS]
- Huestis, P.L., Anovitz, L.M., Kolesnikov, A.I., Jensen, G., Barker, J., Bleuel, M., Gagnon, C., Mildner, D.F.R., Zhang, X., Zong, M., LaVerne, J.A., "Effects of γ -Irradiation, Cation Size, and Salt Concentration on the Aggregation of Boehmite Nanoplatelets," *J. Phys. Chem. C* **127**(10), 4896 (2023). DOI: [10.1021/acs.jpcc.2c07749](https://doi.org/10.1021/acs.jpcc.2c07749) [CHRNS]
- Jakkampudi, T., Lin, Q., Mitra, S., Vijai, A., Qin, W., Kang, A., Chen, J., Ryan, E., Wang, R., Gong, Y., Heinrich, F., Song, J., Di, Y.-P., Tristram-Nagle, S., "Lung SPLUNC1 Peptide Derivatives in the Lipid Membrane Headgroup Kill Gram-Negative Planktonic and Biofilm Bacteria," *Biomacromolecules* **24**(6), 2804 (2023). DOI: [10.1021/acs.biomac.3c00218](https://doi.org/10.1021/acs.biomac.3c00218)
- Jape, S., Bojanowski, C., Wang, G., Jaluvka, D., Sahin, D., Mohamed, W., Wilson, E., "Comparative Structural Rigidity Analysis of the NBSR DDE and the NBSR LEU Fuel Element," *ANL/RTR/TM-22/6*, (2022). DOI: [10.2172/1891095](https://doi.org/10.2172/1891095)
- Jariwala, S., Song, R., Hipp, J.B., Diemer, R.B., Wagner, N.J., Beris, A.N., "A Polydisperse Model for Thixotropic Elasto-Viscoplastic Suspensions of Aggregating Particles using Population Balances," *AiChE J.*, in press. DOI: [10.1002/aic.18184](https://doi.org/10.1002/aic.18184) [CHRNS]

- Jensen, C.J., Quintana, A., Quarterman, P., Grutter, A.J., Balakrishnan, P.P., Zhang, H., Davydov, A.V., Zhang, X., Liu, K., "Nitrogen-Based Magneto-Ionic Manipulation of Exchange Bias in CoFe/MnN Heterostructures," *ACS Nano* **17**(7), 6745 (2023). DOI: [10.1021/acsnano.2c12702](https://doi.org/10.1021/acsnano.2c12702)
- Jensen, E.H., Lombardo, L., Girella, A., Guzik, M.N., Züttel, A., Milanese, C., Whitfield, P., Noréus, D., Sartori, S., "The Effect of Y Content on Structural and Sorption Properties of A₂B₇-Type Phase in the La-Y-Ni-Al-Mn System," *Molecules* **28**(9), 3749 (2023). DOI: [10.3390/molecules28093749](https://doi.org/10.3390/molecules28093749)
- Jeong, S., Yuan, G., Satija, S.K., Jeon, N., Lee, E., Kim, Y., Choi, S., Koo, J., "Polyamide Thin Films with Nanochannel Networks Synthesized at the Liquid-Gas Interface for Water Purification," *J. Membrane Sci.* **657**, 120671 (2022). DOI: [10.1016/j.memsci.2022.120671](https://doi.org/10.1016/j.memsci.2022.120671)
- Jia, X., Ma, P., Tarwa, K., Ma, Y., Wang, Q., "Development of a Novel Colorimetric Sensor Array Based on Oxidized Chitin Nanocrystals and Deep Learning for Monitoring Beef Freshness," *Sensor Actuat. B-Chem.*, in press. DOI: [10.1016/j.snb.2023.133931](https://doi.org/10.1016/j.snb.2023.133931)
- Jia, X., Ma, P., Taylor, K.S.-Y., Tarwa, K., Mao, Y., Wang, Q., "Development of Stable Pickering Emulsions with TEMPO-Oxidized Chitin Nanocrystals for Encapsulation of Quercetin," *Foods* **12**(2), 367 (2023). DOI: [10.3390/foods12020367](https://doi.org/10.3390/foods12020367)
- Jiang, F., Bian, J., Liu, H., Li, S., Bai, X., Zheng, L., Jin, S., Liu, Z., Yang, G.-Y., Hong, L., "Creatinase: Using Increased Entropy to Improve the Activity and Thermostability," *J. Phys. Chem. B* **127**(12), 2671 (2023). DOI: [10.1021/acs.jpcc.2c08062](https://doi.org/10.1021/acs.jpcc.2c08062) [CHRN5]
- Jurns, J., Cook, J.C., Celikten, O., Arnold, P., "Liquid Deuterium Cold Source Concept for the NIST Neutron Source," *IOP Conf. Ser. Mater. Sci. Eng.*, in press.
- Kapahi, C., Sarenac, D., Bleuel, M., Cory, D.G., Heacock, B., Henderson, M.E., Huber, M.G., Taminiau, I., Pushin, D., "High-Transmission Neutron Optical Devices Utilizing Micro-Machined Structures," *QTM Beam Sci.* **7**(1), 10 (2023). DOI: [10.3390/qubs7010010](https://doi.org/10.3390/qubs7010010) [CHRN5]
- Kato, D., Tomita, O., Nelson, R., Kirsanova, M.A., Dronskowski, R., Suzuki, H., Zhong, C., Tassel, C., Ishida, K., Matsuzaki, Y., Brown, C.M., Fujita, K., Fujii, K., Yashima, M., Kobayashi, Y., Saeki, A., Oikawa, I., Takamura, H., Abe, R., Kageyama, H., Gorelik, T.E., Abakumov, A.M., "Bi₁₂O₁₇Cl₂ with a Sextuple Bi-O Layer Composed of Rock-Salt and Fluorite Units and its Structural Conversion through Fluorination to Enhance Photocatalytic Activity," *Adv. Funct. Mater.* **32**(41), 2204112 (2022). DOI: [10.1002/adfm.202204112](https://doi.org/10.1002/adfm.202204112)
- Kelley, E.G., Frewin, M.P.K., Czakkel, O., Nagao, M., "Nanoscale Bending Dynamics in Mixed-Chain Lipid Membranes," *Symmetry* **15**(1), 191 (2023). DOI: [10.3390/sym15010191](https://doi.org/10.3390/sym15010191) [CHRN5]
- Kelley, E.G., Heberle, F.A., "Sensing a Little Friction," *Biophys. J.* **121**(15), 2827 (2022). DOI: [10.1016/j.bpj.2022.06.034](https://doi.org/10.1016/j.bpj.2022.06.034) [CHRN5]
- Khatua, J., Bhattacharya, S., Ding, Q.P., Vrtnik, S., Strydom, A.M., Butch, N.P., Luetkens, H., Kermarrec, E., Ramachandra Rao, M.S., Zorko, A., Furukawa, Y., Khuntia, P., "Spin Liquid State in a Rare-Earth Hyperkagome Lattice," *Phys. Rev. B* **106**(10), 104404 (2022). DOI: [10.1103/PhysRevB.106.104404](https://doi.org/10.1103/PhysRevB.106.104404)
- Klein, R.A., Evans, H.A., Trump, B.A., Udovic, T.J., Brown, C.M., "Neutron Scattering Studies of Materials for Hydrogen Storage," in "Comprehensive Inorganic Chemistry III," edited by Reedijk, J., Poepelmeier, K.R., (Elsevier, Amsterdam, Netherlands) Chap. **10.02**, 3 (2023). DOI: [10.1016/B978-0-12-823144-9.00028-5](https://doi.org/10.1016/B978-0-12-823144-9.00028-5)
- Kline, S.R., "2022 NIST Center for Neutron Research Accomplishments and Opportunities," *NIST SP-1284*, 1 (2022). DOI: [10.6028/NIST.SP.1284](https://doi.org/10.6028/NIST.SP.1284)
- Koegel, A.A., Oswald, I.W.H., Rivera, C., Miller, S.L., Fallon, M.J., Prisk, T.R., Brown, C.M., Neilson, J.R., "Influence of Inorganic Layer Thickness on Methylammonium Dynamics in Hybrid Perovskite Derivatives," *Chem. Mater.* **34**(18), 8316 (2022). DOI: [10.1021/acs.chemmater.2c01868](https://doi.org/10.1021/acs.chemmater.2c01868) [CHRN5]
- Kons, C., Krycka, K.L., Robles, J., Ntallis, N., Pereiro, M., Phan, M.-H., Srikanth, H., Borchers, J.A., Arena, D.A., "Influence of Hard/Soft Layer Ordering on Magnetization Reversal of Bimagnetic Nanoparticles: Implications for Biomedical/Theranostic Applications," *ACS Appl. Nano Mater.* **6**(13), 10986 (2023). DOI: [10.1021/acsanm.3c00510](https://doi.org/10.1021/acsanm.3c00510) [CHRN5]
- Krueger, S., "Planning, Executing and Assessing the Validity of SANS Contrast Variation Experiments," in "Methods in Enzymology, Vol. 677," edited by Pyle, A.M., Christianson, D.W., (Academic Press, Cambridge, MA) Chap. **4**, 127 (2022). DOI: [10.1016/bs.mie.2022.08.023](https://doi.org/10.1016/bs.mie.2022.08.023)
- Kumari, H., Negin, S., Eisenhart, A., Patel, M.B., Beck, T.L., Heinrich, F., Spikes, H.J., Gokel, G.W., "Assessment of a Host-Guest Interaction in a Bilayer Membrane Model," *RSC Adv.* **12**(49), 32046 (2022). DOI: [10.1039/D2RA03851J](https://doi.org/10.1039/D2RA03851J)
- Lee, J., Gao, K.W., Shah, N.J., Kang, C., Snyder, R.L., Abel, B.A., He, L., Teixeira, S.C.M., Coates, G.W., Balsara, N.P., "Relationship between Ion Transport and Phase Behavior in Acetal-Based Polymer Blend Electrolytes Studied by Electrochemical Characterization and Neutron Scattering," *Macromolecules* **55**(24), 11023 (2022). DOI: [10.1021/acs.macromol.2c01724](https://doi.org/10.1021/acs.macromol.2c01724)
- Lee, Y.-F., Whitcomb, K., Wagner, N.J., "Microstructure and Rheology of Shear Thickening Colloidal Suspensions under Transient Flows," *Phys. Fluids* **35**(7), 073308 (2023). DOI: [10.1063/5.0153614](https://doi.org/10.1063/5.0153614) [CHRN5]
- Lefton, J.B., Liu, W., McGuire, C., Lv, B., Brown, C.M., Klein, R.A., Runčevski, T., "Synthesis, Structure and Canted Antiferromagnetism of Layered Cobalt Hydroxide Sorbate," *J. Phys. Chem. Solids*, in press. DOI: [10.1016/j.jpcs.2023.111568](https://doi.org/10.1016/j.jpcs.2023.111568)
- Li, M., Zhou, Y., Zhang, K., Xu, G., Gu, G., Su, F., Chen, X., "Pressure Evolution of Ultrafast Photocarrier Dynamics and Electron-Phonon Coupling in FeTe_{0.3}Se_{0.5}," *Materials* **15**(23), 8467 (2022). DOI: [10.3390/ma15238467](https://doi.org/10.3390/ma15238467)
- Li, Q., Ren, Y., Zhang, Q., Gu, L., Huang, Q., Wu, H., Sun, J., Cao, Y., Lin, K., Xing, X., "Chemical Order-Disorder Nanodomains in Fe₃Pt Bulk Alloy," *Natl. Sci. Rev.* **9**(12), nwac053 (2022). DOI: [10.1093/nsr/nwac053](https://doi.org/10.1093/nsr/nwac053)
- Li, Y., Schwab, N.L., Briber, R.M., Dura, J.A., Van Nguyen, T., "Modification of Nafion's Nanostructure for the Water Management of PEM Fuel Cells," *J. Polym. Sci.* **61**(8), 709 (2023). DOI: [10.1002/pol.20220774](https://doi.org/10.1002/pol.20220774)
- Li, Y., Han, Z., Ma, C., Hong, L., Ding, Y., Chen, Y., Zhao, J., Liu, D., Sun, G., Zuo, T., Cheng, H., Han, C.C., "Structure and Dynamics of Supercooled Water in the Hydration Layer of Poly(Ethylene Glycol)," *Struct. Dynam. US* **9**(5), 054901 (2022). DOI: [10.1063/4.0000158](https://doi.org/10.1063/4.0000158) [CHRN5]
- Liang, H., Webb, M.A., Chawathe, M., Bendejacq, D., de Pablo, J.J., "Understanding the Structure and Rheology of Galactomannan Solutions with Coarse-Grained Modeling," *Macromolecules* **56**(1), 177 (2023). DOI: [10.1021/acs.macromol.2c01781](https://doi.org/10.1021/acs.macromol.2c01781)
- Liang, X., Hu, Q., Wang, Q., Li, W., Zhang, T., Yang, S., Sun, M., Bleuel, M., Yao, G., "Changes in Nanoscale Pore Structures and Mesopore Connectivity as a Result of Artificial Maturation of a Source Rock from the Shanxi Formation, Ordos Basin," *Energ. Fuel* **36**(17), 9967 (2022). DOI: [10.1021/acs.energyfuels.2c01402](https://doi.org/10.1021/acs.energyfuels.2c01402) [CHRN5]
- Liu, A., Liu, S., Zhang, R., Sang, G., Xia, K., "Cyclical Water Vapor Sorption-Induced Structural Alterations of Mine Roof Shale," *Int. J. Coal Geol.* **273**, 104267 (2023). DOI: [10.1016/j.coal.2023.104267](https://doi.org/10.1016/j.coal.2023.104267)

- Liu, C.-H., Cheu, C., Barker, J.G., Yang, L., Nieh, M.-P., "Facile Polymerization in a Bicellar Template to Produce Polymer Nano-Rings," *J. Colloid Interf. Sci.* **630**(Part A), 629 (2023). DOI: [10.1016/j.jcis.2022.09.141](https://doi.org/10.1016/j.jcis.2022.09.141) [CHRNS]
- Liu, C.-H., Krueger, S., Nieh, M.-P., "Synthesis of Polymer Nanoweb via a Lipid Template," *ACS Macro Lett.* **12**(7), 993 (2023). DOI: [10.1021/acsmacrolett.3c00255](https://doi.org/10.1021/acsmacrolett.3c00255) [CHRNS]
- Liu, L., Legg, B.A., Smith, W., Anovitz, L.M., Zhang, X., Harper, R., Pearce, C.I., Rosso, K.M., Stack, A.G., Bleuel, M., Mildner, D.F.R., Schenter, G.K., Clark, A.E., De Yoreo, J.J., Chun, J., Nakouzi, E., "Predicting Outcomes of Nanoparticle Attachment by Connecting Atomistic, Interfacial, Particle, and Aggregate Scales," *ACS Nano*, in press. DOI: [10.1021/acsnano.3c02145](https://doi.org/10.1021/acsnano.3c02145) [CHRNS]
- Liu, S., Xu, Y., Kotta, E.C., Miao, L., Ran, S., Paglione, J., Butch, N.P., Denlinger, J.D., Chuang, Y.-D., Wray, L.A., "Identifying *f*-Electron Symmetries of UTe₂ with O-Edge Resonant Inelastic X-ray Scattering," *Phys. Rev. B* **106**(24), L24111 (2022). DOI: [10.1103/PhysRevB.106.L24111](https://doi.org/10.1103/PhysRevB.106.L24111)
- Liu, S., Li, R., Tyagi, M., Akcora, P., "Confinement Effects in Dynamics of Ionic Liquids with Polymer-Grafted Nanoparticles," *ChemPhysChem* **23**(18), e202200219 (2022). DOI: [10.1002/cphc.202200219](https://doi.org/10.1002/cphc.202200219)
- Liyanage, W.L.N.C., Tang, N., Quigley, L., Borchers, J.A., Grutter, A.J., Maranville, B.B., Sinha, S.K., Reyren, N., Montoya, S.A., Fullerton, E.E., DeBeer-Schmitt, L., Gilbert, D.A., "Three-Dimensional Structure of Hybrid Magnetic Skyrmions Determined by Neutron Scattering," *Phys. Rev. B* **107**(18), 184412 (2023). DOI: [10.1103/PhysRevB.107.184412](https://doi.org/10.1103/PhysRevB.107.184412) [CHRNS]
- Lolla, S., Liang, H., Kusne, A.G., Takeuchi, I., Ratcliff, W., "A Semi-Supervised Deep-Learning Approach for Automatic Crystal Structure Classification," *J. Appl. Crystallogr.* **55**(4), 882 (2022). DOI: [10.1107/S1600576722006069](https://doi.org/10.1107/S1600576722006069) [CHRNS]
- Louden, E.R., Manni, S., Van Zandt, J.E., Leishman, A.W.D., Taufour, V., Bud'ko, S.L., DeBeer-Schmitt, L., Honecker, D., Dewhurst, C.D., Canfield, P.C., Eskildsen, M.R., "Effects of Magnetic and Non-Magnetic Doping on the Vortex Lattice in MgB₂," *J. Appl. Crystallogr.* **55**(4), 693 (2022). DOI: [10.1107/S160057672200468X](https://doi.org/10.1107/S160057672200468X)
- Lynn, J.W., Madhavan, V., Jiao, L., "Editorial: New Heavy Fermion Superconductors," *Front. Electron. Mater.* **2**, 1120381 (2023). DOI: [10.3389/femat.2022.1120381](https://doi.org/10.3389/femat.2022.1120381)
- Ma, C.T., Zhou, W., Kirby, B.J., Poon, S.J., "Interfacial Mixing Effect in a Promising Skyrmionic Material: Ferrimagnetic Mn₄N," *AIP Adv.* **12**(8), 085023 (2022). DOI: [10.1063/5.0109005](https://doi.org/10.1063/5.0109005)
- Mahynski, N.A., Monroe, J.I., Sheen, D.A., Paul, R.L., Chen-Mayer, H.H., Shen, V.K., "Classification and Authentication of Materials using Prompt Gamma Ray Activation Analysis," *J. Radioanal. Nucl. Ch.*, in press. DOI: [10.1007/s10967-023-09024-x](https://doi.org/10.1007/s10967-023-09024-x)
- Majcher, M.J., Himbert, S., Vito, F., Campea, M.A., Dave, R., Jensen, G.V., Rheinstadter, M.C., Smeets, N.M.B., Hoare, T., "Investigating the Kinetics and Structure of Network Formation in Ultraviolet-Photopolymerizable Starch Nanogel Network Hydrogels via Very Small-Angle Neutron Scattering and Small-Amplitude Oscillatory Shear Rheology," *Macromolecules* **55**(16), 7303 (2022). DOI: [10.1021/acs.macromol.2c00874](https://doi.org/10.1021/acs.macromol.2c00874) [CHRNS]
- Majkrzak, C.F., "The Development of Neutron Reflectometry as a Probe of the Nanoscale Structure of Polymer Thin Film Systems—Founded on the Pioneering Work of Professor Thomas P. Russell," *Nanoscale* **15**(10), 4725 (2023). DOI: [10.1039/d2nr06756k](https://doi.org/10.1039/d2nr06756k)
- Majkrzak, C.F., Berk, N.F., Maranville, B.B., Dura, J.A., Jach, T., "The Effect of Transverse Wavefront Width on Specular Neutron Reflection," *J. Appl. Crystallogr.* **55**(Part 4), 787 (2022). DOI: [10.1107/S160057672200440X](https://doi.org/10.1107/S160057672200440X)
- Mamontov, E., "Exploring the Limits of Biological Complexity Amenable to Studies by Incoherent Neutron Spectroscopy," *Life* **12**(8), 1219 (2022). DOI: [10.3390/life12081219](https://doi.org/10.3390/life12081219) [CHRNS]
- Mao, C.-N., Asa-Awuku, A., Zangmeister, C.D., Weaver, J.L., Radney, J.G., "Impactor Collection Efficiencies can Modify the Uncertainty of Multiply Charged Particles in Optical Extinction Measurements," *Aerosol Sci. Tech.* **57**(6), 562 (2023). DOI: [10.1080/02786826.2023.2194350](https://doi.org/10.1080/02786826.2023.2194350)
- Mao, Y., Shi, J., Cai, L., Hwang, W., Shi, Y.-C., "Microstructures of Starch Granules with Different Amylose Contents and Allomorphs as Revealed by Scattering Techniques," *Biomacromolecules* **24**(5), 1980 (2023). DOI: [10.1021/acs.biomac.2c01240](https://doi.org/10.1021/acs.biomac.2c01240)
- Marcial, J., Cicconi, M.R., Pearce, C.I., Klouček, J., Neeway, J.J., Pokorný, R., Vernerová, M., McCloy, J.S., Nienhuis, E.T., Sjöblom, R., Weaver, J.L., Hand, R.J., Hrma, P., Neuville, D.R., Kruger, A.A., "Effect of Network Connectivity on Behavior of Synthetic Broborg Hillfort Glasses," *J. Am. Ceram. Soc.* **106**(3), 1716 (2023). DOI: [10.1111/jace.18778](https://doi.org/10.1111/jace.18778)
- Marlow, J.B., Atkin, R., Warr, G.G., "How does Nanostructure in Ionic Liquids and Hybrid Solvents Affect Surfactant Self-Assembly?" *J. Phys. Chem. B* **127**(7), 1490 (2023). DOI: [10.1021/acs.jpcc.2c07458](https://doi.org/10.1021/acs.jpcc.2c07458)
- Matthews, B.E., Neeway, J.J., Nava Farias, L., Marcial, J., Arey, B.W., Soltis, J., Kovarik, L., Zhu, Z., Schweiger, M.J., Canfield, N., Varga, T., Bowden, M.E., Weaver, J.L., McCloy, J.S., Sjöblom, R., Hjörthner-Holdar, E., Englund, M., Ogenhall, E., Vicenzi, E.P., Corkhill, C.L., Thorpe, C., Hand, R.J., Peeler, D.K., Pearce, C.I., Kruger, A.A., "Micro- and Nanoscale Surface Analysis of Late Iron Age Glass from Broborg, a Vitriified Swedish Hillfort," *Microsc. Microanal.* **29**(1), 50 (2023). DOI: [10.1093/micmic/ozac032](https://doi.org/10.1093/micmic/ozac032)
- McAleer, E.G., Alazzawi, M.K., Hwang, C., LaManna, J.M., Jacobson, D.L., Khaykovich, B., Haber, R.A., Akdoğan, E.K., "Binder Removal from Ceramic Stereolithography Green Bodies: A Neutron Imaging and Thermal Analysis Study," *J. Am. Ceram. Soc.* **106**(7), 4399 (2023). DOI: [10.1111/jace.19095](https://doi.org/10.1111/jace.19095)
- McDannald, A., Frontzek, M., Savici, A.T., Doucet, M., Rodriguez, E.E., Meuse, K., Opsahl-Ong, J., Samarov, D., Takeuchi, I., Ratcliff, W., Kusne, A.G., "ANDIE the Autonomous Neutron Diffraction Explorer," *Neutron News* **34**(2), 6 (2023). DOI: [10.1080/10448632.2023.2190714](https://doi.org/10.1080/10448632.2023.2190714) [CHRNS]
- McDannald, A., Jores, H., DeCost, B., Baumann, A.E., Kusne, A.G., Choudhary, K., Yildirim, T., Siderius, D.W., Wong-Ng, W., Allen, A.J., Stafford, C.M., Ortiz-Montalvo, D.L., "Reproducible Sorbent Materials Foundry for Carbon Capture at Scale," *Cell Rep. Phys. Sci.* **3**(10), 101063 (2022). DOI: [10.1016/j.xcrp.2022.101063](https://doi.org/10.1016/j.xcrp.2022.101063)
- Mekonen, S.M., Kang, C.-J., Chaudhuri, D., Barbalas, D., Ran, S., Kotliar, G., Butch, N.P., Armitage, N.P., "Optical Investigation of the Heavy-Fermion Normal State in Superconducting UTe₂," *Phys. Rev. B* **106**(8), 085125 (2022). DOI: [10.1103/PhysRevB.106.085125](https://doi.org/10.1103/PhysRevB.106.085125)
- Meuse, C.W., Rubinson, K.A., "Spectral Similarity: Full-Wavelength Range Calibration of Circular Dichroism Spectroscopy," *Appl. Spectrosc.* **77**(1), 27 (2023). DOI: [10.1177/00037028221134128](https://doi.org/10.1177/00037028221134128)
- Michalak, D.J., Unger, B., Lorimer, E., Grishaev, A., Williams, C.L., Heinrich, F., Lösche, M., "Structural and Biophysical Properties of Farnesylated KRas Interacting with the Chaperone SmgGDS-558," *Biophys. J.* **121**(19), 3684 (2022). DOI: [10.1016/j.bpj.2022.05.028](https://doi.org/10.1016/j.bpj.2022.05.028)
- Mihăilescu, M., Worcester, D.L., Carroll, C.L., Chamberlin, A.R., White, S.H., "DOTAP: Structure, Hydration, and the Counterion Effect," *Biophys. J.* **122**(6), 1086 (2023). DOI: [10.1016/j.bpj.2023.01.031](https://doi.org/10.1016/j.bpj.2023.01.031)

- Mirzamani, M., Flickinger, M., Kharb, S., Jones, R.L., Ananthapadmanabhan, K., Smith, E., Kumari, H., "Investigating the Effect of Dipropylene Glycol and Mixed-Surfactant Concentrations on Perfume Release," *Colloid Surface. A* **650**, 129508 (2022). DOI: [10.1016/j.colsurfa.2022.129508](https://doi.org/10.1016/j.colsurfa.2022.129508)
- Mitra, S., Coppershylyak, M., Li, Y., Chandrasekhar, B., Koenig, R., Chen, M.-T., Evans, B., Heinrich, F., Deslouches, B., Tristram-Nagle, S., "Novel Helical Trp- and Arg-Rich Antimicrobial Peptides Locate near Membrane Surfaces and Rigidify Lipid Model Membranes," *Adv. Nanobiomed Res.* **3**(5), 2300013 (2023). DOI: [10.1002/anbr.202300013](https://doi.org/10.1002/anbr.202300013)
- Moseley, D.H., Liu, Z., Bone, A.N., Stavretis, S.E., Singh, S.K., Atanasov, M., Lu, Z., Ozerov, M., Thirunavukkuarasu, K., Cheng, Y., Daemen, L.L., Lubert-Perquel, D., Smirnov, D., Neese, F., Ramirez-Cuesta, A.J., Hill, S., Dunbar, K.R., Xue, Z.-L., "Comprehensive Studies of Magnetic Transitions and Spin-Phonon Couplings in the Tetrahedral Cobalt Complex $\text{Co}(\text{AsPh}_3)_2\text{I}_2$," *Inorg. Chem.* **61**(43), 17123 (2022). DOI: [10.1021/acs.inorgchem.2c02604](https://doi.org/10.1021/acs.inorgchem.2c02604)
- Mullangi, D., Evans, H.A., Yildirim, T., Wang, Y., Deng, Z., Zhang, Z., Mai, T.T., Wei, F., Wang, J., Hight Walker, A.R., Brown, C.M., Zhao, D., Canepa, P., Cheetham, A.K., "Noncryogenic Air Separation using Aluminum Formate $\text{Al}(\text{HCOO})_3$ (ALF)," *J. Am. Chem. Soc.* **145**(17), 9850 (2023). DOI: [10.1021/jacs.3c02100](https://doi.org/10.1021/jacs.3c02100)
- Nagao, M., Seto, H., "Neutron Scattering Studies on Dynamics of Lipid Membranes," *Biophys. Rev.* **4**(2), 021306 (2023). DOI: [10.1063/5.0144544](https://doi.org/10.1063/5.0144544) [CHNRNS]
- Nagle, J.F., Jennings, N., Qin, W., Yan, D., Tristram-Nagle, S., Heinrich, F., "Structure of the Gel Phase of diC22:1PC Lipid Bilayers determined by X-ray Diffraction," *Biophys. J.* **122**(6), 1033 (2023). DOI: [10.1016/j.bpj.2022.12.030](https://doi.org/10.1016/j.bpj.2022.12.030)
- Nahman-Lévesque, O., Sarenac, D., Lailey, O., Cory, D.G., Huber, M.G., Pushin, D.A., "Quantum Information approach to the Implementation of a Neutron Cavity," *New J. Phys.* **25**(7), 073016 (2023). DOI: [10.1088/1367-2630/acdb93](https://doi.org/10.1088/1367-2630/acdb93)
- Nakao, H., Nagao, M., Yamada, T., Imamura, K., Nozaki, K., Ikeda, K., Nakano, M., "Impact of Transmembrane Peptides on Individual Lipid Motions and Collective Dynamics of Lipid Bilayers," *Colloid Surface B*, in press. DOI: [10.1016/j.colsurfb.2023.113396](https://doi.org/10.1016/j.colsurfb.2023.113396) [CHNRNS]
- Neil, C.W., Boukhalfa, H., Xu, H., Ware, S.D., Ortiz, J., Avendaño, S., Harp, D., Broome, S., Hjelm, R.P., Mao, Y., Roback, R., Brug, W.P., Stauffer, P.H., "Gas Diffusion through Variably-Water-Saturated Zeolitic Tuff: Implications for Transport following a Subsurface Nuclear Event," *J. Environ. Radioactivity* **250**, 106905 (2022). DOI: [10.1016/j.jenvrad.2022.106905](https://doi.org/10.1016/j.jenvrad.2022.106905)
- Neil, C.W., Hjelm, R.P., Hawley, M.E., Watkins, E.B., Mao, Y., Pawar, R., Xu, H., "Small-Angle Neutron Scattering Investigation of Oil Recovery in Mineralogically Distinct Wolfcamp Shale Strata," *Energ. Fuel* **37**(7), 4937 (2023). DOI: [10.1021/acs.energyfuels.2c03964](https://doi.org/10.1021/acs.energyfuels.2c03964) [CHNRNS]
- Neumann, D., Wu, H., Toby, B.H., "Judith 'Judy' K. Stalick," *Neutron News* **34**(1), 24 (2023). DOI: [10.1080/10448632.2023.2166767](https://doi.org/10.1080/10448632.2023.2166767)
- Ngo, V.A., Queralt-Martín, M., Khan, F., Bergdoll, L., Abramson, J., Bezrukov, S.M., Rostovtseva, T.K., Hoogerheide, D.P., Noskov, S.Y., "The Single Residue K12 Governs the Exceptional Voltage Sensitivity of Mitochondrial Voltage-Dependent Anion Channel Gating," *J. Am. Chem. Soc.* **144**(32), 14564 (2022). DOI: [10.1021/jacs.2c03316](https://doi.org/10.1021/jacs.2c03316)
- Nguyen, M.H.L., Dziura, D., DiPasquale, M., Castillo, S.R., Kelley, E.G., Marquardt, D., "Investigating the Cut-off Effect of *n*-alcohols on Lipid Movement: A Biophysical Study," *Soft Matter* **19**(26), 5001 (2023). DOI: [10.1039/D2SM01583H](https://doi.org/10.1039/D2SM01583H) [CHNRNS]
- Nguyen, N.A., Bowland, C.C., He, L., Osti, N.C., Phan, M.D., Keum, J.K., Tyagi, M., Meek, K.M., Littrell, K.C., Mamontov, E., Ankner, J., Naskar, A.K., "A Sustainable Multi-Dimensional Printable Material," *Adv. Sustain. Syst.* **7**(7), 2300079 (2023). DOI: [10.1002/advsu.202300079](https://doi.org/10.1002/advsu.202300079) [CHNRNS]
- Novakov, S., Meisenheimer, P.B., Pan, G.A., Kezer, P., Vu, N.M., Grutter, A.J., Need, R.F., Mundy, J.A., Heron, J.T., "Composite Spin Hall Conductivity from Non-Collinear Antiferromagnetic Order," *Adv. Mater.*, in press. DOI: [10.1002/adma.202209866](https://doi.org/10.1002/adma.202209866) [CHNRNS]
- Ortiz, B.R., Sarte, P.M., Avidor, A.H., Hay, A., Kenney, E., Kolesnikov, A.I., Pajeroski, D.M., Aczel, A.A., Taddei, K.M., Brown, C.M., Wang, C., Graf, M.J., Seshadri, R., Balents, L., Wilson, S.D., "Quantum Disordered Ground State in the Triangular-Lattice Magnet NaRuO_2 ," *Nat. Phys.* **19**, 943 (2023). DOI: [10.1038/s41567-023-02039-x](https://doi.org/10.1038/s41567-023-02039-x)
- Pan, J., Lee, J., Li, M., Trump, B.A., Lobo, R.F., "Comparative Investigation of Ga- and In-CHA in the Non-Oxidative Ethane Dehydrogenation Reaction," *J. Catalysis* **413**, 812 (2022). DOI: [10.1016/j.jcat.2022.07.018](https://doi.org/10.1016/j.jcat.2022.07.018)
- Pang, Y., Hao, L., Wang, Y., "Convolutional Neural Network Analysis of Radiography Images for Rapid Water Quantification in PEM Fuel Cell," *Appl. Energ.* **321**, 119352 (2022). DOI: [10.1016/j.apenergy.2022.119352](https://doi.org/10.1016/j.apenergy.2022.119352)
- Pang, Y., Wang, Y., "Water Spatial Distribution in Polymer Electrolyte Membrane Fuel Cell: Convolutional Neural Network Analysis of Neutron Radiography," *Energy AI*, in press. DOI: [10.1016/j.egyai.2023.100265](https://doi.org/10.1016/j.egyai.2023.100265)
- Paul, R.L., Mille, M.M., Turkoglu, D.J., Chen-Mayer, H.H., "Prompt Gamma Ray Activation Analysis for Determining Chemical Composition of 3D Printing and Casting Materials used in Biomedical Applications," *J. Radioanal. Nucl. Ch.*, in press. DOI: [10.1007/s10967-023-08967-5](https://doi.org/10.1007/s10967-023-08967-5)
- Pena-Francesch, A., Jung, H., Tyagi, M., Demirel, M.C., "Diffusive Dynamic Modes of Recombinant Squid Ring Teeth Proteins by Neutron Spectroscopy," *Biomacromolecules* **23**(8), 3165 (2022). DOI: [10.1021/acs.biomac.2c00266](https://doi.org/10.1021/acs.biomac.2c00266) [CHNRNS]
- Peng, S., LaManna, J., Periwai, P., Shevchenko, P., "Water Imbibition and Oil Recovery in Shale: Dynamics and Mechanisms using Integrated Centimeter-to-Nanometer-Scale Imaging," *SPE Reserv. Eval. Eng.* **26**(1), 51 (2023). DOI: [10.2118/210567-PA](https://doi.org/10.2118/210567-PA)
- Peplowski, P.N., Elphic, R.C., Fritzler, E.L., Wilson, J.T., "Calibration of NASA's Neutron Spectrometer System (NSS) for Landed Measurements of Hydrogen Content of the Lunar Subsurface," *Nucl. Instrum. Meth. A* **1049**, 168063 (2023). DOI: [10.1016/j.nima.2023.168063](https://doi.org/10.1016/j.nima.2023.168063)
- Perera, R.M., Gupta, S., Li, T., Van Leeuwen, C.J., Bleuel, M., Hong, K., Schneider, G.J., "Nanoscale Lipid/Polymer Hybrid Vesicles: Effects of Triblock Copolymer Composition and Hydrophilic Weight Fraction," *ACS Appl. Polym. Mater.* **4**(12), 8858 (2022). DOI: [10.1021/acsapm.2c01272](https://doi.org/10.1021/acsapm.2c01272) [CHNRNS]
- Perez-Salas, U., Porcar, L., Garg, S., Ayee, M.A.A., Levitan, I., "Effective Parameters Controlling Sterol Transfer: A Time-Resolved Small-Angle Neutron Scattering Study," *J. Membrane Biol.* **255**(4), 423 (2022). DOI: [10.1007/s00232-022-00231-3](https://doi.org/10.1007/s00232-022-00231-3) [CHNRNS]
- Plumb, J., Poudyal, I., Dally, R.L., Daly, S., Wilson, S.D., Islam, Z., "Dark Field X-ray Microscopy Below Liquid-Helium Temperature: The Case of NaMnO_2 ," *Mater. Charact.*, in press. DOI: [10.1016/j.matchar.2023.113174](https://doi.org/10.1016/j.matchar.2023.113174)
- Prisk, T.R., Azuah, R.T., Abernathy, D.L., Granroth, G.E., Sherline, T.E., Sokol, P.E., Hu, J., Boninsegni, M., "Zero-Point Motion of Liquid and Solid Hydrogen," *Phys. Rev. B* **107**(9), 094511 (2023). DOI: [10.1103/PhysRevB.107.094511](https://doi.org/10.1103/PhysRevB.107.094511)
- Qian, J., Dong, Q., Chun, K., Zhu, D., Zhang, X., Mao, Y., Culver, J.N., Tai, S., German, J.R., Dean, D.P., Miller, J.T., Wang, L., Wu, T., Li, T., Brozena, A.H., Briber, R.M., Milton, D.K., Bentley, W.E., Hu, L., "Highly Stable, Antiviral, Antibacterial Cotton Textiles via Molecular Engineering," *Nat. Nanotechnol.* **18**(2), 168 (2023). DOI: [10.1038/s41565-022-01278-y](https://doi.org/10.1038/s41565-022-01278-y)

- Qin, Y., Shen, Y., Hao, Y., Wo, H., Shen, S., Ewings, R.A., Zhao, Y., Harriger, L.W., Lynn, J.W., Zhao, J., "Frustrated Magnetic Interactions and Quenched Spin Fluctuations in CrAs," *Chinese Phys. Lett.* **39**(12), 127501 (2022). DOI: [10.1088/0256-307X/39/12/127501](https://doi.org/10.1088/0256-307X/39/12/127501)
- Qiu, J., Chen, X., Le, A.N., López-Barrón, C.R., Rohde, B.J., White, R.P., Lipson, J.E.G., Krishnamoorti, R., Robertson, M.L., "Thermodynamic Interactions in Polydiene/Polyolefin Blends Containing Diverse Polydiene and Polyolefin Units," *Macromolecules* **56**(6), 2286 (2023). DOI: [10.1021/acs.macromol.2c01866](https://doi.org/10.1021/acs.macromol.2c01866) [CHRNS]
- Quarterman, P., Fan, Y., Chen, Z., Jensen, C.J., Chopdekar, R.V., Gilbert, D.A., Holtz, M.E., Stiles, M.D., Borchers, J.A., Liu, K., Liu, L., Grutter, A.J., "Probing Antiferromagnetic Coupling in Magnetic Insulator/Metal Heterostructures," *Phys. Rev. Mater.* **6**(9), 094418 (2022). DOI: [10.1103/PhysRevMaterials.6.094418](https://doi.org/10.1103/PhysRevMaterials.6.094418)
- Rajendran, M., Queralt-Martín, M., Gurnev, P.A., Rosencrans, W.M., Rovini, A., Jacobs, D., Abrantes, K., Hoogerheide, D.P., Bezrukov, S.M., Rostovtseva, T.K., "Restricting α -Synuclein Transport into Mitochondria by Inhibition of α -Synuclein-VDAC Complexation as a Potential Therapeutic Target for Parkinson's Disease Treatment," *Cell. Mol. Life Sci.* **79**, 368 (2022). DOI: [10.1007/s00018-022-04389-w](https://doi.org/10.1007/s00018-022-04389-w)
- Ranganathan, V.T., Bazmi, S., Wallin, S., Liu, Y., Yethiraj, A., "Is Ficoll a Colloid or Polymer? A Multitechnique Study of a Prototypical Excluded-Volume Macromolecular Crowder," *Macromolecules* **55**(20), 9103 (2022). DOI: [10.1021/acs.macromol.2c00677](https://doi.org/10.1021/acs.macromol.2c00677) [CHRNS]
- Riberolles, S.X.M., Slade, T.J., Dally, R.L., Sarte, P.M., Li, B., Han, T., Lane, H., Stock, C., Bhandari, H., Ghimire, N.J., Abernathy, D.L., Canfield, P.C., Lynn, J.W., Ueland, B.G., McQueeney, R.J., "Orbital Character of the Spin-Reorientation Transition in TbMn_2Sn_8 ," *Nat. Commun.* **14**(1), 2658 (2023). DOI: [10.1038/s41467-023-38174-5](https://doi.org/10.1038/s41467-023-38174-5)
- Romanyukha, A., Consani, K., LaManna, J., Thompson, A., Mintz, J., "Determination of Energy Correction Coefficient for Neutron Albedo Dosimeter. Three Approaches," *Radiat. Meas.* **156**, 106809 (2022). DOI: [10.1016/j.radmeas.2022.106809](https://doi.org/10.1016/j.radmeas.2022.106809)
- Rooks, J., Gilbert, P.H., Porcar, L., Liu, Y., Butler, P., "Anisotropy Factors in Small-Angle Scattering for Dilute Rigid-Rod Suspensions," *J. Appl. Crystallogr.* **56**(3), 683 (2023). DOI: [10.1107/S1600576723002182](https://doi.org/10.1107/S1600576723002182) [CHRNS]
- Roos, M.J., Bleser, S.M., Hernandez, L., Diederich, G.M., Siemens, M.E., Wu, M., Kirby, B.J., Zink, B.L., "Electrical, Optical, and Magnetic Properties of Amorphous Yttrium Iron Oxide Thin Films and Consequences for Non-Local Resistance Measurements," *J. Appl. Phys.* **133**(22), 223901 (2023). DOI: [10.1063/5.0144371](https://doi.org/10.1063/5.0144371)
- Ruiz-Franco, J., Rivas-Barbosa, R., Lara-Peña, M.A., Villanueva-Valencia, J.R., Licea-Claverie, A., Zaccarelli, E., Laurati, M., "Concentration and Temperature Dependent Interactions and State Diagram of Dispersions of Copolymer Microgels," *Soft Matter* **19**(20), 3614 (2023). DOI: [10.1039/D3SM00120B](https://doi.org/10.1039/D3SM00120B)
- Rus, E.D., Dura, J.A., "In Situ Neutron Reflectometry Study of a Tungsten Oxide/Li-Ion Battery Electrolyte Interface," *ACS Appl. Mater. Interfaces* **15**(2), 2832 (2023). DOI: [10.1021/acsami.2c16737](https://doi.org/10.1021/acsami.2c16737)
- Şahin, D., Çelikten, O.Ş., Williams, R.E., Cook, J.C., Weiss, A.G., Newton, T.H., Diamond, D., Majkrzak, C.F., King, H.E., Shen, J., Gurgun, A., Nahmani, E., Baroukh, I.R., Cheng, L.-Y., "NIST Neutron Source Preconceptual Design," [Paper Presentation]. RERTR 2022—42nd International Meeting on Reduced Enrichment for Research and Test Reactors (October 2022, Vienna, Austria) (2022). <https://www.rertr.anl.gov/RERTR42/index.shtml>
- Şahin, D., Newton, T.H., Dewey, S.C., Celikten, O.Ş., Brand, P.C., Cheng, L.-Y., "Lessons Learned on NBSR Licensing Actions," [Paper Presentation]. TRTR & IGORR Research Reactor Conference (June 2023, College Park, MD) (2023). <https://www.trtr.org/2023-conference-archive>
- Şahin, D., Çelikten, O.Ş., Cook, J.C., Weiss, A.G., Newton, T.H., Diamond, D., Majkrzak, C.F., King, H.E., Shen, J., Gurgun, A., Cheng, L.-Y., Kohut, P., Lu, C., Varuttamaseni, A., "Pre-Conceptual Design of the NIST Neutron Source," in "Proceedings of The European Research Reactor Conference," edited by European Nuclear Society, (RRFM 2023, April 2023, Antwerp, Belgium), 192 (2023).
- Saito, M., Tsuyoshi, Y., Nagao, M., "Synchrotron Mössbauer Time Domain Interferometry Sheds Lights on Dynamics of Atoms and Molecules on Nano to Micro Second Scales," *Butsuri* **77**(10), 690 (2022). DOI: [10.11316/butsuri.77.10_690](https://doi.org/10.11316/butsuri.77.10_690) [CHRNS]
- Sarenac, D., Henderson, M.E., Ekinci, H., Clark, C.W., Cory, D.G., DeBeer-Schmitt, L., Huber, M.G., Kapahi, C., Pushin, D.A., "Experimental Realization of Neutron Helical Waves," *Sci. Adv.* **8**(46), eadd2002 (2022). DOI: [10.1126/sciadv.add2002](https://doi.org/10.1126/sciadv.add2002)
- Satchell, N., Quarterman, P., Borchers, J.A., Burnell, G., Birge, N.O., "Absence of Magnetic Interactions in Ni-Nb Ferromagnet-Superconductor Bilayers," *Supercond. Sci. Tech.* **36**(5), 054002 (2023). DOI: [10.1088/1361-6668/acc430](https://doi.org/10.1088/1361-6668/acc430)
- Saurabh, K., Dudas, P.J., Gann, E., Reynolds, V.G., Mukherjee, S., Sunday, D., Martin, T.B., Beaucage, P.A., Chabiny, M.L., DeLongchamp, D.M., Krishnamurthy, A., Ganapathysubramanian, B., "CyRSOX: A GPU-Accelerated Virtual Instrument for Polarized Resonant Soft X-ray Scattering," *J. Appl. Crystallogr.* **56**(3), 868 (2023). DOI: [10.1107/S1600576723002790](https://doi.org/10.1107/S1600576723002790)
- Schöffmann, P., Sarkar, A., Hamed, M.H., Bhatnagar-Schöffmann, T., Pütter, S., Kirby, B.J., Grutter, A.J., Barthel, J., Kentzinger, E., Stellhorn, A., Gloskovskii, A., Müller, M., Brückel, T., "Strain and Charge Contributions to the Magnetoelectric Coupling in Fe_3O_4 /PMN-PT Artificial Multiferroic Heterostructures," *New J. Phys.* **24**(12), 123036 (2022). DOI: [10.1088/1367-2630/acac48](https://doi.org/10.1088/1367-2630/acac48)
- Scott, E.M., Caylor, J., Dewey, M.S., Gao, J., Heikes, C., Hoogerheide, S.F., Mumm, H.P., Nico, J.S., Stevens, J., Ullom, J., Vissers, M., "Large-Area TKIDs for Charged Particle Detection," *J. Low Temp. Phys.* **209**(3), 502 (2022). DOI: [10.1007/s10909-022-02892-9](https://doi.org/10.1007/s10909-022-02892-9)
- Scruggs, B., Sieber, J.R., Paul, R., Chen-Mayer, H., Marlow, A.F., Yen, J.H., "Certification of Standard Reference Material® 1270a Cr-Mo Low Alloy Steel A336 (F-22) (disk form)," *NIST SP* **260-231**, 1 (2022). DOI: [10.6028/NIST.SP.260-231](https://doi.org/10.6028/NIST.SP.260-231)
- Shaposhnik, Y., Çelikten, O.Ş., Cook, J., Weiss, A.G., Şahin, D., "Alternative Reflectors for the NIST Neutron Source," [Paper Presentation]. TRTR & IGORR Research Reactor Conference (June 2023, College Park, MD) (2023). <https://www.trtr.org/2023-conference-archive>
- Shaposhnik, Y., Weiss, A.G., Şahin, D., "The Statistic and Deterministic Kettle," in "Proceedings of the European Research Reactor Conference," edited by European Nuclear Society, (RRFM 2023, April 2023, Antwerp, Belgium), 309 (2023).
- Sharma, K., Agrawal, A., Masud, A., Satija, S.K., Ankner, J.F., Douglas, J.F., Karim, A., "Hiking Down the Free Energy Landscape using Sequential Solvent and Thermal Processing for Versatile Ordering of Block Copolymer Films," *ACS Appl. Mater. Interfaces* **15**(17), 21562 (2023). DOI: [10.1021/acsami.2c21924](https://doi.org/10.1021/acsami.2c21924)
- Sheffels, S., Balakrishnan, P.P., Huang, M., Muramoto, S., Borchers, J.A., Dura, J.A., Grutter, A.J., Beach, G.S.D., "Insight on Hydrogen Injection and GdOx/Co Interface Chemistry from In Operando Neutron Reflectometry and Secondary Ion Mass Spectrometry," *Appl. Phys. Lett.* **122**(2), 022407 (2023). DOI: [10.1063/5.0128835](https://doi.org/10.1063/5.0128835)
- Shen, J., Weiss, A.G., Gurgun, A., Baroukh, I.R., "A Turbulence Model Sensitivity Analysis of Thermal-Hydraulic Properties on the Pre-Conceptual NIST Neutron Source Design," in "Proceedings of the 2023 30th International Conference on Nuclear Engineering," edited by JSME, (2023 30th International Conference on Nuclear Engineering, May 2023, Kyoto, Japan), **ICONE30-1211** (2023).

- Shi, C., Hamann, T., Takeuchi, S., Alexander, G.V., Nolan, A.M., Limpert, M., Fu, Z., O'Neill, J., Godbey, G., Dura, J.A., Wachsmann, E.D., "3D Asymmetric Bilayer Garnet-Hybridized High-Energy-Density Lithium-Sulfur Batteries," *ACS Appl. Mater. Interfaces* **15**(1), 751 (2023). DOI: [10.1021/acsami.2c14087](https://doi.org/10.1021/acsami.2c14087)
- Shimizu, R., Cheng, D., Weaver, J.L., Zhang, M., Lu, B., Wynn, T.A., Burger, R., Kim, M.-C., Zhu, G., Meng, Y.S., "Unraveling the Stable Cathode Electrolyte Interface in all Solid-State Thin-Film Battery Operating at 5 V," *Adv. Energy Mater.* **12**(31), 2201119 (2022). DOI: [10.1002/aenm.202201119](https://doi.org/10.1002/aenm.202201119)
- Smith, E.M., Dudemaine, J., Placke, B., Schäfer, R., Yahne, D.R., DeLazzer, T., Fitterman, A., Beare, J., Gaudet, J., Buhariwalla, C.R.C., Podlesnyak, A., Xu, G., Clancy, J.P., Movshovich, R., Luke, G.M., Ross, K.A., Moessner, R., Benton, O., Bianchi, A.D., Gaulin, B.D., "Quantum Spin Ice Response to a Magnetic Field in the Dipole-Octupole Pyrochlore $\text{Ce}_2\text{Zr}_2\text{O}_7$," *Phys. Rev. B*, in press. DOI: [10.1103/PhysRevB.108.054438](https://doi.org/10.1103/PhysRevB.108.054438)
- Song, Q., Doyle, S., Pan, G.A., El Baggari, I., Segedin, D.F., Córdova Carrizales, D., Nordlander, J., Tzschaschel, C., Ehrets, J.R., Hasan, Z., El-Sherif, H., Krishna, J., Hanson, C., LaBollita, H., Bostwick, A., Jozwiak, C., Rotenberg, E., Xu, S.-Y., Lanzara, A., N'Diaye, A.T., Heikes, C.A., Liu, Y., Paik, H., Brooks, C.M., Pamuk, B., Heron, J.T., Shafer, P., Ratcliff, W.D., Botana, A.S., Moreschini, L., Mundy, J.A., "Antiferromagnetic Metal Phase in an Electron-Doped Rare-Earth Nickelate," *Nat. Phys.* **19**(4), 522 (2023). DOI: [10.1038/s41567-022-01907-2](https://doi.org/10.1038/s41567-022-01907-2)
- Song, S., Kim, J., Lee, J., Kim, H., Miyata, N., Kumar, N., Soh, Y., Jang, J.H., Hwang, C., Kirby, B.J., Park, S., "Vertical Inhomogeneous Magnetic Order in FeRh Film," *Appl. Surf. Sci.* **607**, 154870 (2023). DOI: [10.1016/j.apsusc.2022.154870](https://doi.org/10.1016/j.apsusc.2022.154870)
- Song, Y., Xu, M., Zheng, X., Zhou, C., Shi, N., Huang, Q., Wang, S., Jiang, Y., Xing, X., Chen, J., "A New Method to Enhance the Magnetocaloric Effect in (Sc,Ti)Fe₂ via Magnetic Phase Separation," *J. Mater. Sci. Technol.* **147**, 102 (2023). DOI: [10.1016/j.jmst.2022.11.018](https://doi.org/10.1016/j.jmst.2022.11.018)
- Sonje, J., Thakral, S., Krueger, S., Suryanarayanan, R., "Enabling Efficient Design of Biological Formulations through Advanced Characterization," *Pharm. Res.* **40**, 1459 (2023). DOI: [10.1007/s11095-023-03495-z](https://doi.org/10.1007/s11095-023-03495-z) [CHRNS]
- Stock, C., Roessler, B., Gehring, P.M., Rodriguez-Rivera, J.A., Giles-Donovan, N., Cochran, S., Xu, G., Manuel, P., Gutmann, M.J., Ratcliff, W.D., Fennell, T., Su, Y., Li, X., Luo, H., "Fast Broadband Cluster Spin-Glass Dynamics in $\text{PbFe}_{1/2}\text{Nb}_{1/2}\text{O}_3$," *Phys. Rev. B* **106**(14), 144207 (2022). DOI: [10.1103/PhysRevB.106.144207](https://doi.org/10.1103/PhysRevB.106.144207)
- Stojak Repa, K., Kirby, B.J., Miller, C.W., "Tunable Coupling in Magnetic Thin Film Heterostructures with a Magnetic Phase Transition," *Sci. Rep.* **13**(1), 9538 (2023). DOI: [10.1038/s41598-023-34322-5](https://doi.org/10.1038/s41598-023-34322-5)
- Sun, F., Yang, Y., Zhao, S., Wang, Y., Tang, M., Huang, Q., Ren, Y., Su, H., Wang, B., Zhao, N., Guo, X., Yu, H., "Local Li⁺ Framework Regulation of a Garnet-Type Solid-State Electrolyte," *ACS Energy Lett.* **7**(8), 2835 (2022). DOI: [10.1021/acsenergylett.2c01432](https://doi.org/10.1021/acsenergylett.2c01432)
- Sun, R., Yang, J., Patil, S., Liu, Y., Zuo, X., Lee, A., Yang, W., Wang, Y., Cheng, S., "Relaxation Dynamics of Deformed Polymer Nanocomposites as Revealed by Small-Angle Scattering and Rheology," *Soft Matter* **18**(46), 8867 (2022). DOI: [10.1039/D2SM00775D](https://doi.org/10.1039/D2SM00775D) [CHRNS]
- Sundar, S., Azari, N., Goeks, M.R., Gheidi, S., Abedi, M., Yakovlev, M., Dunsiger, S.R., Wilkinson, J.M., Blundell, S.J., Metz, T.E., Hayes, I.M., Saha, S.R., Lee, S., Woods, A.J., Movshovich, R., Thomas, S.M., Butch, N.P., Rosa, P.F.S., Paglione, J., Sonier, J.E., "Ubiquitous Spin Freezing in the Superconducting State of UTe_2 ," *Commun. Phys.* **6**(1), 24 (2023). DOI: [10.1038/s42005-023-01146-8](https://doi.org/10.1038/s42005-023-01146-8)
- Tan, L., Smith, M.D., Scott, H.L., Yahya, A., Elkins, J.G., Katsaras, J., O'Neill, H.M., Venkatesh Pingali, S., Smith, J.C., Davison, B.H., Nickels, J.D., "Modeling the Partitioning of Amphiphilic Molecules and Co-Solvents in Biomembranes," *J. Appl. Crystallogr.* **55**(6), 1401 (2022). DOI: [10.1107/S1600567222008998](https://doi.org/10.1107/S1600567222008998)
- Tang, N., Liyanage, W.L.N.C., Montoya, S.A., Patel, S., Quigley, L.J., Grutter, A.J., Fitzsimmons, M.R., Sinha, S., Borchers, J.A., Fullerton, E.E., DeBeer-Schmitt, L., Gilbert, D.A., "Skyrmion-Excited Spin-Wave Fractal Networks," *Adv. Mater.*, in press. DOI: [10.1002/adma.202300416](https://doi.org/10.1002/adma.202300416) [CHRNS]
- Tao, Y., Abernathy, D.L., Chen, T., Yildirim, T., Yan, J., Zhou, J., Goodenough, J.B., Louca, D., "Dynamics of Phase Transitions in YVO_3 Investigated via Inelastic Neutron Scattering and First-Principles Calculations," *Neutron News* **33**(3), 24 (2022). DOI: [10.1080/10448632.2022.2091401](https://doi.org/10.1080/10448632.2022.2091401)
- Taylor, C.S., Savadkoobi, M., Tyagi, P., Shoup, J.E., Arena, D.A., Borchers, J.A., Eckert, J., Gopman, D.B., "Sputter Gas Damage in Nanolayered Pt/Co/Ir-Based Synthetic Antiferromagnets for Top-Pinned Magnetic Tunnel Junctions," *ACS Appl. Nano Mater.* **6**(1), 131 (2023). DOI: [10.1021/acsnanm.2c03917](https://doi.org/10.1021/acsnanm.2c03917)
- Tein, Y.S., Thompson, B.R., Majkrzak, C., Maranville, B., Renggli, D., Vermant, J., Wagner, N.J., "Instrument for Measurement of Interfacial Structure-Property Relationships with Decoupled Interfacial Shear and Dilatational Flow: 'Quadrotrough,'" *Rev. Sci. Instrum.* **93**(9), 093903 (2022). DOI: [10.1063/5.0090350](https://doi.org/10.1063/5.0090350) [CHRNS]
- Trainer, C., Armitage, O.R., Lane, H., Rhodes, L.C., Chan, E., Benedičič, I., Rodriguez-Rivera, J.A., Fabelo, O., Stock, C., Wahl, P., "Relating Spin-Polarized STM Imaging and Inelastic Neutron Scattering in the van der Waals Ferromagnet Fe_3GeTe_2 ," *Phys. Rev. B* **106**(8), L081405 (2022). DOI: [10.1103/PhysRevB.106.L081405](https://doi.org/10.1103/PhysRevB.106.L081405) [CHRNS]
- Treiman, A.H., LaManna, J.M., Hussey, D.S., Declue, I., Anovitz, L.M., "Coordinated Neutron and X-ray Computed Tomography of Meteorites: Detection and Distribution of Hydrogen-Bearing Materials," *Meteorit. Planet. Sci.* **57**(10), 1820 (2022). DOI: [10.1111/maps.13904](https://doi.org/10.1111/maps.13904) [CHRNS]
- Trewhella, J., Vachette, P., Bierma, J., Blanchet, C., Brookes, E., Chakravarthy, S., Chatzimagas, L., Cleveland, IV, T.E., Cowieson, N., Crossett, B., Duff, A.P., Franke, D., Gabel, F., Gillilan, R.E., Graewert, M., Grishaev, A., Guss, J.M., Hammel, M., Hopkins, J., Huang, Q., Hub, J.S., Hura, G.L., Irving, T.C., Jeffries, C.M., Jeong, C., Kirby, N., Krueger, S., Martel, A., Matsui, T., Li, N., Pérez, J., Porcar, L., Prangé, T., Rajkovic, I., Rocco, M., Rosenberg, D.J., Ryan, T.M., Seifert, S., Sekiguchi, H., Svergun, D., Teixeira, S., Thureau, A., Weiss, T.M., Whitten, A.E., Wood, K., Zuo, X., "A Round-Robin Approach Provides a Detailed Assessment of Biomolecular Small-Angle Scattering Data Reproducibility and Yields Consensus Curves for Benchmarking," *Acta Crystallogr. D* **78**(11), 1315 (2022). DOI: [10.1107/S2059798322009184](https://doi.org/10.1107/S2059798322009184) [CHRNS]
- Trump, B.A., Qazvini, O.T., Lee, S.J., Jangodaz, E., Zhou, W., Brown, C.M., Telfer, S.G., "Flexing of a Metal-Organic Framework upon Hydrocarbon Adsorption: Atomic Level Insights from Neutron Scattering," *Chem. Mater.* **35**(3), 1387 (2023). DOI: [10.1021/acs.chemmater.2c03450](https://doi.org/10.1021/acs.chemmater.2c03450)
- Wang, J., Yu, Y., Wu, A., Chen Tan, K., Wu, H., He, T., Chen, P., "Fabrication of Lithium Indolide and Derivates for Ion Conduction," *ACS Appl. Mater. Interfaces* **14**(36), 41095 (2022). DOI: [10.1021/acsami.2c12322](https://doi.org/10.1021/acsami.2c12322)
- Wang, K., Composto, R.J., Winey, K.I., "ToF-SIMS Depth Profiling to Measure Nanoparticle and Polymer Diffusion in Polymer Melts," *Macromolecules* **56**(6), 2277 (2023). DOI: [10.1021/acs.macromol.3c00033](https://doi.org/10.1021/acs.macromol.3c00033)
- Wang, X., He, L., Sumner, J., Qian, S., Zhang, Q., O'Neill, H., Mao, Y., Chen, C., Al-Enizi, A.M., Nafady, A., Ma, S., "Spatially Confined Protein Assembly in Hierarchical Mesoporous Metal-Organic Framework," *Nat. Commun.* **14**(1), 973 (2023). DOI: [10.1038/s41467-023-36533-w](https://doi.org/10.1038/s41467-023-36533-w) [CHRNS]
- Waddock, N.J., Sterling, T.C., Vigil, J.A., Gold-Parker, A., Smith, I.C., Ahammed, B., Krogstad, M.J., Ye, F., Voneshen, D., Gehring, P.M., Rappe, A.M., Steinrück, H.-G., Ertekin, E., Karunadasa, H.I., Reznik, D., Toney, M.F., "The Nature of Dynamic Local Order in $\text{CH}_3\text{NH}_3\text{PbI}_3$ and $\text{CH}_3\text{NH}_3\text{PbBr}_3$," *Joule* **7**(5), 1051 (2023). DOI: [10.1016/j.joule.2023.03.017](https://doi.org/10.1016/j.joule.2023.03.017)

- Weaver, J.L., Job, A., Manandhar, K., Takeuchi, I., Downing, R.G., "Energy Broadening of Neutron Depth Profiles by Thin Polyamide Films," *J. Radioanal. Nucl. Ch.* **331**(12), 5013 (2022). DOI: [10.1007/s10967-022-08517-5](https://doi.org/10.1007/s10967-022-08517-5) [CHRNS]
- Weiss, A.G., Aranguren, B., Butt, M.I., Tsvetkov, P.V., Kimber, M.L., McDeavitt, S.M., "A Data-Driven Approach to Predicting Neutron Penetration through Media," *Ann. Nucl. Energy*, in press. DOI: [10.1016/j.anucene.2023.109953](https://doi.org/10.1016/j.anucene.2023.109953)
- Weiss, A.G., Tsvetkov, P.V., Hearne, J., Kimber, M.L., Wootan, D.W., McDeavitt, S.M., "A Sensitivity Analysis to Predict the Neutronics Behavior of Samples Irradiated in the VTR Rabbit System," *Ann. Nucl. Energy* **185**, 109708 (2023). DOI: [10.1016/j.anucene.2023.109708](https://doi.org/10.1016/j.anucene.2023.109708)
- Weiss, A.G., Çelikten, O.Ş., Gurgun, A., Shen, J.S., Şahin, D., Shaposhnik, Y., "Modeling Approach for the Design of the NIST Neutron Source," in "Proceedings of the European Research Reactor Conference 2023," (European Research Reactor Conference 2023, April 2023, Antwerp, Belgium), 202 (2023).
- Weiss, A.G., Gurgun, A., Baroukh, I.R., Shen, J., "Sensitivity Analyses of the Thermal-Hydraulics Safety Margins in the Proposed NIST Neutron Source Design," in "Proceedings of the 2023 30th International Conference on Nuclear Engineering ICONE30," edited by JSME, (2023 30th International Conference on Nuclear Engineering ICONE30, May 2023, Kyoto, Japan), **ICONE30-1223** (2023).
- Whipple, J., Sahin, D., Zino, Y., "Radiation Monitoring System Upgrade for the NBSR," in "Proceedings of the 2023 30th International Conference on Nuclear Engineering ICONE30," edited by JSME, (2023 30th International Conference on Nuclear Engineering ICONE30, May 2023, Kyoto, Japan), **ICONE30-1171** (2023).
- Wietfeldt, F.E., Biswas, R., Caylor, J., Crawford, B., Dewey, M.S., Fomin, N., Greene, G.L., Haddock, C.C., Hoogerheide, S.F., Mumm, H.P., Nico, J.S., Snow, W.M., Zuchegno, J., "Comment on 'Search for Explanation of the Neutron Lifetime Anomaly,'" *Phys. Rev. D* **107**(11), 118501 (2023). DOI: [10.1103/PhysRevD.107.118501](https://doi.org/10.1103/PhysRevD.107.118501)
- Williamson, N.H., Witherspoon, V.J., Cai, T.X., Ravin, R., Horkay, F., Basser, P.J., "Low-Field, High-Gradient NMR Shows Diffusion Contrast Consistent with Localization or Motional Averaging of Water Near Surfaces," *Magn. Reson. Lett.* **3**(2), 90 (2023). DOI: [10.1016/j.mrl.2023.03.009](https://doi.org/10.1016/j.mrl.2023.03.009)
- Will-Cole, A.R., Hart, J.L., Lauter, V., Grutter, A., Dubs, C., Lindner, M., Reimann, T., Valdez, N.R., Pearce, C.J., Monson, T.C., Cha, J.J., Heiman, D., Sun, N.X., "Negligible Magnetic Losses at Low Temperatures in Liquid Phase Epitaxy Grown $Y_3Fe_5O_{12}$ Films," *Phys. Rev. Mater.* **7**(5), 054411 (2023). DOI: [10.1103/PhysRevMaterials.7.054411](https://doi.org/10.1103/PhysRevMaterials.7.054411)
- Witherspoon, V.J., Ito, K., Snyder, C.R., Tyagi, M., Martin, T.B., Beaucage, P.A., Nieuwendaal, R.C., Vallery, R.S., Gidley, D.W., Wilbur, J.D., Welsh, D., Stafford, C.M., Soles, C.L., "Correlating the Diffusion of Water to Performance in Model Reverse Osmosis Polyamides with Controlled Crosslink Densities," *J. Membrane Sci.* **678**, 121670 (2023). DOI: [10.1016/j.memsci.2023.121670](https://doi.org/10.1016/j.memsci.2023.121670) [CHRNS]
- Wong-Ng, W., Yang, Y., Lan, Y., Liu, G., Kafle, A., Liu, W., Hou, J., Windover, D., Huang, Q., Krylyuk, S., Kaduk, J.A., "Powder X-ray Structural Analysis and Bandgap Measurements for $(Ca_xSr_{2-x})MnWO_6$ ($x = 0.25, 0.5, 0.75, 1.5, 1.75$)," *Powder Diffr.* **37**(3), 122 (2022). DOI: [10.1017/S0885715622000185](https://doi.org/10.1017/S0885715622000185)
- Worcester, D.L., Morse, J., Habeck, C.G., "James Byrne (1933–2022)," *Neutron News* **34**(1), 22 (2023). DOI: [10.1080/10448632.2023.2166762](https://doi.org/10.1080/10448632.2023.2166762)
- Wu, H., Zhou, W., Udovic, T.J., Bowman, Jr., R.C., Hauback, B.C., "Characterizing the $ZrBe_2H_2$ Phase Diagram via Neutron Scattering Methods," *Inorganics* **11**(1), 1 (2023). DOI: [10.3390/inorganics11010001](https://doi.org/10.3390/inorganics11010001)
- Wu, V.C., Evans, H.A., Giovine, R., Preefer, M.B., Ong, J., Yoshida, E., Cabelguen, P.-E., Clément, R.J., "Rapid and Energy-Efficient Synthesis of Disordered Rocksalt Cathodes," *Adv. Energy Mater.* **13**(10), 2203860 (2023). DOI: [10.1002/aenm.202203860](https://doi.org/10.1002/aenm.202203860)
- Xi, Y., Murphy, R.P., Zhang, Q., Zemborain, A., Narayanan, S., Chae, J., Choi, S.Q., Fluerasu, A., Wiegart, L., Liu, Y., "Rheology and Dynamics of a Solvent Segregation Driven Gel (SeedGel)," *Soft Matter* **19**(2), 233 (2023). DOI: [10.1039/D2SM01129H](https://doi.org/10.1039/D2SM01129H) [CHRNS]
- Xu, A.Y., Rinee, K.C., Stemple, C., Castellanos, M.M., Bakshi, K., Krueger, S., Curtis, J.E., "Counting the Water: Characterize the Hydration Level of Aluminum Adjuvants using Contrast Matching Small-Angle Neutron Scattering," *Colloid Surface. A* **648**, 129285 (2022). DOI: [10.1016/j.colsurfa.2022.129285](https://doi.org/10.1016/j.colsurfa.2022.129285) [CHRNS]
- Xu, L., Meng, T., Zheng, X., Li, T., Brozena, A.H., Mao, Y., Zhang, Q., Clifford, B.C., Rao, J., Hu, L., "Nanocellulose-Carboxymethylcellulose Electrolyte for Stable, High-Rate Zinc-Ion Batteries," *Adv. Funct. Mater.* **33**(27), 2302098 (2023). DOI: [10.1002/adfm.202302098](https://doi.org/10.1002/adfm.202302098)
- Yadav, A., Zhang, S., Benavides, P.A., Zhou, W., Saha, S., "Electrically Conductive π -Intercalated Graphitic Metal–Organic Framework Containing Alternate π -Donor/Acceptor Stacks," *Angew. Chem. Int. Edit.* **62**(26), e202303819 (2023). DOI: [10.1002/anie.202303819](https://doi.org/10.1002/anie.202303819)
- Yang, C., Xia, J., Cui, C., Pollard, T.P., Vatamanu, J., Faraone, A., Dura, J.A., Tyagi, M., Kattan, A., Thimsen, E., Xu, J., Song, W., Hu, E., Ji, X., Hou, S., Zhang, X., Ding, M.S., Hwang, S., Su, D., Ren, Y., Yang, X.-Q., Wang, H., Borodin, O., Wang, C., "All-Temperature Zinc Batteries with High-Entropy Aqueous Electrolyte," *Nat. Sustain.* **6**(3), 325 (2023). DOI: [10.1038/s41893-022-01028-x](https://doi.org/10.1038/s41893-022-01028-x) [CHRNS]
- Yang, H.-Y., Gaudet, J., Verma, R., Baidya, S., Bahrami, F., Yao, X., Huang, C.-Y., DeBeer-Schmitt, L., Aczel, A.A., Xu, G., Lin, H., Bansil, A., Singh, B., Tafti, F., "Stripe Helical Magnetism and Two Regimes of Anomalous Hall Effect in $NdAlGe$," *Phys. Rev. Mater.* **7**(3), 034202 (2023). DOI: [10.1103/PhysRevMaterials.7.034202](https://doi.org/10.1103/PhysRevMaterials.7.034202)
- Yao, W., Zhao, Y., Qiu, Y., Balz, C., Stewart, J.R., Lynn, J.W., Li, Y., "Magnetic Ground State of the Kitaev $Na_2Co_2TeO_6$ Spin Liquid Candidate," *Phys. Rev. Res.* **5**(2), L022045 (2023). DOI: [10.1103/PhysRevResearch.5.L022045](https://doi.org/10.1103/PhysRevResearch.5.L022045) [CHRNS]
- Yao, X., Gaudet, J., Verma, R., Graf, D.E., Yang, H.-Y., Bahrami, F., Zhang, R., Aczel, A.A., Subedi, S., Torchinsky, D.H., Sun, J., Bansil, A., Huang, S.-M., Singh, B., Blaha, P., Nikolić, P., Tafti, F., "Large Topological Hall Effect and Spiral Magnetic Order in the Weyl Semimetal $SmAlSi_3$," *Phys. Rev. X* **13**(1), 011035 (2023). DOI: [10.1103/PhysRevX.13.011035](https://doi.org/10.1103/PhysRevX.13.011035)
- Yin, X., Hewitt, D.R.O., Zheng, B., Yu, X., Carr, A.J., Grubbs, R.B., Bhatia, S.R., "Aqueous Assembly and Hydrogel Rheology of Sustainable Glyoxylate-Based Copolymers," *ACS Appl. Polym. Mater.* **4**(8), 5493 (2022). DOI: [10.1021/acsapm.2c00542](https://doi.org/10.1021/acsapm.2c00542) [CHRNS]
- Yixin, Z., Shimin, L., Yingfeng, S., "Pore Structures and Fluid Behaviors in Geomaterials," in "Small Angle X-ray and Neutron Scattering with Applications to Geomaterials," edited by McClain, J., (Elsevier, Amsterdam, Netherlands) Chap. **5**, 115 (2023). DOI: [10.1016/B978-0-323-95297-2.00005-X](https://doi.org/10.1016/B978-0-323-95297-2.00005-X)
- Yu, C., Lin, K., Chen, X., Jiang, S., Cao, Y., Li, W., Chen, L., An, K., Chen, Y., Yu, D., Kato, K., Zhang, Q., Gu, L., You, L., Kuang, X., Wu, H., Li, Q., Deng, J., Xing, X., "Superior Zero Thermal Expansion Dual-Phase Alloy via Boron-Migration Mediated Solid-State Reaction," *Nat. Commun.* **14**(1), 3135 (2023). DOI: [10.1038/s41467-023-38929-0](https://doi.org/10.1038/s41467-023-38929-0)
- Yu, Y., Wang, J., Qin, Z., Lv, Y., Pei, Q., Chen Tan, K., Zhang, T., Wu, A., He, T., Wu, H., Lipton, A.S., Chen, P., "Sodium Carbazolide and Derivatives as Solid-State Electrolytes for Sodium-Ion Batteries," *Angew. Chem. Int. Edit.* **135**(26), e202302679 (2023). DOI: [10.1002/ange.202302679](https://doi.org/10.1002/ange.202302679)
- Yuan, X., Krueger, S., Shalaev, E., "Protein-Surfactant and Protein-Protein Interactions during Freeze and Thaw: A Small-Angle Neutron Scattering Study of Lysozyme Solutions with Polysorbate and Poloxamer," *J. Pharm. Sci.* **112**, 76 (2023). DOI: [10.1016/j.xphs.2022.08.017](https://doi.org/10.1016/j.xphs.2022.08.017)

- Yusuf, M., LaManna, J.M., Paul, P.P., Agyeman-Budu, D.N., Cao, C., Dunlop, A.R., Jansen, A.N., Polzin, B.J., Trask, S.E., Tanim, T.R., Dufek, E.J., Thampy, V., Steinrück, H.-G., Toney, M.F., Weker, J.N., "Simultaneous Neutron and X-ray Tomography for Visualization of Graphite Electrode Degradation in Fast-Charged Lithium-Ion Batteries," *Cell Rep. Phys. Sci.* **3**(11), 101145 (2022). DOI: [10.1016/j.xcrp.2022.101145](https://doi.org/10.1016/j.xcrp.2022.101145)
- Zhang, L., Liu, Z., Yang, C., Garcia Sakai, V., Tyagi, M., Hong, L., "Conduction Mechanism in Graphene Oxide Membranes with Varied Water Content: From Proton Hopping Dominant to Ion Diffusion Dominant," *ACS Nano* **16**(9), 13771 (2022). DOI: [10.1021/acsnano.2c00686](https://doi.org/10.1021/acsnano.2c00686) [CHRNS]
- Zhang, M., Liu, Y., Zuo, X., Qian, S., Pingali, S.V., Gillilan, R.E., Huang, Q., Zhang, D., "pH-Dependent Solution Micellar Structure of Amphoteric Polypeptoid Block Copolymers with Positionally Controlled Ionizable Sites," *Biomacromolecules*, in press. DOI: [10.1021/acs.biomac.3c00407](https://doi.org/10.1021/acs.biomac.3c00407)
- Zhang, P., Balakrishnan, P.P., Eckberg, C., Deng, P., Nozaki, T., Chong, S.K., Quarterman, P., Holtz, M.E., Maranville, B.B., Qiu, G., Pan, L., Emmanouilidou, E., Ni, N., Sahashi, M., Grutter, A., Wang, K.L., "Exchange-Biased Quantum Anomalous Hall Effect," *Adv. Mater.*, in press. DOI: [10.1002/adma.202300391](https://doi.org/10.1002/adma.202300391)
- Zhang, W., Ma, Y., Posey, N.D., Lueckheide, M.J., Prabhu, V.M., Douglas, J.F., "Combined Simulation and Experimental Study of Polyampholyte Solution Properties: Effects of Charge Ratio, Hydrophobic Groups, and Polymer Concentration," *Macromolecules* **55**(15), 6750 (2022). DOI: [10.1021/acs.macromol.2c00977](https://doi.org/10.1021/acs.macromol.2c00977)
- Zhang, X.H., Gao, T.R., Fang, L., Fackler, S., Borchers, J.A., Kirby, B.J., Maranville, B.B., Lofland, S.E., N'Diaye, A.T., Arenholz, E., Ullah, A., Cui, J., Skomski, R., Takeuchi, I., "Interfacial Magnetic Vortex Formation in Exchange-Coupled Hard-Soft Magnetic Bilayers," *J. Magn. Magn. Mater.* **560**, 169627 (2022). DOI: [10.1016/j.jmmm.2022.169627](https://doi.org/10.1016/j.jmmm.2022.169627)
- Zhang, X., Lin, R.-B., Alothman, Z.A., Alduhaish, O., Yildirim, T., Zhou, W., Li, J.-R., Chen, B., "Promotion of Methane Storage Capacity with Metal-Organic Frameworks of High Porosity," *Inorg. Chem. Front.* **10**(2), 454 (2023). DOI: [10.1039/D2QI02255A](https://doi.org/10.1039/D2QI02255A)
- Zhang, X., Xu, Y., Halloran, T., Zhong, R., Broholm, C., Cava, R.J., Drichko, N., Armitage, N.P., "A Magnetic Continuum in the Cobalt-Based Honeycomb Magnet $\text{BaCo}_2(\text{AsO}_4)_2$," *Nat. Mater.* **22**(1), 58 (2023). DOI: [10.1038/s41563-022-01403-1](https://doi.org/10.1038/s41563-022-01403-1)
- Zhang, Z., Deng, Z., Evans, H.A., Mullangi, D., Kang, C., Peh, S.B., Wang, Y., Brown, C.M., Wang, J., Canepa, P., Cheetham, A.K., Zhao, D., "Exclusive Recognition of CO_2 from Hydrocarbons by Aluminum Formate with Hydrogen-Confined Pore Cavities," *J. Am. Chem. Soc.* **145**(21), 11643 (2023). DOI: [10.1021/jacs.3c01705](https://doi.org/10.1021/jacs.3c01705)
- Zhao, H., Zhou, Z., Feng, X., Liu, C., Wu, H., Zhou, W., Wang, H., "Hydrogen-Bonded Organic Framework for Red Light-Mediated Photocatalysis," *Nano Res.* **16**(7), 8809 (2023). DOI: [10.1007/s12274-023-5543-z](https://doi.org/10.1007/s12274-023-5543-z)
- Zhao, X., Liu, Y., Zhao, L., Yazdkhasti, A., Mao, Y., Siciliano, A.P., Dai, J., Jing, S., Xie, H., Li, Z., He, S., Clifford, B.C., Li, J., Chen, G.S., Wang, E.Q., Desjarlais, A., Saloni, D., Yu, M., Košny, J., Zhu, J.Y., Gong, A., Hu, L., "A Scalable High-Porosity Wood for Sound Absorption and Thermal Insulation," *Nat. Sustain.* **6**(3), 306 (2023). DOI: [10.1038/s41893-022-01035-y](https://doi.org/10.1038/s41893-022-01035-y)

Instruments and Contacts

(name, tel. 301-975-xxxx, email)

HIGH RESOLUTION POWDER DIFFRACTOMETER (BT-1):

- H. Wu, 2387, hui.wu@nist.gov
- H. Evans, 0616, hayden.evans@nist.gov
- C. M. Brown, 5134, craig.brown@nist.gov

ENGINEERING DIFFRACTOMETER (BT-8):

- T. Gnäupel-Herold, 5380, thomas.gnaeupel-herold@nist.gov

vSANS INSTRUMENT (NG-3) (CHRNS):

- E. Kelley, 8584, elizabeth.kelley@nist.gov
- Y. Liu, 6235, yun.liu@nist.gov
- J. Gaudet, 5010, jonathon.gaudet@nist.gov
- R. P. Murphy, 8544, ryan.murphy@nist.gov
- C. Gagnon, 2020, cedric.gagnon@nist.gov

30-m SANS INSTRUMENT (NG-B):

- P. D. Butler, 2028, paul.butler@nist.gov
- Y. Mao, 6017, yimin.mao@nist.gov
- P. Beaucage, 8367, peter.beaucage@nist.gov
- J. R. Krzywon, 6650, jkrzywon@nist.gov

10-m SANS INSTRUMENT (NG-B) (nSoft):

- J. Seppala, 2836, jonathan.seppala@nist.gov
- K. Weigandt, 8396, kathleen.weigandt@nist.gov
- T. Martin, 8866, tyler.martin@nist.gov
- P. Beaucage, 8367, peter.beaucage@nist.gov

uSANS, PERFECT CRYSTAL SANS (BT-5):

- J. G. Barker, 6732, john.barker@nist.gov
- P. D. Butler, 2028, paul.butler@nist.gov

30-m SANS INSTRUMENT (NG-7):

- S. Teixeira, 4404, susana.marujoteixeira@nist.gov
- J. G. Barker, 6732, john.barker@nist.gov
- J. Gaudet, 5010, jonathon.gaudet@nist.gov
- J. R. Krzywon, 6650, jkrzywon@nist.gov

CANDOR, WHITE-BEAM REFLECTOMETER/DIFFRACTOMETER (CHRNS):

- A. Grutter, 4198, alexander.grutter@nist.gov
- D. Hoogerheide, 8839, david.hoogerheide@nist.gov
- B. Maranville, 6034, brian.maranville@nist.gov
- C. F. Majkrzak, 5251, charles.majkrzak@nist.gov

MAGIK, OFF-SPECULAR REFLECTOMETER (NG-D):

- J. A. Dura, 6251, joseph.dura@nist.gov
- F. Heinrich, 4507, frank.heinrich@nist.gov

POLARIZED BEAM REFLECTOMETER/DIFFRACTOMETER (NG-D):

- C. F. Majkrzak, 5251, cmajkrzak@nist.gov
- J. A. Borchers, 6597, julie.borchers@nist.gov

NEUTRON REFLECTOMETER-HORIZONTAL SAMPLE (NG-7):

- S. K. Satija, 5250, satija@nist.gov

HFBS, HIGH-FLUX BACKSCATTERING SPECTROMETER (NG-2) (CHRNS):

- M. Tyagi, 2046, madhusudan.tyagi@nist.gov
- R. Azuah, 5604, richard.azuah@nist.gov

NSE, NEUTRON SPIN ECHO SPECTROMETER (NG-A) (CHRNS):

- A. Faraone, 5254, antonio.faraone@nist.gov
- M. Nagao, 5505, michihiro.nagao@nist.gov

MACS, MULTI-ANGLE CRYSTAL SPECTROMETER (BT-9) (CHRNS):

- J. A. Rodriguez-Rivera, 6019, jose.rodriguez@nist.gov
- Y. Qiu, 3274, yiming.qiu@nist.gov

DOUBLE-FOCUSING TRIPLE-AXIS SPECTROMETER (BT-7):

- Y. Zhao, 2164, yang.zhao@nist.gov
- R. Dally, 8369, rebecca.dally@nist.gov
- J. W. Lynn, 6246, jeff.lynn@nist.gov

SPINS, SPIN-POLARIZED TRIPLE-AXIS SPECTROMETER (NG-5):

- G. Xu, 4144, guangyong.xu@nist.gov

TRIPLE-AXIS SPECTROMETER (BT-4):

- W. Ratcliff, 4316, william.ratcliff@nist.gov

DCS, DISK-CHOPPER TIME-OF-FLIGHT SPECTROMETER (NG-4):

- N. Butch, 4863, nicholas.butch@nist.gov
- W. Zhou, 8169, wei.zhou@nist.gov
- C. M. Brown, 5134, craig.brown@nist.gov

COLD NEUTRON DEPTH PROFILING (NG-A')::

- J. Weaver, 6311, jamie.weaver@nist.gov

COLD-NEUTRON PROMPT-GAMMA NEUTRON ACTIVATION ANALYSIS (NG-D):

- R. L. Paul, 6287, rpaul@nist.gov
- H. H. Chen-Mayer, 5595, heather.chen-mayer@nist.gov

THERMAL-NEUTRON PROMPT-GAMMA ACTIVATION ANALYSIS (VT-5):

- R. L. Paul, 6287, rpaul@nist.gov

OTHER ACTIVATION ANALYSIS FACILITIES:

- N. Sharp, 3926, nicholas.sharp@nist.gov
- R. L. Paul, 6287, rpaul@nist.gov

THERMAL NEUTRON IMAGING FACILITY (BT-2):

- J. LaManna, 6809, jacob.lamanna@nist.gov
- D. Jacobson, 6207, david.jacobson@nist.gov
- E. Baltic, 4842, eli.baltic@nist.gov
- D. Hussey, 6465, daniel.hussey@nist.gov

COLD NEUTRON IMAGING INSTRUMENT (NG-6):

- D. Hussey, 6465, daniel.hussey@nist.gov
- E. Baltic, 4842, eli.baltic@nist.gov
- D. Jacobson, 6207, david.jacobson@nist.gov
- J. LaManna, 6809, jacob.lamanna@nist.gov

NEUTRON INTERFEROMETER (NG-7):

- M. Huber, 5641, michael.huber@nist.gov
- S. Hoogerheide, 8582, shannon.hoogerheide@nist.gov

QUANTUM-BASED NEUTRON INTERFEROMETER FACILITY (NG-7):

- M. Huber, 5641, michael.huber@nist.gov
- S. Hoogerheide, 8582, shannon.hoogerheide@nist.gov

FUNDAMENTAL NEUTRON PHYSICS STATION (NG-C):

- S. Hoogerheide, 8582, shannon.hoogerheide@nist.gov
- H. P. Mumm, 8355, hans.mumm@nist.gov
- M. S. Dewey, 4843, maynard.dewey@nist.gov
- J. Nico, 4663, jeffrey.nico@nist.gov

PhAND: ADVANCED NEUTRON DETECTOR DEVELOPMENT (NG-6a):

- H. P. Mumm, 8355, hans.mumm@nist.gov
- C. B. Shahi, 8194, chandra.shahi@nist.gov

α-γ: ABSOLUTE NEUTRON COUNTER (NG-6m):

- H. P. Mumm, 8355, hans.mumm@nist.gov
- M. S. Dewey, 4843, maynard.dewey@nist.gov

INTERFEROMETER FOR FUNDAMENTAL PHYSICS (NG-6u):

- M. Huber, 5641, michael.huber@nist.gov
- D. Hussey, 6465, daniel.hussey@nist.gov

THEORY AND MODELING:

- J. E. Curtis, 3959, joseph.curtis@nist.gov
- T. Yildirim, 6228, taner@nist.gov

NEUTRON TEST STATION (PHADES):

- S. Watson, 6232, shannon.watson@nist.gov

INSTRUMENTS UNDER DEVELOPMENT:

PoLAR:

- L. Harriger, 8360, leland.harriger@nist.gov

NIST Center For Neutron Research Contacts

Copies of annual reports, facility information, user information, and research proposal guidelines are available electronically.

Please visit our website: <http://www.ncnr.nist.gov>

FOR A PAPER COPY OF THIS REPORT:

Steve Kline
301-975-6243
steven.kline@nist.gov

FOR GENERAL INFORMATION ON THE FACILITY:

Jim Adams
301-975-6210
james.adams@nist.gov

Dan Neumann
301-975-5252
dan.neumann@nist.gov

FOR INFORMATION ON VISITING THE FACILITY AND/OR USER ACCESS QUESTIONS:

Julie Keyser
301-975-8200
julie.keyser@nist.gov

Mary Ann FitzGerald
301-975-8200
maryann.fitzgerald@nist.gov

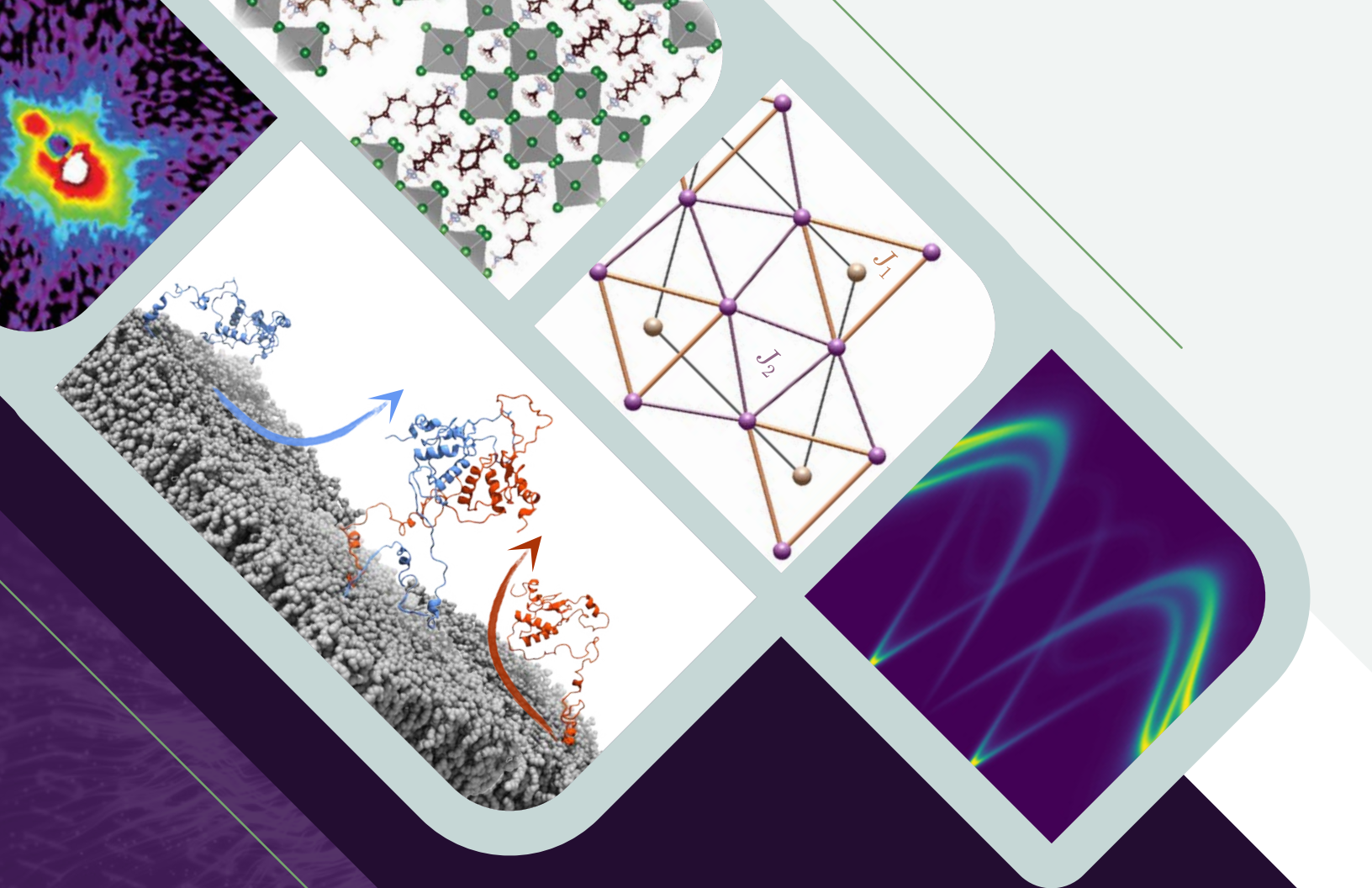
Becky Ogg
301-975-8200
rebecca.ogg@nist.gov

FOR INFORMATION ON PERFORMING RESEARCH AT THE FACILITY:

Yamali Hernandez
301-975-5295
yamali.hernandez@nist.gov

FACILITY ADDRESS:

NIST Center for Neutron Research
National Institute of Standards and Technology
100 Bureau Drive, Mail Stop 6100
Gaithersburg, MD 20899-6100 USA



NIST

**National Institute of
Standards and Technology**
U.S. Department of Commerce

2023

NIST CENTER FOR NEUTRON RESEARCH

National Institute of Standards and Technology
100 Bureau Drive, MS 6100
Gaithersburg, MD 20899-6100

www.ncnr.nist.gov